International School for Advanced Studies

PhD Thesis

Local and non-local correlations in Topological Insulators and Weyl Semimetals

Candidate: Lorenzo Crippa
Supervisors: Prof. Massimo Capone
Dr. Adriano Amaricci

September 2020

Contents

Introduction

The study of *topologically ordered* phases of matter has experienced a rapidly growing interest in recent years. Such phases elude the conventional classification based on broken symmetry, as they differ one from another in a more subtle way than a liquid from a solid or a paramagnet from a ferromagnet. Indeed, two samples of the same material in the same external conditions could have different topological phases, merely as a consequence of their thickness or of the direction of their surface. As abstract as the concept may be, the experimental consequences of topology are definitely real and observable: a conveniently engineered material in a specific topological phase can, for example, exhibit dissipation-less conducting states at the boundary, whereas a topologically trivial sample is insulating.

What does *topology* have to do with the classification of the phases of matter? Generally speaking, topology concerns the study of the properties of an object which remain unaltered by continuous deformations. At a formal level, such deformations are defined in terms of suitable maps, named *homeomorphisms*, from the parameter space the system depends upon to the space of physical states of the system itself. The topological properties of the system are then revealed by studying the properties of any such map against deformations.

Consistently with this very broad definition, topological phases have little requirements on the specific constituents of the system. Hence, theoretical and experimental realizations of topologically nontrivial systems vary wildly: from bosons to fermions, from electronic crystals to optical lattices, from metamaterials to circuits to classical setups made up of masses and springs, carefully engineered samples can exhibit nontrivial physical responses.

It is natural to ask what role topology can play in the realm of solid state physics. In this case, the response properties of materials arise from the behavior of the conduction electrons, hence we consider the map relating the periodic k-space, i.e. the Brillouin zone, with the space of Bloch electronic wavefunctions. Then, Band Theory of solids allows us to derive a dispersion law for the energies eigenvalues of the system as a function of k which form the *band structure*. This, in turn, is at the base of the usual classification of materials as metals or insulators depending on the filling of the bands. The concept of topology adds a new flavour to this classification, showing that not all the insulators are equal. Indeed, the topological characterization introduces a finer distinction among band insulating states based on the geometrical properties of the Bloch states.

The topological state of the system can be characterized by means of dimensionless, discrete quantities, known as *topological invariants*. These invariants identify a class of systems all topologically equivalent under smooth deformations. As such, the topological invariants can only change across a continuous *topological quantum phase transition*, going from one class to another. Yet, the change of the invariant itself can only be discontinuous, signalling an overall modification of the properties of the system class, with consequent abrupt variation of all the features mentioned above. By contrast, as long as the topological invariants are nonzero, all

the nontrivial topological properties are *protected*, i.e. they are (generally) not destroyed by perturbations or disorder.
For the systems we will encounter in this work, topological protection is guaranteed by *symmetries*, such as for example Time-Reversal symmetry which forbids hybridization between counter-propagating edge states.

However, it is well established that the Band Theory description does not alone exhaust the variety of materials that solid state physics deals with: some elements and compounds, by virtue of the properties of their atomic orbitals, can not be described in terms of a single-particle theory. These systems, known as *strongly correlated materials*, show a variety of features that one-particle band theory cannot adequately explain. The most paradigmatic hallmark of strong correlation is the Mott insulator, a material in which strong interactions lead to the localization of the electrons, hence to an insulating behaviour in a partially filled band, in striking constrast with the Band Theory description. The Mott insulator, and very often the states realized in its proximity, will therefore be inaccessible to Band Theory, and hence to the standard topological classification based on it. In light of these limitations, the topological description of strongly correlated materials had to adapt. Indeed, an entire framework known as Topological Field Theory has been developed in order to describe the geometric properties of phases where the band structure does not correctly capture the relevant physics of the system.

From a theoretical point of view, it is possible to start from a non-interacting system for which Band Theory works perfectly and to continuously "turn on" electronic interaction. As opposed to the variation of single-particle parameters, there is no reason why the topological nature of the solutions should be protected from the inclusion of interactions. The increase of electronic interactions forces us to redefine the mapping in the larger context of Topological Field Theory. Accordingly, all the topological invariants of the noninteracting system have to be extended or reformulated, as the hopping structure of the system, at the root of their definition, is now competing with the localization effects following from high electronic correlation.

Many intriguing questions therefore arise: is it possible to define an "adiabatic" continuation of topological phases for increasing values of electronic interaction? Is there a substantial difference between local and momentum-dependent effects of correlation on the topological mapping? In the case the topology of the noninteracting system is not completely washed away, what is the effect of interaction on the topological protection of the relevant quantities of the system, and on the features of the relative phase transitions?

In this thesis we will answer some of these questions studying concrete models of interacting topological systems, namely two-dimensional Quantum Spin Hall insulator and Weyl semimetals. We will investigate the evolution of the topological phases of the system, as well as the transitions among them, for increasing values of the electronic interaction. We will uncover some interesting phenomena which will ultimately put to the test the intrinsic protection of the topological properties.

The thesis is organized as follows:

- In Chapter 1 we will give a brief excursus on the description of topological phases of matter, from their experimental discovery to their systematization as a consequence of quantum entanglement and symmetry. We will then follow the historical path that brought to the definition of the Quantum Spin-Hall insulators, and provide a derivation of the associated topological invariants. Among these systems, we will especially focus on the Bernevig-Hughes-Zhang (BHZ) Hamiltonian, the first Quantum Spin Hall insulator to find experimental proof in a quantum-well setup. Due to its simplicity and versatility,

this will constitute the theoretical model at the base of our study.

- In Chapter 2 we will concentrate on the second half of the picture, outlining a path that leads from the Band Theory of solids to the discovery of strongly correlated effects and phases. We will briefly touch on the theory of Landau-Fermi liquid and those states that fall outside its description, and describe the Green's function framework which is at the base of many methods devoted to the study of strongly correlated systems. We will then derive the most used expressions for the interaction Hamiltonians of such systems. Finally, we will see how the definition of topological invariants can be conveniently broadened beyond Band Theory to account for the presence of interaction.

- Chapter 3 will be devoted to the illustration of the main solution methods we employ in our work, the most well-known of which is Dynamical Mean-Field theory (DMFT). We will then introduce some cluster-based solution methods, which aim to describe the physics of the full interacting system by directly solving a finite subset of sites. In particular, we will concentrate on the Cluster-DMFT, an extension of the previously mentioned single-site DMFT, and on the Variational Cluster Approximation, which draws its roots in a different approach known as Self-Energy Functional Theory.

- In Chapter 4 we will show the practical implementation of the previously outlined methods: in particular, we will describe the technical realization of an Exact Diagonalization-based solver for the interacting fermion problem. We will touch on the way the Fock space is constructed and how its exponentially increasing size can be kept under control through some assumptions on conserved quantum numbers. We will present some benchmarks related to our implementation of the code, and comment on the way the ED routine can serve as the core of a general-purpose (C)-DMFT or VCA solver.

- Chapter 5 will contain our analysis on a derivative of the BHZ model introduced in Chapter 1. In particular, we will focus on a perturbed version of its three-dimensional extension, breaking Time-Reversal symmetry. We will describe the interesting topological phase this system supports, touching on the protection of the gapless points of the band structure and their related topological invariants. Making use of the notions of Chapter 2 and single-site DMFT we will then describe the way the topological transitions are affected by the presence of electronic interaction, finding surprising consequences for the topological protection of the previously listed quantities.

- Finally, in Chapter 6 we will return to the original 2d BHZ, which in the context of single-site DMFT is known to show a *discontinuous* topological phase transition at high values of electronic interaction. We will seek confirmation for these results under the lens of the cluster methods described in Chapter 3, assessing the role of non-local effects of correlations in the determination of the topology of the interacting system.

Chapter 1

A short introduction to topological matter

1.1 From Landau theory to topological order

Physical matter organizes into a plethora of different configurations, resulting in a rich variety of structures and phases, the careful classification of which is indeed an extraordinary task. The size of this challenge can be dramatically reduced considering that microscopically different systems can show the same properties and behaviour. If we find a systematic way to group physical systems based on a unifying principle, their classification becomes far easier and, at the same time, provides us with a powerful descriptive theory.

The realization of this intuition is due to Landau, who introduced the concept of *order parameter* to characterize the different phases of matter and the transitions between them. The order parameter is a local quantity, often an observable, whose value discriminates univocally between two different phases of matter. Based on this idea, Landau formulated his theory of phase transitions [1] which provides an effective description of the transformation of a system from one phase to another, where the complexity of the microscopical system is replaced by a simplified expression of the free energy function written in terms of the order parameter and external fields.

The Landau theory of phase transitions underlines the important relation between the physical properties of a system and its symmetries, i.e. the invariance of such system under the action of specific transformations. The idea of this relation, although conceptually simple, is indeed very general and deeply rooted in the laws of nature, and provides a natural explanation to many physical phenomena. For example, the electric field emanating from a point charge has no reason to privilege a spatial direction, since every spatial direction can be transformed into another by rotation. Hence the field is radial, and the potential is spheric.
If the order parameter can be described as a vector, in absence of an explicitly *symmetry breaking* term, such as the coupling with an external field, there is no reason for Landau's free energy to privilege a certain direction of the order parameter. Hence the energy functional can only depend on its modulus.
However, in the phase where it is finite, the order parameter must necessarily assume one among the possible values, therefore spontaneously reducing the symmetry of the system. The model will still be symmetric, but the solution is not. This mechanism is known as *spontaneous symmetry breaking*.

Landau's approach is considerably general and allows to describe a huge variety of phenomena: from boiling water to magnetization loss in a overheated magnet, to superconductivity. The simplest version of the theory is, however, based on the assumption that the order parameter is a homogeneous quantity. It is, in other words, a mean-field theory. A significant advance towards an accurate description of the phase transitions came with the development of Landau-Ginzburg Theory (LGT) [2]. The order parameter becomes a function of the position and, accordingly, the free energy becomes a functional. The inclusion of these spatial fluctuations of the order parameter plays indeed a prominent role in the description of phase transitions. For instance, the correlation length of fluctuations diverges at the critical temperature, where the phase transition from a disordered to an ordered phase happens. More than that, the fluctuations can destroy a mean-field order parameter. This happens when the dimensionality is reduced according to what has been called the Ginzburg criterion.

The fluctuations of the order parameter also unveil an intriguing consequence of spontaneous symmetry breaking. A gapless excitation, known as the Goldstone mode, exists for every broken continuous symmetry. A Goldstone mode is a collective excitation with vanishing energy for an arbitrary low momentum and is, in a sense, the way the system remembers that it has singled out one ground state among infinitely many others. For example, an ordered ferromagnet supports spin waves whose energy cost vanishes with the increase of their wavelength.

The theory of spontaneous symmetry breaking and associated gapless excitations has far reaching consequences. It is at the base of the description of an enormous range of phenomena, from the rotational invariance-breaking in magnetic ordering with the already mentioned spin waves (or magnons) to the translational symmetry-breaking liquid-solid transition, with associated acoustic vibrations (phonons), to superconductivity and superfluidity. In particular, this latter example is historically at the base of the formulation of the Anderson-Higgs mechanism [3], which accounts for the Goldstone modes becoming massive due to interaction with a gauge field. Remarkably, this was the starting point of crucial results in condensed matter (as the field-theoretical explanation of the Meissner effect) and particle physics [4].

Given the many successes of the LGT it is very hard to overstate its descriptive power. On the contrary, precisely because the theory is so general and far-reaching, for a long period it was believed to completely exhaust the description of phase transitions. This conception was put to the test by Anderson [5, 6], who introduced a new theoretical phase of matter called Quantum Spin Liquid (QSL) in relation with high-T_c superconductivity. The QSL is an elusive phase whose existence has been for a long time subject of debate. A broad definition describes it as a system of spins which are highly correlated, but do not order even at zero temperature [7]. The main feature of a QSL is therefore its long-range entanglement, as is apparent by the illustrative example of the so called Kitaev toric code [8]. This is a two-dimensional periodic square lattice model in which spin-1/2 particles sit on the links between lattice sites. Two types of operators act on the model: they are called "stars" and "plaquettes". These correspond to the product of the spin-x component of the links around a vertex and the spin-z component around a minimal lattice square, as shown in figure Fig. 1.1. The elementary excitations of such a model are obtained by flipping the sign of such operators, changing the sign of an odd number of spin-x per star or spin-z per plaquette.

Interestingly, there is no way to write an eigenstate of this model as a product state in a purely local basis. If one attempts such a description, e.g. in the local σ_i^x basis, the ground state eigenvectors will be superpositions of states having a given number of closed "loops" of flipped x-component spins encircling the torus in the $\hat{x}$ and $\hat{y}$ direction. Moreover, one will find

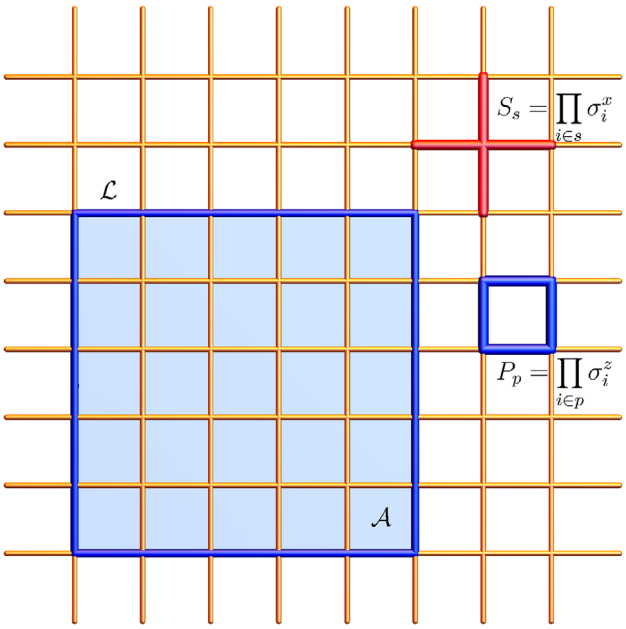

Figure 1.1: *Scheme of the toric code lattice model with associated star and plaquette operators. Figure taken from* [7]*. A "loop" operator, showing the flipping of spin around a close contour, is also shown. This particular loop does not wind around one of the torus directions, so a state presenting it is equivalent to the trivial ground state.*

the ground-state is actually only 4-fold degenerate, with the orthogonal eigenvectors differing by the *parity* of the number of loops encircling the torus in the two spatial directions.

This structure of the ground state poses a serious challenge to a Landau-Ginzburg description of this phase: any local observable -that is, any observable relative to an area smaller than the whole loop- cannot effectively distinguish one ground state from the others. Nevertheless, the ground states can be distinguished in a different perspective, that mathematicians would call "topological", i.e. related to a discrete quantity (the parity of the number of loops) which is unresponsive to local perturbations.

Hence, a new paradigm to describe phases of matter had to be developed. It has become known as the theory of *topological order*, and its birth can be dated back to Wen [9]. Differently from LGT, in this framework quantum systems are classified according to their entanglement. Let us consider as an example the transverse field Ising model:

$$H = -B \sum_i \sigma^x - J \sum_{i,j} \sigma_i^z \sigma_j^z \tag{1.1}$$

and focus on the two opposite limits $J = 0$ and $B = 0$. In the σ^z basis, the two limiting ground states are, respectively, $\otimes(|\uparrow\rangle + |\downarrow\rangle)_i$ and the degenerate $\otimes|\uparrow\rangle_i$ and $\otimes|\downarrow\rangle_i$. These two states are in different Landau-Ginzburg classes, since they behave differently under the spin-inversion symmetry $\sigma^z \to -\sigma^z$. Yet, they can both be written as a direct product state. Hence from an entanglement range perspective they belong to the same topological classification. Wen's description of topological phases classifies the ground state of gapped systems [10, 11] in terms of a *local unitary evolution* mapping one ground state into the other. If such an evolution operator exists, the two ground states belong to the same phase in a topological order sense.

Based on this definition, all the states connected to non-entangled direct product states belong to the same short-range entangled (SRE) *trivial* topological phase. In contrast, different entanglement patterns belong to distinct *non-trivial* long-range entangled (LRE) topological phases like the ground states of the toric code. The classification becomes even richer if we include symmetries into the picture. If we consider, among local unitary evolution operators, those that respect certain symmetries of the model, the SRE class breaks up. Some SRE states belong to equivalence classes with different broken symmetries. In this classification we recover, for example, the phase distinction of the two ground states of the transverse field Ising model. Other states belong to different SRE classes even without breaking any symmetry but merely because of the lack of a suitable local unitary evolution. Among these states, which show *symmetry-protected topological order*, we find systems we will briefly comment on in this chapter, such as the Haldane model and, crucially for the main topic of this thesis, topological and band insulators, the topological order of which is protected by Time-Reversal symmetry.

Once a classification of topologically ordered phases is established, it is necessary to find appropriate quantities (which replace the order parameter of Landau phase transitions) to distinguish one phase from the other. These are called *topological invariants* and stem from many sources: they can be related to experimentally measurable quantities such as the Hall conductance, and their derivations have historically been based, among others, on the Kubo formula, modern theory of polarization, form and number of surface states in a finite sample or parity considerations on the eigenstates of the bulk system. Recent works [12, 13] have also considered topological invariants, such as the so-called *entanglement Chern number*, based on the properties of quantum entanglement in a many-body ground state, a perspective more closely related to the concept of topological order we have briefly outlined. In the following sections we will rapidly go over a series of topological effects and models, which historically lead to the discovery of the Time-Reversal Symmetry protected Quantum Spin Hall effect and, relatedly, to the formulation of the Bernevig-Hughes-Zhang model, that will be the basis on which the results of this thesis will be built.

1.2 Quantum Hall effect

Although the concepts of topological states of matter and of topological invariants might seem closer to a mathematical classification than to a physical one, they have prominent observable consequences.

In fact, the first evidence of the insurgence of topological effects was obtained experimentally, before a theoretical explanation was derived. The introduction of the concept of topology in a condensed matter framework usually dates back to 1980, with the discovery of the Quantum Hall Effect (QHE) by Von Klitzing, Dorda and Pepper [14]. As the name suggests, the QHE is an extension beyond the classical Drude model of the Hall effect, i.e. the occurrence of a voltage drop in the direction perpendicular to the flow of a current, in presence of a magnetic field along the out-of-plane direction. The Hall potential is a response to the effect of the Lorentz force, that bends the trajectory of the electrons away from the direction of the external electric field. As such, the classical theory predicts a linear behaviour for the transverse resistivity ρ_{xy}, according to the relation

$$\rho_{xy} = \frac{B}{ne} \tag{1.2}$$

where n is the density of charge carriers. The experimental results, however, show a series of

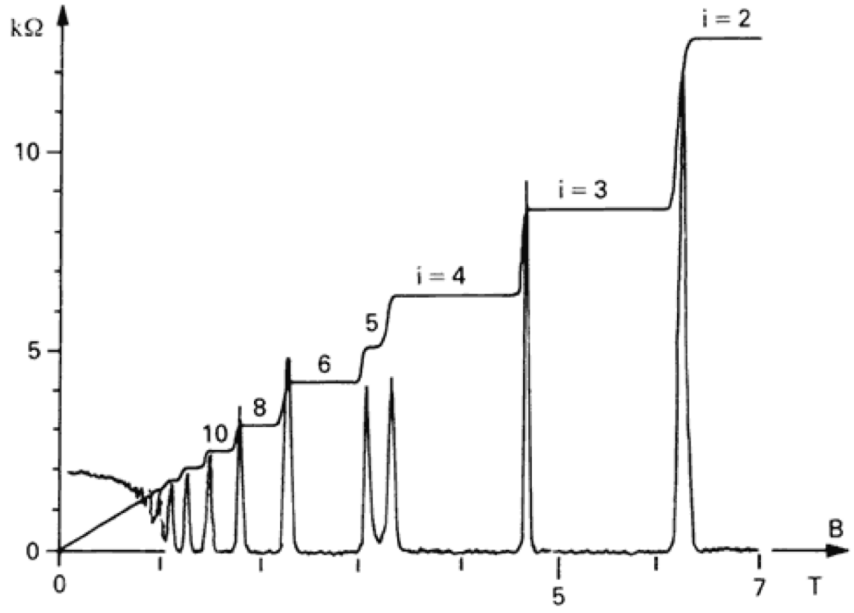

Figure 1.2: *The longitudinal and transverse Hall resistivity as a function of the magnetic feld (Kosmos 1986). The plateaux of the transverse Hall resistivity are clearly visible. The series of spikes represent the behaviour of the longitudinal resistance, which is zero inside the plateaux: this is due to the fact that, if n Landau levels are completely filled, there cannot be longitudinal current, and therefore in turn no dissipation.*

plateaux of resistivity for increasing B, following the ladder law

$$\rho_{xy} = \frac{2\pi\hbar}{e^2\nu} \tag{1.3}$$

ν being measured to be an integer with a stunning precision (one part in 10^9). Given the form of this relation and the physical quantities involved, this behaviour was readily linked to the physics of Landau levels, when the Fermi energy of the system sits in the gap between two such levels. The width of the plateaux was associated to the presence of localized states due to disorder in the sample, that do not contribute to conduction. At this level already, the stability of the plateaux in spite of (and actually precisely due to) disorder starts to unveil the topological nature of this phenomenon. A subsequent step was to recognize that, as the filled-Landau-level system is a bulk insulator with zero longitudinal conductance, the Hall current must be due to states localized on the border. The work by Halperin [15] and Laughlin [16], showed that the finite Hall conductance manifested itself to probing (hence for a finite size sample) via conducting states localized purely at the edge. In addition, Laughlin's argument showed that the origin of the different Hall conductance values was gauge related, which he accomplished using a cylindrical-geometric Hall effect sample threaded by a gauge magnetic flux, its variation acting as a control parameter.
This was the first instance of what in Topological Band Theory is known as *bulk-edge correspondence*, a distinctive feature of topological systems which associates the non-trivial nature of the bulk insulating band structure to the presence of surface states crossing the bandgap.

Such correspondence, verified for many different systems, is strictly related to the topological protection of the gap: this can only close at the interface of systems belonging to different phases with different values for the invariants (included the trivial case of the vacuum).

For lattice systems, the relation between the Quantum Hall conductance and the properties of the Bloch wavefunctions of the material was elucidated in the pioneering work of Thouless, Kohmoto, Nightingale and den Nijs (TKNN) [17]. A two-dimensional lattice with periodic boundary conditions and in presence of magnetic and electric fields is considered. From the Kubo formula applied to the Hall conductivity the authors obtain an expression, known as TKNN formula, for the Quantum Hall conductance σ_{xy}:

$$\sigma_{xy} = \frac{ie^2}{\hbar} \sum_{\alpha} \int_{\mathbf{MBZ}} \frac{d^2k}{(2\pi)^2} \langle \partial_y u^{\alpha}_{\mathbf{k}} | \partial_x u^{\alpha}_{\mathbf{k}} \rangle - \langle \partial_x u^{\alpha}_{\mathbf{k}} | \partial_y u^{\alpha}_{\mathbf{k}} \rangle \tag{1.4}$$

where $|u^{\alpha}_{\mathbf{k}}\rangle$ is the α-th occupied Bloch state and $\mathbf{k}$ lives in the 2-dimensional Magnetic Brillouin Zone, i.e. the shrunk Brillouin zone accounting for the reduced translational invariance of the lattice due to the presence of the magnetic field. A requirement for this expression, consistent with the previous observations, is for the system to be a bulk insulator, with a finite bandgap everywhere in the k-space.

The TKNN formula is remarkable for different reasons. It is a very general relation, which does not in principle depend on the presence of specific terms, such an external magnetic field, but only on the possibility of defining Bloch states in a periodic k-space. Second, it links for the first time a measurable quantity, i.e. the Quantum Hall conductance, to the geometry of the Bloch states. Indeed, the expression under the integral is nothing else but the Berry curvature, which in turn is linked to the geometrical phase acquired by a wave-function over a close loop in a parameter space, in this case the momentum space. Incidentally, the insulating character of the band structure is required for of the calculation of this phase, since it relies on the hypotheses of the Adiabatic theorem. Finally and most importantly, the result of the integral is a constant integer, called *first Chern number*, as follows from a variety of arguments both physical (Dirac quantization of charge) and mathematical (Gauss-Bonnet theorem and theory of homotopy groups). The TKNN invariant for a Quantum Hall system is therefore generally considered the first historical example of *topological invariant*.

1.3 Quantum Anomalous Hall Effect and Haldane model

As we discussed in the previous section, the TKNN formula for quantum Hall conductance does not explicitly rely on the presence of a magnetic potential. The evaluation of the conductance requires only to know the form of the eigenvectors of the system in a periodic parameter space. The most natural example is the Brillouin Zone, which is defined under the only necessary hypothesis that the relative lattice system is translational invariant.
It is now important to determine the conditions under which the invariant is nonzero. We start from the simplest realization of a two-dimensional system with two bands, which is the minimal model to have a gap in the absence of interactions. The simplest Bloch Hamiltonian will then be expressed, as for any 2×2 Hermitian matrix, in the general form

$$H(\mathbf{k}) = \vec{q}(\mathbf{k}) \cdot \vec{\sigma} + \epsilon(\mathbf{k}) \cdot \mathbb{I} \tag{1.5}$$

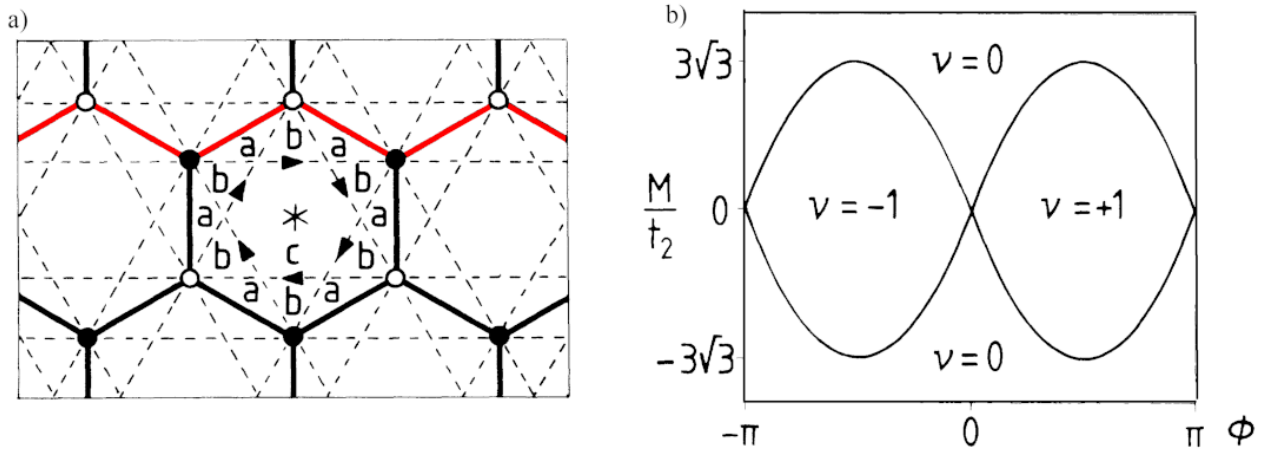

Figure 1.3: *Original images adapted from Haldane's 1988 paper* [18]. a) *The schematic realization of the model, a honeycomb lattice with first and second nearest neighbour hopping. The nnn hopping has a phase (black arrow) due to the magnetic field. The red line shows the shape of the "zig-zag" border of a honeycomb lattice.* b) *Double-sinusoid phase diagram in the* $M - \phi$ *plane (the values of* ν *are inverted with respect to the text by an overall phase choice).*

where $\mathbf{k}$ lives in the 2-dimensional toroidal BZ and $\sigma_{x,y,z}$ are the Pauli matrices. The energy gap between the two bands is given by $2|\vec{q}(\mathbf{k})|$, so the system will be an insulator provided that $\vec{q} \neq 0$ everywhere. The topological characterization of such a system is thusly obtained: if we consider the versor $\vec{n}(\mathbf{k})$ in the direction of $\vec{q}(\mathbf{k})$, it spans a 2-dimensional spherical surface known as the *Bloch sphere*. Hence, the Hamiltonian can be seen as a map from the 2-dimensional torus $\mathbf{T}$, where $\mathbf{k}$-vectors live, to such a sphere. The Chern number is in this case defined as

$$C = \frac{1}{4\pi} \int_{\mathbf{T}} \vec{n} \cdot \left(\frac{\partial \vec{n}}{\partial k_x} \times \frac{\partial \vec{n}}{\partial k_y} \right) \tag{1.6}$$

and represents *winding number* of the torus on the sphere, which is the number of times the former "wraps" around the latter via the map given by H. This integer quantity will be the topological invariant of the system. A system with a non-zero Chern number will be called *Chern insulator*.

Historically, the first theoretical system describing a non-trivial Chern insulator was introduced in 1988 by Haldane [18], who considered a two-dimensional honeycomb lattice which is invariant under time-reversal, inversion and C_3 symmetries and displays a two-atom unit cell forming two sub-lattices A and B, which plays the role of a chiral degree of freedom. As it is universally know, this is nothing but graphene, which has been experimentally realized in 2004 by Geim and Novoselov [20].

Interestingly, the electronic dispersion of graphene shows two gapless points

$$K(K') = \frac{2\pi}{3a} \left(1, \pm \frac{1}{\sqrt{3}} \right),$$

where a is the bond length, related by Time-Reversal symmetry.

Near these points the linearized Bloch Hamiltonan has a linear Dirac form, i.e. it can be proven

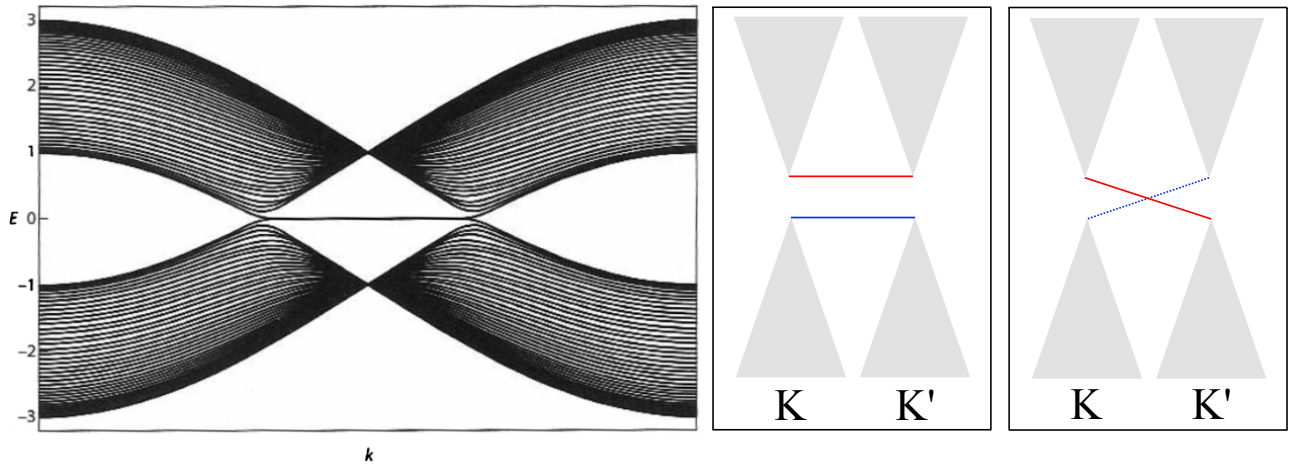

Figure 1.4: *On the left, band structure for a stripe of graphene with open boundary conditions along a zig-zag edge (picture from [19]). This example in particular refers to a sample with an even number of sites in the finite direction, so that the sites on opposite surfaces belong to opposite sublattices. In the middle and right panels, the effect of a Semenoff and an Haldane mass term on the gap, respectively. The red and blue surface states are localized on opposite sublattices and surfaces. The use of a dotted line in the right panel reminds that the two states do not live on the same edge of the stripe.*

to satisfy

$$\begin{aligned} H_K(\mathbf{k}) &= H(K+\mathbf{k}) = v_f(k_x\tau_x + k_y\tau_y) \\ H_{K'}(\mathbf{k}) &= H(K'+\mathbf{k}) = H(-K+\mathbf{k}) = v_f(-k_x\tau_x + k_y\tau_y) \end{aligned} \tag{1.7}$$

where the coefficient v_f is called Fermi velocity. We have used the notation τ_i for the Pauli matrices to highlight the fact that they refer to a sublattice and not a spin degree of freedom. In order to have a Chern insulator, a gap must be open. If the topology of the system is nontrivial, gap-closing edge states will then appear. We consider a stripe of graphene with open boundary conditions in one spatial direction. In particular we will focus on the so-called "zig-zag" border, where the open edge consists of alternating A and B sublattice sites along the red line drawn in Fig. 1.3a.
The band structure for this setup, in the one-dimensional Brillouin zone corresponding to the periodic spatial direction, features edge states with vanishing energy in the thermodynamic limit. An example for a stripe with an even number of sites in the finite direction is given in Fig. 1.4 (though the form of the edge states heavily depends on the specifics of the stripe, as thoroughly analysed for example in [19]). The two zero energy states live on the sublattices A and B respectively, and on the opposite edges of the stripe. They merge with the bulk bands at the projections of the Dirac points K and K'.
A trivial way to open a gap in this system would be to break inversion symmetry by including a term proportional to τ_z in the Hamiltonian, which is known as *Semenoff mass*. Its presence would shift the energies of the sites A and B upwards and downwards respectively, detaching the relative surface states from zero energy and leaving the gap open, as schematically shown in the middle panel of Fig. 1.4. Since no gap-closing surface state is present, the system will in this case be topologically trivial.

A more ingenious way of gapping the spectrum is to add a time-reversal symmetry (TRS)-breaking *Haldane mass* term, that adds a mass of opposite sign to the Dirac points at K and K'. Due to the different behaviour at the high-symmetry points, this term has to be k-dependent, and its effect will not be a rigid energy shift of the two A and B sublattices. In this case, the surface states will still connect the detached vertices of the cones according to the mass. However, since K and K' will have masses of different sign, the edge modes will have to connect the cones by crossing the gap, as sketched in the right panel of Fig. 1.4. The presence of the gap-closing edge mode, related to a nontrivial Hall conductance, is a hallmark of the topological character for such a TRS-breaking system.

These ideas are included in a simple tight-binding model, which builds upon a Hubbard model on the honeycomb lattice and cleverly relies on the presence of a magnetic field, whose total flux per plaquette is however zero (mod 2π). This setup preserves translational symmetry while avoiding Landau levels. It then provides a description of the Quantum analogous of the Anomalous Hall Effect (QAHE), which in its classical form depends on the magnetization of the material and not on an external magnetic field.
Haldane's Hamiltonian has the following tight-binding form in second quantization[1]:

$$\hat{H} = t_1 \sum_{\langle ij \rangle} c_i^\dagger c_j + t_2 \sum_{\langle\langle ij \rangle\rangle} e^{-i\nu_{ij}\phi} c_i^\dagger c_j + M \sum_i \alpha_i c_i^\dagger c_i \tag{1.8}$$

where $\alpha_i = \pm 1$ if $i \in A,\ B$ sublattice, ϕ is a phase factor associated to the next-nearest-neighbour hopping term due to the presence of the magnetic field. The direction of the next-nearest-neighbour hopping is given by

$$\nu_{ij} = \text{sign}(\mathbf{d}_1 \times \mathbf{d}_2)_z = \pm 1$$

where $\mathbf{d}_1$ and $\mathbf{d}_2$ are the vectors along the two bonds constituting the next nearest-neighbour hopping path. It has to be noted that the system preserves Time-Reversal and Inversion symmetries only for $\phi = 0, \pi$ and $M = 0$ respectively. Therefore, for a generic ϕ the Dirac points are no longer TRS-related. In the $\mathbf{k}$-space the Haldane Hamiltonian has the form

$$\hat{H} = \sum_{\mathbf{k}} \Psi_{\mathbf{k}}^\dagger H(\mathbf{k}) \Psi_{\mathbf{k}} \tag{1.9}$$

where $\Psi_{\mathbf{k}}^{(\dagger)} = (c_{\mathbf{k}A}^{(\dagger)}, c_{\mathbf{k}B}^{(\dagger)})$ and the Hamiltonian matrix $H(\mathbf{k})$ has the wanted Chern insulator form

$$H(\mathbf{k}) = \epsilon(\mathbf{k})\mathbb{I} + \sum_{i=1}^{3} d_i(\mathbf{k})\tau_i$$

where ϵ and d_i are conveniently defined trigonometric functions of the momentum components. A direct computation of the Berry curvature, and the associated Chern number for the Haldane model, allows to construct the well-known "double-sinusoid" phase-diagram reported in Fig. 1.3b. The topology of the system is determined by the phase ϕ and the ratio $\frac{M}{t_2}$. The Chern number is $-\text{sign}(\phi)$ inside the lobes delimited by the equation $\frac{M}{t_2} = \pm 3\sqrt{3}\sin(\phi)$.
The phase diagram of the Haldane model helps to clarify the role of gapless points. Let us

[1] we will use henceforth the "hat" notation to refer to operators in second quantization, except for the creation/annihilation operators $c^\dagger, c$ and arrays of the same.

consider the system in a fictitious three-dimensional space $k_x, k_y, \lambda = M/t_2$ for a fixed $\phi > 0$. This can be thought of as a stack of "planes", each of which is actually a two-dimensional Brillouin zone. We can now draw a parallel between this situation and two charges of opposite sign emitting an electric field in a three-dimensional space. The calculation of the flux of the field is possible everywhere except on the planes on which the charges sit, since the field strength is diverging at the origin.
Accordingly, if we interpret the two gapless points at K and K' as sources of "Berry fluxes" with opposite sign (which manifests in the opposite Chern number), the flux of the regions outside the interval (λ_1, λ_2) will cancel our, whereas inside the same interval the total flux will be finite. The calculation of the Berry flux is not possible on the planes $\lambda_{1,2}$, where the system is not gapless. Thus, in our analogy, as a charge is a source for the electric field a gapless Dirac point in the electronic band structure can be seen as a source of the Berry flux. We will expand on this notion in Chapter 5, where we will more thoroughly address the properties of the Dirac Hamiltonian in the context of topological semimetals.
The ground-breaking result of Haldane has hinted at the possibility of realizing a non-trivial topological state without an applied magnetic field, by simply breaking TRS. Yet, the very existence of such an anomalous Quantum Hall insulator has been proven experimentally only in 2013 [21], measuring the Hall conductance of a thin layer of the topologically nontrivial compound $Cr_{0.15}(Bi_{0.1}Sb_{0.9})_{1.85}Te_3$ with TRS-breaking ferromagnetic ordering and so, in a sense, proceeding in the opposite direction of our narration, as we shell see.

1.4 Quantum Spin Hall Insulators and $\mathbb{Z}_2$ invariant

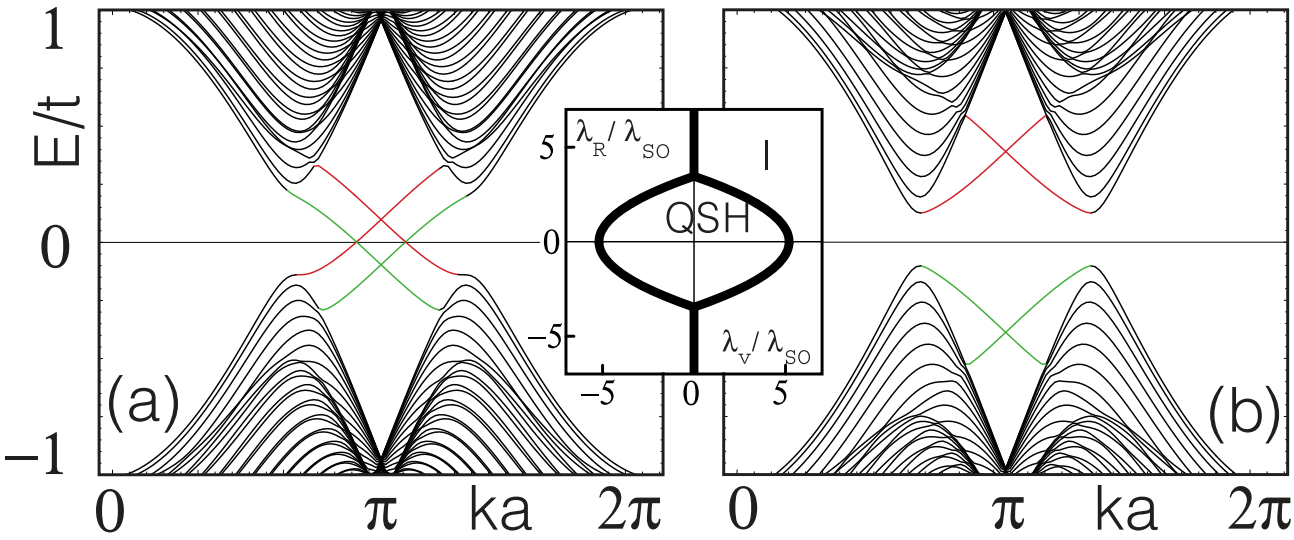

Figure 1.5: *Band diagrams for a one-dimensional Kane-Mele strip in the the QSH and trivial states, with $\lambda_{SO} = 0.06t$ and $\lambda_R = 0.05t$. λ_V is $0.1t$ and $0.4t$ respectively. The color represents the states living on the same edge, which cross at a TRIM. In the middle, the diamond QSH phase diagram as a function of λ_R and λ_v. Image taken from [22].*

The Haldane model realizes a QAHE insulator, which exhibits nontrivial Hall conductance without the need for Landau levels, at the cost of breaking Time-Reversal symmetry. Many

years from the seminal work of Haldane, the search for alternative mechanisms to gap at the Dirac cones led to the discovery of novel states of matter and the individuation of systems with non-trivial topological character preserving TRS. These *topological insulators* are not distinct from trivial *band insulators* in the sense of the Landau theory of phase transitions, but they have a symmetry-protected topological order.

The rising interest in spin currents following to the experimental work of Kato [23] and, on the theoretical side, of Murakami, Nagaosa and Zhang [24], led to the breakthrough proposal of a Quantum Spin Hall Insulator (QSHI) in the fundamental work of Kane and Mele [25]. The authors considered the effects of Spin-Orbit Coupling (SOC) as a mean to open a gap at the Dirac nodes. Interestingly, it was realized that the SOC term in graphene naturally takes the form of a chiral-dependent next-nearest-neighbour term similar to all intents and purposes to the Haldane mass, but preserving TRS through the inclusion of spin into the picture. Accordingly, the Kane-Mele model consists of two copies of the Haldane model, one per spin orientation, related by TRS.

A suitable form of the mass term near the Dirac points and in a continuum model can be derived imposting the correct symmetries. First of all, it has to anticommute with the unperturbed Hamiltonian in the sublattice space. This is necessary to open a gap, otherwise the result of the perturbation would simply be a shift of the gapless points. Given the form of the Dirac Hamiltonian near the gapless points, which is proportional to $k_i\tau_i$ for $i = x, y$, this entails a dependence to the Pauli matrix τ_z in the sublattice space.

The mass term has then to apply to both spin blocks of the Hamiltonian, either with the same value in each block, which trivially corresponds to two copies of the Inversion-symmetry-breaking mass-term of the Haldane model, or with opposite sign for the two spins, which implies a dependence on the Pauli matrix σ_z in the spin space.

Finally, we recall that the Dirac points K and K' are TRS-related. The expression of the T operators in the spin and sublattice spaces is, respectively,

$$T = -i\sigma_y\mathcal{K} \qquad \text{and} \qquad T = \tau_0\mathcal{K} \tag{1.10}$$

where $\mathcal{K}$ is the complex conjugation operator and we use the notation $\sigma_0, \tau_0 = \mathbb{I}_{2\times 2}$. Recalling the form of the Dirac Hamiltonian around K and K' (1.7), and the general relation for TRS invariance of the Hamiltonian matrix

$$H(-\mathbf{k}) = TH(\mathbf{k})T^{-1},$$

we can see that TRS between the K and K' points will be preserved if the Hamiltonian has the following form:

$$\begin{aligned} H_K(\mathbf{k}) &= v_f(k_x\sigma_0 \otimes \tau_x + k_y\sigma_0 \otimes \tau_y) + \lambda_{SO}\sigma_z \otimes \tau_z \\ H_{K'}(\mathbf{k}) &= v_f(-k_x\sigma_0 \otimes \tau_x + k_y\sigma_0 \otimes \tau_y) - \lambda_{SO}\sigma_z \otimes \tau_z \end{aligned} \tag{1.11}$$

where the terms in parenthesis simply represent the two opposite-spin copies of the Dirac Hamiltonian. From (1.11) we note that the presence of the spin degree of freedom allows us to write a Haldane mass term (with opposite sign at the two Dirac points) while preserving TRS. The subscript SO in the λ coefficient reflects the fact that this mass term, which couples momentum with spin degrees of freedom, can only arise from spin-orbit coupling. The eigenvalues of (1.11), degenerate in spin and identical at the two Dirac points, will be of the form

$$E_{\pm,\sigma} = \pm\sqrt{v_f^2(k_x^2 + k_y^2) + \lambda_{SO}^2}. \tag{1.12}$$

where the first term is the Dirac dispersion and the second is the TRS-preserving mass gap.

The tight-binding expression of the Kane-Mele Hamiltonian on a honeycomb lattice is the following [22]:

$$\hat{H} = t\sum_{\langle i,j\rangle}\Psi_i^\dagger\Psi_j + i\lambda_{SO}\sum_{\langle\langle i,j\rangle\rangle}\nu_{i,j}\Psi_i^\dagger\sigma_z\Psi_j + i\lambda_R\sum_{\langle i,j\rangle}\Psi_i^\dagger(\overrightarrow{s}\times\mathbf{d}_{ij})_z\Psi_j + \lambda_v\sum_i\alpha_i\Psi_i^\dagger\Psi_i. \quad (1.13)$$

where the creation and annihilation operators are written in the combined spin notation $\Psi_i^{(\dagger)} = (c_{i\uparrow}^{(\dagger)}, c_{i\downarrow}^{(\dagger)})$. The first term is the usual nearest-neighbour hopping in the honeycomb lattice. The second is responsible for the TRS-preserving opening of the gap, by giving an opposite Haldane mass to the two spin blocks. The factor

$$\nu_{ij} = \frac{2}{\sqrt{3}}(\mathbf{d}_1\times\mathbf{d}_2)_z = \pm 1$$

is, similarly to the Haldane model, defined in terms of the versors in the direction of the two bonds constituting the path of the electron going from site i to site j. The other terms are included to test the robustness of the topological phase: the third term, a nearest neighbour Rashba coupling, is responsible for the breaking of the mirror symmetry $z \to -z$, while the last one violates inversion symmetry, in a way similar to the M term of the Haldane model.
In reciprocal space, the Hamiltonian of the model has a form of the type (1.9), where now $\Psi_{\mathbf{k}}^{(\dagger)}$ is the four-dimensional operator $(c_{\mathbf{k},A\uparrow}^{(\dagger)}, c_{\mathbf{k}B\uparrow}^{(\dagger)}, c_{\mathbf{k}A\downarrow}^{(\dagger)}, c_{\mathbf{k}B\downarrow}^{(\dagger)})$ and the Hamiltonian matrix is

$$H(\mathbf{k}) = \sum_{a=1}^{5} d_a(\mathbf{k})\Gamma^a + \sum_{a<b=1}^{5} d_{ab}(\mathbf{k})\Gamma^{ab}. \quad (1.14)$$

The d terms are trigonometric functions of the momentum components, and the Γ matrices span the 16 generators of the $SU(4)$ matrix group except for Γ^0, the identity matrix. In particular, the five Γ^a are the so-called Dirac matrices satisfying the Clifford algebra

$$[\Gamma^\mu, \Gamma^\nu]_+ = 2\delta_{\mu\nu}\mathbb{I}_{4\times 4}$$

while the remaining Γ^{ab} are obtained from the commutators of the Dirac matrices,

$$\Gamma^{\mu\nu} = \frac{1}{2i}[\Gamma^\mu, \Gamma^\nu].$$

We will not derive the formal expression for the Kane-Mele model in reciprocal space. We will however deal more thoroughly with the Dirac matrices in the context of the Bernevig-Hughes-Zhang model we will define in the next section.
We now have to identify the invariant that accounts for the nontrivial topology of the Kane-Mele model. A possible choice is the sum of the Chern numbers of each spin block. However, it can be deduced from the form of the λ_{SO} term that the two spin blocks always contribute with equal and opposite Chern numbers, since they correspond to symmetric points on the $M = 0$ line of the Haldane phase diagram in Fig. 1.3b.
We can approach the search for the topological invariant from a different angle by considering a finite sample of the Kane-Mele model, again with a zig-zag border, and studying its edge

states. It is known that, in a fermionic TRS systems, every band has an orthogonal "twin", called Kramers partner, that satisfies $E_1(\mathbf{k}) = E_2(-\mathbf{k})$ for every $\mathbf{k}$ in the Brillouin zone. The two bands will be degenerate in k-points that are invariant under TRS, the so-called Time-Reversal Invariant Momenta (TRIMs). In this model, due to the symmetries of the system, the Kramers partners have opposite spins. Therefore, we will have at each edge of the system a number of pairs of counter-propagating helical edge states crossing at TRIMs.
The way such states could open a gap would be through backscattering, and here it becomes clear how the topological phase of the Kane-Mele model is *protected* by Time-Reversal symmetry. Indeed, the time-reversal operator for fermionic systems is antiunitary, and satisfies the relation

$$T^2 = \pm 1$$

for systems with total integer and half-integer spin respectively. Accordingly, from the definition of the TRS operator (1.10) it can be shown that the scattering probability for a state and its Kramers partners has to satisfy

$$\langle T\phi|H|\phi\rangle = -\langle T\phi|H|\phi\rangle = 0. \tag{1.15}$$

In general, if we consider the combined scattering probability of n helical modes with their counter-propagating Kramers partners we get an overall factor $(-1)^n$.
Then, if the number of Kramers pairs of edge states is odd there is no single-particle backscattering term that can open a gap in the band structure, while such a term can exist for an even number of Kramers pairs. Accordingly, the invariant associated to a TRS-protected topological insulator has to do with the parity of the number of Kramers pairs at the edge, which suggests a binary $\mathbb{Z}_2$ classification.
We refer to these systems as Quantum Spin Hall insulators (QSHI). Although no overall Hall conductance is present, in the non-trivial phase the spin currents for the different spins will be counter-propagating, realizing the so-called *helical* or *spin-momentum locking*, with a net "spin voltage drop" as pictured in Fig. 1.8.
By directly solving the Hamiltonian of a finite Kane-Mele model, and assessing the presence of gap-closing surface states, the topological phase diagram can be obtained: it is usually represented as a diamond in the $\lambda_r - \lambda_v$ plane (see Fig. 1.5), the nontrivial phase being the inner region. For $\lambda_r = 0$, the system experiences a topological transition for $\lambda_v = 3\sqrt{3}\lambda_{SO}$. The topologically nontrivial phase can survive, at least for small values of λ_v, if the Rashba term is finite but smaller than $2\sqrt{3}\lambda_{SO}$.

There are many equivalent ways to derive the $\mathbb{Z}_2$ topological invariant considering bulk properties instead of the edge states. The original Kane-Mele derivation is geometrical and based on the *Pfaffian* of the matrix of occupied Bloch states. In a subsequent work, Fu and Kane [26] started from the modern theory of polarization [27] to qualify the $\mathbb{Z}_2$ invariant in terms of a *time-reversal polarization*, or geometrically as an obstruction to the definition of a smooth gauge in the BZ.

The existence of $\mathbb{Z}_2$ invariants has also been extended to three-dimensional systems: a mathematical argument based on homotopy was developed by Moore and Balents [28], but a more intuitive one based on relations between two- and three-dimensional Brillouin zones was presented by Fu, Kane and Mele [29]. We will briefly present the derivation of the bulk $\mathbb{Z}_2$ invariant in Appendix A, along with the simplified expression for the invariant in the case the

system also possesses Inversion symmetry, which will turn out to be of the general form [30]

$$(-1)^{\nu} = \prod_i \prod_n \xi_{2n}(\Lambda_i) \tag{1.16}$$

where ν is the topological invariant, Λ_i is the i-th TRIM in the Brillouin zone and ξ_{2n} is the parity eigenvalue of the $2n$-th occupied band, or equivalently of the n-th Kramers pair.

1.5 The Bernevig-Hughes-Zhang model

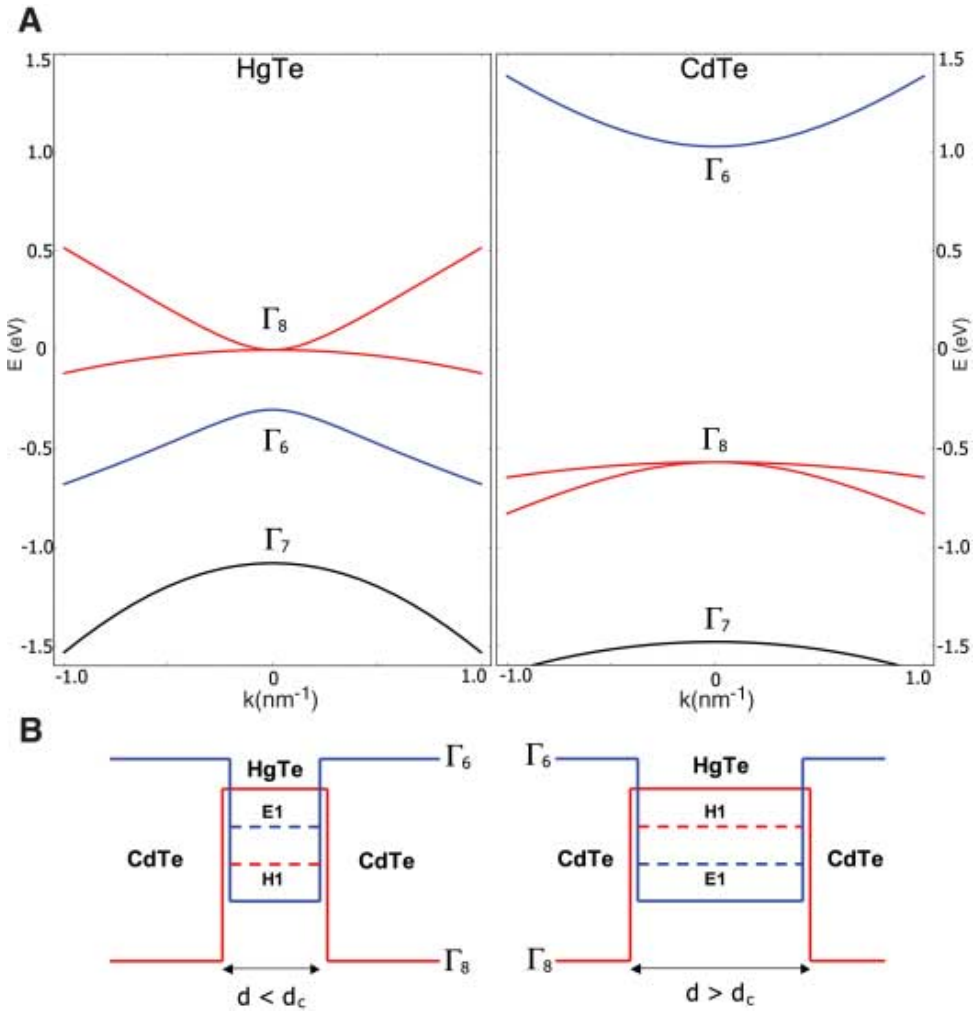

Figure 1.6: *Band structure for a*CdTe/HgTe/CdTe *quantum well, as per* [31]. a) *The band dispersion of* CdTe, *following the standard order, and of* HgTe, *with an inverted bandgap between the* Γ_6 *and light-heavy hole* Γ_8 *bands.* b) *The relevant subband structure of the quantum well: for* $d < d_c$ *the system behaves like* CdTe, *while increasing the width* HgTe*-like behaviour takes over.*

The key idea put forward with the introduction of the Kane-Mele model is that the presence of SOC can introduce non-trivial topological states in the graphene lattice. Following this original proposal a quest to discover or realize such novel phases of matter began. Unfortunately,

it turned out pretty soon that graphene was not a good candidate to realize QSHI. Indeed the gap opened by the spin-orbit interaction was found out to be only of the order of 10^{-3} meV [32].
A different approach, based on HgTe/CdTe quantum well as possible candidate to realize a QSHI, was proposed in 2006 by Bernevig, Hughes and Zhang (BHZ) [31].
They predicted the existence of a pair of helical edge states over a critical value d_c of the thickness of the heterostructure, which would instead be a trivial insulator for $d < d_c$. The peculiar topological properties of this compound are a consequence of the electronic structure near the Fermi level. Both HgTe and CdTe have, near the Γ point, a s-like band Γ_6 and two p-type bands split by spin-orbit coupling into a $J = \frac{3}{2}$ Γ_8 (made out of the angular momentum 1 of the p-orbitals and electron spin 1/2) and a $J = \frac{1}{2}$ Γ_7. While CdTe has a large energy gap between the valence Γ_7 and Γ_8 bands and the conduction Γ_6 band, HgTe crucially presents an inverted bandgap around the Γ point. This effect is due to the large mass of Hg, which ultimately pushes the s-like band Γ_6 below the Fermi level and, thus, below Γ_8 [31, 33]. A schematic representation of the situation can be seen in Fig. 1.6. Neglecting the Γ_7 band, which is always firmly in the valence region, the system can be described by the six-component spinor made out by the two atomic states for Γ_6 and the four atomic states for Γ_8.
When the quantum well is grown, for example in the z direction, the cubic symmetry is reduced to an axial rotational symmetry in the plane. In this case, the six bands combine to form the spin up and down states of three quantum well subbands known as $E1$, $H1$ and $L1$. Of these, the $L1$ subband is separate in energy from the other two, that sit close enough to the Fermi level to let us describe the physics of the system by an effective 4-band model. At the Γ point, where the in-plane momentum vanishes, m_J is still a good quantum number. Here, the 4 states can be described as $|E1, \pm\rangle$, linear combination of the Γ_6 and Γ_8 bands with $m_J = \pm\frac{1}{2}$, and $|H1, \pm\rangle$, linear combination of the Γ_8 bands with $m_J = \pm\frac{3}{2}$. Away from Γ, these states can mix. Since $|\Gamma_6, m_J = \pm\frac{1}{2}\rangle$ and $|\Gamma_8, m_J = \pm\frac{3}{2}\rangle$ have opposite parity under two-dimensional spatial reflection, any coupling element between $E1$ and $H1$ has to be odd in momentum. Moreover, as the $|H1\rangle$ bands are linear combinations of the p-orbitals $p_x \pm ip_y$, to preserve rotational symmetry the matrix elements will have to be proportional to $k_x \pm ik_y$, which will require the diagonal elements of a matrix Hamiltonian formulation to be even functions of k_x and k_y, including k-independent terms. A detailed derivation of these properties, starting from the 6-dimensional Kane Hamiltonian and making use of the $\mathbf{k} \cdot \mathbf{p}$ perturbation theory, is presented in the supplemental material of the original article [31].
Following such symmetry considerations it is possible to derive the Hamiltonian describing the system in proximity of the Γ point:

$$H_{eff}(\mathbf{k}) = \begin{pmatrix} H(\mathbf{k}) & 0 \\ 0 & H^*(-\mathbf{k}) \end{pmatrix} \tag{1.17}$$

where the two spin-blocks, related by TRS analogously to the Kane-Mele case, have the form of an Haldane-like Chern insulator: $H(\mathbf{k}) = \epsilon(\mathbf{k})\mathbb{I} + d_i(\mathbf{k})\sigma_i$.
Actually, real HgTe features a small inversion-symmetry breaking term coupling the two spin blocks. However this term is in general too weak to close the bandgap, hence the inversion symmetric system is in the same topological phase by adiabaticity.
The experimental confirmation of the existence of a QSHI in HgTe/CdTe quantum wells was obtained in Würzburg by the group of Molenkamp [34]. This breakthrough experiment demonstrated the presence of topologically protected gapless edge states in absence of applied magnetic field. A brief overview of the relevant results is provided in Fig. 1.8.

To correctly describe the topological phase diagram of the system, it is important to identify what is the control parameter driving the topological quantum phase transitions. In the HgTe/CdTe quantum well realization of the BHZ model, topology is governed by the width of the well. For a thin quantum well, the physics is dominated by the "normal" CdTe behaviour, the bands being conventionally ordered. Once the thickness is increased over a critical value $d_c \approx 6.35nm$, HgTe-like behaviour takes over and the bandgap is inverted around Γ. Formally, since the phenomenon determining the topological phase is the subband inversion near Γ, the relevant parameter will take the form of a local mass term.

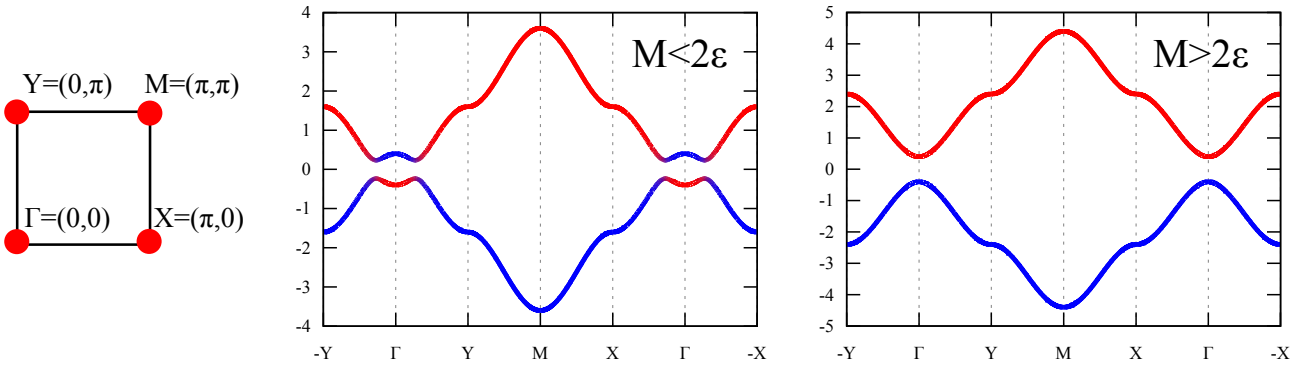

Figure 1.7: *Band structure for the model (1.18) in the two distinct topological phases: in the nontrivial phase ($M < 2\epsilon$) the orbital character of the bandgap is inverted around Γ, while it is not in the trivial phase ($M > 2\epsilon$). The bands are plotted along a high-symmetry bath touching the points highlighted in the scheme on the left (and their symmetric one with respect to Γ).*

In this thesis we study the momentum-space version of a tight-binding Hamiltonian which respects the symmetries of the BHZ theory and it reproduces the above dispersion when linearized around the Γ point. Its derivation is reported in Appendix A, along with that of the $\mathbb{Z}_2$ topological invariant and the classification of the model. The resulting $H(\mathbf{k})$ for a two-dimensional square Brillouin zone has the following form:

$$H(\mathbf{k}) = \big[M - \epsilon(\cos(k_x) + \cos(k_y))\big]\Gamma^5 + \lambda_{SO}\sin(k_x)\Gamma^1 + \lambda_{SO}\sin(k_y)\Gamma^2 \tag{1.18}$$

where Γ^i are the 4×4 Dirac matrices acting in the spin and orbital subspaces defined as

$$\begin{aligned} \Gamma^0 &= \sigma_0 \otimes \tau_0, \quad \Gamma^1 = \sigma_z \otimes \tau_x, \quad \Gamma^2 = -\sigma_0 \otimes \tau_y \\ \Gamma^3 &= \sigma_x \otimes \tau_x, \quad \Gamma^4 = -\sigma_y \otimes \tau_x, \quad \Gamma^5 = \sigma_0 \otimes \tau_z \end{aligned} \tag{1.19}$$

It is easy to verify that the k-dependent terms satisfy the symmetries of the quantum-well setup introduced above. The first term, which is proportional to the diagonal Γ^5 matrix, depends from a "mass" term M and an hopping energy ϵ coupled to an even function of $k_{x,y}$. The first quantity in particular is related to the energy difference between the two orbitals (which in the quantum well realization correspond to the subbands $E1$ and $H1$), and it will ve the control parameter to drive the system across the topological transition.

The off-diagonal terms of the Hamiltonian are, instead, odd functions of the momentum, which is again in agreement with the requirements of the BHZ setup.
The system has naturally four bands with dispersion

$$E_{\pm,\sigma} = \pm\sqrt{\big[M - \epsilon\big(\cos(k_x) + \cos(k_y)\big)\big]^2 + \lambda_{SO}^2\big(\sin^2(k_x) + \sin^2(k_y)\big)}. \tag{1.20}$$

The bands are doubly degenerate in spin, and the topology of the system depends on the specifics of their orbital character.
As previously stated, the topological character of the solution of the model is governed by the mass M. In particular the gap closes at Γ for

$$M = 2\epsilon \tag{1.21}$$

Here, the dispersion around the Γ point has the typical Dirac cone shape.
As proven in Appendix A, and as it can be seen in Fig. 1.7, for lower values of M the bandgap around the Γ point is inverted. Considering the different parity of the two orbitals, this corresponds to a change of the parity eigenvalue of the occupied Kramers partners in one TRIM, and gives an overall nonzero topological invariant as obtained by (1.16). For higher values of M, the parity eigenvalues of the occupied states are the same at every TRIM, and the value of ν is 0.
The Hamiltonian (1.18) has some important advantages with respect to the Kane-Mele model. It is defined on a cubic lattice, which is easier to treat than the honeycomb one. Moreover, instead of the sublattice degree of freedom, it is based on a local orbital degree of freedom, which makes it perfectly suitable to be studied within Dynamical Mean-Field theory, that maps the lattice model onto an effective dynamical local theory (see Chapter 3). With minor modifications it can be extended to three spatial dimensions, and TRS or IS-breaking terms can be added, generating fascinating *gapless* topological phases, that we will thoroughly indroduce in Chapter 5. We will therefore use this expression, or others closely related to it, as the non-interacting part of a many-body Hamiltonian aimed at investigating the combined effects of electronic correlation and topological order.

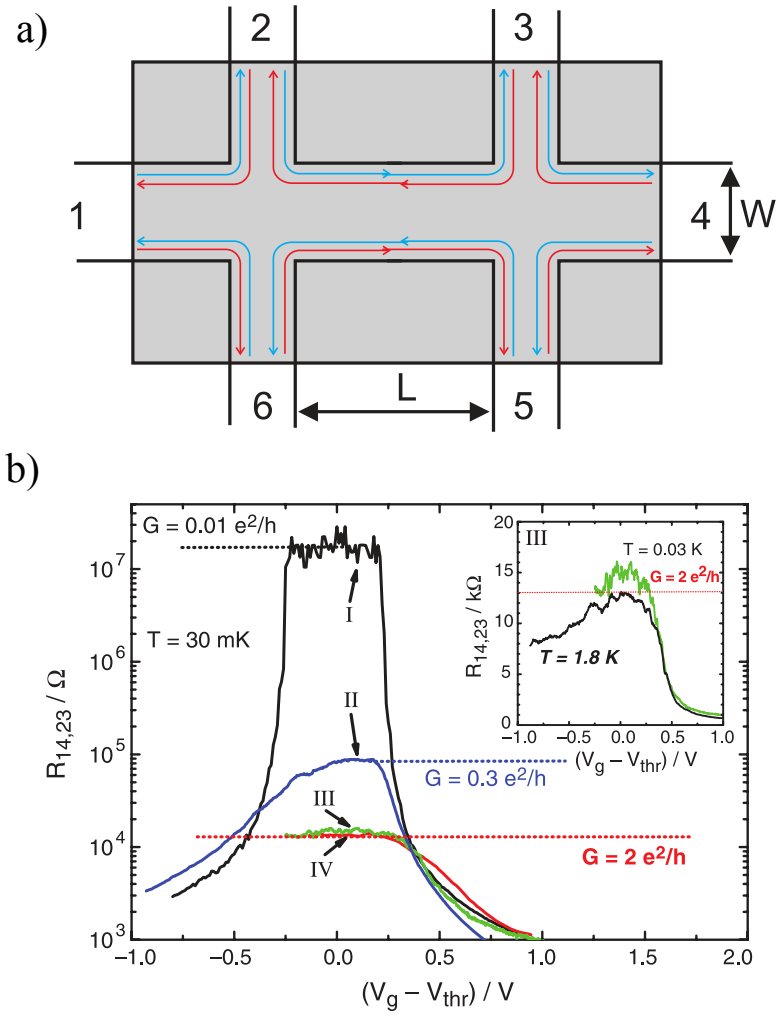

Figure 1.8: *Experimental confirmation of QSHE as per* [34]. a) *Schematic setup of the Hall bar used to measure conductance. The applied voltage is between electrodes 1 and 4, with four probe points transversally placed.* b) *The lines refer to the longitudinal resistance* $R_{1,4/2,3} = V_{23}/I_{14}$. *The curves are centered around the value* V_{thr} *of maximum resistance. Curve* I *refers to a thin QW, for which a trivial behaviour is expected. Indeed, when the applied voltage sits in an energy gap for the system, the huge resistance indicates an insulating behaviour. Curve* II *refers to a QW thicker than the critical value* $d_c \approx 6.35nm$*: in this care the resistance is greatly reduced, therefore gap-closing states appear. Decreasing the distance L between the probes, the results become cleaner and nearer to Landauer's expected value of conductance for 2 non-backscattering modes* $\frac{2e^2}{h}$ *(curves* III *and* IV*). The inset shows how these states have to be localized at the edge: the two curves show the resistivity plateaux for values of W differing by a factor 2. The substantial equivalence of the results confirms that the width of the sample does not affect resistance, hence the conductive modes have to be localized at the edge. Notice how the conductance and resistance measured is longitudinal, not transverse: it is not a Hall conductance. Then again, this is not a QHI. If we imagine to remove terminals 3 and 5 from the scheme in a), we have that the electrons emitted in the system from 1 are spin-separated to terminals 2 and 6, creating a "spin Hall voltage" transverse to the applied one.*

Chapter 2

Concepts and models for interacting electron systems

The theory of topological properties of matter we presented in the previous chapter heavily relies on the Band Theory of solids [35], a framework that has proven do be extremely successful. As we shall briefly discuss in the following, this approach assumes a single-particle picture, in which the many-body electronic states are simply built by populating the eigenstates of an effective single-particle Hamiltonian. This assumes that the effects of the interaction are neglected or treated in terms of a one-body potential. However, in several materials this approximation breaks down because the interaction has a major effect on the electronic properties. These are the so-called *strongly correlated electrons materials*, a name which refers to the fact that the electrons can no longer be seen as independent one from another. In this chapter we briefly review some important aspects of the physics of strongly interacting electronic systems which are useful to introduce the new results of this thesis.
The band theory of solids moves its steps from the work of Bloch [36], that recognized that a particle moving in a periodic potential has eigenstates of the form

$$\psi_{n,\mathbf{k}}(\mathbf{r}) = e^{i\mathbf{k}\cdot\mathbf{r}} u_{n,\mathbf{k}}(\mathbf{r}) \tag{2.1}$$

where $\mathbf{k}$ is a quantum number known as quasi-momentum or crystal momentum, living in the reciprocal space of the ionic lattice, and $u_{n,\mathbf{k}}$ is a periodic function. The index n, which is known as *band index*, labels the eigenstates. Though $\mathbf{k}$ is not the linear momentum of the electron, all quantum mechanical relations, such as the semiclassical equations of motions based on Ehrenfest's theorem, can be expressed in term of the eigenvalues $\epsilon_n(\mathbf{k})$ of an effective single-particle Schrödinger equation for the associated $u_{n,\mathbf{k}}$, and the crystal momentum itself.
Consistently with the name of the relative index n, the eigenvalues form *bands* with a given dispersion in $\mathbf{k}$ and possibly separated by energy gaps. In the absence of explicit interaction terms, the ground state is obtained by filling the low-energy levels with the given number of electrons. This construction leads to the first success of the band theory of solids, namely the classifications of metals and insulators. When the chemical potential of the system sits in a gap between a completely full and an empty band, the system is known as an insulator, and any excitation has a finite energy cost. On the other hand if the highest populated band is only partially filled, low-energy excitations are possible and the system is a metal. The partially filled band is called conduction band.
A handy derivation of the band structure of solids is the tight-binding approximation: this

technique recognizes that the inner electrons are completely localized around the atom at each lattice site, partially screening its charge. As a result, the outer electrons are less bound, living in the so-called "extended states": their atomic orbitals, which constitute the periodic part of a Bloch wavefunction, partially overlap. The corresponding overlap integral gives the hopping amplitude t. The tight-binding Hamiltonian so obtained is therefore defined as a function of the on-site energies and the hopping amplitudes. In real space, an analogous formulation can be obtained through the Wannier wavefunctions [37], defined as the Fourier transform of the Bloch waves in the crystal lattice basis.
The extension of this formalism to second quantization is straightforward: an Hamiltonian having on-site energy ϵ_0 and hopping amplitude t_{ij} from site j to site i will have the form (disregarding the spin index)

$$\hat{H} = \sum_i \epsilon_0 c_i^\dagger c_i + \sum_{ij} t_{ij} c_i^\dagger c_j. \tag{2.2}$$

By introducing the formalism of second quantization, and considering a ground state made up of filled levels, we are naturally stepping in the territory of many-body problems. This comes with a fundamental complication: in multi-particle systems the inter-electron Coulomb interaction cannot be idly disregarded. Even accounting for the effect of screening, it is still comparable with the kinetic energy even in good metals. The explanation of the robustness of this method against Coulomb interaction stems from adiabatic evolution, and came by the work of Landau in 1956 on ^{3}He, later expanded by Abrikosov and Khalatnikov [38].

2.1 Landau-Fermi liquid theory

The idea at the base of Landau's Fermi liquid theory is that the electrons in a metal are usually at a temperature which is vastly inferior than the Fermi temperature scale of the system, which is of the order of $\sim 10^4 K$. We can therefore consider only low-lying excited states. Landau's argument starts by considering a non-interacting ground state and adds a particle whose energy and momentum lie just outside the Fermi sphere. Then, interactions are assumed to be adiabatically turned on, with the process sufficiently slow as not to permit level crossing in the evolution of the Hamiltonian. Landau's conclusion is then that the fully interacting system excitations can be described in complete analogy with the non-interacting ones. The difference between the non-interacting and the interacting systems, disregarded in the form of the Hamiltonian, will be reabsorbed into the definition of the excitations, which will no longer be electrons but *quasiparticles*. Crucially, the distribution function of these quasiparticles will still be a sharp Fermi distribution, and accordingly a Fermi sphere will be defined, whose volume will not vary from that of a non-interacting system as stated by Luttinger's theorem [39].
The key concepts that make this paradigm work are the presence of the Fermi surface, a sharp cutoff between occupied and free energy states, and the Pauli principle, that only allows transitions from below to above the Fermi surface. The excitation processes we consider are of this type: an electron with momentum slightly higher than the Fermi momentum is added to the system. As long as energy and momentum conservation are respected, it can interact with an electron inside the Fermi sphere promoting it to another low-lying excited state, creating therefore a hole inside the sphere itself. The added electron, which has energy ω, can only dig $\omega_1 < \omega$ deep inside the Fermi surface, and the promoted electron can have at most $\omega+\omega_1$ energy outside the Fermi sphere. Therefore, by Fermi's golden rule, the probability of transition, which

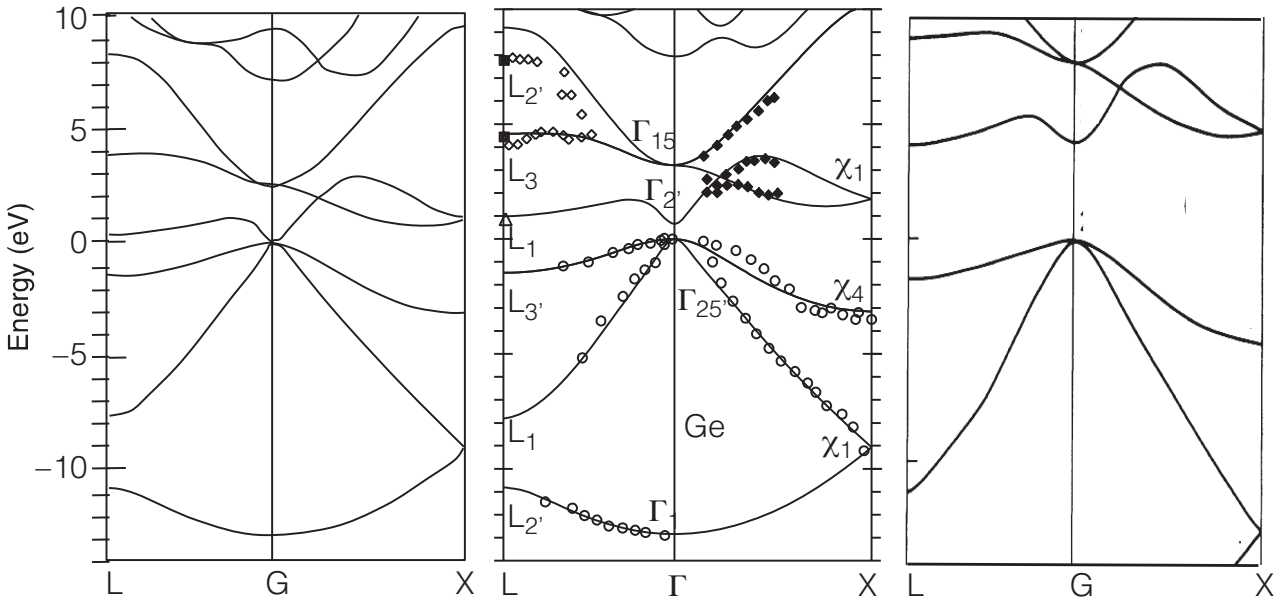

Figure 2.1: *Band diagrams for Ge (composite image from [40]) for LDA, GW and Hartree-Fock approximations. The middle panel approximates quite well the photoemission and inverse photoemission data (circles). The bandgap problem is evident for the other two approximations: Hartree-Fock captures well the insulating character of* Ge*, but screening of Coulomb interaction is not well accounted for, leading to a much too large bandgap. By contrast, Kohn-Sham eigenvalues underestimate the gap, describing* Ge *as a metal.*

is proportional to the inverse lifetime of the excitation, will be $\propto \omega^2$. The lifetime therefore grows faster, for excitations near the Fermi energy, than the period of the wavefunction, hence for a low-lying excitation the quasiparticle behaves just like an infinite-lived real particle.
This result is remarkable: in presence of electronic interactions, the system near the Fermi level can be described as a gas of noninteracting particle-like quantities, with vanishing scattering probability. We can picture a quasiparticle in this way: an added electron surrounded by a cloud of particle-hole excitations, thus having different effective mass than a free electron but equally vanishing scattering probability.

2.2 Many-Body concepts in band theory

Landau-Fermi liquid theory can shine a new light on the electronic band structure: if an electron is added to an interacting system, the whole band structure is not washed away. Rather, the corresponding quasiparticle progressively fills the available spots in the bands.
As previously stated, the distinction between metals and insulators from a band theory perspective stems from the position of the Fermi energy in relation to the bands: if it crosses a partially occupied band the system is a metal, while if it lies inside a forbidden *bandgap* between occupied and empty bands the system is an insulator.
The bandgap is in itself a many-body concept, since it compares the energy of system with a different number of electrons living in different sectors of the Fock space. The estimation of

the bandgap has crucial applications in everyday technology, and is therefore the subject of intensive study.
The "bandgap problem" shows the limitations of mean-field methods in the description of real system, such as Hartree-Fock (a Slater determinant based mean-field technique) or DFT (which relies on en auxiliary noninteracting system described by the Kohn-Sham Hamiltonian) in the LDA approximation: famously, the estimated gap of Ge is underestimated by DFT-LDA and overestimated by HF, as it can be seen it Fig. 2.1. While in the first case the band structure is not really an appropriate tool to the end of bandgap estimation, due to the way the auxiliary system is introduced, Hartree-Fock is in principle a completely legitimate approach: precisely, by Koopman's theorem, the HF excitation energy is the energy cost of adding or removing an electron if the rest of the electrons are not allowed to reorganize, every fluctuation being frozen in a non-interacting Slater determinant [41]. The failure of Hartree-Fock to correctly estimate the bandgap of certain solids clearly shows that the paradigm of independent particles, that "see" each other only by Fermi statistics, does not include important effects which determine the value of the energy gap, even for simple systems in which the single-particle approximations describe accurately the groundstate properties. Here lies the reason for the one of the general definitions of correlation as "everything beyond Hartree-Fock".

2.3 Green's function and spectral weight

The validity of a specific theory is, as always, to be supported by experimental results. The way the predicted properties of a solid state system can be investigated is by measuring its response to an appropriate probe. This is usually done by adding or removing a particle from the system at hand, for example via excitation through the shining of light of a certain energy and momentum.
Given a perturbation term

$$\hat{H}' = \int dr(\eta(r,t)c_r^\dagger + \eta^*(r,t)c_r) \tag{2.3}$$

for suitable Grassmann variables η, η^* [42], that acts as a source/sink of particles ad a given point, we can measure the average of the destruction operator at a certain position and time in response to such a perturbation. By the theory of linear response, this would depend on a response function, the *single-particle Green's* function, defined as

$$G(r_2 - r_1, t_2 - t_1) = -i\theta(t_2 - t_1)\langle[c_{r_2,t_2}, c^\dagger_{r_1,t_1}]\rangle \tag{2.4}$$

where the square brackets denote a fermionic anticommutator and the θ-function is included to preserve causality. This expression can be also written in momentum space so that, for a translational-invariant system, the Green's function has the form

$$G(\mathbf{k}, t_2 - t_1) = -i\theta(t_2 - t_1)\langle[c_{\mathbf{k},t_2}, c^\dagger_{\mathbf{k},t_1}]\rangle \tag{2.5}$$

As customary in linear response theory, we can express its Fourier-transform in frequency domain via the *Lehmann spectral representation*

$$G(\mathbf{k},\omega) = \frac{1}{Z}\sum_{n,m}\langle n|c_\mathbf{k}|m\rangle\langle m|c^\dagger_\mathbf{k}|n\rangle\frac{e^{-\beta E_n} + e^{-\beta E_m}}{\omega + E_n - E_m + i\delta} \tag{2.6}$$

where Z is the partition function, $|m\rangle$ and $|n\rangle$ are eigenstates of the Hamiltonian of the system with eigenvalues E_n and E_n, and the term $i\delta$ is the usual convergence factor.
This quantity can be analytically continued to the whole complex plane and generally expressed as

$$G(\mathbf{k},\omega) = \int dz A(\mathbf{k},z)\frac{1}{\omega - z} \tag{2.7}$$

where $A(\mathbf{k},z)$ is known as the *spectral function*, which from the two previous equation has the form

$$A(\mathbf{k},\omega) = \frac{1}{Z}\sum_{mn}\left(e^{-\beta E_n} + e^{-\beta E_m}\right)\left|\langle n|c_{\mathbf{k}}|m\rangle\right|^2 \delta(\omega - E_m + E_n). \tag{2.8}$$

This expression has a precise physical meaning: it is the density of states for a transition from a state to another involving the creation of a single particle excitation with momentum $\mathbf{k}$ and energy ω. Not surprisingly, for a non-interacting Hamiltonian the spectral function is just a collection of deltas, reflecting the fact that the only allowed excitation of a non-interacting system are those that sit on the electronic band structure. Relatedly, the Green's function of a non-interacting system will have the form

$$G(\mathbf{k},\omega) = \frac{1}{\omega - \epsilon_{\mathbf{k}}} \tag{2.9}$$

the poles of which correspond to the eigenvalues of the Hamiltonian, and so to the infinitely-lived single-particle excitations of a non-interacting system.
The spectral function is precisely what's measured in photoemission experiments, where photons of given $\mathbf{k}$ and ω are used to create single-particle excitations. The Green's function approach therefore seems well sounded as a starting point to examine the spectrum of excitations of a correlated system, which shows nontrivial effects beyond band theory.

2.4 Correlation effects on the Green's function

In the previous section we have stressed that the existence of single particle excitations with an infinite lifetime is associated to a specific form of the Green's function, showing a pole at the frequency corresponding to the excitation energy, and to a delta contribution at that frequency in the spectral function. In this section we discuss how this analytical structure is altered by the interactions.
We expect that, when the Landau theory holds, even in the presence of interactions, the low-energy excitations retain the behaviour of the non-interacting system at least at low temperature. However, the validity of the Landau scheme is based on the assumption that the interaction does not induce phase transitions. When the interaction becomes large, as it happens typically for materials characterized by narrow bands (for example materials where the bands have $3d$ and $4f$ character), the Green's function may exhibit properties that render a description in terms of quasiparticles no longer possible.

In completely general terms, the effect of the interaction on the single-particle Green's function is embodied by the *Self-Energy* $\Sigma(\mathbf{k},\omega)$, entering the definition of the Green's function as

$$G(\mathbf{k},\omega) = \frac{1}{\omega - \epsilon_{\mathbf{k}} - \Sigma(\mathbf{k},\omega)} \tag{2.10}$$

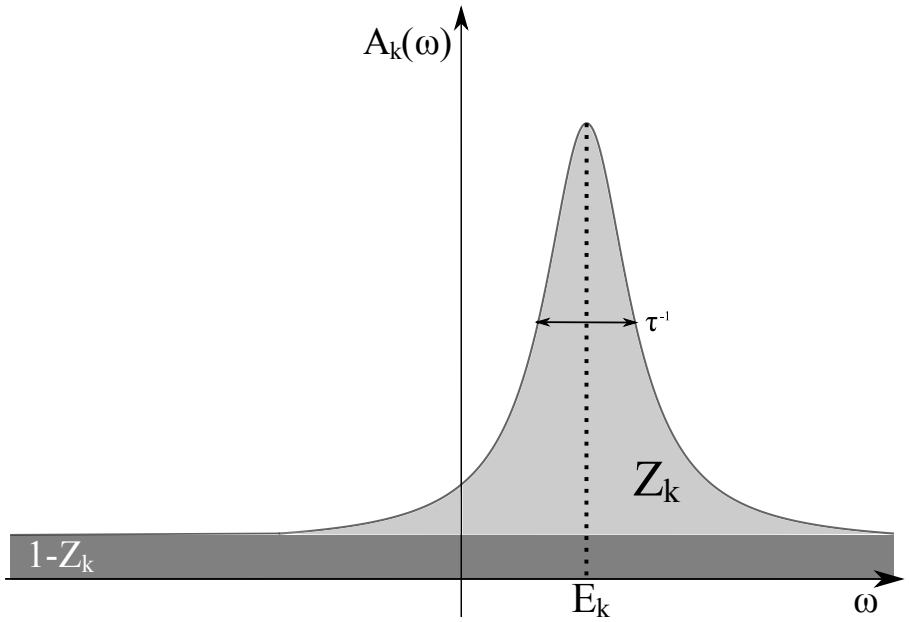

Figure 2.2: *Graphical representation of the spectral function $A_k(\omega)$ at a fixed k as a function of ω for a Landau Fermi liquid. The shape of a peak, a delta for a non-interacting system, is now a broadened Lorentzian. The broadening is controlled by the inverse lifetime $\frac{1}{\tau}$, which is proportional to $\mathrm{Im}\Sigma_k(\omega)$. The area enclosed in the Lorentzian corresponds to a (not in scale) fraction Z_k of the normalized spectral weight, the rest being an incoherent background. The value of Z_k, as well as the position of the peak close to the Fermi energy, is related to the real part of the Self-Energy $\mathrm{Re}\Sigma_k(\omega)$. Real and imaginary parts are, of course, in turn related by Kramers-Kronig relation.*

which, given (2.9), is a way of rewriting of the usual Dyson's equation relating the bare Green's function to the fully dressed one. Calculating the Self-Energy amounts to solving the many-body problem through one of the very many methods available, both perturbative in the interaction (with Feynman-diagram derived techniques as GW) and non-perturbative (as in DMFT, where no expansion in the interaction term is made).
We now discuss the effect of the Self-Energy in general terms: the expression for $A(\mathbf{k},\omega)$ can be recast as

$$A(\mathbf{k},\omega) = -\frac{1}{\pi}\frac{\mathrm{Im}\Sigma(\mathbf{k},\omega)}{(\omega - \epsilon_{\mathbf{k}} - \mathrm{Re}\Sigma(\mathbf{k},\omega))^2 + \mathrm{Im}\Sigma(\mathbf{k},\omega)^2} \tag{2.11}$$

where we see that the real and imaginary part of Σ contribute in different ways.
Let us consider the effect of $\Sigma(\mathbf{k},\omega)$ on a Landau-Fermi liquid quasiparticle peak: the δ distribution is now a Lorentzian (see Fig. 2.2) with a broadening given by the imaginary part of the Self-Energy. Transformed back in the time domain, this implies a damping factor on the Green's function, which is related to the inverse of $\mathrm{Im}\Sigma$ and is identified to be the lifetime of the quasiparticle. From the considerations of the previous sections, a Landau-Fermi liquid Self-Energy has to have an imaginary part vanishing as ω^2 for $\omega \to 0$.
The energy of the excitation is instead given by the first term in parenthesis at the denominator of (2.11): the real part of the Self-Energy is therefore responsible for the shift in energy of the poles of the Green's function, providing a renormalization of the effective Hamiltonian band

structure. This shift of the poles can dramatically alter the properties of the system, and even influence its phase transitions as we will see in chapters 5 and 6.
In the Landau-Fermi liquid framework, we are mostly interested in excitations near the Fermi energy. Let us therefore consider the linearized dispersion relations near k_F (dropping for simplicity of notation the vector character) for the non-interacting and renormalized energy eigenvalues:

$$\epsilon(k) = \frac{k_F}{m}(k - k_F) \qquad \tilde{\epsilon}(k) = \frac{k_F}{m^*}(k - k_F) \tag{2.12}$$

where the two parameters m and $m*$ have the meaning of masses. The second especially is the "effective mass" of the quasiparticle, and encloses all the effects of the interaction. We can relate the effective mass to the Self-Energy by expanding the expression for $\tilde{\epsilon}$ obtained from (2.11):

$$\frac{\mathrm{d}\tilde{\epsilon}(k)}{\mathrm{d}k} = \frac{\mathrm{d}\epsilon(k)}{\mathrm{d}k} + \frac{\partial \mathrm{Re}\Sigma(k,\omega)}{\partial k} + \frac{\partial \mathrm{Re}\Sigma(k,\omega)}{\partial \omega}\bigg|_{\omega=\tilde{\epsilon}(k)} \frac{\partial \tilde{\epsilon}(k)}{\partial k} \tag{2.13}$$

and then use (2.12) near the Fermi momentum to get a relation between the effective mass and the Self-Energy:

$$\frac{m}{m^*} = \frac{1 + \dfrac{m}{k_F}\dfrac{\partial \mathrm{Re}\Sigma(k,E_F)}{\partial k}\Big|_{k_F}}{1 - \dfrac{\partial \mathrm{Re}\Sigma(k,\omega)}{\partial \omega}\Big|_{\tilde{\epsilon}_F}} \tag{2.14}$$

The real part of the Self-Energy has a further effect on the quasiparticle description of the system: from the properties of the δ-function, the spectral function of the quasiparticle (disregarding lifetime) can be rewritten as

$$A(k,\omega) = Z_k \delta(\omega - \tilde{\epsilon}(k)) \tag{2.15}$$

where Z_k is the *quasiparticle weight* given by

$$Z_k = \left[\frac{\partial}{\partial \omega}(\omega - \epsilon(k) - \mathrm{Re}\Sigma(k,\omega))\Big|_{\tilde{\epsilon}_F}\right]^{-1} = \frac{1}{1 - \dfrac{\partial \mathrm{Re}\Sigma(k,\omega)}{\partial \omega}\Big|_{\tilde{\epsilon}_F}} \tag{2.16}$$

which is in general smaller than 1.

This means that the excitation of a Landau-Fermi liquid can be described by quasi-particles with a weight Z_k, the rest being contained in an incoherent background with no clear energy-momentum relation.
As we anticipated above, photoemission experiments access directly the spectral function, and therefore the parameters we just introduced like the renormalized dispersion, effective mass and quasiparticle weight. In particular, the so-called Angle-resolved photoemission (ARPES, see Fig. 2.3) allows to measure the momentum dependence of this properties, which is evidently crucial for the description of the electronic structure. This kind of experiments allows both to extract Fermi-liquid parameters and to detect deviations from -or even a breakdown of- the LFL paradigm. This can be associated to a change in the functional form of the low-energy state, which can give rise to non-Fermi liquid metals, or a complete disappearance of weight: for example, if the Self-Energy in (2.11) experiences a divergence in its imaginary part near the Fermi level, a spectral gap will open in the corresponding Green's function. Moreover, by

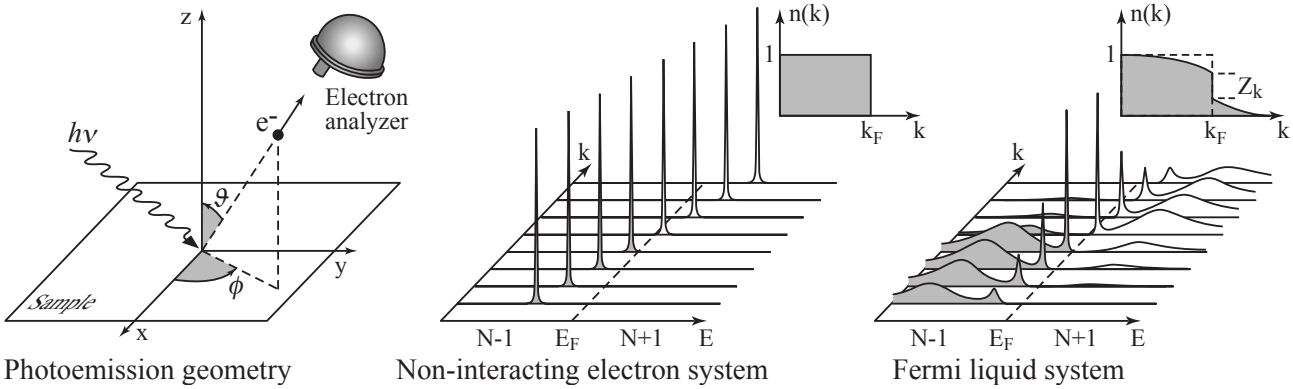

Figure 2.3: *Representation (adapted from [43] through [40]) of the spectral function as retrieved by photoemission experiments:* a) *ARPES measurement setup* b) *Spectral weight and distribution function for a non-interacting electron system and* c) *for an interacting one. The peaks have broadened, signalling a finite lifetime for the quasiparticles. Part of the spectral weight is depleted into the high-frequency sidebands, and the sharp cutoff at the Fermi momentum is replaced by a reduced jump of height proportional to Z_k. Incidentally, the persistence of the jump signals the possibility of still describing the system as a Landau-Fermi liquid. When $Z_k \to 0$ this description breaks down and there is no longer a defined Fermi surface.*

Kramers-Krönig relations, the quasiparticle weight Z_k will be reduced to 0 and the description in terms of a renormalized band structure will lose its meaning. As we shall see, this behaviour is associated to a correlation-induced metal-insulators transition, which goes under the name of Mott Hubbard transition.

2.5 Hamiltonian models for interacting systems

The Green's function is, as we have seen, a very powerful tool to describe interacting systems, both theoretically and by comparison with experimental results. At the core of its definition rests the temporal evolution of the system, which is governed by its Hamiltonian. We will now comment on the best way of enclosing into a tight-binding Hamiltonian formulation the effects of Coulomb interaction.

Depending on their quantum numbers, atomic orbitals have wildly varying shapes and characteristics: some of those (s and p) are generally very delocalized, meaning that their radial component decays slowly away from the atomic nucleus, and therefore present a high enough overlap in crystals as to make a mean-field single-particle description based on band theory well sound. Other orbitals however, as the d and f, which especially characterize transition metals or heavy-elements compounds, decay much more rapidly away from the nucleus: electrons sitting in these orbitals will "feel" each other much more strongly, and a description based on a single-particle pictures becomes inaccurate. When modelling a system presenting both kinds of orbitals, it is a common procedure to select the appropriate "low-energy" subspace responsible for the relevant physics, treating the effects of the other degrees of freedom in terms of both *renormalization* of the system parameters and *screening* of the Coulomb interaction, which is explicitly considered only for the relevant orbitals.

This procedure goes by the name of *downfolding*; let us see an example of its application for

a generic system presenting both delocalized orbitals (e.g. p) and highly localized d orbitals, the latter near the Fermi energy. Since the metal-insulator character of the system will mostly depend on the behaviour of the d orbitals, we can write the Hamiltonian as [44]

$$\begin{pmatrix} H_{pp} & H_{pd} \\ H_{dp} & H_{dd} \end{pmatrix} \begin{bmatrix} |\mathbf{k}, p\rangle \\ |\mathbf{k}, d\rangle \end{bmatrix} = \epsilon \begin{pmatrix} \mathbb{I}_{pp} & 0 \\ 0 & \mathbb{I}_{dd} \end{pmatrix} \begin{bmatrix} |\mathbf{k}, p\rangle \\ |\mathbf{k}, d\rangle \end{bmatrix} \tag{2.17}$$

and then obtain, by the usual formula for block diagonalization of a matrix, the reduced operator for the eigenvalue equation in the d basis as

$$H^{\epsilon}_{dd} = H_{dd} - H_{dp}(H_{pp} - \epsilon \mathbb{I}_{pp})^{-1} H_{pd} \tag{2.18}$$

The Hamiltonian for the relevant d subspace is expressed in a basis having the same symmetries as the atomic orbitals under consideration, but will account for the effects of the downfolded degrees of freedom by having *renormalized* hopping integrals. These will introduce distortions such as, for example, inter-orbital hopping, a wider radial wavefunction than that of the atomic orbitals or a a shift of the barycentre of the bands, what is called a *crystal-field splitting*.
Once the renormalized hopping integrals in the chosen tight-binding basis have been obtained, the interaction term is added. In principle, in considering the interaction between electrons in different orbitals and lattice sites one has to include every term of the Coulomb interaction tensor with elements

$$U_{\alpha'\beta'\beta\alpha} = \int \mathrm{d}\mathbf{r}_1 \mathrm{d}\mathbf{r}_2 \psi^*_{\alpha'}(\mathbf{r}_2)\psi^*_{\beta'}(\mathbf{r}_1) V(\mathbf{r}_1 - \mathbf{r}_2)\psi_{\beta}(\mathbf{r}_1)\psi_{\alpha}(\mathbf{r}_2) \tag{2.19}$$

which represents the coulomb interaction between two electron that scatter from orbitals α, β to α', β'. This is the general expression of Coulomb interaction, not accounting for screening effects. Obviously, this expression requires the calculation of a great quantity of terms, so some simplifications are in order. One may, for example, consider only local interactions, that is exclude all integrals where the orbitals are not on the same site.
A further simplification, assuming spherical symmetry, comes from the expression of the atomic wavefunction in spherical coordinates in the form $\psi_{nlm}(\mathbf{r}) = R_{nl}(r)Y^l_m(\theta, \phi)$ where n, l, m are the usual quantum numbers. The Coulomb interaction term has a space dependence given by

$$\frac{1}{|\mathbf{r}_1 - \mathbf{r}_2|} = \sum_{k=0}^{\infty} \frac{\min(r_1, r_2)^k}{\max(r_1, r_2)^{k+1}} \frac{4\pi}{2k+1} \sum_{q=-k}^{k} Y^k_q(\theta_2, \phi_2) Y^{*k}_q(\theta_1, \phi_1) \tag{2.20}$$

which, inserted in (2.19), determines the form of the U coefficients via angular integrals, which can be calculated in terms of Clebsch-Gordan coefficients, and radial Slater integrals [45] defined as

$$F_k = \int \mathrm{d}r_1 r_1^2 \int \mathrm{d}r_2 r_2^2 R^2_{nl}(r_1) \frac{\min(r_1, r_2)^k}{\max(r_1, r_2)^{k+1}} R^2_{nl}(r_2) \tag{2.21}$$

The number of integrals to be calculated can also be reduced by using some famous simplified expressions, the most known of which is due to Kanamori [46] and involves only a subset of the previous integrals, namely

$$U = \int d\mathbf{r}_1 d\mathbf{r}_2 |\psi_\alpha(\mathbf{r}_1)|^2 V(\mathbf{r}_1 - \mathbf{r}_2) |\psi_\alpha(\mathbf{r}_2)|^2 \tag{2.22}$$

$$U' = \int d\mathbf{r}_1 d\mathbf{r}_2 |\psi_\alpha(\mathbf{r}_1)|^2 V(\mathbf{r}_1 - \mathbf{r}_2) |\psi_\beta(\mathbf{r}_2)|^2 \tag{2.23}$$

$$J = \int d\mathbf{r}_1 d\mathbf{r}_2 \psi^*_\alpha(\mathbf{r}_1) \psi^*_\beta(\mathbf{r}_1) V(\mathbf{r}_1 - \mathbf{r}_2) \psi_\alpha(\mathbf{r}_2) \psi_\beta(\mathbf{r}_2) \tag{2.24}$$

$$J' = \int d\mathbf{r}_1 d\mathbf{r}_2 \psi^*_\alpha(\mathbf{r}_1) \psi^*_\alpha(\mathbf{r}_1) V(\mathbf{r}_1 - \mathbf{r}_2) \psi_\beta(\mathbf{r}_2) \psi_\beta(\mathbf{r}_2) \tag{2.25}$$

In the common case of narrow d-orbitals the wavefunctions can be chosen real, so that the last two coefficients, J and J' are equal. The full many-body atomic Hamiltonian in second quantization then takes on each site the form [47]

$$\begin{aligned} \hat{H}_{int} = U \sum_\alpha \hat{n}_{\alpha\uparrow}\hat{n}_{\alpha\downarrow} + U' \sum_{\alpha\neq\beta} \hat{n}_{\alpha\uparrow}\hat{n}_{\beta\downarrow} + (U' - J) \sum_{\alpha<\beta,\sigma} \hat{n}_{\alpha\sigma}\hat{n}_{\beta\sigma} - \\ J \sum_{\alpha\neq\beta} c^\dagger_{\alpha\uparrow} c_{\alpha\downarrow} c^\dagger_{\beta\downarrow} c_{\beta\uparrow} + J \sum_{\alpha\neq\beta} c^\dagger_{\alpha\uparrow} c^\dagger_{\alpha\downarrow} c_{\beta\downarrow} c_{\beta\uparrow} \end{aligned} \tag{2.26}$$

where $\hat{n}_{\alpha\sigma} = c^\dagger_{\alpha\sigma} c_{\alpha\sigma}$. The first three terms involve only density-density interactions, between electrons with opposite spins in the same orbital (U), opposite spins in different orbitals ($U' < U$) and parallel spins in different orbitals. The last two are the aptly-named spin-flip and pair-hopping terms, which describe processes in which two electrons change spin or hop together from an orbital to another respectively.
Though the form of the Kanamori Hamiltonian neglects some of the integrals (2.19), and therefore encloses some assumptions on the effects of screening that are not completely general, it has two properties that make it very appealing: first, it is consistent with the Hund rules [48], which aim to determine the preferred electronic ground state configuration for a multi-orbital atom; the one that, in order,

- Maximizes the total spin S
- Maximizes the total angular momentum L
- For less(more) than half-filling minimizes(maximizes) $|L - S|$.

The general idea between these rules is the minimization of Coulomb potential for the stable electronic configuration: famously, the first one for a couple of atoms favours an antisymmetric radial wavefunction, which intuitively puts the electrons further apart.
Another advantage of the Kanamori formulation is that, provided a suitable relation between its parameters, it exhibits full rotational invariance with respect to composite charge-spin-orbital transformations, denoted as $U(1) \otimes SU(2) \otimes O(3)$ symmetry: the usual example is that of the d-orbitals in transition metal oxides, which in a cubic crystal field are split in the lower energy 3-fold degenerate t_{2g} and higher energy e_g orbitals. For the t_{2g} case, rotational invariance is apparent if we define the charge, spin and pseudospin operators[1]

$$\hat{N} = \sum_{\alpha\sigma} \hat{n}_{\alpha\sigma} \qquad \vec{S} = \frac{1}{2} \sum_\alpha \sum_{\sigma\sigma'} c^\dagger_{\alpha\sigma} \vec{\tau}_{\sigma\sigma'} c_{\alpha\sigma'} \qquad \hat{T}_\alpha = \frac{1}{2} \sum_\sigma c^\dagger_{\beta\sigma} \epsilon_{\alpha\beta\gamma} c_{\gamma,\sigma} \tag{2.27}$$

[1] to avoid confusion, we indicate the Pauli matrices by τ, while $\epsilon_{\alpha\beta\gamma}$ is the antisymmetric tensor

and impose $U' = U - 2J$. The Hamiltonian takes the fully rotational-invariant form

$$H_{t_{2g}} = (U - 3J)\frac{\hat{N}(\hat{N}-1)}{2} - 2J\overrightarrow{S}^2 - \frac{J}{2}\overrightarrow{T}^2 + \frac{5}{2}J\hat{N} \tag{2.28}$$

The requirement $U' = U - 2J$ is also valid for the e_g doublet and assuming cubic symmetry, as was shown by Castellani et al. in the case of V_2O_3 [49]. The cubic-symmetric Kanamori interaction then takes the form

$$H_{e_g} = (U - J)\frac{\hat{N}(\hat{N}-1)}{2} + 2J(T_x^2 + T_z^2) - J\hat{N} \tag{2.29}$$

where the pseudospin operator $\overrightarrow{T}$ is now given in terms of the Pauli matrices τ analogously to $\overrightarrow{S}$. It is important to stress that these formulations of interactions are, at this stage, purely theoretical. It is then a matter of deciding which one best fits the real material at hand, and which values of the parameters are optimal (various techniques have been developed to this end, such as CLDA [50] or CRPA [51]).

2.6 Correlation-driven phase transitions

As we have seen, the standard procedure to study correlation effects in any real or toy model is to identify the relevant bands, derive an appropriate non-interacting Hamiltonian for the subspace spanned by the corresponding atomic orbitals and then add the Coulomb interaction in one of its many formulations, with an eye to the specific symmetries of the model.
The minimal example of the application of this procedure is the one-orbital *Hubbard model*, proposed and developed in a series of papers in 1963-67 [52–55], which in real space corresponds to a collection of lattice sites each of which supports a maximum of two electrons with opposite spin. This model doesn't feature any of the many effects of Hund physics (such as increase or decrease of the Coulomb repulsion by Hund coupling depending on the filling, or the lowering of the Kondo temperature in an impurity problem), but is perfectly adequate to investigate the interplay between delocalization and correlation effects. A suitable tight binding expression of the Hamiltonian is

$$\hat{H} = -t\sum_{\langle ij\rangle,\sigma} c_{i\sigma}^\dagger c_{j\sigma} + U\sum_i \hat{n}_i^\dagger \hat{n}_i \tag{2.30}$$

where the non-interacting part is reduced to the mere hopping between lattice sites (in this case restricted to nearest-neighbour), and the effect of the Coulomb interaction is to discourage the double-occupation of each lattice site, with an associate energy cost U.
Equation (2.30) gives a formal expression to a thought experiment setup originally conceived by Mott in 1949 [56]: he considered an array of hydrogen atoms not allowed to form molecules; if the atoms are close to each other, a band description for the system will be feasible due to the strong overlap between the outer orbitals. In the opposite limit, if the atoms are far apart each one will behave as isolated and the system as a whole will be in an insulating state, with the band structure losing any meaning. At the same time, one limit encourages while the other forbids electron hopping. Intuitively then, for a certain value of interatomic distance, the system undergoes a transition between a metallic state and an insulating one, which is known as a *Mott insulator*. This is not associated to the usual definition of an insulator in terms of a

bandgap, but is entirely driven by correlation, more specifically the energetic price to pay for two electrons to reside in the same orbital. The Mott transition is therefore to be sought as a function of the ratio between the bandwidth W, depending on t, and the interaction U.
In its formal simplicity, the Hubbard model has established itself as the theoretical go-to model for the description of interacting electrons, and is at the base of the explanation of intriguing insulating behaviour presented by many compounds, such as NiO [57] or V_2O_3 [58].
The 1-dimensional Hubbard chain was solved exactly by Lieb and Wu [59] by means of the Bethe ansatz: at T=0 the system is a metal for any U/t, except at half-filling; there, for every finite value of U the system becomes a Mott insulator, presenting a characteristic two-peaked spectral function at $\omega = 0$ and $\omega = U$, the so-called Hubbard bands associated to the absence or presence of doubly-occupied sites respectively. In any case, the one-dimensional Hubbard model shows no Mott transition as a function of U/t.
In higher dimensions this transition does appear at a finite U/t: however, while the 1-dimensional solution is exact, in any other case we can only rely on approximate solution methods. These can be perturbative or non-perturbative in the interaction, and are based on different numerical frameworks. In the next chapter we will present some of the most well-established non-perturbative solution methods, namely Dynamical Mean-Field theory and its cluster derivatives, and the related but philosophically distinct Self-Energy Functional Theory, in the context of an Exact Diagonalization-based solver.

2.7 Interacting topological invariants

The formulation of topological invariants provided in Chapter 1, from the TKNN index associated to Quantum Hall Effect to the $\mathbb{Z}_2$ formula for a Quantum Spin Hall system in presence of Time-Reversal and Inversion symmetries, relies on the definition of Bloch states in the framework of band theory. Therefore, all these concepts have in principle no obvious extension to the realm of interacting systems, especially those system in which Landau-Fermi liquid theory is not applicable.
However, it is possible to extend the definitions of topological invariants to a more general realm in which the band structure is not explicit or even defined, relying on the Topological Field Theory, an effective field-theoretical framework [60] specifically designed to overcome the difficulties exhibited by Topological Band Theory (TBT) in describing interacting systems. Within this framework, one retains direct access to the relevant observables, such as the Hall conductance, and to the related topological invariants, which are however defined in terms of the Green's function of the system. As we have seen in the previous sections, the Green's function is perfectly suited to describe the properties of both interacting and non-interacting systems, so through the field-theoretical approach the topological properties of systems such as Mott insulators [61] become well defined, as well as the topological phase diagrams in presence of interaction, as shown in Fig. 2.4.
At its core, the Topological Field Theory is a response theory: given a fermionic system coupled to an external field, its nontrivial topological properties will be encoded in the response function to the field. Let us take as an example the (2+1)-dimensional Quantum Hall system, which was the starting point of our study of topological invariants. In this case, the external field is obviously the electromagnetic field A. From the action of the whole system, an effective action depending only on the external field is obtained by integrating out the fermions, giving

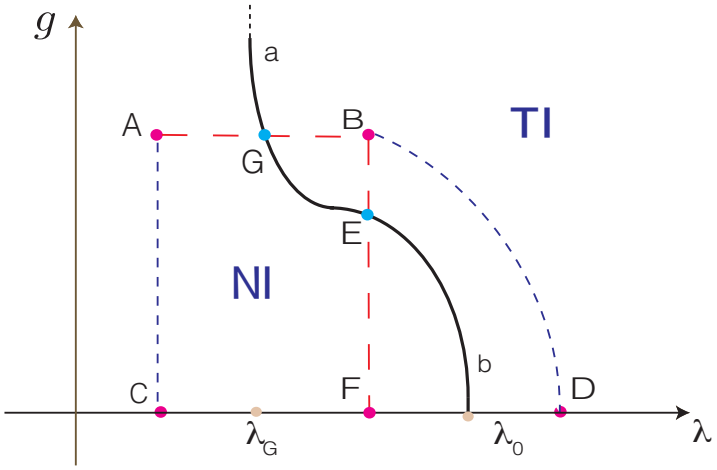

Figure 2.4: *Interacting phase diagram (from [62]) of a topological phase transition. The λ axis represents a generic non-interacting parameter, such as a hopping amplitude or crystal-field splitting, while on the g axis the switching on of electronic interaction is visualized. As long as G is nonsingular, everywhere but on the ab black curve, the topological invariant is still well defined. The insurgence of a correlation-driven topological phase transition can be seen on the curve BF: the interacting system in B has a different topological invariant from its non-interacting counterpart in F.*

at the leading order in A

$$S_{eff} = \frac{1}{2}\int d^3x d^3x' \chi_{\mu\nu}(x,x') A_\mu(x) A_\nu(x') \tag{2.31}$$

where x is the (2+1)-dimensioanl spacetime coordinate and χ is the linear response function of the fermionic system, that will in general depend on its Green's function. Through a gradient expansion on the response function, then, we can obtain all the terms preserve the symmetries of the model, such as translational, rotational and gauge invariance. One of such terms is the Maxwell action

$$S_{Max} = -\frac{1}{4}\int d^3x F_{\mu\nu}F^{\mu\nu} \tag{2.32}$$

where F is the usual electromagnetic tensor.
Some terms in the gradient expansion of χ do not in general preserve gauge invariance. They will meet this criterium only provided that their coefficient satisfies a global condition. Thus, the system will or won't show a specific response to the applied field (such as, in our example, the transverse Hall conductance) depending on the value of a given function of G, which will constitute the topological invariant.
The field-theoretical derivation of the topological invariants is, in general, quite involved; however, under certain hypotheses a less convoluted -and computationally demanding- expression can be derived. In the following paragraphs we will briefly go over the formal definitions of the interacting invariants relevant to our study, and the equivalent simpler formulations we will be using in the next chapters. Some of the relative calculations are reported in Appendix A.

2.7.1 TFT invariant for (2+1)-dimensional QHAE

The (2+1)-dimensional Quantum Hall effect is historically one of the first examples of application of TFT, as showed by Zhang in 1992 [63]. In the gradient expansion of the response function mentioned in the previous section, there is a term of lower order than the Maxwell term: this is the so-called Chern-Simons term, that gives origin to an effective action of the type

$$S_{CS} = \frac{N_2}{4\pi} \int d^3x A_\mu \epsilon^{\mu\nu\tau} \partial_\nu A_\tau \tag{2.33}$$

This term is gauge invariant, and therefore acceptable, provided that the associated topological invariant, which is the coefficient [64]

$$N_2 = \frac{1}{24\pi^2} \int dk_0 d^2k \mathrm{Tr}[\epsilon^{\mu\nu\rho} G\partial_\mu G^{-1} G\partial_\nu G^{-1} G\partial_\rho G^{-1}] \tag{2.34}$$

takes an integer value.
The main drawback of this expression is the inherent difficulty of its calculation, involving an integral on the k-space[2] as well as on the Matsubara axis k_0. However, as shown by Wang and Zhang [65], there is an equivalent way of treating this problem based on an effective Hamiltonian description, hence recovering the simplicity of TBT while maintaining the descriptive power of TFT with regards to interacting systems. This approach starts from the eigenstates of the inverse Green's function

$$G^{-1}(i\omega, k)|\alpha(i\omega, k\rangle = \mu_\alpha(i\omega, k)|\alpha(i\omega, k)\rangle \tag{2.35}$$

which are the same as those of G, with reciprocal eigenvalues. Those are real numbers, and thus the eigenvectors can be divided in two classes depending on the sign of $\mu_\alpha(0, k)$ (assuming no μ_α is zero, i.e. G is nonsingular). These are called right and left zeros, spanning k-subspaces called right and left space. Due to the orthogonality of eigenvectors, all the vectors in the R-space are orthogonal to those in the L-space. This enables us to define a generalized TKNN invariant based on an orthonormal base of the R-space. Its expression is

$$C_1 = \frac{1}{2\pi} \int d^2k F_{xy}, \tag{2.36}$$

where the "generalized Berry curvature" is

$$F_{ij} = \partial_i A_j - \partial_j A_i \tag{2.37}$$

and its associated connection is

$$A_i = -i \sum_{\alpha \in R-Space} \langle k\alpha|\partial_{k_i}|k\alpha\rangle, \tag{2.38}$$

where $|k\alpha\rangle = |\alpha(i\omega = 0, k)\rangle$. This expression is formally similar to its non-interacting counterpart; it is however not defined on the basis of Bloch functions of a non-interacting Hamiltonian but on the R-zeros and R-space of the Green's function of an interacting many-body problem,

[2] in this section, dealing with general definitions of TFT, we will use the notation k for the general n-dimensional momentum, forgoing the bold notation for the 2d/3d case.

though in the non-interacting limit the two concepts evidently coincide. A further step that brings the calculation of interacting topological invariants closer to familiar TBT concepts involves a way of dealing with the dynamical properties of the Green's function. As shown in Appendix A, it's possible to derive the interacting topological invariant from the properties of the Green's function at zero frequency or, equivalently, from the band dispersion of an effective *topological Hamiltonian*

$$H_{top}(k) = -G^{-1}(0,k) = H(k) + \Sigma(k,0) \tag{2.39}$$

thereby making the calculation of the invariant fully analogous to the TBT case.

2.7.2 TFT invariant for a (4+1)-dimensional TRS system

The form of the topological term in the (2+1)-dimensional effective action breaks time-reversal symmetry, under which $A_0 \to A_0$ and $\mathbf{A} \to -\mathbf{A}$. TRS is instead preserved in 4+1 dimensions, where the effective topological action takes the form

$$S_{eff} = \frac{N_4}{24\pi^2} \int d^5x \epsilon^{\mu\nu\rho\sigma\tau} A_\mu \partial_\nu A_\rho \partial_\sigma A_\tau \tag{2.40}$$

and the topological invariant is the coefficient [62]

$$N_4 = \frac{\pi^2}{15} \int \frac{dk_0 d^4k}{(2\pi)^5} \mathrm{Tr}\left[\epsilon^{\mu\nu\rho\sigma\tau} G\partial_\mu G^{-1} G\partial_\nu G^{-1} G\partial_\rho G^{-1} G\partial_\sigma G^{-1} G\partial_\tau G^{-1}\right] \tag{2.41}$$

in which again k_0 is the Matsubara frequency. Similarly to the two-dimensional case, an equivalence can be proven between this expression and the second Chern number

$$C_2 = \frac{1}{32\pi^2} \int d^4k \epsilon^{ijkl} \mathrm{Tr}[F_{ij} F_{kl}] \tag{2.42}$$

where the generalized Berry curvature

$$F_{ij}^{\alpha\beta} = \partial_i A_j^{\alpha\beta} - \partial_j A_i^{\alpha\beta} + i[A_i, A_j]^{\alpha\beta} \tag{2.43}$$

is is obtained from

$$A_i^{\alpha\beta}(k) = -i\langle k\alpha | \frac{\partial}{\partial k_i} | k\beta \rangle \tag{2.44}$$

where again $|k\alpha\rangle$ is an orthonormal base of the R-space. This again reduces to the expression for the second Chern number as defined from the Bloch wavefunctions for a non-interacting system. The (4+1)-dimensional TRS topological insulator can be considered the starting point to define the TFT invariants for $(2+1)$ and $(3+1)$-dimensional TRS topological insulators.

2.7.3 TFT invariants for TRS and IS systems

In 2008, Qi, Hughes and Zhang [60] developed, starting from (2.40), the general TFT for (2+1) and (3+1)-dimensional time-reversal invariant systems by means of a procedure known as *dimensional reduction*. Later work by Wang and Zhang have determined the form of a general topological invariant for TRS systems, which in 3d has the expression [62]

$$P_3 = \frac{\pi}{6} \int_0^1 du \int \frac{d^4k}{(2\pi)^4} \mathrm{Tr}[\epsilon^{\mu\nu\rho\sigma} G\partial_\mu G^{-1} G\partial_\nu G^{-1} G\partial_{rho} G^{-1} G\partial_\sigma G^{-1} G\partial_u G^{-1}] \tag{2.45}$$

in which k is the quadrimomentum with imaginary first component and u is what is called a Weiss-Zumino-Witten (WZW) extension parameter, that continuously connects the full Green's function $G(i\omega, k, u = 0)$ with a trivial constant reference function $G(i\omega, k, u = 1)$. The derivation of this result, while quite involved, is conceptually similar to the way in which the time-reversal polarization for the non-interacting system was derived by Fu and Kane.
The form of this invariant again makes it rather difficult to practically calculate. However, if the system possesses Inversion symmetry in addition to TRS, the calculation of the invariant can be dramatically simplified, as proven by Wang, Qi and Zhang in 2012 [66].
The derivation of the expression makes use of the same concepts involved in the $N_2 = C_1$ demonstration provided in Appendix A. Essentially, it again relies on the concept of R-space and R-zero, based on the sign of the eigenvalues of the Green's function at zero frequency and at a TRIM $\mu_\alpha(0, \Lambda_i)$. The associated eigenvector $|\alpha\rangle$ is chosen as to be simultaneously an eigenvector of the parity operator Π, since G and Π commute at the TRIMs.
The topological invariant Δ is defined as

$$(-1)^\Delta = \prod_{R-zero} \eta_\alpha^{1/2} \tag{2.46}$$

where the product is restricted to the states $|\alpha(0, \Lambda_i)\rangle$ whose associated eigenvalue $\mu_\alpha(0, \Lambda_i)$ is positive, and η_α is the parity eigenvalue for the state.
A R-zero can be transformed in a L-zero, and vice-versa, providing that during the transformation the Green's function experiences a singularity, which in TBT language corresponds to the closure of the gap. This happens when an eigenvalue of G^{-1} is passing through the origin (or through the compactified ∞ point, making $\det G = 0$, with similar consequences).
At the core of the demonstration is the proof of the equivalence mod 2 of the variation of Δ and $2P_3$ if the Green's function undergoes a deformation, parametrized by a conveniently chosen parameter λ, that involves passing through a singularity when $\lambda = 0$.
From symmetry requirements on G, it can be shown that at $\lambda = 0$ a couple of degenerate R(L)-zeros with negative parity cross the singularity and change topological class from R to L or vice-versa, contributing an overall factor of -1 in (2.46).
The consequent variation of Δ by 1 mod 2 is then seen to coincide with that of $2P_3$. This is done via geometrical considerations, following from the fact that (2.45) can be rewritten to represent the winding number W from the five-dimensional space spanned by frequency, momentum and WZW extension parameter to the space of Green's functions $GL(N, \mathbb{C})$.
Together with the fact that, in the non-interacting limit, the relation $2P_3 = \Delta$ mod 2 holds [67], this proves that the expression for Δ is a good $\mathbb{Z}_2$ topological quantum number for three-dimensional TRS and IS systems. Once again, the calculation of the topological invariant for an interacting Hamiltonian based on the BHZ model is then greatly simplified, reduced to the calculation of the same invariant for an effective *topological Hamiltonian*

$$H_{top}(k) = H(k) + \Sigma(k, \omega = 0). \tag{2.47}$$

The derivation of the two-dimensional counterpart of this invariant (and therefore also of the "weak" 3d topological invariants) is completely analogous, the only difference being the number of the TRIMs. This invariants are well-defined as long as a gap is open; in this thesis we will consider two and three-dimensional system with TRS and IS, and TRS-breaking three-dimensional systems for which the $\mathbb{Z}_2$ invariants will be only considered in the gapped phase. In all cases, the use of a formula of the type (2.46) is fully justified.

Chapter 3

Dynamical Mean-Field Theory and Cluster Methods for Strongly Correlated Fermions

In the previous chapter we have commented on the effects of Coulomb interaction on electronic systems, showing how correlation can substantially modify the single-particle picture, altering the expected values of some quantities (such as the bandgap of insulating systems) and even rendering the description in term of electronic band structure meaningless. We have also touched on the fascinating subject of correlation-driven phase transitions, addressing the Mott Hubbard transition occurring in systems with narrow atomic orbitals such as transition metals and related compounds.
As we briefly mentioned, even the simplest correlated model, the single-band Hubbard model, has not been solved exactly beyond the peculiar one-dimensional case. The study of this model and of the Mott-Hubbard transition has historically been the driving force towards the development of approximate solution methods for correlated electronic systems, both perturbative in the interaction and nonperturbative. We will concentrate, in this chapter, on the latter kind of approaches. Various fundamental steps towards the solution of the Mott transition problem occurred already in the 1960s, when the model was introduced by Hubbard, Kanamori and Gutzwiller. The first and third authors also pioneered two complementary approximate approaches which are more suited for the insulating and metallic sides of the transition, respectively. The two approximations can only certain aspects of the behaviour of the system near the Mott transition, which will be somehow reconciled and summed up nicely by the techniques we will examine in this chapter.

The Gutzwiller approach to the Mott transition [68–70] is based on a variational ansatz followed by a further approximation. The wave function is a Slater determinant (the non-interacting solution of the model in the original formulation) multiplied by a function which gives different weights to configurations with different number of doubly occupied sites:

$$|\Psi_G\rangle = \prod_i^N g^{\hat{n}_{i\uparrow}\hat{n}_{i\downarrow}} |\Psi_0\rangle \tag{3.1}$$

where g is a variational parameter and N is the number of sites. The energy of the system is then minimized with respect to such ground state, usually through variational Monte Carlo algorithms. However, the expectation value of the Hamiltonian in this state can not be com-

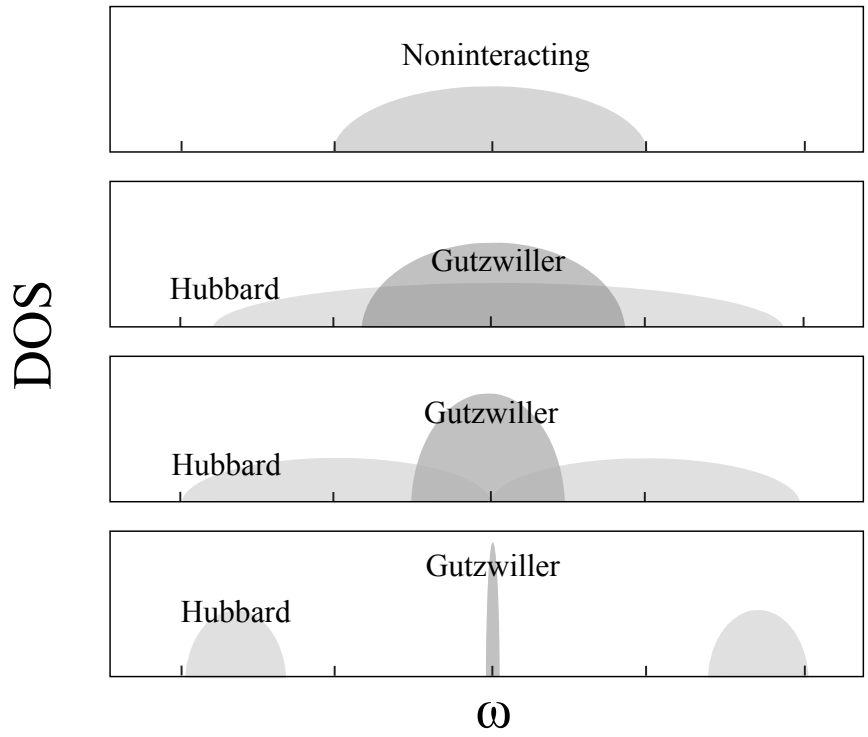

Figure 3.1: *Sketch of the evolution of spectral weight distribution in the Gutzwiller and Hubbard III approximations for a semicircular density of states. The two methods address the insurgence of a correlation-driven insulating phases from a low-energy and high-energy perspective respectively.*

puted exactly and one usually resorts to a further approximation which turns out to become the exact expectation value only in the limit of infinite coordination. Within this approach, the onset of correlations is described in terms of a progressive "destruction" on the non-interacting groundstate, which describes a metal. In particular the solution describes a metal with the same Fermi surface of the non-interacting system, but a reduced bandwidth (i.e. an increased effective mass) as long as such a solution exists. As we stated in the previous chapter, a Mott transition is expected to take place, in more than one dimension, for half-filling and a finite interaction U. In Gutzwiller's picture, as applied by Brinkman and Rice [71], this is associated to the shrinking of the density of states around the Fermi level with U up until a critical value U_c, after which the solution has zero kinetic energy and no double occupancy. The effective mass of the quasiparticle excitations diverges at U_c, signalling the breakdown of the Landau-Fermi liquid description and the insurgence of a phase transition.
A different approach to the Mott transition was devised by Hubbard in a series of seminal papers [52–55], and is based on a Green's function description. Starting from the atomic limit $t = 0$, the lattice hopping is introduced as a correction to the one-particle Green's function, which in turn takes the form:

$$G_\sigma(\mathbf{k},\omega) = \frac{1}{[\omega - \epsilon_0 - \Sigma_\sigma(\omega)] - \Delta\epsilon(\mathbf{k})} \tag{3.2}$$

where the expression in parenthesis is completely referred to the isolated interacting sites, while

$\Delta\epsilon(\mathbf{k}) = \epsilon(\mathbf{k}) - \epsilon_0$ represents the lattice effects in the noninteracting limit. This expression for the Green's function is at the base of various approximations, designed to be exact in the non-interacting case ($\Sigma = 0$) and in the atomic limit ($\Delta = 0$). The first approximation proposed by Hubbard was to assume Σ and Δ to be completely oblivious to one another. Although capable of capturing the insurgence of Hubbard bands, this approximation is rather crude, as it predicts the opening of a spectral gap for any finite value of U and any partial filling. An improvement was obtained using the so-called "Hubbard III" approximation, in which each electron is seen as propagating in an alloy-like system made up by all opposite-spin electrons, treated as fixed scatterers. The local Green's function for the interacting lattice, obtained through a k-space summation of an expression of the type (3.2), is then compared with the weighted average of the Green's functions for a site with or without an opposite spin electron, namely

$$G_\sigma(\omega) = n_{-\sigma}\frac{1}{\omega - \epsilon_0 - \Delta(\omega) - \Sigma(\omega)} + (1 - n_{-\sigma})\frac{1}{\omega - \epsilon_0 - U - \Delta(\omega) - \Sigma(\omega)} \tag{3.3}$$

where Δ is the hybridization due to the crystal and the $n_{-\sigma}$ is the weight of the average. Equations (3.2) and (3.3) form a close set of self-consistent expressions, through which Σ can be determined. The Hubbard III approximation accounts qualitatively for the solution we expect in in the Mott insulating phase, with two "Hubbard bands" separated by a Mott gap. Still, it approximates the local dynamics of the system with a static disorder, therefore incorrectly picturing the Landau-Fermi liquid physics near the Fermi level. As we can see in Fig. 3.1, the evolution of the spectral function is different for the two approaches: the Gutzwiller scheme captures well the evolution of the effective mass and density of states near the Fermi level in proximity of the Mott transition, but it does not account for the high energy Hubbard bands that characterize the Mott insulating state. On the contrary, by treating the local Green's function as an average of those of the two Hubbard bands, the Hubbard III approximation incorrectly describes the low-energy physics of the system, for example attributing a finite lifetime to excitations at the Fermi level in a metal (which is at odds with the Landau-Fermi liquid description). We will see that Dynamical Mean-Field Theory somehow keeps the good aspects of the two methods connecting them in a unifying picture.

3.1 Dynamical Mean-Field Theory

In the context of the Green's function approach, the problem of strongly interacting fermionic systems has found a new, powerful method of solution in the Dynamical Mean-Field Theory and in its extensions. These methods, analogously to the classical description of magnetism in an Ising model [72], aim to obtain an approximate description of a correlated lattice from the perspective of a single-site effective problem, embedded in a conveniently defined "bath" describing the coupling between the degrees of freedom of the correlated site and the rest of the lattice. The effects of the latter will be encoded into a *Weiss field*, which in the parallel with the Ising mean-field case corresponds to the effective magnetic field coupled to the local spin of the site.

The great improvement is that, in contrast with classic models, here the mean-field description is *dynamical* because, while disregarding the spatial fluctuations of the relevant quantities at hand (as for magnetization in the mean-field Ising analogy) it fully takes into account the quantum dynamics in the time (or frequency) domain. The *Green's function* of the effective single-site model will correctly describe all the processes in which fermions are created and

destroyed at the correlated site, coming from and returning to the bath.
As in the static mean-field approaches, the optimal form of the effective field will be self-consistently determined by requiring that the Green's function of the effective local theory coincides with the local component of the lattice Green's function.

However, the Weiss field which describes the effect of the lattice on every given site is now not a number but a time (or frequency) dependent quantity, obtained through the exact solution of a finite quantum many body problem. The effective problem will be described by an action of the form

$$S_{eff} = -\int_0^\beta d\tau \int_0^\beta d\tau' \sum_\sigma c^\dagger_{0\sigma}(\tau)\mathcal{G}_0^{-1}(\tau-\tau')c_{0\sigma}(\tau') + U\int_0^\beta d\tau \hat{n}_{0\uparrow}(\tau)\hat{n}_{0\downarrow}(\tau) \tag{3.4}$$

where the role of the Weiss field $\mathcal{G}_0$ is that of a bare Green's function in a Gaussian integral, and the second term explicitly treats the local Coulomb interaction. Since it is dependent on ω, the Weiss field is capable of describing all the energy scales of the interacting problem. In this sense, it constitutes an improvement over mean-field techniques such as Hartree-Fock, that can only address one energy scale through the use of static order parameters, hence being accurate only in some restricted scenarios such as the Landau-Fermi liquid regime. Dynamical mean-field methods are well suited to address the Mott transition, where the characteristic energy scale defining the physics of the system varies drastically; we therefore can expect, through their use, a "reconciliation" of the features exhibited by the Gutzwiller and Hubbard III approximations. Historically, the idea of providing a solution for quantum many-body problems via this local interacting self-consistent approximation methods originated with the work of Metzner and Vollhardt [73] and Müller-Hartmann [74] on the limit of infinite dimension. Since the method is still mean-field, it is in fact expected to be exact in this limit. As we shall see, the correct scaling of the hopping amplitude in the limit of infinite dimensions is at the basis of the approximation producing the effective action of DMFT.
The biggest step towards a derivation of a viable self-consistent method for a dynamical Mean-Field theory came from the work of Georges and Kotliar in 1992 [75], where the mapping between the fully interacting lattice model and a local impurity problem coupled to a conduction band was proposed.

3.1.1 Derivation by cavity method

Among the derivations of the DMFT self-consistency equations (see for example [76, 77] and [78, 79]), the "cavity method" is the most well known and instructive, due to its parallel with the static Mean-Field construction, of which it represents an extension. This approach aims to construct an effective local theory for a single arbitrary site by averaging out all the non-local degrees of freedom. A review of the calculations involved can be found in Appendix B, yet we briefly discuss the derivation for the case of single-band Hubbard model to provide an overview of the self-consistent DMFT construction. The aim of the method is to provide an explicit way of obtaining and updating the Weiss function defined in (3.4). We start by expressing the full action of the interacting lattice as the sum of three terms,

$$S = S^{(o)} + S_0 + \Delta S \tag{3.5}$$

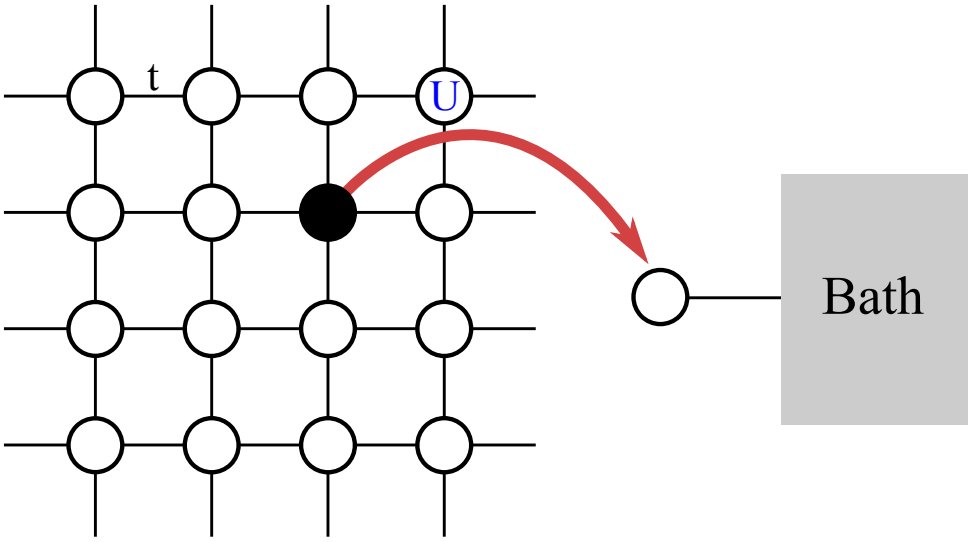

Figure 3.2: *Scheme of the DMFT approximation in the cavity method derivation: one site is removed from the lattice and treated separately. The isolated site is solved numerically as an impurity coupled to a "conduction band" represented by a noninteracting bath.*

where

$$S_0 = \int_0^\beta d\tau \left[\sum_\sigma c^\dagger_{0\sigma}(\tau)(\frac{\partial}{\partial\tau} - \mu)c_{0\sigma}(\tau) + U\hat{n}_{0\uparrow}(\tau)\hat{n}_{0\downarrow}(\tau) \right] \tag{3.6}$$

is the local action of the cavity,

$$\Delta S = -\int_0^\beta d\tau \sum_{i\sigma} \left[t_{i0} c^\dagger_{i\sigma}(\tau) c_{0\sigma}(\tau) + h.c. \right] \tag{3.7}$$

describes the hybridization between the cavity and the rest of the lattice and the last term $S^{(o)}$ is relative to the rest of the lattice alone. The lattice degrees of freedom are then traced out in the partition function, that can be written as

$$\mathcal{Z} = \int \prod_i \mathcal{D}c^\dagger_{0\sigma} \mathcal{D}c_{0\sigma} e^{-S_0} \int \prod_{i\neq 0} \mathcal{D}c^\dagger_{i\sigma} \mathcal{D}c_{i\sigma} e^{-S^{(o)} - \Delta S} \tag{3.8}$$

or, in terms of an ensemble average over $S^{(o)}$

$$\mathcal{Z} = \mathcal{Z}^{(o)} \int \prod_\sigma \mathcal{D}c^\dagger_{0\sigma} \mathcal{D}c_{0\sigma} e^{-S_0} \left\langle e^{-\Delta S} \right\rangle_{(o)} \tag{3.9}$$

Concerning the last exponential, using linked-cluster theorem, it is straightforward to recognize in it the generator of the connected (cavity) Green's functions. Expanding in power series the resulting term gives rise to cavity Green's function to all orders. Up to this point no approximation has been made. Now, an important simplification is obtained considering the ∞-dimension limit: the scaling of the hopping amplitude between sites i and j as $1/\sqrt{d}^{|i-j|}$, necessary so that kinetic and interaction energies remain of the same order of magnitude, implies that every term of order > 2 decays at least as $1/d$. As a result, the only surviving terms are

those corresponding to the single-particle Green's function $G_{ij}^{(o)}$. The resulting effective action takes the form

$$S_{eff} = S_0 + \int_0^\beta d\tau_1 \int_0^\beta d\tau_2 \sum_\sigma c_{0\sigma}^\dagger(\tau_1) \sum_{ij} t_{i0} t_{0j} G_{ij}^{(o)}(\tau_1 - \tau_2) c_{0\sigma}(\tau_2). \tag{3.10}$$

We now make use of the relation between he Green's function of the full lattice with that of the lattice with the cavity removed,

$$G_{ij}^{(o)} = G_{ij} - \frac{G_{i0} G_{0j}}{G_{00}} \tag{3.11}$$

to obtain an explicit form for the Weiss Green's function in (3.4):

$$\mathcal{G}_0^{-1}(i\omega_n) = i\omega_n + \mu - \sum_{ij} t_{i0} t_{0j} \left[G_{ij}(i\omega_n) - G_{i0}(i\omega_n) G_{00}^{-1}(i\omega_n) G_{0j}(i\omega_n) \right] \tag{3.12}$$

which establishes a relation between the Mean-Field Green's function and that of the fully interacting lattice.
Through (3.12) we can obtain the self-consistency condition for the DMFT method: given an expression for the Weiss field, the effective problem Eq. (3.4) is solved to obtain the impurity Green's function $G_{imp}(i\omega_n)$ and, ultimately, the impurity self-energy function $\Sigma(i\omega_n)$ which satisfies the Dyson equation

$$\Sigma(i\omega_n) = \mathcal{G}_0^{-1}(i\omega_n) - G_{imp}^{-1}(i\omega_n). \tag{3.13}$$

Σ, which due to the mean-field nature of the method is completely local, is instrumental in obtaining the local interacting Green's function of the original system as

$$G_{loc}(i\omega_n) = \sum_{\mathbf{k}} G(\mathbf{k}, i\omega_n) \tag{3.14}$$

where

$$G(\mathbf{k}, i\omega_n) = \frac{1}{i\omega_n + \mu - \epsilon_{\mathbf{k}} - \Sigma(i\omega_n)} \tag{3.15}$$

which corresponds in real space to the ij summation appearing in (3.12). After some algebraic calculations, the local Green's function G_{loc} is shown to satisfy the self-consistency condition

$$\mathcal{G}_0(i\omega_n)^{-1} = i\omega_n + \mu + G_{loc}(i\omega_n)^{-1} - R[G_{loc}(i\omega_n)] \ . \tag{3.16}$$

The last term is the reciprocal function of the Hilbert transform of the density of states of the lattice defined as

$$\tilde{D}(z) = \int_{-\infty}^{\infty} d\epsilon \frac{D(\epsilon)}{z - \epsilon}, \qquad R[\tilde{D}(z)] = z \tag{3.17}$$

in which $D(\epsilon)$ is the noninteracting density of states

$$D(\epsilon) = \sum_{\mathbf{k}} \delta(\epsilon - \epsilon_{\mathbf{k}}). \tag{3.18}$$

Once the method has converged, the self-consistency condition (3.16) implies that $G_{loc}(i\omega_n)$ is identified with the full impurity Green's function $G_{imp}(i\omega_n)$.

In the infinite dimension limit, where mean-field is exact, the previous relations are simplified, as it is famously shown in the slightly different situation of a lattice without a definite dimensionality but a definite coordination number, the Cayley tree. In this system, each site is connected to each other by only one path, creating a distinctive branch structure. We will in particular consider the $z \to \infty$ situation, known as Bethe lattice, which is for all intents and purposes analogous to the infinite-dimension limit. In this situation, the nearest-neighbour hopping scales as $t_{ij} \to t/\sqrt{z}$ and the noninteracting density of states has the semicircular shape [80]

$$D(\epsilon) = \frac{1}{2\pi t^2}\sqrt{4t^2 - \epsilon^2} \tag{3.19}$$

which is nonzero in the range $[-2t; 2t]$. The great simplification of the Bethe lattice stems from equation (3.11). If a site is removed, the only path connecting its neighbours is severed, therefore the relative Green's function in the presence of the cavity $G^{(o)}_{ij}$ becomes diagonal. The removal of a link changes the coordination of a factor $1/z$, so that in the limit $z \to \infty$ the effect is negligible. These observations, together with the complete translational invariance of the lattice, make it possible to assume instead of (3.11) the much simpler form

$$G^{(o)}_{ij} = \delta_{ij} G^{(o)}_{ii} = G_{ii} = G_{00}. \tag{3.20}$$

This leads to the simplified Hilbert and inverse Hilbert transforms

$$\tilde{D}(z) = \frac{z - s\sqrt{z^2 - 4t^2}}{2t^2} \qquad R(G) = t^2 G + 1/G \tag{3.21}$$

which immediately satisfy the self-consistency condition with

$$\mathcal{G}_0^{-1}(i\omega_n) = i\omega_n + \mu - t^2 G(i\omega_n). \tag{3.22}$$

Other than in the infinite dimensions limit, DMFT is exact in two other scenarios: the noninteracting limit $U = 0$, where $G_{loc} = \mathcal{G}_0$, and the atomic limit, where the density of states is a δ function and it holds:

$$\mathcal{G}_0^{-1}(i\omega_n) = i\omega_\nu + \mu \tag{3.23}$$

The Green's function of each isolated site is then

$$G(i\omega_n) = \frac{1 - n/2}{i\omega_n + \mu} + \frac{n/2}{i\omega_n + \mu - U} \tag{3.24}$$

with

$$n/2 = \frac{e^{\beta\mu} + e^{2\beta\mu - \beta U}}{1 + 2e^{\beta\mu} + e^{2\beta\mu - 2U}} \tag{3.25}$$

which is the same results we can get directly from Lehmann representation calculations on an isolated site.

3.1.2 Hamiltonian formulation

As discussed above the crux of DMFT is to replace the full interacting lattice problem with an effective model consisting of an interacting site coupled to an effective self-consistent bath.

Such single-site system is yet a complex quantum many-body problem, which describes the local quantum fluctuations of the lattice problem. It is straightforward to observe the similarity of the effective problem described by the action Eq. (3.10) with a single-impurity Anderson model [81] (SIAM). The SIAM Hamiltonian has the form

$$\hat{H}_{AIM} = \sum_{\sigma} \epsilon_0 c^{\dagger}_{0\sigma} c_{0,\sigma} + \sum_{l\sigma} \epsilon_l a^{\dagger}_{l\sigma} a_{l\sigma} + \sum_{l\sigma} V_l (a^{\dagger}_{l\sigma} c_{0\sigma} + c^{\dagger}_{0\sigma} a_{l\sigma}) - \mu \sum_{\sigma} c^{\dagger}_{0\sigma} c_{0\sigma} + U \hat{n}_{0\uparrow} \hat{n}_{0\downarrow}, \quad (3.26)$$

that is quadratic in the operators $a, a^{\dagger}$ associated to the conduction band. The expression of the action for this impurity model can be split in two of two parts, which we can express as

$$S_0 = \int_0^{\beta} \sum_{\sigma} c^{\dagger}_{0\sigma}(\tau)(\partial_\tau + \epsilon_0 - \mu) c_{0\sigma}(\tau) + U \hat{n}_{0\uparrow}(\tau) \hat{n}_{0\downarrow}(\tau) \quad (3.27)$$

$$\Delta S = \int_0^{\beta} d\tau \sum_{l\sigma} a^{\dagger}_{l\sigma}(\tau)(\partial_\tau + \epsilon_l) a_{l\sigma}(\tau) + V_l (a^{\dagger}_{l\sigma}(\tau) c_{0\sigma}(\tau) + \text{h.c.}) \quad (3.28)$$

where the first term relates to the impurity and the second refers to the bath electrons and the bath-impurity hybridization term. Once we pass to the frequency domain, and integrate out the bath degrees of freedom, we can express the effective action for the impurity as the sum of the interacting part

$$\int_0^{\beta} d\tau U \hat{n}_{0\uparrow}(\tau) \hat{n}_{0\downarrow}(\tau)$$

and a noninteracting quadratic term governed by the AIM Green's function

$$\mathcal{G}_0^{-1}(i\omega_n)_{AIM} = i\omega_n + \mu - \epsilon_0 - \int_{-\infty}^{\infty} d\omega \frac{\Delta(\omega)}{i\omega_n - \omega}. \quad (3.29)$$

Here, the hybridization function Δ is has the form

$$\Delta(\omega) = \sum_{l\sigma} V_l^2 \delta(\omega - \epsilon_l) \quad (3.30)$$

and corresponds to a density of states associated to the conduction band. As such, the SIAM provides a Hamiltonian representation of the effective action for the impurity problem in terms of the (infinitely many) bath parameters ϵ and V. These two sets of parameters determining the hybridization function have then to be self-consistently determined in order to solve the DMFT equations.

3.1.3 Mott transition and Phase Diagram

As we recall, the Gutzwiller and Hubbard approaches to the Mott transition predict, for the semicircular DOS, two different scenarios. The first shows the shrinking of the spectral distribution around the Fermi level, corresponding to an increase of the effective mass of quasiparticles that eventually diverges at the phase transition. The second predicts a progressive broadening of the DOS at high frequencies and the eventual creation of a gap around the Fermi level.
In DMFT, the distribution of the spectral weight for increasing U assumes the distinctive three-peak structure shown in of Fig. 3.3, which can be nicely compared to the combined picture presented by Gutzwiller and Hubbard III approximations in Fig. 3.1. The central peak

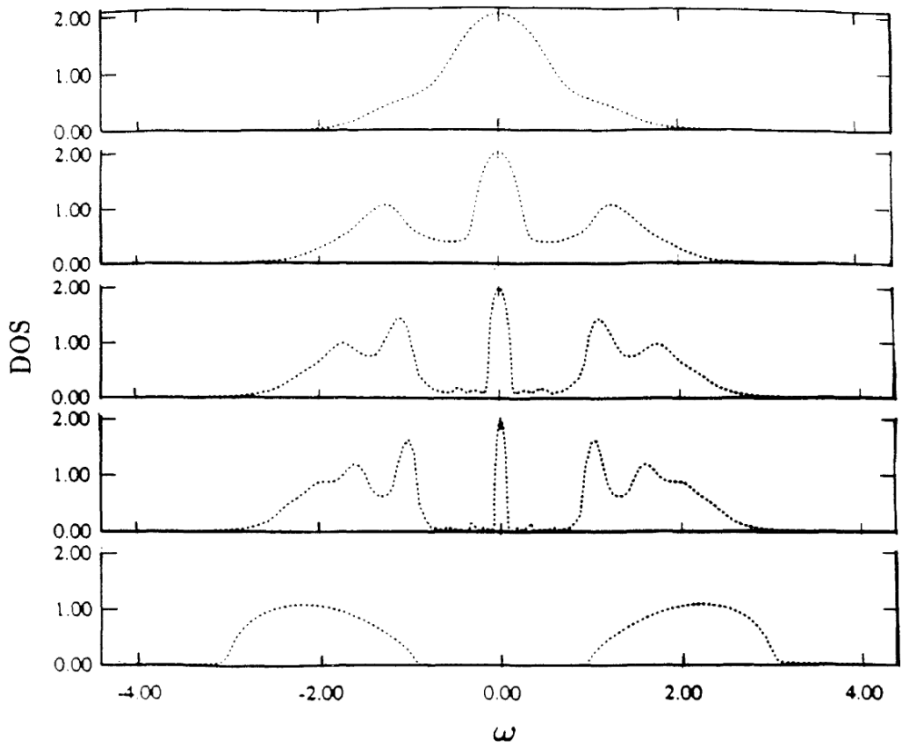

Figure 3.3: *DOS of the Bethe lattice in the infinite correlation limit for increasing* $U = 1, 2, 2.7, 3, 4$ *respectively. The results were obtained from a simpler perturbative approach (IPT), that works best for low values of U but can capture correctly the physics of a Half-filled Hubbard model for higher interaction values* [82]. *A comparison with Fig. 3.1 shows that DMFT effectively sums up the low-energy Gutzwiller and high energy Hubbard descriptions.*

corresponds to the quasiparticle part of the spectrum and has a Fermi liquid behaviour with a fraction of the total spectral weight Z. The two broad bands at high and low frequencies are the Hubbard bands accounting for the atomic-like non Fermi liquid behaviour, they are separated in energy by a factor of order U and have spectral weight $(1 - Z)$. The behaviour of the central peak follows a Brinkman-Rice type evolution, with an increase of the effective quasiparticle mass approaching the Mott transition; the sidebands gap, linearly growing with U, follows instead a Hubbard-like behaviour.
Fig. 3.4 sketches a phase diagram for the paramagnetic solution of a two-dimensional Hubbard model as a function of the ratio U/D and the temperature T/D where $D = 2t$, as obtained by different methods. Let us concentrate on the first one, which refers to single-site DMFT we presented in the previous sections: in the shaded region, there is coexistence between the metallic and insulating solution. For a finite temperature, the insulating solution extends up to U_{c1} where, in the Hubbard picture, the two sidebands merge eliminating the gap at the Fermi energy. The metallic solution is instead present up to U_{c2}, where the quasiparticle weight Z vanishes and the effective mass diverges, as in the Brinkman-Rice picture. For low temperature, the values of U_{c1} and U_{c2} are approximatively $\approx 2.35D$ and $\approx 2.9D$ respectively. At zero temperature, the first-order phase transition line touches the boundary of the coexistence region at a the critical point U_{c2}.

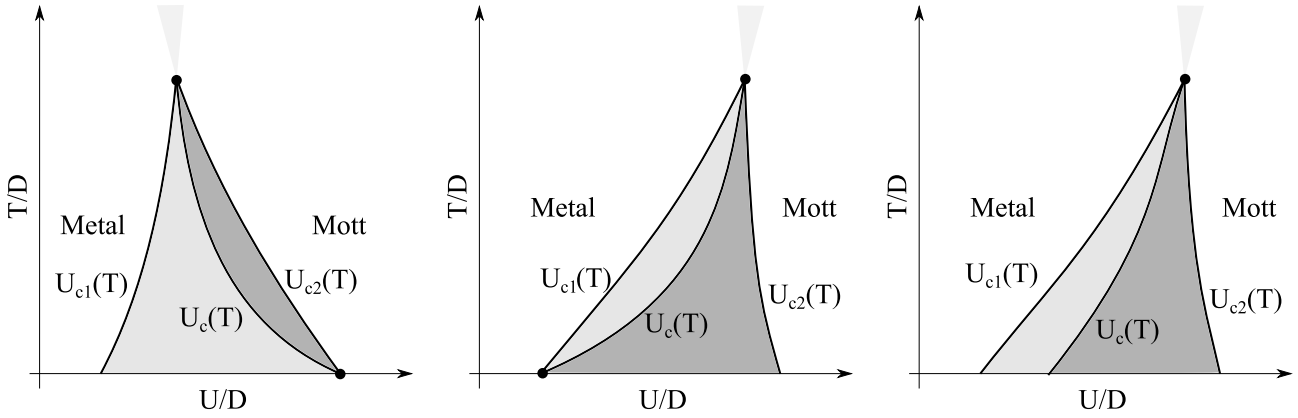

Figure 3.4: *Sketches of the phase diagram for the metal-insulator transition as predicted by DMFT, CDMFT and VCA in the paramagnetic phase. The shaded areas (light-dark grey) correspond to the metal and insulator-stable phases inside the coexistence region of the two solutions. The line traversing the coexistence region is the first-order phase transition line, that terminates in a critical point at finite T (over which a crossover region is present). For DMFT, the slope of the line is negative, while it is positive for CDMFT and VCA. The line terminates in a critical point at the border of the coexistence region in DMFT (and cluster derivatives) while SFT-based methods may show the persistence of the* 1^{st}*-order character of the transition even at T=0, as shown on the right panel of Fig. 3.7.*

One of the possible objections to this picture is that, at least in its paramagnetic declination, it does not include the effects of magnetic correlations (such as antiferromagnetism) and therefore describes an insulator with an entropy which approaches asymptotically the extensive value $\approx N \ln 2$. This clearly favours the insulator at higher temperatures and determines the negative slope of the first-order transition line. These potential limitations of the method can be addressed via cluster extensions of the single-site DMFT method, such as the Cluster-DMFT, which we will explicitly treat in the next section and whose phase diagram is represented in the middle panel of Fig. 3.4. In this framework, the insulator has lower entropy due to short-range singlet formation [83], and the slope of the transition line is positive.
Within DMFT it can be shown rigorously [84] that the zero-temperature Mott transition point coincides with the upper U_{c2}, while in CDMFT it appears numerically to coincide with U_{c1}. However, there is no a priori reason why U_c should coincide with one of the spinodals. In the third panel in Fig. 3.4 is related to Variational Cluster Approximation, a technique we will also introduce in the following sections, which is related to DMFT but moves its step from a different underlying principle. The related phase diagram [85] shows the persistence of a first-order phase transition down to zero temperature, with the metallic/insulating character of the stable phase changing inside the coexistence region.

3.2 Cluster methods

As previously discussed DMFT is characterized by a momentum-independent self-energy $\Sigma(\omega)$, which only depends on frequency. This can be computed in the effective local theory, hence it is a purely local which normalizes the lattice Green's function. All the space fluctuations are

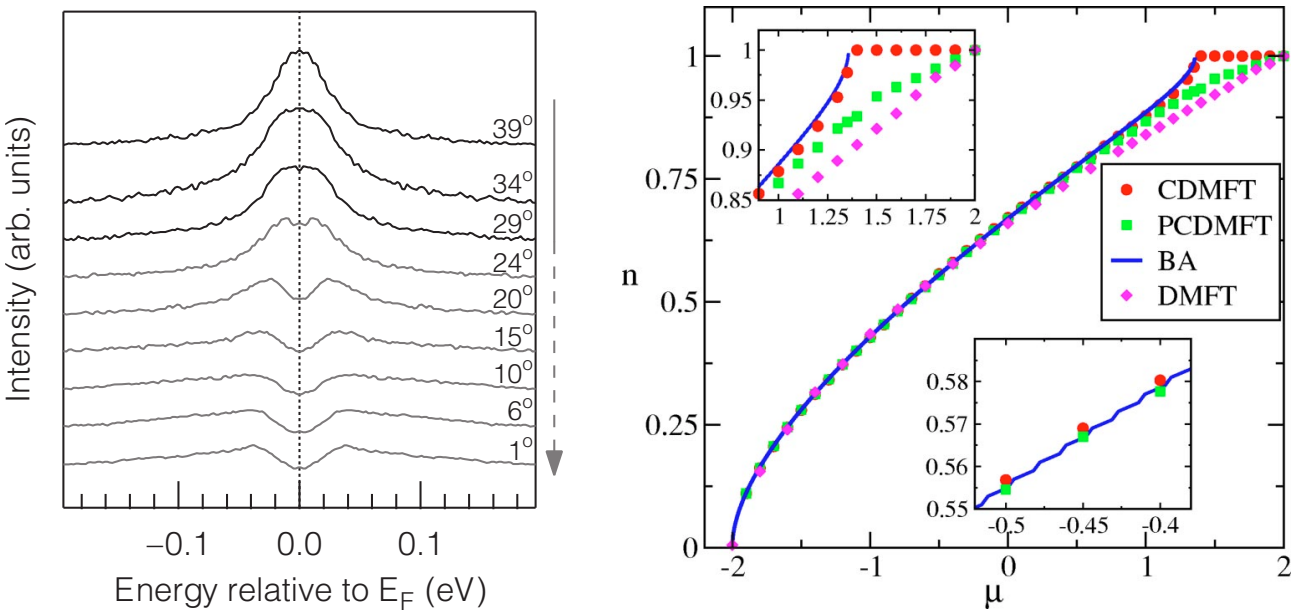

Figure 3.5: *Two examples of nontrivial effects recovered by cluster-based methods: a) the pseudogap behaviour as measured by ARPES in a sample of $Bi_2Sr_2CaCu_2O_{8+x}$ (cfr. [40]); the angle corresponds to different k-directions in the Brillouin Zone. b) density as a function of the chemical potential for a Hubbard chain: the CDMFT result, which correctly replicates the exact Bethe Ansatz one, features a divergence in compressibility (the derivative of the plotted quantity), which is not present in single-site DMFT results. Picture taken from [86].*

frozen and this gives rise to some issues like the previously cited overestimation of the insulating state entropy.

An interesting experimental example [87] of a situation in which a local self-energy may be inadequate comes from high-temperature superconductors based on CuO_2 planes. For a very low doping and $T > T_c$, ARPES measurements give a well-defined peak at the Fermi energy in the diagonal direction of the BZ, but near the boundary at $(0, \pi)$ the emission spectrum has a minimum at the Fermi energy, that is referred to as a "pseudogap". This is clearly an effect of correlation, and therefore any information regarding this effect must be embedded in the Self-Energy of the model, that in turn has to be momentum-dependent to correctly capture the pseudogap behaviour.

A further example of a feature that can not be captured by single-site DMFT is the density-driven Mott transition in a one-dimensional Hubbard model [86]: while the exact Bethe ansatz solution predicts a divergence in compressibility $\kappa = \partial n / \partial \mu$ at the Mott transition, single-site DMFT finds no such behaviour. In recent years, many cluster-oriented extensions of DMFT have been proposed, both in real space (CDMFT) and in reciprocal space (DCA [88]). A different approach to the cluster problem has also been developed from a variational principle based on the Self-Energy. We will focus on the real-space Cluster DMFT, and on a different approach called Self-Energy Functional theory, more specifically on one of its derivate methods which is the previously mentioned VCA.

3.2.1 Cluster DMFT

A well-known and successful extension of DMFT is the real-space Cluster-DMFT [89, 90]. It replaces the single impurity with a set of N lattice sites with open boundary conditions, coupled to a frequency dependent bath again determined self-consistently. Correspondingly, all the dynamical correlation functions and the Weiss field have an additional $N \times N$ matrix structure, i.e. an explicit dependence on the spatial non-local degrees of freedom inside the cluster. Given a cluster self-energy function $\mathbf{\Sigma}_c(i\omega_n)$, the local cluster Green's function reads:

$$\mathbf{G}(i\omega_n) = \sum_{\mathbf{k}\in RBZ} \frac{1}{(i\omega_n + \mu)\mathbb{I} - \mathbf{H}(\mathbf{k}) - \mathbf{\Sigma}_c(i\omega_n)} \tag{3.31}$$

Here, $\mathbf{H}(\mathbf{k})$ is the one-body part of the Hamiltonian of the lattice expressed in a base that preserves translational invariance.
For example, dividing a n-dimensional cubic lattice in $N_{x_1} \times ... \times N_{x_n}$-sized clusters redefines the length of Bravais lattice vector, which in turn shrinks the size of the Brillouin Zone by N_{x_i} in the k_i direction. Any quantity can then be rewritten in the mixed (i, k) representation, where i labels the internal site of the cluster and k the k-vector in the Reduced Brillouin Zone, i.e. the Brillouin zone corresponding to the unit cell created by cluster itself.

The 1-dimensional case can be used as an illustrative example. The hopping matrix of a 1-dimensional Hubbard model with lattice spacing $a = 1$ and hopping amplitude t is $H(k) = -2t\cos(k)$. If the lattice is divided in 2-site clusters, the same kinetic part of the Hamiltonian will be written in the mixed representation as

$$\mathbf{H}(k) = \begin{bmatrix} 0 & -t(1+e^{-2ik}) \\ -t(1+e^{2ik}) & 0 \end{bmatrix} \tag{3.32}$$

where now $k \in$ the Reduced Brillouin Zone $[-\pi/2, \pi/2]$.
We will henceforth use the bold notation to indicate matrices in the mixed representation or generally in the cluster basis, and intend fractions as (3.31) as a formal matrix inversion.
All the self-consistency equations valid for the single-site DMFT are translated into the cluster extension, making use of this mixed representation. The original periodicity, along with the dependence on $\mathbf{k} \in BZ$ of the quantities that are local in the cluster basis, can be recovered through periodization, which will be discussed later. However, the determination of the effective bath can be a little more subtle with respect to the single-site DMFT. In particular, to ease the computation, the symmetries of the cluster can be taken into account when generating the bath. A way to do that is to set up a block-diagonal structure consistent with the irreducible representations of the symmetries exhibited by the cluster [91]. In this way, the symmetries for each block of the bath Green' function are explicitly selected. Another way to immediately take the symmetries of the cluster into account is to consider a bath whose Green's function is based on a replica of the cluster Hamiltonian [92], using the so-called *reduced parametrization scheme*, which we will briefly comment on in Chapter 4.

A substantial difference between DMFT and its cluster extension has to be underlined. While for DMFT the limit $d \to \infty$ is exact and the method is well suited to describe lattice problems with a high coordination number, applying the same limit to the CDMFT would lead to the decay of nonlocal terms in the expansion of S_{eff}, therefore producing a local Self-Energy and taking us back to the single-site picture. Then again, in a finite-dimensional limit the approximation in the derivation of S_{eff} becomes more crude. CDMFT is therefore

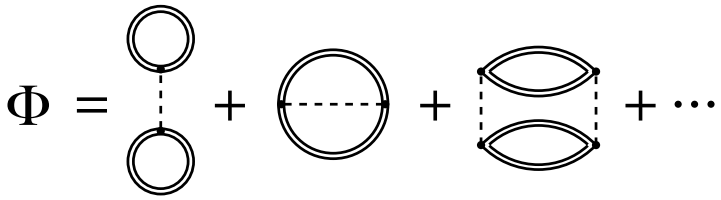

Figure 3.6: *First terms of the skeleton expansion of the Luttinger-Ward functional, picture from* [96].

"intrinsically" an approximation, whose quality depends in a systematic way on the size of the cluster, a trait that it shares with a class of cluster frameworks based on a different inspiring principle, that we will now introduce.

3.2.2 Self-Energy Functional Theory and derivatives

A different, though related, approach to the solution of interacting electron systems is based on a variational principle called Self-Energy Functional Theory. This approach was originally proposed by Potthoff [93] and is based on the framework of Cluster Perturbation Theory (CPT) [94, 95]: at the core of this method is the fact that, while we cannot access the exact solution for an infinite correlated lattice, we can solve finite-size systems through various numerical techniques, some of which we will show in the next chapter. Then, we can approximate the full lattice of interacting fermions with a collection of clusters related by a one-body hopping Hamiltonian. The relation between the cluster and full lattice Green's function has a form similar to the Dyson equation, if one treats the inter-cluster coupling as a perturbation:

$$\mathbf{G}(\omega) = \frac{1}{\mathbf{G}'(\omega)^{-1} - \mathbf{V}} \tag{3.33}$$

where $\mathbf{G}$ and $\mathbf{G}'$ refer to the lattice and cluster Green's function and $\mathbf{V}$ is the inter-cluster hopping. This relation is exact in the noninteracting limit, where $\mathbf{G}$ and $\mathbf{G}'$ only depend on the hopping matrix $\mathbf{H}$ (and the coupling $\mathbf{V}$); its extension to the interacting realm constitutes the core of the CPT approximation. A crucial observation comes from the fact that both $\mathbf{G}'$ and $\mathbf{V}$ can be redefined in terms of other hopping parameters $\tilde{t} = t + \Delta t$. While this has no effect in the noninteracting case, it generates a different approximated result for the interacting $\mathbf{G}$ for every choice of one-body hopping Hamiltonian. Hence, there is a way of improving over the CPT approximation by finding a way of "sorting" the reference systems and choosing the best. To this end, a variational principle is needed.

Luttinger-Ward generating functional

The *Luttinger-Ward functional* $\hat{\Phi}_U[\mathbf{G}]$[1], introduced in 1960, is a scalar functional without explicit physical meaning originally derived [39] order by order in a diagrammatic perturbation expansion. It is defined as the the sum at any order of all closed, connected, and fully dressed skeleton diagrams, i.e. closed Feynman diagrams without self-energy insertions and with all

[1]The hat notation is used in this case to identify the functionals, and not second quantization operators. However, due to the different spaces in which these quantities are defined, this should cause no confusion.

free propagators replaced by fully interacting ones, as it can be seen in Fig. 3.6. The domain of the functional is a space of functions to which the physical Green's function of the system with the given interaction U belongs. The Luttinger-Ward functional has these very useful properties:

- its functional derivative with respect to its argument is

$$\frac{1}{T}\frac{\delta\hat{\Phi}_U[\mathbf{G}]}{\delta\mathbf{G}} = \hat{\mathbf{\Sigma}}_U[\mathbf{G}] \tag{3.34}$$

  where the functional $\hat{\mathbf{\Sigma}}_U$ is, if evaluated at a physical $\mathbf{G}$, the associated Self-Energy $\mathbf{\Sigma}_{\mathbf{H},U}$

- if evaluated on the physical $\mathbf{G}$, its value $\hat{\Phi}_U[\mathbf{G}_{t,U}] = \Phi_{\mathbf{H},U}$ is related to the Grand potential of the system by

$$\Omega_{\mathbf{H},U} = \Phi_{\mathbf{H},U} + \mathrm{Tr}\ln\mathbf{G}_{\mathbf{H},U} - \mathrm{Tr}(\mathbf{\Sigma}_{\mathbf{H},U}\mathbf{G}_{\mathbf{H},U}) \tag{3.35}$$

- it only depends on U, therefore it is universal for all the systems with the same expression for the interaction

- it vanishes at the noninteracting limit

A derivation of these properties is presented in Appendix B.

SFT and Ω potential

The derivation of the SFT variational principle is based on the invertibility assumption for the functional $\hat{\mathbf{\Sigma}}_U[\mathbf{G}]$, which is assumed to hold at least locally. This assumption is generally safe away from a critical point. Then, the Legendre transform of the functional can be constructed in term of the inverse functional of $\hat{\mathbf{\Sigma}}$, which we will call $\hat{\mathbf{G}}$, in the form

$$\hat{F}_U[\mathbf{\Sigma}] = \hat{\Phi}_U[\hat{\mathbf{G}}_U[\mathbf{\Sigma}]] - \mathrm{Tr}(\mathbf{\Sigma}\hat{\mathbf{G}}_U[\mathbf{\Sigma}]) \tag{3.36}$$

which satisfies the functional derivative

$$\frac{1}{T}\frac{\delta\hat{F}_U[\mathbf{\Sigma}]}{\delta\mathbf{\Sigma}} = -\hat{\mathbf{G}}_U[\mathbf{\Sigma}] \tag{3.37}$$

We can then define the *Self-Energy functional* that gives name to the theory as

$$\hat{\Omega}[\mathbf{\Sigma}] = \mathrm{Tr}\log\frac{1}{\mathbf{G}_0^{-1} - \mathbf{\Sigma}} + \hat{F}_U[\mathbf{\Sigma}] \tag{3.38}$$

where the trace is intended as a sum over frequencies and site indices (or wavevectors). From the property relating the grand potential to the Luttinger-Ward functional and from Dyson's equation, it's easy to note that if $\mathbf{G}$ and $\mathbf{\Sigma}$ are the dynamical quantities of a physical system, Ω is its grand potential. Moreover, it can be immediately seen that the Dyson's equation for an interacting system is satisfied when

$$\frac{\delta\hat{\Omega}_{\mathbf{H},U}[\mathbf{\Sigma}]}{\delta\mathbf{\Sigma}} = 0 \tag{3.39}$$

which constitutes the variational principle at the core of SFT.
The last step to the formulation of the theory is to recognize that, as a functional of $\mathbf{\Sigma}$ living in the space of Self-Energies, the first term in (3.38) is purely non-interacting and depends on the characteristics of the hopping matrix embedded in $\mathbf{G}_0$, while the second, which involves the Legendre transform of the Luttinger-Ward functional $\hat{\Phi}$, is universal for all system sharing the same interaction form irrespective of the features of the hopping matrix. Hence the arduous task of calculating $\Phi_{\mathbf{H},U}$ can be avoided entirely, as long as a reference system with the same interaction part as the whole lattice is used, by calculating

$$\hat{\Omega}[\mathbf{\Sigma}] = \Omega' + \mathrm{Tr}\,\log\frac{1}{\mathbf{G}_0^{-1} - \mathbf{\Sigma}} - \mathrm{Tr}\,\log\frac{1}{\mathbf{G}_0^{\prime -1} - \mathbf{\Sigma}} \tag{3.40}$$

Here, $\Omega^{'}$ is the evaluation of $\hat{\Omega}$ for the physical system consisting of the reference finite cluster, which is directly obtainable as its grand potential, and the remaining terms are non-interacting and easily obtainable in practice as a functional of $\mathbf{\Sigma}$ or, in turn, as a function of a certain parametrization of $\mathbf{\Sigma}$ depending on some parameters, as represented inf Fig. 3.7.

Just like DMFT this approach it is non-perturbative, hence it is well suited to describe phenomena like the Kondo effect [97]. Remarkably, the internal energy of the physical system is immediately obtained as the value of the Ω functional at the stationary points. This enables us to rapidly analyse the details of a phase transition. Differently from the self-consistent DMFT approach, this method allows to find and classify all the physical solutions according to their energy.

Interestingly, equation (3.38) unveils the relation between the SFT approach and the DMFT self-consistency: let us consider the derivative of this equation with respect to some parameters h on which $\mathbf{\Sigma}$ depends. Using the universality of F, we obtain

$$\frac{\partial}{\partial h}\hat{\Omega}[\mathbf{\Sigma}_h] = \frac{1}{\beta}\sum_{nij\sigma}\left(\mathrm{Tr}\frac{1}{\mathbf{G}_0^{-1}(i\omega_n) - \mathbf{\Sigma}(i\omega_n)} - \mathbf{G}'(i\omega_n)\right)_{ij\sigma}\frac{\partial \Sigma_{ji\sigma}(i\omega_n)}{\partial h}, \tag{3.41}$$

where the meaning of the trace is a $\mathbf{k}$-sum. In the case in which the auxiliary system is a single-site Anderson impurity model coupled with a bath (which will clearly not be present in the original lattice Green's function), the Self-Energy will in this case be completely on-site and the functional trace effectively gives us the local Green's function for the lattice. Then, the formula in parenthesis is precisely the DMFT self-consistency relation between the local Green's function an the impurity one calculated from the effective action. The difference between the two methods stems from the fact that, while DMFT strives to make the expression in parenthesis as small as possible, SFT seeks to nullify the total derivative, to which end making it orthogonal to $\partial\Sigma/\partial h$ is sufficient.

VCA

In principle. SFT requires the calculation of the optimal Self-Energy satisfying the stationarity condition. We need however to find a systematic way to travel in the $\mathbf{\Sigma}$ space until we find the stationary point. This leads to the definition of the Variational Cluster Approximation: instead of moving in the full space of Self-Energies, we restrict ourselves to a subspaces of $\mathbf{\Sigma}$s which share a functional dependence on some parameters: these can be, for example, an enhanced intra-cluster hopping $t^{'}$, a staggered magnetic field, an hybridization V and on-site energy ϵ for

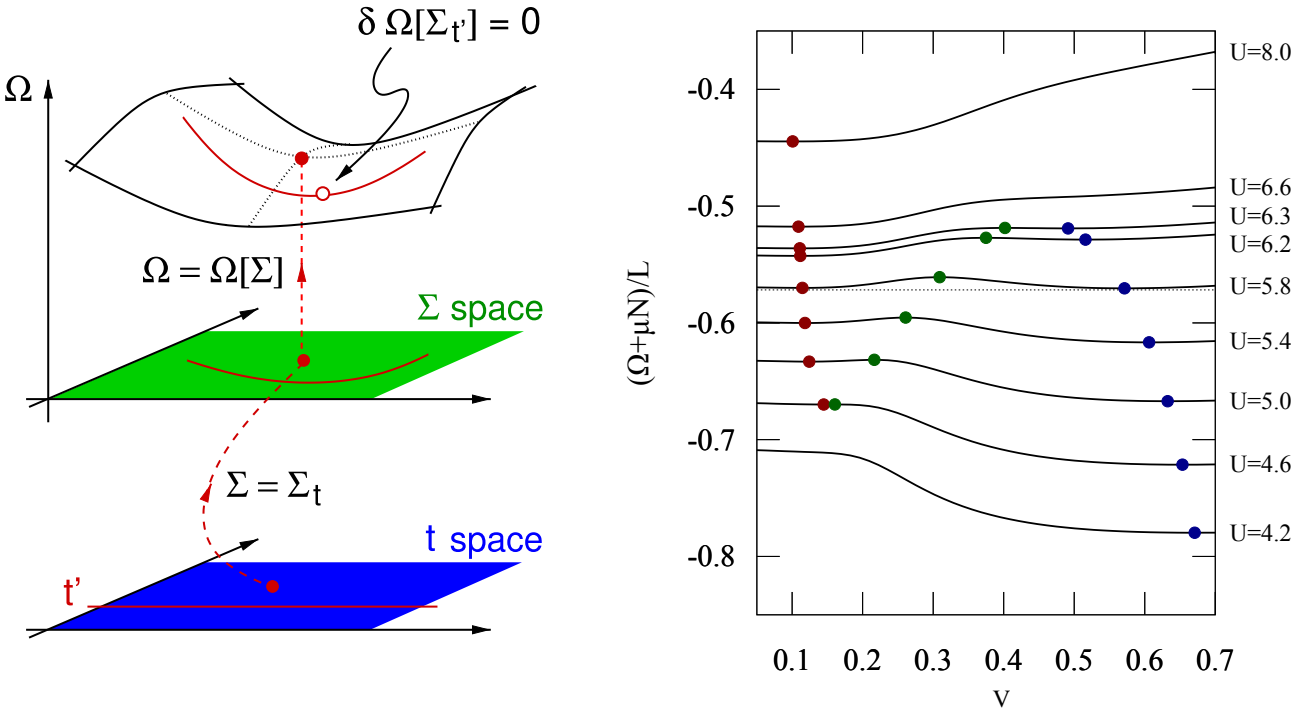

Figure 3.7: *On the left, representation of the* Ω *functional taking value in a space of trial self-energies, themselves depending on variational parameters, picture from* [96]. *On the right, the behaviour of the* Ω *potential of a two-dimensional Hubbard model for various values of* U *and a reference system consisting of a square plaquette with one bath site for each correlated site. The bath sites energy is fixed at the chemical potential, and the variational parameter is the bath hybridization* V *(same for all the sites by symmetry). The results were obtained with the code presented in Chapter 4 to replicate those of* [85]. *The method finds metastable solutions (green dots) and ranks the stable ones in order of energy: the presence of a first-order phase transition at* $\mathrm{T} = 0$ *is evident at* $\mathrm{U} = 5.8$.

some effective bath sites, included to improve the description of local temporal correlations, and so on.

The search of the stationary points in the Self-Energy functions space is turned into a function minimization, the variables being the parameters of the variational cluster, as schematically depicted in the left panel of Fig. 3.7. Given the general form of the cluster Green's function

$$\mathbf{G'}^{-1} = (\omega + \mu)\mathbb{I} - \mathbf{H'} - \mathbf{\Delta}(\omega) - \mathbf{\Sigma}(\omega) \tag{3.42}$$

where $\mathbf{H'}$ is the cluster hopping matrix, $\mathbf{\Sigma}$ is the Self-Energy of the isolated system and $\mathbf{\Delta}$ is an hybridization part [98]

$$[\mathbf{\Delta}]_{ij}(\omega) = \sum_i \frac{V_{i\alpha} V^*_{j\alpha}}{\omega - \epsilon_\alpha}$$

for the optionally-added bath sites labelled by α, the practical formula for Ω at zero temperature is, as we will briefly comment in Chapter 4,

$$\Omega = E^{GS}_{cluster} - \int \frac{\mathrm{d}\omega}{\pi} \sum_{\mathbf{k}} \log \left| \det \left(\mathbb{I} + \left(\mathbf{H'} + \mathbf{\Delta}(\omega) - \mathbf{H}(\mathbf{k}) \right) \mathbf{G'}(\omega) \right) \right|. \tag{3.43}$$

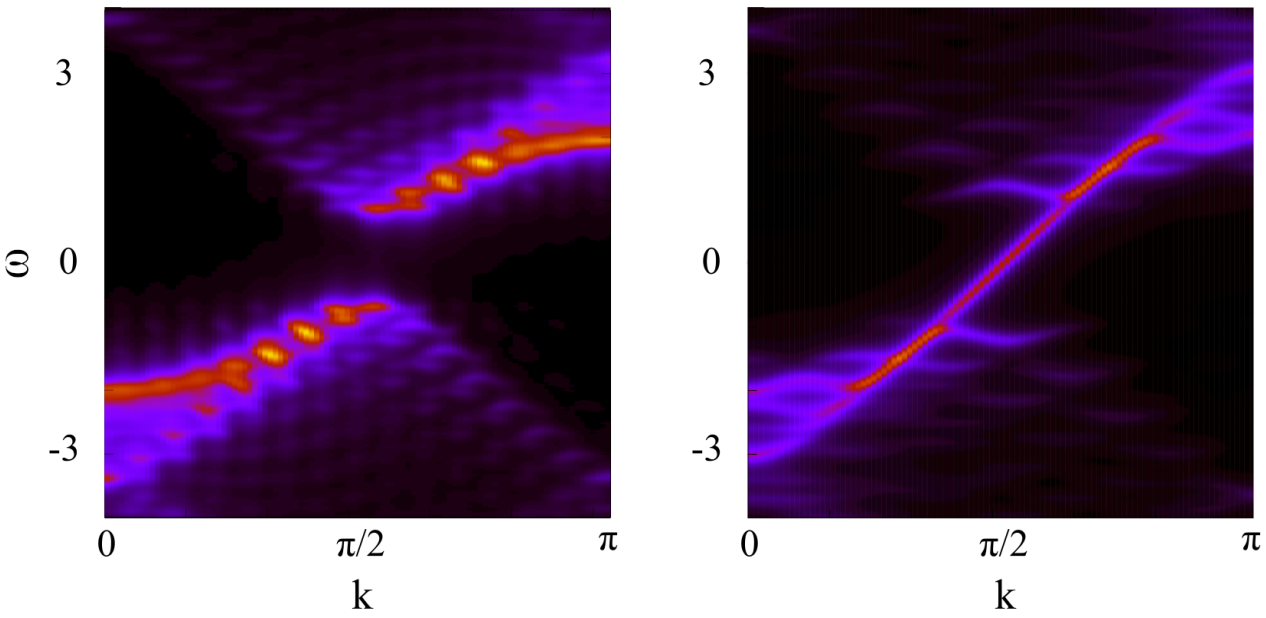

Figure 3.8: *Spectral function $A(k,\omega)$ for a 1-dimensional Hubbard chain with $U/t = 4$ in the G (left) and Σ (right) periodization schemes. The unphysical weight at the Fermi level is evident in the latter case. The two simulations were obtained with a CPT calculation (that is equivalent to an un-optimized SFT result for the variational parameters set to be equal to the full-lattice ones) and for a 10-site cluster in the G scheme and a 4-site cluster in the Σ. This to show the peculiar "wavy" behaviour of the DOS, which is akin to an aliasing effect due to the form of the periodization formula: increasing the "sampling", that in this case corresponds to increasing the number of cluster sites, the effect becomes less prominent.*

This is effectively a function of the single-particle parameters on which $\mathbf{\Delta}$ and $\mathbf{H}'$ are defined. Its stationary points are the physical solutions of the system, as shown in the right panel of Fig. 3.7. The Variational Cluster Approximation comes with some nice properties: stemming from SFT it is a nonperturbative method; it is also *internally consistent*, i.e. all observables derive from an explicit expression for the thermodynamic potential Ω. Finally, it is systematic in the sense that increasing the cluster size improves the quality of the approximation (though this comes, especially for exact-diagonalization based solvers, at a rapidly increasing computational cost).
Its main drawback, however, rests in the fact that we don't have any a priori knowledge of the optimal form of the Self-Energy. Hence, we cannot guarantee that the specific parametrization we choose for the Self-Energy gives stationary points of the Ω functional at all, since we have no information on the specifics of the $\mathbf{\Sigma}$ subspace we are spanning. We also don't have any information on the evolution of the stationary point under a systematic enlargement of the reference system. Finally, from an operational point of view, we have to consider that all stationary points, including local maxima and saddle points, are in principle acceptable solutions. Their identification via minimization routines could therefore prove to be quite complicated.

3.2.3 Observables and periodization

All the quantities obtained via the cluster methods introduced above are defined in the cluster-superlattice mixed representation. This basis is perfectly fine to determine many properties of the material, such as the one-body observables, through the general formula [99]

$$\mathcal{O} = \frac{1}{N}\sum_{\mathbf{k}\in RBZ}\int_0^\infty \frac{d\omega}{\pi}\mathrm{Re}\left\{\mathrm{Tr}\left[\mathbf{s}(\mathbf{k})\mathbf{G}(\mathbf{k},i\omega)\right] - \frac{\mathrm{Tr}\ \mathbf{s}(\mathbf{k})}{i\omega - a}\right\} \tag{3.44}$$

where $\mathbf{s}$ is the general 1-body matrix expression of the observable operator, $\mathbf{G}$ is the lattice Green's function obtained from

$$\mathbf{G}(\mathbf{k},\omega) = \frac{1}{(\omega+\mu)\mathbb{I} - \mathbf{H}(\mathbf{k}) - \mathbf{\Sigma}(\omega)} \tag{3.45}$$

and the last term, dependent on a real parameter $a \approx 1$, is included for normalization reasons. To our ends, since topological properties are related to the gap, the unperiodized system is again perfectly adequate.
Nevertheless, it might be interesting to retrieve the original periodicity of the results, for example to achieve a good comparison between cluster and single-site description and in general to obtain k-dependent quantities inaccessible from a DMFT perspective. There are many ad-hoc prescriptions to achieve such a goal: they generally rely on the residual translational invariance in the superlattice to recover a k-dependent quantity from its site-dependent analogous; the difference between the schemes is the quantity to be periodized.
The most well-known (though not unique) periodization schemes are the aptly named G-scheme [95], where the cluster Green's function is recast into a k-dependent form via

$$G_{per}(\mathbf{k},\omega) = \frac{1}{N_c}\sum_{ij} e^{-i\mathbf{k}\cdot(\mathbf{r}_i-\mathbf{r}_j)}[\mathbf{G}]_{ij}(\mathbf{k},\omega) \tag{3.46}$$

where the original Green's function (3.45) is evaluated at the original lattice $\mathbf{k}$-points, and the Σ-scheme [86, 89], where a similar procedure is done on the Self-Energy via

$$\Sigma_{per}(\mathbf{k},\omega) = \frac{1}{N_c}\sum_{ij} e^{-i\mathbf{k}\cdot(\mathbf{r}_i-\mathbf{r}_j)}[\mathbf{\Sigma}]_{ij}(\omega). \tag{3.47}$$

In both cases, the other relevant quantities are obtained through Dyson's equation, given the easy form of the noninteracting Green's function in the original basis.
These schemes have a certain degree of conventionality, as they are in fact weighted averages of quantities that may not be well-behaved. A well-known example is the unphysical results given by the Σ-scheme in describing the Mott transition, which are pictured in Fig. 3.8. In this case, the Self-energy presents a divergence near the Fermi level, which accounts for the breakdown of the Landau-Fermi liquid description. The Sigma scheme, therefore, is effectively averaging divergent quantities, which leads to the wrong result of nonzero spectral weight inside the Mott gap. The Σ-scheme is, though, accurate inside the Landau-Fermi liquid phase, where the Self-Energy has no divergence. That, along with its being much faster computation-wise, is the reason why, whenever resorting to a periodization scheme will be required, we will henceforth be able to safely rely on the Σ-scheme, as the topological phases we will be considering are not inside the Mott insulator regime.

Chapter 4

Massively parallel exact diagonalization algorithm for impurity problems

The methods outlined in the previous chapter to treat strongly correlated systems ultimately rely on the solution of effective models which, although simplified, still describe complex quantum many-body problems. Such effective models belong to a class of quantum impurity problems, featuring one or few interacting electronic levels possibly coupled to an effective bath of non-interacting electrons. The early success of DMFT and SFT methods has largely pushed the development of numerical techniques to tackle quantum impurity models. We arbitrarily divide these numerical methods in two sets: namely Hamiltonian and non-Hamiltonian based methods. The Hamiltonian based methods rely on the determination of a discretized Hamiltonian spectrum whereas the non-Hamiltonian ones do not need to inspect the Hamiltonian spectrum to construct the solution, although a formal Hamiltonian expression might still be required in some cases.

A suitable example of non-Hamiltonian based methods is the continuous-time Quantum Monte Carlo (CT-QMC) [100]. This method of solution relies on the effective action representation of the quantum impurity problem, allowing for different approximation schemes to construct the solution. The CT-QMC algorithm essentially consists in a Monte Carlo sampling across arbitrary perturbative orders in a suitable, non-self-consistent, expansion of one term of the action. Different types of perturbative expansions can be envisaged, giving rise to different flavours of the CT-QMC algorithm. The common feature of this kind of methods is their ability to deal with an infinite effective bath, which is described in terms of the hybridization function with the impurity. The CT-QMC algorithm proved over the years to be extremely efficient and several improvements have been devised. Yet, some limitations are still intrinsic to the method. The most important being the Fermi sign problem, which can prevent the use of CT-QMC method in some multi-orbital systems or require the use of suitable (sometime non-justified) approximations in some particular circumstances. Moreover, the CT-QMC algorithm is limited to finite temperature and can access directly dynamical quantities only the Matsubara axis (at equilibrium). As such, an ill-defined analytic continuation has to be performed to get quantities on the real-axis to be compared to experiments.

The Hamiltonian based methods includes, for example, the Exact Diagonalization (ED), the Numerical Renormalization Group (NRG) [101, 102], the Density Matrix Renormalization Group (DMRG) [103–106]. The key approximation here is to introduce a discretization of the quantum impurity problem, which ultimately allows to obtain the spectrum of the effective

system. The knowledge of the Hamiltonian spectrum gives access to a number of benefits: zero and extremely low temperature calculations, dynamical quantities in the entire complex plane, arbitrary form of the interaction or presence of any off-diagonal coupling. The most serious problem suffered by any Hamiltonian based method is represented by the exponential growth of the Fock space, which in turn limits the size of the discretized problem weakening the approximation. The use of renormalization group schemes has recently allowed to alleviate this issue by truncating the Fock basis in some way [107, 108] at the cost of loosing some of the benefits listed above. In the context of ED methods, the need to reach larger systems sizes and/or to improve the execution time has pushed the search for stable multi-threaded, distributed memory parallel algorithms [109]. It is important to stress that reaching the highest level of optimization is not only desirable to speed-up the calculations, but it is mandatory when dealing with clusters of few sites and/or fully interacting multi-orbital problems. In this case the number of degrees of freedom is so large that the ED problem can only be tackled exploiting massively parallel scaling in large scale HPC facilities.

In this chapter, we describe the details of a massively parallel ED algorithm for multi-orbital quantum impurity systems, to be used in combination with any of the methods outlined in the previous chapter. First we will discuss the specifics of the exact diagonalization algorithm, its parallel implementation and optimization. Then we will briefly comment on the different paths departing from the ED solution: the application to (C)DMFT, which require an appropriate bath fitting procedure, and the search for stationary points of the SFT functional.

4.1 The Exact Diagonalization method

Exact Diagonalization is a generic numerical method to solve the eigenvalue problem for a finite system, obtaining the spectrum of a matrix or at least a part of its eigenvalues and eigenvectors. This method applies with relatively few modifications to a variety of problems, from spin systems to fermions or bosons on small lattices with suitable boundary conditions, to electron-phonon coupled systems and more. In the following we will focus on the ED algorithm as a method to solve strongly correlated electron systems, such as the generic quantum impurity problems emerging in the context of DMFT, CDMFT or SFT. From a general point of view the ED algorithm can be divided in few steps:

1. Organization of the Hilbert space and basis representation.
2. Construction of the Hamiltonian matrix, solution of the eigenvalue problem.
3. Calculation of the quantities of interests.

The Hamiltonian is solved in real space, directly expressing the elements of the basis in terms of electronic configurations. It is quite intuitive to realize that the dimensionality of a finite system grows exponentially with the number of sites. Thus, already for small systems of few sites the matrix representing the Hamiltonian becomes too large, making it impossible to store it, let alone to diagonalize it.

A simplification of the problem comes from the observation that the Hamiltonian matrix is sparse, i.e. has a largely reduced number of finite entries with respect to the total. This allows to largely reduce the memory space required for the matrix, by only storing the values of the non-zero elements along with their location. The sparse nature of the matrix also impacts

on the determination of the spectrum, as testified by the vast field of powerful and generic algorithms specifically devised to solve this type of problem [110–113]. The common trait of such methods is their reliance on a linear operation such as the matrix-vector product. This constitutes by far the biggest portion of the required computational time, taking often more than 90% of the total execution time. Thus, optimizing this part of the algorithm is critical to reduce the overall computational effort and solve lager systems. In the following we will discuss how to achieve a massively parallel scaling of the ED algorithm by optimizing the way the matrix-vector product is executed.

In the following we consider a system of N_s electronic levels. In order to make contact with generalized quantum impurity problems, we henceforth assume that a fraction N_{imp} of such electrons interact via a local repulsion term, while the remaining $N_s - N_{imp}$ (the "bath" levels) are non-interacting. In a typical setup, considering for example a set of interacting electrons on N_l sites and N_α orbitals, each coupled to a set of N_b bath levels, the total number of electronic levels is $N_s = N_l \times N_\alpha \times (N_b+1)$. The generic Hamiltonian of the system we want to solve can be written in second-quantized form (where $a_{i\alpha\sigma}$ and $c_{i\alpha\sigma}$ respectively refer to the noninteracting and interacting levels at site i, orbital α and spin σ):

$$\begin{aligned}\hat{H} = &\sum_{i\alpha\beta\sigma} H^{loc}_{\alpha\beta\sigma} c^\dagger_{i\alpha\sigma} c_{i\beta\sigma} + \sum_{i\neq j\alpha\beta\sigma} H_{ij\alpha\beta\sigma} c^\dagger_{i\alpha\sigma} c_{j\beta\sigma} + \text{h.c.} + \hat{H}_{int}(c^\dagger, c) \\ &+ \sum_{\nu\alpha\beta\sigma} h^\nu_{\alpha\beta\sigma} a^\dagger_{\nu\alpha\sigma} a_{\nu\beta\sigma} + \text{h.c.} \\ &+ \sum_{i\nu\alpha\sigma} V_{i\nu\alpha\sigma} c^\dagger_{i\alpha\sigma} a_{\nu\alpha\sigma} + \text{h.c.}\end{aligned} \tag{4.1}$$

where H^{loc} and H are, respectively, the non-interacting part of the local and non-local Hamiltonians of the impurity electrons. H_{int} is the local multi-orbital interaction in one of its established expressions, such as the Kanamori formulation introduced in Chapter 2. Finally, h is the Hamiltonian for the bath electrons and V the hybridization among the impurity and bath electrons. By specifying explicitly the form of the different terms appearing in (4.1) we realize different models which apply equivalently to either DMFT, CDMFT or VCA.

4.1.1 The Fock space and conserved quantum numbers

The starting point of any ED algorithm is the construction of the Fock space of the problem. The local Hilbert space of the electrons on a single site is $\mathcal{H} = \{|0\rangle, |\uparrow\rangle, |\downarrow\rangle, |\uparrow\downarrow\rangle\}$. The Fock space of an N_s-level system is then:

$$\mathcal{F} = \bigoplus_{n=0}^{N_s} S_+ \mathcal{H}^{\otimes n},$$

where S_+ is the anti-symmetrization operator, $\bigoplus$ is the direct sum and $\bigotimes$ the tensor product. The Fock space has a total dimension of $\dim(\mathcal{H})^{N_s} = 4^{N_s} = 2^{2N_s}$, exponentially growing with the number of electronic levels N_s. The last equality points out the equivalence among the system of N_s interacting electrons and a system of $2N_s$ interacting spins.

The solution of the eigenvalue problem can be simplified by taking into account the conserved quantities of the model. From a general point of view, the Hamiltonian (4.1) conserves the charge $\hat{N}$ and the spin component $\hat{S}_z$, at least if we assume that no terms which break the spin

conservation are present, (e.g. local spin-orbital coupling, in-plane magnetic field, etc.). This fact can be conveniently expressed as a conservation of the number of spin $\uparrow$ and $\downarrow$ electrons, i.e. $\hat{N}_\uparrow$, $\hat{N}_\downarrow$. Moreover, if the terms H^{loc}, H and h are diagonal, the number of spin $\uparrow$ and $\downarrow$ electrons *per orbital* are conserved, i.e. $\hat{N}^\alpha_\uparrow$, $\hat{N}^\alpha_\downarrow$, where $\alpha = 1, \ldots, N_\alpha$. In order to formally unify the treatment of such two cases, we introduce some convenient parameters: namely the number of conserved operators per spin $N_{ud} = 1$ (N_α) and the number of bits $N_{bit} = N_s$ (N_s/N_α), whose meaning will become clear in the following, for conserved total (orbital-resolved) number of electrons with $\uparrow$ and $\downarrow$ spin. In the following, we will indicate the set of conserved quantum numbers (QN)s with the tuple $[\vec{N}_\uparrow, \vec{N}_\downarrow]$, where ($\sigma = \uparrow, \downarrow$):

$$\vec{N}_\sigma = \begin{cases} N_{1\sigma} \equiv N_\sigma, & \text{if } N_{ud} = 1 \\ [N_{1\sigma}, \ldots, N_{N_\alpha \sigma}], & \text{if } N_{ud} = N_\alpha \end{cases} \tag{4.2}$$

The existence of a set of conserved QNs introduces a great simplification in the treatment of the problem: the Fock space of the system factorizes in a number of sub-spaces of reduced dimension, each corresponding to a given value of the QNs tuple. We indicate such reduced space with the term *sector* and the symbol $\mathcal{S}([\vec{N}_\uparrow, \vec{N}_\downarrow])$ or just $\mathcal{S}$ where no confusion can arise. The dimension of each sector is given by the number of ways we can arrange $N_{\alpha\sigma}$ elements into N_{bit} positions:

$$\dim\mathcal{S}([\vec{N}_\uparrow, \vec{N}_\downarrow]) = \prod_{\alpha=1}^{N_{ud}} \binom{N_{bit}}{N_{\alpha\uparrow}} \prod_{\alpha=1}^{N_{ud}} \binom{N_{bit}}{N_{\alpha\downarrow}} = \prod_{\alpha=1}^{N_{ud}} D_{\alpha\uparrow} \prod_{\alpha=1}^{N_{ud}} D_{\alpha\downarrow} \overset{\text{def}}{=} D_\uparrow D_\downarrow = D_\mathcal{S} \tag{4.3}$$

where we introduced the symbols D_σ and $D_{\alpha\sigma}$ to indicate the dimension of total and orbital spin sub-space associated to the given set of QNs. Note that $D_\sigma \equiv D_{1,\sigma}$ for $N_{ud} = 1$.

4.1.2 Basis states construction

A natural representation of the basis states for the Fock space $\mathcal{F}$ is obtained in the occupation number formalism of second quantization. Such *Fock basis* for a finite system of N_s electrons is composed of states of the form

$$|\vec{n}\rangle = |n_{1\uparrow}, \ldots, n_{N_s\uparrow}, n_{1\downarrow}, \ldots, n_{N_s\downarrow}\rangle$$

where each element $n_{a\sigma} = 0, 1$ describes the absence or the presence of an electron with spin σ at the level a. Together to such states we introduce the non-Hermitian annihilation and creation operators, respectively $c_{a\sigma}$ and $c^\dagger_{a\sigma}$, which act on the states $|\vec{n}\rangle$ as:

$$c_{a\sigma}|\vec{n}\rangle = \begin{cases} (-1)^{\sum_{i\sigma'<a\sigma} n_{i\sigma'}} |n_{1\uparrow}, \ldots, n_{a\sigma} - 1, \ldots, n_{N_s\downarrow}\rangle, & \text{if } n_{a\sigma} = 1 \\ = 0, \text{ otherwise} \end{cases} \tag{4.4}$$

$$c^\dagger_{a\sigma}|\vec{n}\rangle = \begin{cases} (-1)^{\sum_{i\sigma'<a\sigma} n_{i\sigma'}} |n_{1\uparrow}, \ldots, n_{a\sigma} + 1, \ldots, n_{N_s\downarrow}\rangle, & \text{if } n_{a\sigma} = 0 \\ = 0, \text{ otherwise} \end{cases} \tag{4.5}$$

and satisfy anti-commutation relations. Each state $|\vec{n}\rangle$ of the Fock basis can then be obtained by applying a suitable product string of construction and annihilation operators onto the empty state $|\vec{0}\rangle$.

It is straightforward to realize that each state is then represented as a string of zeros and ones, i.e. the binary representation of a given integer number. Thus, the Fock basis of an electronic (or spin) system is naturally described by the set of integer numbers such that $|\vec{n}\rangle = |I\rangle$ with $I = 0, \dots, 2^{2N_s} - 1$. This observation suggests to encode each state of the Fock basis in a computer using a sequence of $2N_s$ bits or, equivalently, an integer number in a fixed 32bit representation (though modern architectures make 64bit representations also accessible, extending the reach of this approach). However, as we discussed above, the exponentially growing size of the Fock space will make such representation quickly unpractical. A solution to this problem is achieved by exploiting the previously outlined symmetries of the model. Given a set of QNs $[\vec{N}_\uparrow, \vec{N}_\downarrow]$ we can decompose the Fock state $|\vec{n}\rangle$ as

$$|\vec{n}\rangle = \prod_{\alpha=1}^{N_{ud}} \prod_{\sigma=\uparrow\downarrow} |n_1 \dots n_{N_{bit}}\rangle_{\alpha\sigma} = \begin{cases} |\vec{n}_\uparrow\rangle|\vec{n}_\downarrow\rangle, \text{ if } N_{ud} = 1 \\ |\vec{n}_{1\uparrow}\rangle \cdots |\vec{n}_{N_{ud}\uparrow}\rangle|\vec{n}_{1\downarrow}\rangle \cdots |\vec{n}_{N_{ud}\downarrow}\rangle, \text{ if } N_{ud} = N_\alpha \end{cases} \tag{4.6}$$

so that, if total number of spin $\uparrow$, $\downarrow$ electrons are conserved any state is identified by two binary sequences of $N_{bit} = N_s$ bits, one per spin orientation. If moreover the number of spin $\uparrow$, $\downarrow$ electrons are conserved for each orbital, the states are decomposed into two sets of binary sequences (one set per spin orientation), with each sequence made of $N_{bit} = N_s/N_\alpha$ bits. This clarifies the meaning of the parameter N_{bit}.

It is natural to associate each binary sequence to a suitable tuple of integer numbers such as to univocally identify the Fock state. This procedure has been put forward in [114] for the case of $N_{ud} = 1$. Here we extend it to the case where the number of electrons is conserved not only per spin but also per orbital. As such, we have:

$$I \to [\vec{I}_\uparrow, \vec{I}_\downarrow]$$

where $I = 0, \dots, 2^{2N_s} - 1$ and $\vec{I}_\sigma = [I_{1\sigma}, \dots, I_{N_{ud}\sigma}]$ with $I_{\alpha\sigma} = 0, \dots, 2^{N_{bit}} - 1$. Through this decomposition, each state can be described by the smallest bit set compatible with the conserved QNs. The relation between the Fock state index I and its tuple decomposition can be easily inverted:

$$I = I_1 + \sum_{i=2}^{2N_{ud}} (I_i - 1) 2^{N_{bit}(i-1)} \tag{4.7}$$

where we rearranged the tuple as $[\vec{I}_\uparrow, \vec{I}_\downarrow] = [I_1, \dots, I_{2N_{ud}}]$.

Such organization of the Fock states can be readily used to construct a suitable basis for any sector $\mathcal{S}([\vec{N}_\uparrow, \vec{N}_\downarrow])$. The goal of the procedure is to identify the Fock states which hold exactly $[\vec{N}_\uparrow, \vec{N}_\downarrow]$ electrons in each channel, i.e. the states which binary decomposition contains exactly $N_{\alpha\sigma}$ particles in each channel. In this way we associate to a given Fock state $|\vec{n}\rangle$ and its integer representation I, containing the correct bit decomposition dictated by the QNs, a state $|i\rangle$ and an integer i, with $i = 1, \dots, D_{\mathcal{S}}$. In our implementation this procedure is performed keeping track of the QNs based decomposition of the states. Thus, we introduce a suitable *map* $\vec{\mathcal{M}}$, operationally consisting of a data structure which holds $2N_{ud}$ integer arrays. Each array in $\vec{\mathcal{M}}$ has a length $D_{\alpha\sigma}$ (see (4.3)). The arrays are constructed iteratively by looping over the integers $I_{\alpha\sigma} = 0, \dots, 2^{N_{bit}} - 1$, for any $\alpha = 1, \dots, N_{ud}$, $\sigma = \uparrow, \downarrow$, the index is appended into the array if its bit decomposition corresponds to the required QNs value, as shown in listing 1.

```
do iud=1,Ns_Ud                    !>For each orbital
  dim=0                           !>For the Up spin configuration
  do iup=0,2**Nbit-1              !>Loop over the number of levels for one orbital
    nup_ = popcnt(iup)            !>Count the number of 1 bits (occupied states)
    if(nup_ /= Nups(iud))cycle    !>Disregard binary configurations with the wrong occupation
    dim  = dim+1                  !>Else increase the index counter for the viable states...
    H(iud)%map(dim) = iup         !>And store the corresponding index in the map
  enddo
  dim=0                           !>Repeat for the Down spin configuration
  do idw=0,2**Nbit-1
    ndw_= popcnt(idw)
    if(ndw_ /= Ndws(iud))cycle
    dim = dim+1
    H(iud+Ns_Ud)%map(dim) = idw
  enddo
enddo
```

Listing 1: *Fortran code snippet relative to the construction of the map $\vec{\mathcal{M}}$, which is in this case encoded in the structure H. This consists of multiple arrays, one per conserved Quantum Number, each of which is a collection of integer numbers whose binary representation is a vector belonging to the specific sector under consideration.*

Through the map $\vec{\mathcal{M}}$ we associate to each tuple of integers identifying a Fock state a new tuple specific for each sector, as follows:

$$I = [\vec{I}_\uparrow, \vec{I}_\downarrow] \xrightarrow{\vec{\mathcal{M}}} [\vec{i}_\uparrow, \vec{i}_\downarrow] = i$$

where $\vec{i}_\sigma = [i_{1\sigma}, \dots, i_{N_{ud}\sigma}]$ and $i_{\alpha\sigma} = 1, \dots, D_{\alpha\sigma}$. The tuple $[\vec{i}_\uparrow, \vec{i}_\downarrow]$ univocally identifies a basis state $|i\rangle = |\vec{i}_\uparrow, \vec{i}_\downarrow\rangle$ of the Sector $\mathcal{S}$, through a relation similar to Eq. (4.7):

$$i = i_{1\uparrow} + \sum_\sigma \sum_{l=2}^{N_{ud}} (i_{l\sigma} - 1) \prod_{\alpha=1}^{l-1} D_{\alpha\sigma} \tag{4.8}$$

The entries in each array of the map, connecting the states of sector $\mathcal{S}$ to the Fock basis, are monotonously ordered making such map invertible. However, it is straightforward to realize that the inverse map would have the entire Fock space has a domain, making it highly inefficient to be stored in memory. Instead, we perform reverse-lookup in each array using a binary search algorithm, which compares the binary representation at hand with those associated to the indices belonging to the sector in a bisection method fashion. Note that while access to the map is of $O(1)$ in time, the reverse access is only $O(N \log(N))$. Yet, the great advantage of not having to store the inverse map in memory overcomes this little loss in the access rate.

4.1.3 Hamiltonian matrix representation

As discussed above the presence of conserved QNs can be used to reduce the dimensions of the problem by separating the Fock space in a number of smaller sub-spaces. Accordingly, the matrix representing the system Hamiltonian in the Fock space shows a block diagonal structure. Each block corresponds to a given set of QNs and describes the Hamiltonian of a sector $\mathcal{S}([\vec{N}_\uparrow, \vec{N}_\downarrow])$. This reduces the solution of the problem, i.e. the calculation of the spectrum or a part of it, to the analysis of the sequence of sector Hamiltonians.

In each sector, the Hamiltonian of the system has the following general form:

$$H_{\mathcal{S}} = H_d + H_\uparrow \otimes \mathbb{I}_\downarrow + \mathbb{I}_\uparrow \otimes H_\downarrow + H_{nd} \tag{4.9}$$

where H_d is a diagonal term containing the local part of the Hamiltonian and the density-density terms of the Kanamori interaction, the H_σ components describe all the hopping terms of electrons with spin $\sigma = \uparrow, \downarrow$ and the term H_{nd} contains all the remaining non-diagonal elements, namely the spin-exchange and pair-hopping part of the Kanamori interaction.

```
1   do i=1,Dim                                          !> Loop over the states of Sector S
2      call state2indices(i,[DimUps,DimDws],Indices)    !> Tuple decomposition of i
3      do iud=1,Ns_Ud
4         mup = Hs(iud)%map(Indices(iud))               !> Map i_{α,σ} → I_{ασ}
5         mdw = Hs(iud+Ns_Ud)%map(Indices(iud+Ns_ud))
6         Nups(iud,:) = Bdecomp(mup,Ns_Orb)             !> Binary decomposition with Ns_Orb-bits
7         Ndws(iud,:) = Bdecomp(mdw,Ns_Orb)
8       enddo
9       !> Insert element in position H_d(i,i)
10    enddo
```

Listing 2: *Fortran code snipped relative to the Hamiltonian H_d construction.*

Indeed, if the QNs are conserved per orbital, i.e. if $H_{nd} \equiv 0$ and no inter-orbital local hopping terms are present, H_σ further splits into a sum of smaller terms:

$$H_\sigma = \sum_{\alpha=1}^{N_\alpha} \mathbb{I}_{1\sigma} \otimes \cdots \otimes H_{\alpha\sigma} \otimes \cdots \otimes \mathbb{I}_{N_\alpha\sigma}$$

The particular decomposition of the sector Hamiltonian in Eq. 4.9 has a twofold benefic effect on the diagonalization procedure: the matrix-vector product operation is considerably sped up and the memory storage of the Hamiltonian matrix is greatly reduced.

In any given sector $\mathcal{S}$, the Hamiltonian matrix is a square hermitian matrix of dimension $D_{\mathcal{S}}^2$. The overall low connectivity of the electronic systems we consider is reflected into a very sparse nature of the Hamiltonian matrix, which hosts at most $O(N_s) \ll D_{\mathcal{S}}$ elements on each row. A suitable data structure can be designed to store all the non-zero elements value and positions of such matrix, while keeping access along each row to order $O(1)$. We achieve this by using a suitable hash-table, set up as a set of $2D_{\mathcal{S}}$ rows with dynamic length separately holding the values and position of each entry. The memory cost of such sparse matrix storage would then be bounded above by $O(N_s D_{\mathcal{S}})$. Yet, this storage guarantees $O(1)$ access to the matrix element, which is a key feature in performing matrix-vector products.

However, thanks to the Hamiltonian structure in Eq. 4.9 we can achieve a further gain in the memory footprint storing each matrix component separately. The diagonal term H_d corresponds to a single vector of length $D_{\mathcal{S}}$. The tensor product structure of the hopping terms can be readily reconstructed by storing each $H_{\alpha\sigma}$ in a tuple of sparse matrices, the total dimension of which is at most of order $O(N_{ud} N_s \max(D_{\alpha\sigma}))$, in general much smaller than $O(N_s D_{\mathcal{S}})$. Finally, H_{nd} can only be stored as a separate sparse matrix with leading dimension $D_{\mathcal{S}}$. However, this matrix has a very sparse nature containing at most few, i.e. of the order of one or two, elements per row. Thus, its memory cost is well bounded.

```
!> Loop over all conserved QNs for spin=↑, iorb= α
do iorb=1,Ns_Ud
   !> Loop over the states/integers j_α↑ for this component
   do jup=1,DimUps(iorb)
      !> Map j_α↑ in the sector into J_α↑ in Fock space
      mup          = Hs(iorb)%map(jup)
      !> Binary decomposition with Ns_Orb bits
      Nups(iorb,:) = bdecomp(mup,Ns_Orb)
      !... (condition for the finiteness of the hopping element)
      !> Apply c_2^† c_1 |J_α↑⟩ = |I_α↑⟩
      call c(1,mup,k1,sg1)
      call cdg(2,k1,k2,sg2)
      !> Map back I_α↑ to i_α↑
      iup  = binary_search(Hs(iorb)%map,k2)
      !>
      !> Insert element in H_α↑(i,j)
      !...
   enddo
enddo
```

Listing 3: *Fortran code snippet related to the construction of the Hamiltonian term* $H_{\alpha\uparrow}$

The construction of the Hamiltonian matrix is performed independently on each term, using an iterative loop across the different components of the sector basis. Note that the construction of the small matrices $H_{\alpha\sigma}$ only involves loop over the components $|i_{\alpha\sigma}\rangle$ of the sector basis:

$$\begin{aligned}\langle\vec{i}_\uparrow\vec{i}_\downarrow|H_{\mathcal{S}}|\vec{j}_\uparrow\vec{j}_\downarrow\rangle &= \langle\vec{i}_\uparrow\vec{i}_\downarrow|H_d + H_\uparrow\otimes\mathbb{I}_\downarrow + \mathbb{I}_\uparrow\otimes H_\downarrow + H_{nd}|\vec{j}_\uparrow\vec{j}_\downarrow\rangle \\ &= \langle\vec{i}_\uparrow\vec{i}_\downarrow|H_d|\vec{i}_\uparrow\vec{i}_\downarrow\rangle + \langle\vec{i}_\uparrow\vec{i}_\downarrow|H_{nd}|\vec{j}_\uparrow\vec{j}_\downarrow\rangle + \langle\vec{i}_\uparrow|H_\uparrow|\vec{j}_\uparrow\rangle\delta_{\vec{i}_\downarrow\vec{j}_\downarrow} + \delta_{\vec{i}_\uparrow\vec{j}_\uparrow}\langle\vec{i}_\downarrow|H_\downarrow|\vec{j}_\downarrow\rangle\end{aligned} \tag{4.10}$$

As an example we report in the listings 2 and 3 a fragment of the code which build the diagonal matrix H_d and $H_{\alpha\uparrow}$, respectively.

Finally, it is worth observing that for very large systems storing the Hamiltonian matrices in the memory in highly inefficient. In such cases, we rely on a storage-free diagonalization algorithm which performs the necessary matrix-vector products on-the-fly, i.e. without storing the sparse matrix. This algorithm has in general a considerably negative impact onto the execution time, which however can be managed with a good scaling in a massively parallel framework.

4.1.4 The Lanczos method

The sector Hamiltonians thus obtained have now to be diagonalized in order to find the ground state. One of the simplest and most widespread methods for the approximate solution of an eigenvalue problem is the Lanczos method for hermitian matrices [110], which falls in the previously mentioned category of methods requiring a computationally demanding matrix-vector product as the only problem-dependent input. At its core, the method is an extension of the steepest descent one, and amounts to a clever change of basis for the Hamiltonian, which is then diagonalized in a subset of the new basis. The larger the subset, the more accurate the result.

Let us consider a $N \times N$ hermitian Hamiltonian; starting from a random normalized vector $|v_0\rangle$ we construct the basis of the so-called *Krylov space* [112] as $\mathcal{K} = \text{span}\{|v_0\rangle, H|v_0\rangle, \ldots, H^d|v_0\rangle\}$

(where, crucially, $d \ll n$) in the following way:

$$b_1|v_1\rangle = H|v_0\rangle - a_0|v_0\rangle \tag{4.11}$$

and

$$b_2|v_2\rangle = H|v_2\rangle - \sum_{i=0}^{1} |v_i\rangle\langle v_i|H|v_1\rangle = H|v_1\rangle - a_1|v_1\rangle - b_1|v_0\rangle \tag{4.12}$$

where all the vectors are normalized to 1 and the relevant parameters are $a_n = \langle v_n|H|v_n\rangle$ and b_n, which is the norm of the unnormalized n-th basis vector. It is easy to prove that such basis vectors are orthogonal.

The key observation is that, from the fourth basis vector on, this construction method only involves the two preceding ones: as an example, for $|v_3\rangle$ the $i = 0$ term of the sum in (4.12) is

$$\langle v_0|H|v_2\rangle = b_1\langle v_1|v_2\rangle + a_0\langle v_0|v_2\rangle = 0 \tag{4.13}$$

as immediately follows from the hermiticity of the problem and from the definition and orthogonality of the previously obtained vectors. This construction has two positive consequences: the expression of the Hamiltonian in the Krylov basis is tridiagonal and of the form

$$H_{\mathcal{K}} = \begin{bmatrix} a_0 & b_1 & 0 & \cdots & 0 \\ b_1 & a_1 & b_2 & \cdots & 0 \\ 0 & b_2 & a_2 & \cdots & 0 \\ \vdots & \vdots & \vdots & \ddots & \vdots \\ 0 & 0 & 0 & a_{d-1} & b_d \\ 0 & 0 & 0 & b_d & a_d \end{bmatrix} \tag{4.14}$$

and the only quantities necessary to the determination of the ground state eigenvalue are the coefficients a_n and b_n, that can be easily stored. Indeed, if the eigenvalue is the only quantity we are interested in, we will only need to keep in memory two vectors at a time, by virtue of the specifics of the basis construction. Clearly, the approximation rapidly improves with increasing d, and convergence to the ground state is exponential, as proven by Kaniel and Paige [115]. As previously stated, the pivotal part of the Lanczos method is the matrix-vector product calculation. Note that, for a sparse system the matrix-vector product is an operation of order $\mathcal{O}(n)$, with respect to a conventional order $\mathcal{O}(n^2)$ of a dense matrix.

The simple Lanczos method, although powerful, suffers from several problems. The most important is given by the emergence of the so-called *ghosts* states: spurious unphysical solutions appearing as an effect of the lack of orthogonality in the numerically-determined Krylov basis.

To overcome this issues successive improvements of the Lanczos method have been devised. The most straightforward generalization is the so-called block Lanczos scheme. This features the use of a collection of initial orthogonal vectors $\{|v_1\rangle, \ldots, |v_M\rangle\}$ rather than a single one. At each step the Hamiltonian is multiplied by all the vectors, generating a much larger Krylov basis and faster tridiagonal reduction of the matrix itself. Imposing orthogonality across the block vectors at each step ensure a more stable calculation and a reduction of the ghost problem. A further refinement of the methods is obtained performing a partial re-orthogonalization within the Krylov basis or using Arnoldi implicit restarting [111]. In the majority of cases, e.g. in absence of severe degeneracies in the spectrum, these improvements guarantee a numerically exact calculation of suitable parts of the spectrum at the price of a larger numerical cost

and memory footprint. Notwithstanding these improvements, some existing highly optimized packages [116] guarantee an execution time equal or smaller than simple Lanczos with a way larger level of accuracy, as we shall see in Sec. 4.2.

```
1       tmp = vin
2       vin = vout/beta
3       vout= -beta*tmp
4       !> External MPI parallel Matrix-Vector product H_S v_in
5       call MatVec(size(vin),vin,tmp)
6      vout = vout + tmp
7       !> Perform scalar products using a share of the vectors a_p
8       !> Mpi Reduce summing all processes contribution: a = sum_p a_p .
9       atmp = dot_product(vin,vout); call AllReduce_MPI(MpiComm,atmp,alfa)
10      vout = vout - alfa*vin
11      btmp = dot_product(vout,vout); call AllReduce_MPI(MpiComm,btmp,beta)
12      beta = sqrt(beta)
```

Listing 4: *Source code template for parallel Lanczos step.*

4.1.5 Matrix-vector product: parallel algorithm

Thanks to the multi-core architecture of modern supercomputers, it is possible to greatly improve the execution time of a demanding routine by splitting the required operation between multiple processors, a technique that is called parallelization. Since this procedure relies on communication between different CPUs, its implementation is not trivial at all and, if not properly engineered, can in some cases even lead to an actual degradation of performance.

The Lanczos-based methods outlined above contains only linear operations, such as scalar products, which can then be readily performed in parallel, see for example Listing 4. As we discussed above the most time consuming part of any ED method is instead represented by the matrix-vector product: $|w\rangle = H_{\mathcal{S}}|v\rangle$ or, projecting onto the sector basis, $w_i = \sum_j [H_{\mathcal{S}}]_{ij} v_j$. We have already seen how the sector structure can improve the total diagonalization time of the Hamiltonian; in this section we discuss how to use the distributed memory *Message Passing Interface* (MPI) framework [117] to design a massively parallel execution of the matrix-vector product within each sector.

`MPI_Gather` algorithm: A simple and generic approach to parallelization can be achieved as follows. Let us consider the expansion of the vector $|v\rangle$ onto the sector basis $|v\rangle = \sum_i v_i |i\rangle$. The vector elements v_i are distributed across the `p` CPU in data chunks of `Q = `$D_{\mathcal{S}}$`/p + R` length, where `R=mod(`$D_{\mathcal{S}}$`,p)` for the first CPU and `R=0` otherwise. In order to distribute the burden of the matrix-vector product among the processes we assign a share `Q` of rows of the matrix $H_{\mathcal{S}}$ to each process, consistently with the splitting of the vector $|v\rangle$. In doing that, it is important to distinguish between local and non-local elements of the vector, i.e. the share of the vector which resides in the memory of a given process and the remaining shares which lives on the memory of the other processes. In fact, in performing the matrix-vector product we will have a local and a non-local contribution. The first comes from the product of the `Q` $\times$ `Q` diagonal blocks of $H_{\mathcal{S}}$ and the local parts of the vector $|v\rangle$, the second from the multiplication between the remaining elements of the matrix share and the vector, as schematically pictured in

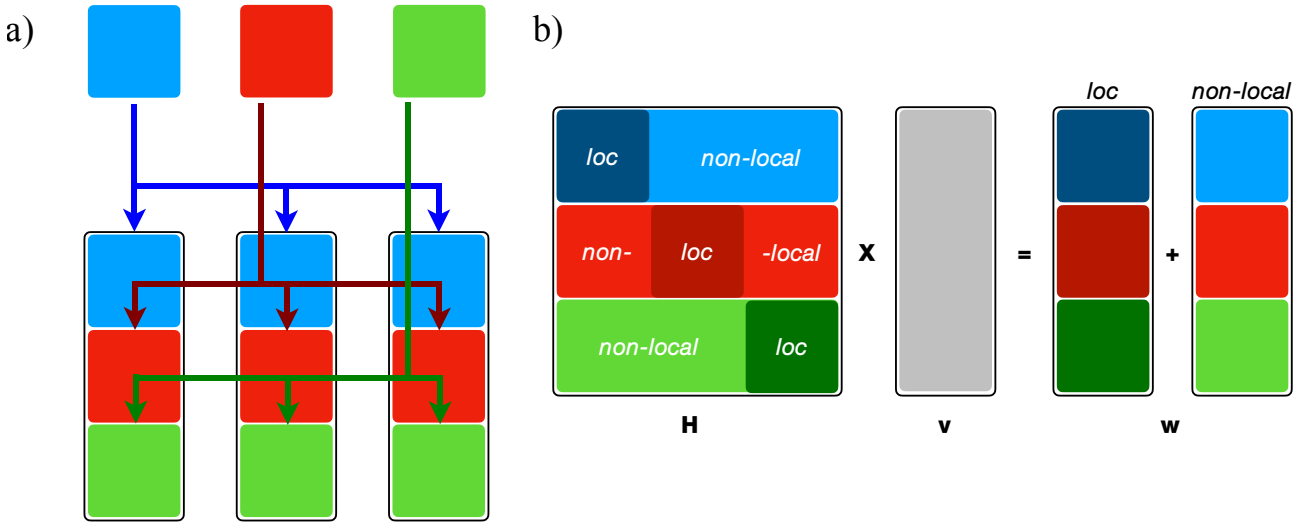

Figure 4.1: *Schematic representation of the parallel execution of the $H_S|v\rangle$ matrix-vector product. The vector is distributed onto the different process. Similarly, a share of the rows of the matrix are stored on each process, dividing the local part of the diagonal block from the remaining entries. The `MPI_AllGatherV` procedure is used to aggregate the vector before performing the product.*

Fig. 4.1. While the first part of the product can be executed locally on each process, the second part requires to reconstruct the distributed vector $|v\rangle$. This is achieved using the MPI function `MPI_AllGatherV`, which involves the communication of the vector share from each process to all the other processes. The implementation of this algorithm is reported in listing 5.

The analysis of the parallel scaling of algorithm 5 however reveals a major flaw. Upon increasing the number of MPI processes `p`, the gain deriving from the decreased size `Q` of the vector share ($\simeq 1/$`p`) is rapidly balanced and overcome by the inter-processors communication in `MPI_AllGatherV`. Each call to this MPI procedure requires a massive amount of data transfer across all processors, which is the main bottleneck of the algorithm. Such communication congestion ultimately prevents to achieve an optimal parallel scaling. In practice, under normal conditions the speed up already saturates for a number of processes of the order of ten.

`MPI_AlltoAll` algorithm: A much better parallelization procedure can be devised by exploiting the setup we introduced above. First we observe that, in the sector basis $|\vec{i}_\uparrow \vec{i}_\downarrow\rangle$, a generic vector $|v\rangle$ can be decomposed as:

$$|v\rangle = \sum_i v_i |i\rangle = \sum_{\vec{i}_\uparrow \vec{i}_\downarrow} \alpha_{\vec{i}_\uparrow} \alpha_{\vec{i}_\downarrow} |\vec{i}_\uparrow \vec{i}_\downarrow\rangle = \sum_{i_\uparrow=1}^{D_\uparrow} \sum_{i_\downarrow=1}^{D_\downarrow} \alpha_{i_\uparrow} \alpha_{i_\downarrow} |i_\uparrow\rangle |i_\downarrow\rangle \tag{4.15}$$

where each parameter $\alpha_{\vec{i}_\sigma}$ is a tuple of complex numbers given by the projections of the vector $|v\rangle$ onto each of the element of the basis, i.e. $\langle v|i_{\alpha\sigma}\rangle$. In the last equality we rearranged the terms noting that, using the relation (4.8), the tuples $\alpha_{\vec{i}_\uparrow} \alpha_{\vec{i}_\downarrow}$ and the states $|\vec{i}_\uparrow \vec{i}_\downarrow\rangle$ can be recast, respectively, in a couple of scalars $\alpha_\uparrow \alpha_\downarrow$ and states of the form $|i_\uparrow\rangle|i_\downarrow\rangle$. The sector basis states are ordered so that the spin-$\uparrow$ index runs faster than the spin-$\downarrow$ one. We can then rearrange

```
    !> MatVec(Nloc,v,Hv)
    MpiShift = spH0%Ishift !shift the total index to the process index
    Hv=0d0
    !> The size of the diagonal block (Q in the text)
    do i=1,Nloc
       !> Run through the nonzero elements stored in the sparse matrix structure's
       !> local component
       do j=1,spH0%loc(i)%Size
          Hv(i) = Hv(i) + spH0%loc(i)%vals(j)*v(spH0%loc(i)%cols(j)-MpiShift)
       end do
    end do
    !
    !> Non-Local part: auxiliary indices for vector gathering
    allocate(Counts(0:MpiSize-1)) ; Counts(0:)=0
    allocate(Offset(0:MpiSize-1)) ; Offset(0:)=0
    Counts(0:)        = N/MpiSize
    Counts(MpiSize-1) = N/MpiSize+mod(N,MpiSize)
    do i=1,MpiSize-1
       Offset(i) = Counts(i-1) + Offset(i-1)
    enddo
    allocate(vin(N)) ; vin = zero
    !> Gather the vector on each core
    call MPI_Allgatherv(&
         v(1:Nloc),Nloc,MPI_Double_Complex,&
         vin      ,Counts,Offset,MPI_Double_Complex,&
         MpiComm,MpiIerr)
    !> Perform the matrix-vector product for the nonlocal part
    do i=1,Nloc
       matmul: do j=1,spH0%row(i)%Size
          Hv(i) = Hv(i) + spH0%row(i)%vals(j)*vin(spH0%row(i)%cols(j))
       end do matmul
    end do
```

Listing 5: *Source code for the parallel execution of the matrix-vector product using the* ***MPI_AllGatherV*** *procedure, a schematic view of which is presented in Fig. 4.1*

the representation of any vector $|v\rangle$ in terms of a matrix, whose columns correspond to a set of spin-$\uparrow$ components for a given fixed spin-$\downarrow$ configuration:

$$\{v_i\}_{i=1,\dots,D_\uparrow D_\downarrow} \doteq \begin{pmatrix} \alpha_{1_\uparrow}\alpha_{1_\downarrow} \\ \vdots \\ \alpha_{D_\uparrow}\alpha_{1_\downarrow} \\ \vdots \\ \alpha_{1_\uparrow}\alpha_{D_\downarrow} \\ \vdots \\ \alpha_{D_\uparrow}\alpha_{D_\downarrow} \end{pmatrix} = \begin{pmatrix} \alpha_{1_\uparrow}\alpha_{1_\downarrow} & \alpha_{1_\uparrow}\alpha_{2_\downarrow} & \dots & \alpha_{1_\uparrow}\alpha_{D_\downarrow} \\ \alpha_{2_\uparrow}\alpha_{1_\downarrow} & \alpha_{2_\uparrow}\alpha_{2_\downarrow} & \dots & \alpha_{2_\uparrow}\alpha_{D_\downarrow} \\ & \dots & \dots & \\ \alpha_{D_\uparrow}\alpha_{1_\downarrow} & \alpha_{D_\uparrow}\alpha_{2_\downarrow} & \dots & \alpha_{D_\uparrow}\alpha_{D_\downarrow} \end{pmatrix} \tag{4.16}$$

Here lies a great simplification in the product with the Hamiltonian (4.9). In particular, exploiting the decomposition in (4.10), we can design a massively parallel algorithm for the matrix-vector product which overcomes the severe limitations related to the inter-processors communication.

To begin with, we distribute the vector parameters across the MPI processes. We assign to each process a number $\mathtt{Q}_\downarrow = D_\downarrow/\mathtt{p}$ of columns. The rest $\mathtt{R}_\downarrow = \mathtt{mod}(D_\downarrow, \mathtt{p})$, if present, is

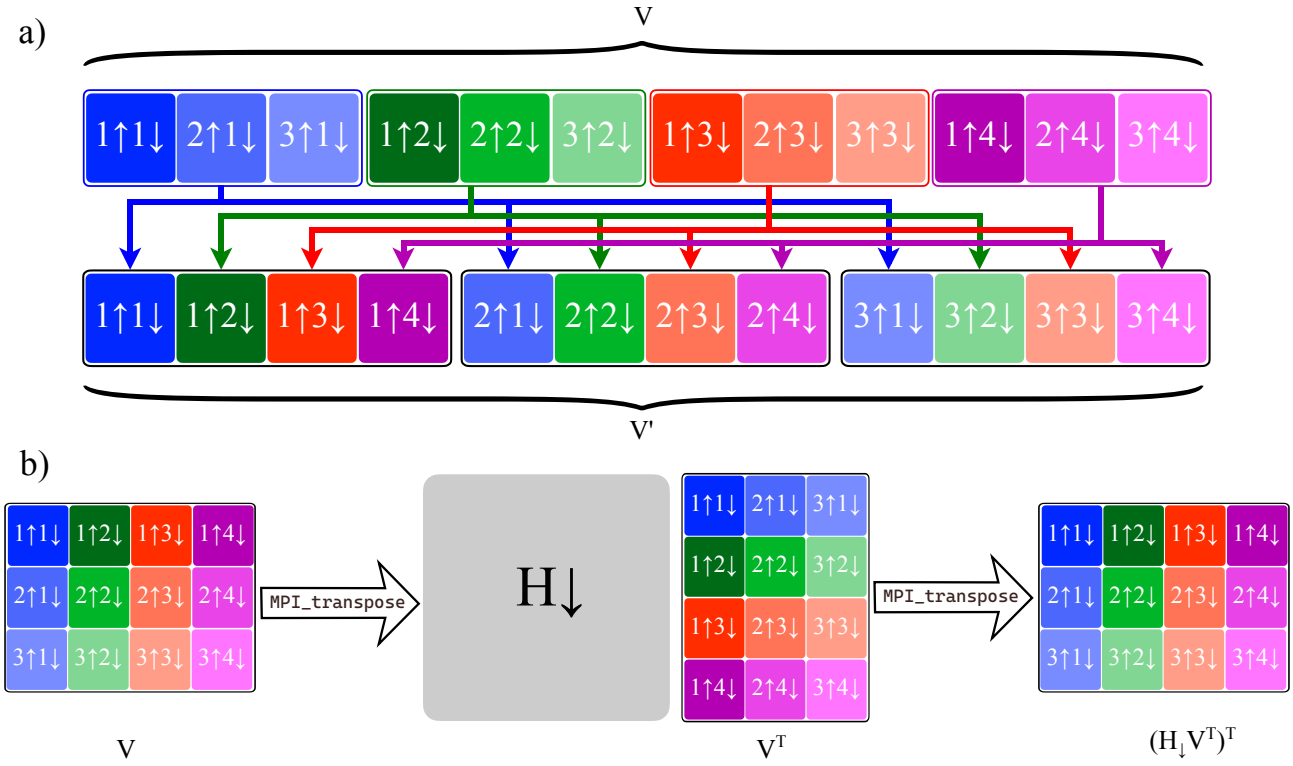

Figure 4.2: *Schematic representation of the parallel execution of the $H|v\rangle$ matrix-vector product for the $\downarrow$ spin. For sake of simplicity we indicate each component component $a_{i_\uparrow} a_{i_\downarrow}$ using its subscripts $i_\uparrow i_\downarrow$ only. a) Schematic representation of the* `MPI_AlltoAllv` *execution on a vector with $D_\uparrow = 3$, $D_\downarrow = 4$. The different main colors of the blocks represents the parts of the vector handled by different processes* $\mathtt{p} = 4$*. The transformed vector V' has contiguous elements in the memory along the $\downarrow$ index. b) Representation of the matrix-vector $H_\downarrow \cdot v$ product based on the parallel transposition of the input vector and its resultant as described in listing 6.*

reassigned to the first $\mathtt{R}_\downarrow$ processes. Differently to the previous case, this partitioning of the matrix corresponds to distributing $\mathtt{Q} = D_\uparrow \times \mathtt{Q}_\downarrow$ vector elements to each process.

Each term in (4.10) contributing to the matrix-vector product is then separately evaluated as follows:

$\mathbf{H_d}$: the diagonal term H_d of the Hamiltonian is scattered among processes, assigning $\mathtt{Q}$ rows, i.e. elements, to each CPU. Notably, the multiplication $H_d|v\rangle$ takes place locally in the memory on each process, i.e. with no need of further MPI communication.

$\mathbf{H_\uparrow \otimes \mathbb{I}_\downarrow}$: The matrix-vector product with of the term $H_\uparrow \otimes \mathbb{I}_\downarrow$ involves only $\uparrow$-electrons configurations. This corresponds to run along the elements of each column of the matrix defined in (4.16). Within our MPI decomposition, these elements are stored contiguously in the memory of each process. As such, like for the diagonal part, this term of the product is performed locally in the memory, provided the (small) Hamiltonian $H_\uparrow$ is known to each process.

$\mathbb{I}_\uparrow \otimes \mathbf{H}_\downarrow$: The multiplication with the term $\mathbb{I}_\uparrow \otimes H_\downarrow$ involves only spin-$\downarrow$ configurations. This corresponds to run along the rows of the matrix (4.16), which ultimately leads to a highly non-local access to the memory. In a serial implementation this introduces only a small performance degradation due to irregular cache access. However, in a parallel setup such non-locality represents a serious possible bottleneck, since heavy MPI communication is necessary to transfer columns among different processes. A simple, yet effective, solution to this problem is to exchange the $\uparrow$- and $\downarrow$-electrons indices $[\vec{i}_\uparrow, \vec{i}_\downarrow] \to [\vec{i}_\downarrow, \vec{i}_\uparrow]$. This corresponds to a transposition of the matrix (4.16). As a consequence, the matrix-vector product is performed by running over columns of the transposed matrix thus recovering the locality in the memory. The collective transposition of a data set requires a suitable all-to-all communication. To this purpose, the MPI library makes available a parallel procedure, `MPI_AlltoAllv` [109, 117], which transfers data such that the `j`-block, sent from the process `i`, is received by process `j` and placed as block `i`. The corresponding communication pattern is schematically depicted in Fig. 4.2a. Although apparently heavy, the communicational burden involved in the interexchange of data among all processes in `MPI_AlltoAllv` involves the minimum amount of data transfer. As such, we expect this operation to unlock excellent parallel scaling.

A template of the source code for this task is shown in listing 6: we first determine (lines 5-10) the number of elements to send for each process. By construction the amount of data to be received in the transposed buffer is obtained by transposing the `Sendcounts` array itself, (lines 11-13). The relative offset is quickly evaluated summing over the number of elements to send/receive, see lines 15-28. We perform the matrix transposition proceeding column-by-column, see lines 30-35. Note that some process may run out of columns to send because of the incommensurability of the matrix size with the number of processes. In this case MPI allows sending empty arrays. The final array is arranged in row-major mode, as such a local transposition (within each process) is required to reorder the data in column-major mode [109].

The resulting matrix-vector product of the $\downarrow$-electrons part of the Hamiltonian proceeds in three steps: i) the vector $|v\rangle$ is transposed using collective MPI communication; ii) multiplication is performed locally on each process; iii) the resulting vector is transposed back and added up to the result. A template of the source code for the spin-$\downarrow$ matrix-vector product is reported in listing 7.

$\mathbf{H}_{\mathbf{nd}}$: Finally we need to take care of the non-diagonal term H_{nd} in the sector Hamiltonian. This matrix, which contains the few elements coming from spin-exchange and pair-hopping terms of the Kanamori interaction, can not be reduced to any favourable form to perform a parallel matrix-vector product. For this term we need to rely on the less-scalable `MPI_Gather`-algorithm. As discussed above, this amount to perform a collective gathering of the distributed vector, while the H_{nd} matrix gets row-distributed among all processes. As we will see in the next section, the inclusion of this term leads to a dramatic reduction of the parallel scalability of the algorithm, yet a substantial gain is achieved for a reasonable number of processes. However, this consideration offers a valid (though admittedly operational) reason to choose, where possible, the density-density Kanamori as the full expression for the interaction.

4.2 Benchmarks

In this section we present some benchmark results for the massively parallel ED algorithm outlined above. The calculations have been performed on the *Ulysses* HPC in Trieste, using

```
    counts = Nrow/MpiSize
    Ntot   = Ncol/MpiSize; if(mod(Ncol,MpiSize)/=0)Ntot=Ntot+1
    !
    do i=1,qcol
       do irank=0,MpiSize-1
          send_counts(irank,i) = counts
          if(irank < mod(Nrow,MpiSize))send_counts(irank,i) = counts+1
       enddo
    enddo
    do i=1,Ntot
       call MPI_AllToAll(send_counts(0:,i),1,MPI_INTEGER,&
                         recv_counts(0:,i),1,MPI_INTEGER,&
                         MpiComm,ierr)
    enddo
    !
    do i=1,Ntot
       do irank=1,MpiSize-1
          send_offset(irank,i) = send_counts(irank-1,i) + send_offset(irank-1,i)
       enddo
    enddo
    recv_offset(0,1) = 0
    do i=2,Ntot
       recv_offset(0,i) = sum(recv_counts(0,:i-1))
    enddo
    do i=1,Ntot
       do irank=1,MpiSize-1
          recv_offset(irank,i) = recv_offset(irank-1,i) + sum(recv_counts(irank-1,:))
       enddo
    enddo
    !
    do j=1,Ntot
       call MPI_AllToAllV(&
            A(:,j),send_counts(:,j),send_offset(:,j),MPI_DOUBLE_PRECISION,&
            B(:,:),recv_counts(:,j),recv_offset(:,j),MPI_DOUBLE_PRECISION,&
            MpiComm,ierr)
    enddo
    call local_transpose(b,ncol,qrow)
```

Listing 6: *Source code for the* `MPI_transpose` *routine referenced in Fig. 4.2b.*

Intel Xeon E5-2680 v2 processors with 2 sockets, 10 cores, 2 threads per core and 40 GB RAM. We considered a multi-orbital single impurity Anderson model with a total of N_s sites, using random energies levels for the effective bath and constant hopping amplitude. The tests have been executed in the half-filling sector $n_\uparrow = n_\downarrow$ using total spin-dependent occupation QNs. This setup corresponds to the worst case scenario for our implementation. We evaluated the lowest state of the spectrum using the Lanczos algorithm. In order to reduce the intrinsic errors, we performed repeated calculation for each set of parameters. The data presented below have been averaged over such repeated calculations.

To begin with, we analysed the net speed-up of the diagonalization algorithm. The results are reported in Fig. 4.3 for an increasing number of total electronic levels N_s. For small systems, i.e. $N_s = 12$, the speed-up saturates for a number of CPU $n > 300$. This should be associated to the ratio between calculation and communication time which, for such a small system, quickly becomes unfavourable. The situation gradually improves for larger systems. In particular, we observed a sub-ideal scaling for $N_s = 15$ with a slight tendency to saturation only for the largest

```
    mpiQup=DimUp/MpiSize
    if(MpiRank<mod(DimUp,MpiSize))MpiQup=MpiQup+1
    !> Get transposed input vector:
    call vector_transpose_MPI(DimUp,MpiQdw,v,DimDw,MpiQup,vt)
    !> Execute product: local and contiguous in memory.
    Hvt=0d0
    do idw=1,MpiQup              !<= Transposed order:  column-wise DW <--> UP
       do iup=1,DimDw            !<= Transposed order:  column-wise DW <--> UP
          i = iup + (idw-1)*DimDw
          hxv_dw: do jj=1,spH0dws(1)%row(iup)%Size
             jup = spH0dws(1)%row(iup)%cols(jj)
             jdw = idw
             j   = jup + (jdw-1)*DimDw
             val = spH0dws(1)%row(iup)%vals(jj)
             Hvt(i) = Hvt(i) + val*vt(j)
          end do hxv_dw
       enddo
    end do
    !> Transpose back result:
    call vector_transpose_MPI(DimDw,mpiQup,Hvt,DimUp,mpiQdw,vt)
    !> Add up.
    Hv = Hv + Vt
```

Listing 7: *Source code for the parallel matrix-vector product of the spin-↓ part of the sector Hamiltonian with a given input vector.*

accessible number of processes (see inset). For $N_s = 18$ the scaling remains nearly ideal up to $n > 200$.

Next, to test the solidity of the scaling with respect to the intrinsic properties of the Lanczos algorithm, we compared a rather simple Lanczos implementation with respect to a fully fledged Parallel-ARPACK method [118]. The memory footprint, as well as the number of matrix-vector operations, can be dramatically different for the two methods. In particular, for the P-ARPACK calculations we used a block of `ncv` $= 10$ vectors. As such one can in principle expect a dramatically different scaling behavior. Yet, the results reported in the left panel of Fig. 4.4, showing the behavior of the total elapsed time as a function of the CPU number, reveal that the scaling of the two methods is very similar (i.e. the same order of magnitude). Interestingly, despite its higher complexity, the more optimized P-ARPACK algorithm performed consistently better than the simple and less-optimized Lanczos method.

An important aspect to consider, in anticipation of the analysis of the next chapters, is the scaling behaviour with respect to the number of orbitals. The presence of multiple orbitals introduces two major changes in the Hamiltonian. The first is in the interaction term. The density-density terms of the interactions are diagonal and, thus, do not affect the scaling. On the contrary, the pair-hopping and spin-exchange can have a dramatic impact on the parallel execution, thus we neglect such term for now and postpone the analysis of their influence to the next paragraphs. The second change affects the hopping terms. In a multi-orbital system the hopping matrices generally include more values than the single orbital, due to the presence of several hopping channels among orbitals.
In order to characterize this aspect, we studied the scaling of the algorithm as a function of increasing orbital number. In the right panel of Fig. 4.4 we show the evolution of the time per Lanczos iteration as a function of the CPU number, for a system of $N_s = 15$ and different

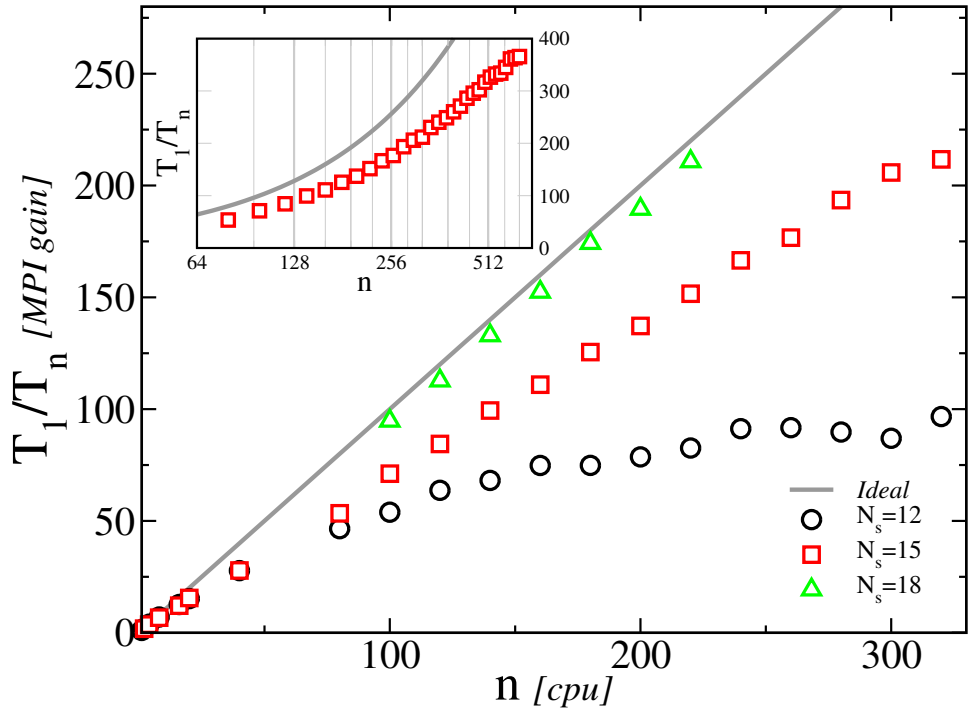

Figure 4.3: *Speedup for a system of a N_s-level system as a function of the number of CPU used, as compared to an ideal (linear) scaling. In the inset a wider range of CPUs is plotted for $N_s = 15$ using a log-scale along the x-axis. The result shows the saturation of the parallel gain for $n > 512$.*

number of orbitals. Our results show that the single Lanczos iteration time is essentially independent of the number of orbitals. However, as shown in the inset of the figure, the number of iterations required to determine the lowest eigenstate increases linearly with the number of orbitals. We conclude that, although the resulting total time has an excellent sub-linear scaling with the number of processes, it linearly depends on the number of orbitals, i.e. the more the orbitals the larger the solution time for a fixed number of processes.

Finally, we characterized how the inclusion of non-diagonal terms of in the sector Hamiltonian affect the scaling behavior of our algorithm. As we discussed above, terms like pair-hopping and spin-exchange cannot be reduced to hopping events involving the single spin orientation. As such we can not take advantage of the special properties of the basis states to perform the parallel matrix-vector product. This is expected to largely affect the nearly optimal scaling observed for the case of density-density interaction only. In order to quantify this effect we report in Fig. 4.5 the speed-up as a function of the CPU number comparing density-density and full Kanamori interactions in two systems with three and five orbitals. In agreement with previous results, the density-density interaction gives rise to a sublinear scaling, which tends to saturates at $n > 600$ processes. For the full Kanamori case the behavior is very different. An initial good speed-up obtained with few tens of processes, rapidly saturates to a value of $50 - 75$ for any number of CPU $n > 100$. In fact, above this threshold the burden of the MPI communication needed to reconstruct the vector and perform the matrix-vector product for H_{nd} becomes predominant and prevents further improvement of the scaling.

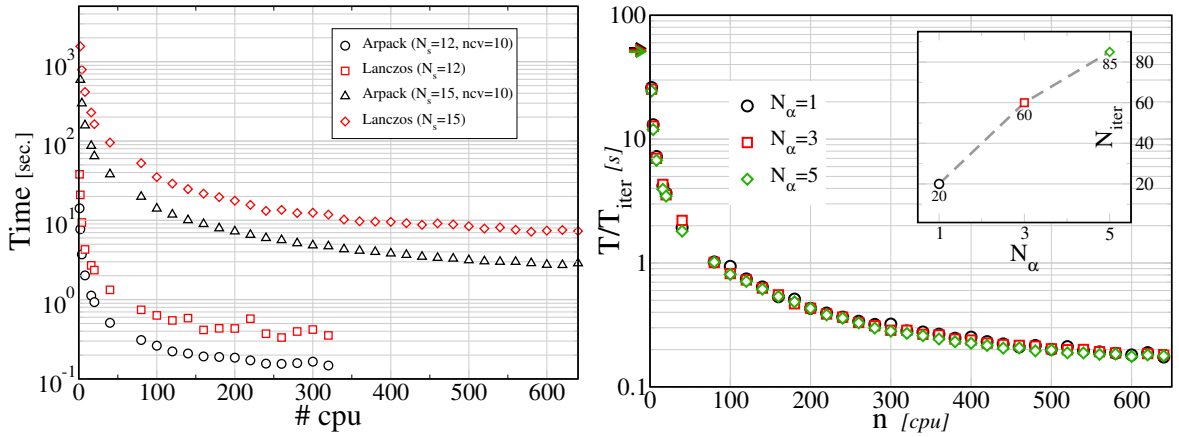

Figure 4.4: a) *Comparison of the execution time as a function of the number of CPUs for a system of N_s levels between P-ARPACK and Lanczos methods.* b) *Execution time of the Lanczos iteration for systems with a different number of orbitals, as a function of the number of CPUs employed.*

4.3 Application to (C)DMFT and SFT methods

In the previous section, we outlined the specifics of the exact diagonalization routine that operates on the effective problem (be it the impurity+bath system in (C)DMFT or the variational cluster in VCA) and determines the lowest energy eigenvalues and associated eigenvectors. This result is then acted upon to obtain all the relevant quantities required by the method of interest. Effectively, the exact diagonalization part acts as a "black-box" routine which, once provided with a defined number of inputs, gives a determined amount of results, e.g. the ground state eigenvalue and eigenvector, using a simplified *reverse communication strategy*.

In the following we briefly discuss the general steps required in the application of the ED algorithm to the methods outlined in the previous chapter. In particular, we outline the calculation of the Green's functions, the determination of the effective bath and the evaluation of the self-energy functional Ω.

4.3.1 Dynamical response functions

The key quantity linking the effective problem to the full lattice one both in DMFT and VCA is the Self-Energy Σ, that is calculated from the Dyson equation for the impurity/cluster. The calculation of Σ therefore effectively amounts to the determination of G. The calculation of the Green's function (for simplicity at T=0) stems from the usual division of the retarded G in greater and lesser:

$$G_{ij}(\omega) = G^{<}_{ij} + G^{>}_{ij} = \langle \Psi_G | c_i^{\dagger} \frac{1}{\omega + H - E_G} c_j | \Psi_G \rangle + \langle \Psi_G | c_i \frac{1}{\omega - H + E_G} c_j^{\dagger} | \Psi_G \rangle \qquad (4.17)$$

where the indices i, j generically refer to all the levels of the electronic system at hand (i.e. sites and orbitals under our spin-decoupled assumptions). Let us consider, as an example, the calculation of the on-site Green's function $G^{<} := G^{<}_{ii}$. Chosen $|v_0\rangle = |\Psi_c\rangle := c_i|\Psi_G\rangle$ as the first vector for the base of a suitable Krylov space, and condensing $z = \omega + E_G$, we can approximate

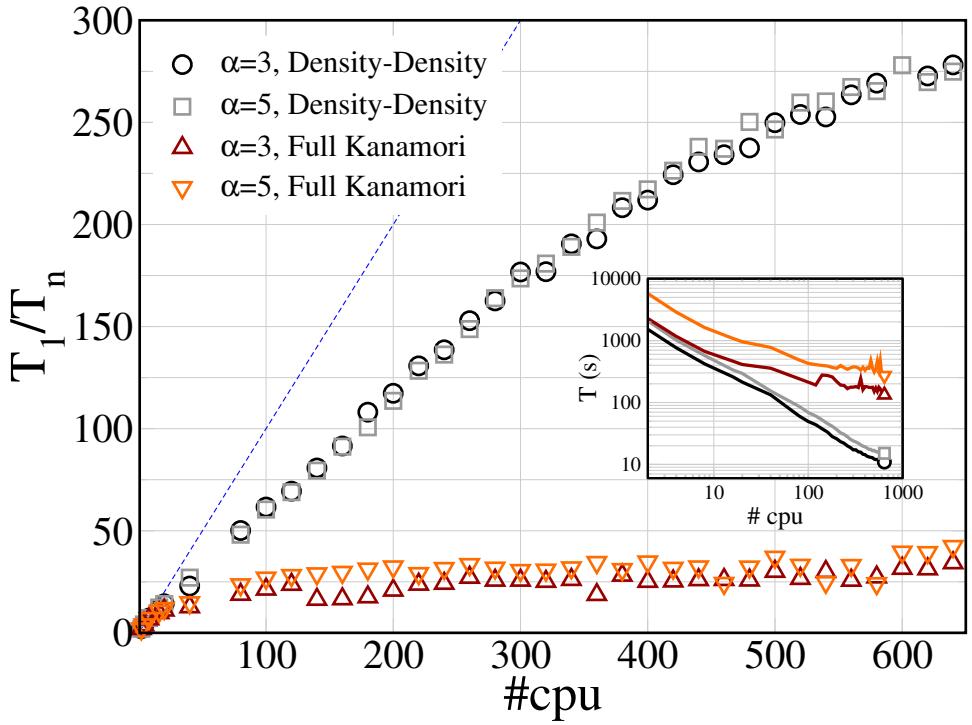

Figure 4.5: *Speedup of the parallel method with respect to the ideal scaling (dotted blue lune) for a system with α orbitals and different forms of the interaction: while the density-density Kanamori scales sub-linearly, the inclusion of H_{nd} quickly saturates the gain.*

the Green's function as

$$G^{<}(\omega) \approx \left\langle \Psi_c \middle| \frac{1}{z - H_{\mathcal{K}}} \middle| \Psi_c \right\rangle = \sum_{n=0}^{N_{lanc}} \frac{\langle \Psi_c | \Psi_n \rangle \langle \Psi_n | \Psi_c \rangle}{\omega - E_n + E_G} \tag{4.18}$$

where E_n and $|\Psi_n\rangle$ are the first N_{lanc} approximated eigenvalues and eigenvectors of the original problem obtained by Lanczos and $H_{\mathcal{K}}$ is the associated tridiagonal matrix. Evidently, there is an abuse of notation in (4.18), since the dimensions of Ψ_c and $H_{\mathcal{K}}$ do not in general check out. Let us however assume the Krylov space has the same dimension as the original one (meaning the Lanczos approximation is now simply a change of basis): in order to calculate the Green's function, we are only interested in the element $(z - H_{\mathcal{K}})^{-1}_{00}$ which, from Cramer's theorem and the Laplace formula for determinants, can be found from the solution of the continuous fraction

$$\cfrac{1}{z - a_0 - \cfrac{b_1^2}{\omega - a_1 - \cfrac{b^2}{z - a_2 - \dots}}}. \tag{4.19}$$

In practice, a truncation will happen at the N_{lanc}-th element, restoring the approximation. There is an alternative way of calculating the Green's function [109, 119], which will prove handy in storing the minimal amount of information required to recover the full form of G at any frequency. The spectral representation of the Green's function is indeed the simple

collection of poles

$$G^{<}(\omega) = \sum_{n=0}^{N_{lanc}} \frac{|\psi_n^0|^2}{\omega - E_n + E_G} \tag{4.20}$$

where ψ_n^l is the l-th component of the of the n-th eigenvector of the tridiagonal matrix (4.14) and $|v_l\rangle$ is the Lanczos basis constructed from $|\Psi_c\rangle$. As a consequence of the Lanczos procedure it holds, for the n-th approximated eigenvector of the problem,

$$|\Psi_n\rangle = \sum_{l=0}^{N_{lanc}} \psi_n^l |v_l\rangle. \tag{4.21}$$

The matrix element $\langle\Psi_c|\Psi_n\rangle$ in (4.18) is therefore ψ_n^0, and the Green's function can thus be recovered: starting from the Ground State eigenvector of the effective problem, resulting from exact diagonalization, we obtain the starting Lanczos vector $|\Psi_c\rangle$ by applying the annihilation operator in the same way as previously described. The operator is applied by a single core, and the resulting vector is then broadcast to all the other ones. The parallel Lanczos tridiagonalization procedure outlined in listing 4 is then invoked, and the diagonal a and subdiagonal b of $H_{\mathcal{K}}$ are obtained. The Lanczos matrix is then exactly diagonalized to retrieve the eigenvalues E_n and the eigenvector matrix Z, whose first row is made up of the needed ψ_n^0 coefficients. The reduced size of the Lanczos matrix makes it viable to use serial exact diagonalization procedures to this end. The Green's function is then calculated as a simple sum of poles, given by the eigenvalues, weighted by the ψ coefficients. The same procedure (with opposite sign on E at the denominator) is performed for the greater G.
Both the continuous fraction and spectral sum approaches rely on the fact that $|\Psi_c\rangle$ appears in both bra and ket in equation (4.18). However, in the multi-orbital and cluster cases, $\mathbf{G}$ is actually a matrix with nondiagonal entries which also have to be calculated. A clever trick to achieve this goal is to consider the response function defined as

$$G^{+}(\omega) = \langle\Psi_G|(c_i^\dagger + c_i^\dagger)\frac{1}{\omega + H - E_g}(c_i + c_i)|\Psi_G\rangle \tag{4.22}$$

(where i, j are the generic site-orbital indices) and then obtaining, from it and the previously calculated diagonal components, the off-diagonal part as

$$G_{ij}(\omega) = \frac{1}{2}\Big(G^{+}(\omega) - G_{ii}(\omega) - G_{jj}(\omega)\Big) \tag{4.23}$$

This equation works if we assume $G_{ab} = G_{ba}$. Under the more general hypothesis where this doesn't hold we have to calculate the two auxiliary Green's functions

$$G^{1}(\omega) = \langle\Psi_G|(c_i^\dagger + c_j^\dagger)\frac{1}{\omega + H - E_g}(c_i + c_j)|\Psi_G\rangle \tag{4.24}$$

and

$$G^{\mathbb{i}}(\omega) = \langle\Psi_G|(c_i^\dagger - ic_j^\dagger)\frac{1}{\omega + H - E_g}(c_i + ic_j)|\Psi_G\rangle \tag{4.25}$$

to obtain

$$G_{ij}(\omega) = \frac{1}{2}\Big(G^{1}(\omega) + G^{\mathbb{i}}(\omega) - (1-i)G_{ii}(\omega) - (1-i)G_{jj}(\omega)\Big) \tag{4.26}$$

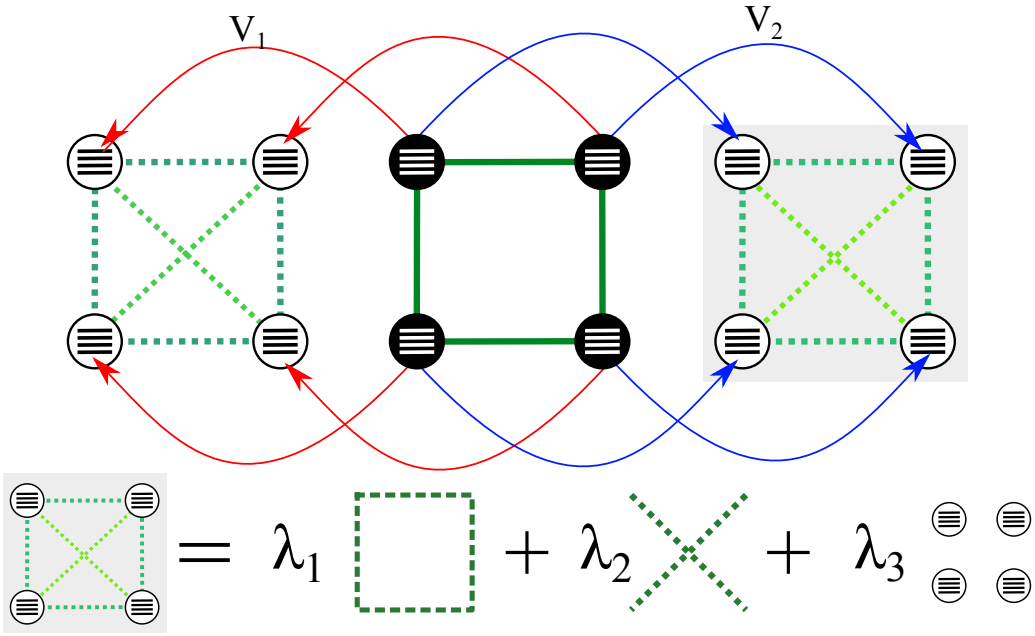

Figure 4.6: *A sketch of a reduced parametrization for a 4-site multi-orbital cluster with two bath replicas. On the bottom, the construction of the replica in terms of variational parameters and constant matrices with given symmetries.*

4.3.2 DMFT and derivatives: bath construction and fit

Once the Green's function of the effective model is obtained, the path followed by different methods diverges. In the case of DMFT and derivatives, the Self-Energy is calculated, and the corresponding local lattice Green's function is obtained as described in Chapter 3. At each step of the DMFT loop, the value of the obtained Green's functions are checked against the previous ones to determine whether convergence has been reached. If this is not the case, some effective parameters have to be tuned to reach convergence. Since in every loop the interacting site or cluster structure remains exactly the same, the only tunable quantity is the bath Green's function depending on the effective parameters which in Chapter 3 we generally called ϵ and V. The way in which the optimal value for these are determined is by the minimization of the distance function between the Weiss Green's function and that of the effective impurity model, which amounts to [120]

$$\chi^2 = \frac{1}{N}\sum_{n=0}^{N} |\mathcal{G}_0(i\omega_n) - \mathcal{G}_0^{IM}(i\omega_n)|^2 \tag{4.27}$$

or, equivalently, of their inverse (which directly depends, in the case of the AIM, on the hybridization Δ). Operationally, this is done via a n-dimensional function minimization, the shape of which is in principle unknown. Indeed, this is the trickiest part of the (C)DMFT loop, since we heavily rely on the minimization to properly find the global minimum of the distance, without insight on the soundness of the results until convergence is near, and more generally without any guarantee such a convergence can be reached. These problems are amplified in the multi-orbital and cluster case, where the formula (4.27) encloses a summation over site and orbital indices, and the risk of converging to a spurious solution that breaks some symmetries of the model due to numerical effects grows larger and larger.

For the single-site case, the usual form of the Anderson impurity model requires a bath made up of different decoupled levels, with hybridization between each level and the interacting effective system. In the case of many orbitals, each bath site has the same internal structure of the interacting site. Considering the number of hybridization parameters, this amounts to a total of $(N_{bath}+1)\cdot N_{orb}$ variables to be fitted, with the number doubling if we consider distinct spins. We can restrict the parametrization by imposing, between the orbitals, every symmetry the original lattice system exhibits, thereby having to fit only a fraction of the total number of parameters. While this may not be a huge computational relief, we are effectively preventing any unwanted loss of symmetry due to numerical effects.
The situation becomes more complicated in the cluster case, where each interacting site in the cluster in principle has an hybridization V with each bath site. A great simplification, that preserves the symmetries of the model and reduces the number of fit parameters, comes from the so-called *reduced* or *constrained* parametrization [121] which trades the diagonal form of the bath on-site energies for that of the hybridization matrix V. The bath is made up of "replica" clusters (cfr. Fig. 4.6) of the same size of the interacting one, and each interacting site couples with its counterpart in the i-th replica with the same amplitude V_i. The complexity is shifted into the replicas, which now have an internal hopping structure that, to preserve the symmetries of the model, can be chosen to mimic that of the interacting cluster. The way this is realized in practice is by implementing a bath replica structure of the type

$$\mathbf{H}_{bath} = \sum_i \lambda_i \mathcal{O}_i \tag{4.28}$$

where $\{\lambda_i\}$ are *real* parameters and $\{\mathcal{O}_i\}$ are constant matrices that couple to each parameter so that the final form of H_{bath} is that of an Hermitian hopping matrix of our choice. This is extremely convenient, since the minimization routine will always act on a real vector and we can in principle choose what part of lattice hopping Hamiltonian we want the replicas to possess, enhance or suppress. The explicit expression of the bath makes it also easier to calculate the gradient of the χ^2 function, which is required by any conjugate-gradient-based minimization routine. In fact, considering the properties of the derivative of the inverse of a matrix, we obtain for the hybridization function $\mathbf{\Delta}$, identifying the vector of parameters$\{V,\lambda\} := x$,

$$\begin{aligned}\frac{\mathrm{d}\mathbf{\Delta}}{\mathrm{d}x} &= \frac{\mathrm{d}}{\mathrm{d}x}\sum_i \frac{V_i^2}{(\epsilon+\mu)\mathbb{I} - \sum_j \lambda_j \mathcal{O}_j} \\ &= \left[\left\{\frac{2V_i}{(\epsilon+\mu)\mathbb{I} - \sum_j \lambda_j \mathcal{O}_j}\right\}_i, \left\{V_i^2 \frac{1}{(\epsilon+\mu)\mathbb{I} - \sum_j \lambda_j \mathcal{O}_j}\mathcal{O}_i \frac{1}{(\epsilon+\mu)\mathbb{I} - \sum_j \lambda_j \mathcal{O}_j}\right\}_i\right]\end{aligned} \tag{4.29}$$

and the gradient of the Weiss Green's function by definition is simply

$$\frac{\mathrm{d}\mathbf{G}_0}{\mathrm{d}x} = -\mathbf{G}_0^{-1}\left(-\frac{\mathrm{d}\mathbf{\Delta}}{\mathrm{d}x}\right)\mathbf{G}_0^{-1} \tag{4.30}$$

Through this expression, the exact gradient of the function χ^2 can be calculated, and the function itself minimized with respect to the parameters $\{V,\lambda\}$. The Exact Diagonalization routine will then be called with the updated bath Hamiltonian, and so on until convergence is reached.

4.3.3 VCA: calculation of Ω

In VCA, the main output of the ED routine we are interested in is the full Green's function of the reference cluster: in fact, the goal of the method is the derivation of the Ω potential from the expression

$$\Omega = \Omega' - \mathrm{Tr}\,\log\left(\mathbf{G}_0^{-1} - \mathbf{\Sigma}\right) + \mathrm{Tr}\,\log\left(\mathbf{G}_0^{'-1} - \mathbf{\Sigma}\right) \tag{4.31}$$

where the trace is intended over $\mathbf{k}$-points, residual degrees of freedom (orbitals, spin ecc.) and Matsubara frequencies. Through some algebraic manipulation [98] and making use of Dyson's equation for the reference system, the operational form of the previous equation becomes

$$\Omega = E_{cluster}^{GS} - \frac{1}{\pi}\int_0^\infty \mathrm{d}\omega \sum_{\mathbf{k}} \log\left|\det\left(\mathbb{I} + \left(\mathbf{H}' + \mathbf{\Delta}(\omega) - \mathbf{H}(\mathbf{k})\right)\mathbf{G}'(i\omega)\right)\right| \tag{4.32}$$

where $\mathbf{G}'(\omega)$ is the cluster Green's function as derived in the previous section, $\mathbf{\Delta}(\omega)$ is the hybridization function of the "dummy" bath (if present), $\mathbf{H}'$ and $\mathbf{H}(\mathbf{k})$ are the hopping matrices appearing in $\mathbf{G}_0'$ and $\mathbf{G}_0$ respectively, expressed in the mixed representation outlined in Chapter 3, and $\mathbf{k}$ lives in the Reduced Brillouin Zone.
This equation can then be solved in two ways: the first is analytical, and involves explicitly calculating the integral over the Matsubara frequencies obtaining [122]

$$\Omega = \Omega' - \sum_{\omega'_r<0} \omega'_r + \int_{RBZ} \sum_{\omega_r(\mathbf{k})<0} \omega_r(\mathbf{k}) \tag{4.33}$$

where ω and ω' are the poles of the full lattice Green's function and the cluster one in Lehmann representation. While the first sum is rapidly obtained, the second entails the calculation of the poles of the Green's function $\mathbf{G}(\mathbf{k}) = (\mathbf{G}_0(\mathbf{k}) - \mathbf{\Sigma})^{-1}$ for each k-point in the reduced Brillouin zone through a method similar to the one outlined in the previous section, which is a process of order $N_{\mathbf{k}} N_{lanc}^3$ [98]. As discussed by Senechal, and proven via direct calculation [123], a generally faster way of calculating the Ω functional is a direct numerical computation of the sum over k-vectors in the RBZ (obtained through a fixed or dynamically adjustable mesh) followed by an integration, again numeric, on the frequency axis.
This method is in particular suited to our way of recovering the Green's function $\mathbf{G}'(i\omega)$. Once the Green's function's weight and poles have been found, with the process previously described, the value of $\mathbf{G}$ at any frequency is obtained via a simple summation. Then, we can collect all the Green's functions weights and poles decomposition into a suitable data structure in order to to make the calculation of $\mathbf{G}'(i\omega)$ readily available through a single function call. As this is the only interacting quantity appearing under the integral in (4.32), no other diagonalization procedure is required, apart from the calculation of the determinant of a comparatively tiny matrix.
The numerical integration over frequencies can be easily taken care of by functions such as `QAGI`, belonging to the QUADPACK library [124], addressing integration on semi-infinite or infinite intervals. The finite T case, where Matsubara frequencies are discrete, requires the calculation of more than one Lanczos eigenvalues and eigenvectors (which is well in the capability of ARPACK) and some non cataclysmic modifications to the routine, as detailed in [125].

In VCA, the whole ED routine has as main aim the calculation of the scalar quantity Ω. Therefore, all the above described procedures can be seen as an overall function $\Omega = \Omega(\overrightarrow{x})$ where $\overrightarrow{x}$ is the full set of variational parameters considered.

The solution of the method will therefore be given by a wrapping minimization function, ranging from simple one-dimensional Brent methods, to multidimensional simplex or conjugate-gradient techniques. Choosing the best cluster approximation and minimization routine for a given problem is effectively a single task, since one has to carefully evaluate the shape of the Ω surface for the chosen parametrization of $\mathbf{\Sigma}$, and consequently estimate the computational cost of each method (a gradient based method, for example, becomes increasingly costly for a higher number of parameters since the unknown shape of $\Omega(\overrightarrow{x})$ dictates that $\nabla\Omega$ has to be obtained numerically). Constrained minimization methods (such for example `l-BFGS-b` [126]) are also an useful tool to be considered, since the behaviour of Ω for diverging values of the parameters could be monotonically decreasing, rendering a search for local minima quite complicated. Finally, it is important to note that VCA doesn't strictly require the localization of the minima of Ω, but is satisfied by maxima and, trickily, saddle points. If no minimum is found, the costly possibility of searching for minima of the modulus of the gradient of Ω has to be considered.
Once the wanted stationary point of Ω has been found, the corresponding $\mathbf{\Sigma}$ is used in the calculation of the full Green's function of the lattice model through

$$\mathbf{G}(\mathbf{k},\omega) = (\mathbf{G}_0^{-1}(\mathbf{k}) - \mathbf{\Sigma}(\omega))^{-1}. \tag{4.34}$$

This quantity can be equivalently calculated from $\mathbf{G}'$ via the hypotheses of VCA, by remembering that

$$\mathbf{G}(\mathbf{k},\omega) = \frac{1}{(\omega+\mu)\mathbb{I} - \mathbf{H}(\mathbf{k}) - \mathbf{\Sigma}(\omega)} = \left[\mathbf{G}'(\omega)^{-1} + \mathbf{H}' + \mathbf{\Delta} - \mathbf{H}(\mathbf{k})\right]^{-1}. \tag{4.35}$$

All the one-body observables and periodized quantities can then be obtained with the formulas included in Chapter 3.

Chapter 5

A model for interacting Weyl Semimetals

In Chapter 1 we have shown that the existence of a topological insulating state is strictly related to the presence of a gap. More than that, the gap itself is topologically protected, meaning that its closure can only happen at a topological phase transition.
However, the realm of topologically nontrivial systems extends beyond the insulating phase, though the conserved quantities and topological responses become more subtly defined.
A crucial result has been reported in [127], where a gapless phase emerges in a finite region connecting a Quantum Spin Hall insulator and a trivial band insulator in a three-dimensional system where one between Time-Reversal and Inversion symmetry is broken.
We can picture this result as a broadening, in the parameter space, of the gapless transition point, which in the symmetric case displays a doubly-degenerate Dirac cone, into a semimetallic region where the degeneracy on the cone is lifted and two non-degenerate cones appear in the Brillouin zone, separated in momentum space.
Moving towards the boundary of the topologically trivial phase, the cones *shift* along a trajectory in the momentum space, and eventually come to coincide: only then a gap can be opened. These systems have been baptized as Weyl semimetals, because they can be described mathematically in terms of the Weyl solution of Dirac equation.
Weyl semimetals exhibit fascinating transport phenomena, related to the chiral anomaly, which we will briefly address in the first part of this chapter, and relativistic electronic dispersion at low energy, and have recently become a major focus of theoretical and experimental research, in a variety of materials ranging from pyrochlore iridates and tantalum monopnictides [128–140] to synthetic materials such as optical lattices with laser-assisted tunneling or Josephson junctions [141–143].
In general, it seems that what is protected in these systems is precisely their gapless nature. The question now is what is protecting it, what is the associated topological invariant and what nontrivial responses the gapless phase possesses.
In this chapter we contribute to the debate on Weyl semimetals considering a simple generalization of the BHZ model which features this solution and supplementing it with a Hubbard-like interaction.

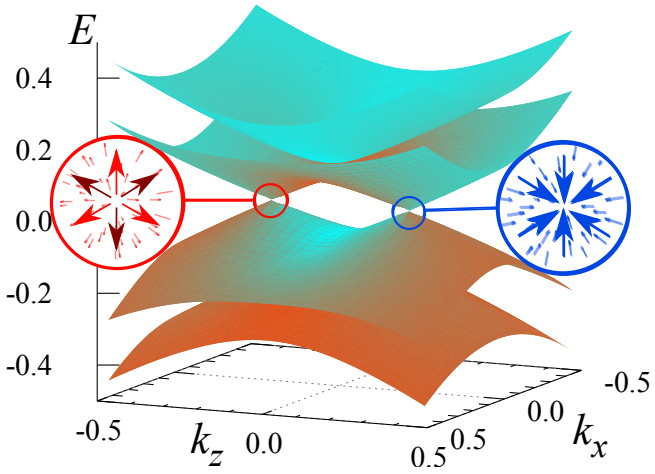

Figure 5.1: *Band structure of a Weyl Semimetal along the plane on which the Weyl points sit: the picture refers to the 4-band model we will study in the chapter. Two band-touching points can be seen as sources and sinks of Berry curvature, and the gaplessness of the system is protected by their separation in k-space. When the Weyl points coincide the system can be gapped. Picture originally from* [144].

5.1 Generalities on Weyl semimetals

5.1.1 Hamiltonian and topology

We begin our discussion from a general treatment of the topological properties of Weyl semimetals before discussing a microscopic model which presents these states. Since the Hamiltonian near a gapless point comes from that of a Dirac cone with lifted degeneracy, it is linear in the crystal momentum relative to that of the node, and has the general expression

$$H(\mathbf{k}) = \sum_{i,j=[x,y,z]} v_{ij} k_i \sigma_j \tag{5.1}$$

where the v matrix has the meaning of a velocity and obviously determines the slope of the cone, while k_i and σ_i are the components of the momentum and of the spin in a three-dimensional space.
Assuming spatial isotropy we can always diagonalize the matrix via a rotation in momentum space yielding the 3×3 identity and the equation can be recast in the familiar form

$$H(\mathbf{k}) = \chi v \mathbf{k} \cdot \overrightarrow{\sigma} \tag{5.2}$$

where v is now a real number. This formula is strikingly similar to that describing a massless spin-1/2 Weyl fermion, which can be seen as half of a Dirac fermion. For this reason we will refer to the position of the point as a Weyl point and we will name the dispersion accordingly. The factor χ is in general given by the sign of the determinant of $[v_{ij}]$, and will play an important role in determining the topological invariant of the system.
In the first chapter we mentioned how the Dirac cones in graphene could be easily split by means of a local mass term coupled to σ_z, introducing an energy offset between the two sublattices. This was possible since none of the terms in the unperturbed Hamiltonian was coupled to σ_z. If

we consider instead a three-dimensional cone in the vicinity of a gapless point, we can represent the Hamiltonian of the two levels that touch at the gapless point in the following way [145]:

$$H = \begin{pmatrix} \delta E & \psi_1 + i\psi_2 \\ \psi_1 - i\psi_2 & -\delta E \end{pmatrix}. \tag{5.3}$$

with real $\delta E, \psi_1, \phi_2$, which is the most general way of writing a 2×2 Hermitian matrix except for a rigid energy shift. The separation between the eigenvalues is $\Delta E = 2\sqrt{\delta E^2 + \psi_1^2 + \psi_2^2}$, and a gapless point is obtained if all the three independent parameters are exactly zero. Perturbing any parameter from zero should in principle open a gap.
However, since we are in three dimensions, the three parameters can be put in correspondence with the three components of the momentum. Therefore any perturbation of the three parameters $\delta E, \psi_1, \psi_2$ can be reabsorbed by varying the three momentum-space coordinates for the position of the node, hence the gapless point survives. This is the reason why Weyl fermions are massless and it explains the robustness of the gapless state in a Weyl semimetal.
The Hamiltonian (5.2) is also similar to that of the Chern insulator we introduced in Chapter 1, but it entails a crucial difference. In the three-dimensional case, the system is not an insulator and the Chern number can not be used as a global topological invariant, since the momentum sum will include the point where $\overrightarrow{q}(\mathbf{k}) = \mathbf{k} = 0$.
Nevertheless, the gapless point provides in a sense a topological characterization of its surroundings, as it acts as a source or sink of Berry flux according to the value of χ.
The Weyl Hamiltonian (5.2) has the same form of a spin in a magnetic field, $H = \mathbf{B} \cdot \overrightarrow{\sigma}$, where the role of the magnetic field is played by the momentum vector $\chi v \mathbf{k}$. Expressing the eigenstates of the spin in the direction of the field in spherical coordinates as

$$\psi_{\frac{1}{2}}(\theta, \phi) = \begin{pmatrix} \cos(\theta/2)e^{-i\phi} \\ \sin(\theta/2) \end{pmatrix} \qquad \psi_{-\frac{1}{2}}(\theta, \phi) = \begin{pmatrix} \sin(\theta/2) \\ -\cos(\theta/2)e^{i\phi} \end{pmatrix} \tag{5.4}$$

and calculating the corresponding Berry curvature, the total Berry flux of the occupied band through a sphere enclosing the origin (which corresponds to the Weyl point) will be $2\pi\chi$. The last quantity, which is ± 1, is known as the *chirality* of the node. According to Gauss's law, this flux is constant no matter the surface we choose around the node, as long as it encircles only one Weyl point.
The chirality seems therefore a good candidate to play the role of a topological invariant for the three-dimensional system, at least in the region close to a node. Let us consider a circle in the three-dimensional Brillouin zone on the $k_x - k_y$ plane where the Weyl point sits, containing the node and being parametrized by $\lambda \in [0, 2\pi]$ through $\mathbf{k}_\lambda = [k_x(\lambda), k_y(\lambda)]$. We can construct a surface by translating the circle along the k_z direction assuming periodic boundary conditions, as sketched in Fig. 5.2. In this way we have the two-dimensional Brillouin zone of an insulating material (as the surface never crosses the node, which is in our hypothesis the only gapless point) in the periodic space $[\lambda, k_z]$, the Hamiltonian of which is in one-to-one correspondence with the three-dimensional original one through

$$H(\lambda, k_z) \to H(\mathbf{k}_\lambda, k_z). \tag{5.5}$$

Following the same argument we used for the Haldane model, this system has nonzero Chern number because it is traversed by the nonzero Berry flux originating from the monopole with charge χ; it is therefore a two-dimensional Quantum Hall insulator. This dimensional reduction

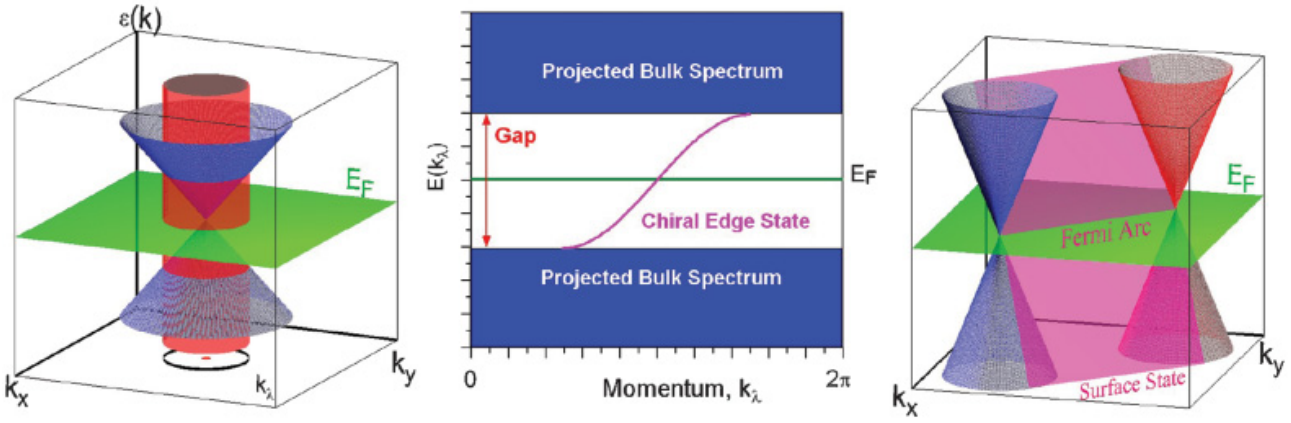

Figure 5.2: *Schematic representation of the surface states of a Weyl semimetal (picture taken from [147]). On the left, a projection of the cone on a two-dimensional space. The red cylinder is unwound in the middle panel, and corresponds to an effective Brillouin zone presenting a gapless edge state. This will cross the Fermi energy at some value of k_λ, and the collection of the relative points will form a zero-energy Fermi arc.*

argument can be directly applied also in the TFT formulation of the invariant, since the equivalence between the first Chern number calculated from the Green's function and that obtained from the topological Hamiltonian has been firmly established, as shown in Appendix A. This argument has an immediate intuitive consequence, which incidentally constitutes a proof of the fermion-doubling theorem by Nielsen and Ninomiya [146]: making use of the analogy with flux originating from a monopole, we consider a cylindrical surface in the three-dimensional BZ as the Gauss surface, growing its base until it merges with the boundary of the BZ. The only surfaces left will be the top and bottom ones, which have opposite normal vectors and therefore contribute with opposite sign to the total flux, which as we know is proportional to χ. From this, it follows that if we imagine to "sweep past" the Weyl point with a two-dimensional surface, the associated Chern number with vary by χ upon passing the node. But since the three-dimensional Brillouin Zone is periodic, there must be an even number of variations through a complete sweep of it with a two-dimensional plane, hence the total number of Weyl points is even, and they come in the same quantity for each chirality.
To sum up, a three-dimensional semimetal with broken TRS or IS, that accounts for a non-degenerate band crossing, can have a nontrivial topological character: this is encoded in the number of band-crossings that exhibit a nonzero Chern flux through any surface enclosing each and only one of them. The gaplessness of the system is topologically protected, not by discrete symmetries as in graphene or other two-dimensional materials, but by dimensionality, which forbids the opening of a mass gap in the Weyl equation, and by translational invariance, since the Weyl points of opposite chirality survive by being separate in the Brillouin zone.

5.1.2 Surface states

We have established that a three-dimensional system can locally "inherit" the topology of a gapped Chern insulator and be in a nontrivial phase even without the presence of a bandgap for

every k-point in the Brillouin zone. In order to qualify as topologically nontrivial, this system should display gapless surface states and peculiar responses to the application of an external field. The Weyl semimetal shows indeed both.
Let us focus again on the two-dimensional toroidal surface enclosing the gapless point in the three-dimensional BZ and now suppose to give the system a border in real space, for example at $z = 0$: we expect a chiral gapless surface state for the associated two-dimensional system, that will cross 0 energy at some value λ_0, that is at certain $[k_x(\lambda_0), k_y(\lambda_0)]$(see the middle and right panels of Fig. 5.2). This argument can be applied for any surface, as long as the total chirality of the enclosed Weyl points is $\neq 0$. In the end, the three-dimensional system with a real-space border will show a surface band separated in energy from the bulk away from the Weyl points. The bulk-surface gap will then vanish at the nodes. If we assume the bulk system to be half-filled, with a vanishing Fermi surface limited to the Weyl points, the corresponding zero-energy edge states for the finite-size sample will consist in a "string" in k-space, known as *Fermi arc*, originating and ending from the projections of the Weyl points on the surface Brillouin Zone. The connectivity of the Weyl points is an interesting subject: given a set of 2N nodes with chiralities equally split between positive and negative, how should their projections be connected on the surface BZ? There is no general answer, since the k-direction in which a zero-energy state has a normalizable expression depends on the specifics of the Hamiltonian. More than that, the connectivity and the shape of the arcs can be tuned in a toy model by varying specific parameters in the Hamiltonian, as it was proven in various recent works both numerically and analytically using transfer matrix techniques, see for example [148].

5.1.3 Topological response

The anomalous current response associated to the Weyl semimetal is quite fascinating. It is, in fact, a condensed matter manifestation of the Adler-Bell-Jackiw anomaly of field theory, as shown by Nielsen an Ninomiya [149], and accordingly it has a very elegant derivation from Topological Field Theory, a brief review of which can for example be found in [150]. We will provide a more practical approach to this effect, which can be seen as an imbalance of occupation of electrons at Weyl points with opposite chiralities in the presence of a magnetic and an electric field.
Let us consider an $A \times L_z$ chunk of material exhibiting Weyl semimetal behaviour, with an applied magnetic field $\mathbf{B}$. This will cause the electron states to split in Landau levels with density AB/Φ_0 where Φ_0 is the flux quantum. Nielsen and Ninomiya proved that, in this case, the levels are one-dimensional modes dispersing along the direction of the applied field: in particular, the zeroth Landau level near a Weyl point has a linear dispersion, whose group velocity is positive or negative depending on the chirality of the node and given by

$$\epsilon_0 = -\chi v \hbar \mathbf{k} \cdot \mathbf{B} \tag{5.6}$$

If an electric field is applied in the same direction as $\mathbf{B}$, the electrons will be accelerated according to

$$\hbar \dot{\mathbf{k}} = -e\mathbf{E} \tag{5.7}$$

which will have the effect of transferring electrons from the surroundings of one Weyl node to the other. This will create an electron number imbalance in the 1d Landau level given by

$$\frac{dN_\chi^{1d}}{dt} = \frac{\chi \dot{\mathbf{k}}}{L_z/2\pi} = -e\chi L_z \frac{E}{h}. \tag{5.8}$$

The explanation of the previous formula is simple: the difference in the number of electrons around the two Weyl points is increased by one if the variation in momentum provided by the electric field equals the spacing in momentum for the electrons in the Landau level ($L_z/2\pi$). This formula is easily extended to three dimensions remembering the Landau level density, so that the total number difference is

$$\frac{dN_\chi}{dt} = -\chi L_z A \frac{e^2}{h^2} EB \tag{5.9}$$

In the most general formulation, the expression of charge density imbalance due to the chiral anomaly is then the famous formula

$$\frac{dn_\chi}{dt} = -\chi \frac{e^2}{h^2} \mathbf{E} \cdot \mathbf{B} \tag{5.10}$$

This formula provides another argument in favour of Nielsen-Ninomiya theorem: the necessity of having an equal number of opposite-chirality Weyl point is in fact a direct consequence of the conservation of charge. Of course, the electrons do not simply disappear from a Weyl point to reappear in the other: the Weyl points are connected via bulk states and, if there is a surface,via Fermi arcs. In fact, an electron can travel through the bulk with a given wavevector, reach the surface of the material, scatter to the opposite wavevector through the Fermi arc as an effect of the Lorentz force and resume its journey into the bulk. Accordingly, for a slab of material, there will be two Fermi arcs living on the two opposite surfaces, connecting the projections of the Weyl point on those.
The chiral anomaly has many interesting consequences which lend themselves to experimental proof: an immediate one is the fact that the separation in momentum space between the Weyl nodes requires a large momentum scattering for the charge imbalance to be relaxed. Hence, the longitudinal conductivity along the direction of **B** grows linearly with B, a phenomenon that is known as negative magnetorisistence, which has been observed experimentally by Kim et al. on a compound of $Bi_{0.97}Sb_{0.03}$ [151].
The Weyl semimetals present other intriguing phenomena such as an anomalous Hall effect [152] and nonlocal transport [153], that however fall outside the scope of this work. To our ends, we will consider the bulk properties of a 4-band theoretical model with broken TRS, and discuss the behaviour of the Weyl points in presence of interaction, briefly commenting also on the Fermi arcs.

5.2 A microscopic model for Weyl semimetals

As originally proposed by Murakami in [127], a region of Weyl semimetal can be obtained starting from a three-dimensional model which features a topological phase transition and both time-reversal and inversion symmetry. Breaking one of the two symmetry, the doubly degenerate gapless point is split, yielding, in three dimensions, the Weyl semimetallic state.
In this section we present the construction of the three-dimensional generalization of the two-dimensional BHZ model that was outlined at the end of Chapter 1. After introducing the model, we will include strong interactions and will discuss the effect on the Weyl semimetal phase.
Recalling the Dirac matrices and their expression in terms of a couple of Pauli matrices σ_i and

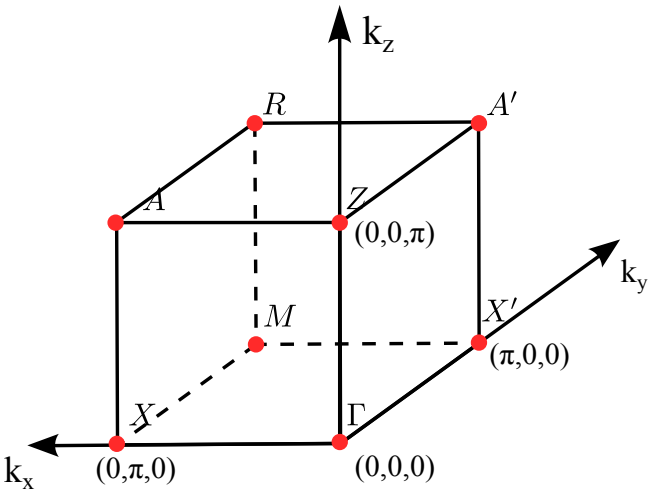

Figure 5.3: *3d BHZ High-Symmetry points location (adapted from [154]).*

τ_i acting on the spin and orbital subspaces respectively,

$$\Gamma^0 = \mathbb{I} \otimes \mathbb{I} \quad \Gamma^1 = \sigma_z \otimes \tau_x \quad \Gamma^2 = -\mathbb{I} \otimes \tau_y \quad \Gamma^3 = \sigma_x \otimes \tau_x \quad \Gamma^4 = -\sigma_y \otimes \tau_x \quad \Gamma^5 = \mathbb{I} \otimes \tau_z, \tag{5.11}$$

we can write the BHZ Hamiltonian operator as

$$\hat{H}_{BHZ} = \sum_{\mathbf{k}} \Psi^\dagger(\mathbf{k}) H(\mathbf{k}) \Psi(\mathbf{k}) \tag{5.12}$$

in the basis spanned by the the 4-component operator $\Psi(\mathbf{k}) = (c_{\mathbf{k}a\uparrow}, c_{\mathbf{k}b\uparrow}, c_{\mathbf{k}a\downarrow}, c_{\mathbf{k}b\downarrow})$. The momentum $\mathbf{k}$ lives in the two-dimensional Brillouin zone of the square lattice and the matrix $H(\mathbf{k})$ has the form

$$H(\mathbf{k}) = \big[M - \epsilon(\cos(k_x) + \cos(k_y))\big]\Gamma^5 + \lambda \sin(k_x)\Gamma^1 + \lambda \sin k_y \Gamma^2 \tag{5.13}$$

We generalize the BHZ model by simply including a hopping along the third dimension k_z. This amounts to an obvious change in the diagonal term proportional to the unit matrix Γ^5 which becomes simply

$$\Gamma^5 \cdot \big[M - \epsilon(\cos(k_x) + \cos(k_y) + \cos(k_z))\big] \tag{5.14}$$

In three dimensions we define a four-component vector of $\mathbb{Z}_2$ topological invariants $(\nu_0; \nu_1, \nu_2, \nu_3)$, which can be evaluated according to the relation

$$(-1)^{\nu_c} = \prod_{i \in \mathcal{A}_c, \alpha} \eta_{i\alpha}^{1/2} \tag{5.15}$$

where the index α runs on the occupied bands and the index i on the TRIMS belonging to a specific path. $\eta_{i\alpha} = \pm 1$ are the eigenvalues of the parity at the TRIMs. For the three "weak" topological indices $\nu_{1,2,3}$ these are the corners of the face of the three-dimensional Brillouin Zone parallel to each Cartesian direction, while for ν_0 the index runs on all 8 the High-Symmetry points, as shown in Fig. 5.3.

We can classify the topological phase of the system by looking at the value of the $\mathbb{Z}_2$ invariant on two opposite faces of the cube in Fig. 5.3, for example $k_z = 0$ and $k_z = \pi$. With this choice we can easily use the same condition on band inversion that we have used to compute the topological invariant for the BHZ model, treating $\cos(k_z)$ as a fixed parameter.
The model projected on the $k_z = 0$ plane is trivial if $M > 3\epsilon$ and topological if $M < 3\epsilon$, while for the model in the $k_z = \pi$ plane the gap closes at $M = \epsilon$. So, restricting ourselves to the positive M region, the topological phase diagram will present three different phases

- $0 < M < \epsilon$: $\mathbb{Z}_2(k_z = 0) = 1$ and $\mathbb{Z}_2(k_z = \pi) = 1 \rightarrow$ Weak TI
- $\epsilon < M < 3\epsilon$: $\mathbb{Z}_2(k_z = 0) = 1$ and $\mathbb{Z}_2(k_z = \pi) = 0 \rightarrow$ Strong TI
- $M > 3\epsilon$: $\mathbb{Z}_2(k_z = 0) = 0$ and $\mathbb{Z}_2(k_z = \pi) = 0 \rightarrow$ Trivial insulator

However, the three-dimensional Hamiltonian we defined is not yet the model we are looking for. It is straightforward to find that the eigenvalues of the Hamiltonian in the 3d k-space are spin-degenerate and they read

$$E_{\pm,\sigma} = \pm\sqrt{\Big(M - \epsilon\big(\cos(k_x) + \cos(k_y) + \cos(k_z)\big)\Big)^2 + \lambda^2\Big(\sin^2(k_x) + \sin^2(k_y)\Big)}. \tag{5.16}$$

It's easy to note that they present gapless points for every value of $0 < k_z < \pi$. To protect the gap, and therefore the topology of the system, we can introduce a spin-orbit coupling term along the k_z direction. Furthermore in order to preserve TRS, the new term has to couple the two TR-connected blocks and to be an odd function of k_z, since spin is odd under TRS. The simplest term that accomplishes this is of the form

$$\lambda_z \sin(k_z)\sigma_x \otimes \tau_x.$$

In the following we will drop the pedex in the SOC coupling, assuming therefore $\lambda_z = \lambda$, and express all energies in units of ϵ.
The Hamiltonian for the three-dimensional BHZ model will still be of the form (5.12), but with $\mathbf{k} = [k_x, k_y, k_z]$ living in a three-dimensional cubic Brillouin zone and

$$\begin{aligned} H(\mathbf{k}) = &\big[M - \epsilon(\cos(k_x) + \cos(k_y) + \cos(k_z))\big]\Gamma^5 \\ &+\lambda\big(\sin(k_x)\Gamma^1 - \sin(k_y)\Gamma^2 + \sin(k_z)\Gamma^3\big). \end{aligned} \tag{5.17}$$

Eq. (5.17) has the same phase diagram we outlined above, namely it is a trivial insulator for $M > 3$, a STI for $1 < M < 3$ and a WTI for $0 < M < 1$. At the transition points, for $M = 1$ the model has doubly degenerate Dirac cones at the X, X′ and Z points of the BZ, while for $M = 3$ only at the Γ point. In principle, the two transition points are expected to turn into windows of Weyl semimetal once a time-reversal breaking perturbation is added. It will turn out that the transition between STI and band insulator is the most interesting in this context, hence we will mainly focus on range of M around 3.
We now finally come to the inclusion of the time-reversal-breaking term which is expected to stabilize the Weyl semimetal. A perturbation of the type $b_z\sigma_z \otimes \tau_z$ is the most natural candidate, since it is conveniently diagonal in our basis and evidently breaks TRS between the two spin blocks of the Hamiltonian. We will restrict ourselves to the case $b_z < \frac{\lambda}{2}$, which leads to the

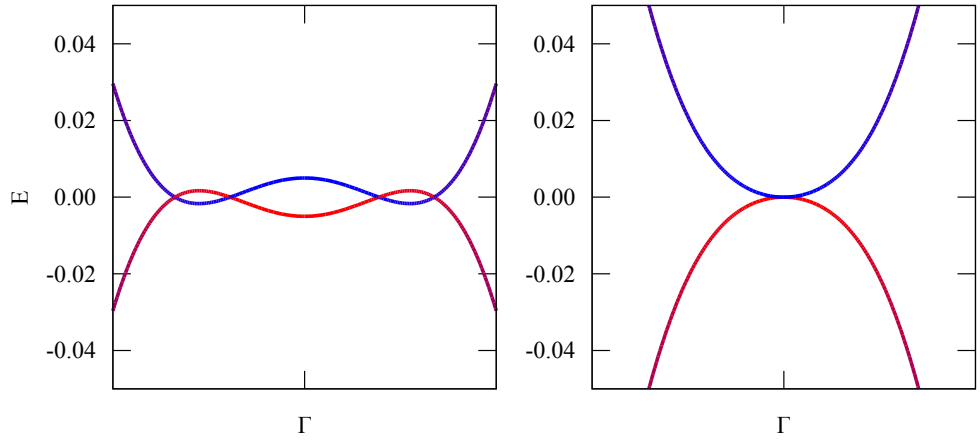

Figure 5.4: *Band dispersion close to the Fermi level along* $-Z \to \Gamma \to Z$ *for* $\lambda = 0.5$ *and in the proximity of* $M \approx 3 - b_z$*. The colour represents the orbital character and is related to the parity eigenvalue.* a) *for* $b_z = 0.3$*, the perturbation value determines a splitting of the opposite-spin bands such that multiple gap-closing points arise. The two innermost points then merge together, leaving the remaining two as the only Weyl points couple left for the entirety of the WSM region.* b) *for* $b_z = 0.1$*, the bands only touch at* Γ*, creating a single couple of Weyl points.*

simplest scenario for the gap opening. Indeed for larger b_z, as it can be seen in Fig. 5.4, the large value of the perturbation determines such a big splitting of the opposite-spin bands that multiple gapless points arise in the proximity of $M = 3 - b_z$. In our case, instead, the number of Weyl points generating from each band-touching is always two.

A finite value of b_z breaks the TRS and lifts the spin degeneracy, though without giving rise to a net magnetization. As a consequence the Dirac cone at the transition point splits into two Weyl cones separated in momentum space.

While the full expression of the eigenvalues of the Hamiltonian is quite long and not particularly insightful, we can however have an idea of the trajectories followed by the Weyl points as the perturbation is changed by considering the linearized version of H around the Γ point, where $\cos(k_i) \approx 1$ and $\sin(k_i) \approx k_i$. Here the four eigenvalues have the form

$$\begin{aligned} E_{\pm,\sigma} &\approx \pm\sqrt{\left(M-3\right)^2 + b_z^2 + \lambda^2\left(k_x^2+k_y^2+k_z^2\right) + \sigma 2 b_z \sqrt{\left(\lambda k_z\right)^2 + \left(M-3\right)^2}} \\ &= \pm\sqrt{\left(\lambda k_x\right)^2 + \left(\lambda k_y\right)^2 + \left(\sqrt{\left(\lambda k_z\right)^2 + \left(M-3\right)^2} + \sigma b_z\right)^2} \end{aligned} \tag{5.18}$$

where $\sigma = \pm 1$ identifies the spin species. From this expression it is clear that the Weyl points move symmetrically along k_z with respect to the high-symmetry point, where they annihilate at the borders of the semimetallic region.

In Fig. 5.5 we show the evolution of the band structure as a function of M in a region around $M = 3$. As expected, we find a Weyl semimetal region intruding between the topological QSHI and the trivial band insulator.

For $M < 3 - b_z$ we recover the inverted-gap QSHI of the BHZ model. It is important to notice that the classification of the gapped phase has been made with respect to the topological

invariant of the unperturbed system, even if the the relative formula is in principle inapplicable to a TRS-breaking system. However, by virtue of the preservation of the bandgap, the two states belong to the same topological phase, since a phase transition can only be achieved with the closure of the gap for a noninteracting system. The $\mathbb{Z}_2$ topological invariant is therefore still adequate to describe the insulating states of the system.
For $M = 3 - b_z$, which marks the boundary of the WSM region, the two spin blocks are decoupled at the Γ point. In this specific point only the spin-up block will present a gapless point for $\mathbf{k} = 0$, while the spin-down block is gapped. An analogous situation, with spin up and down exchanging their roles, is realized at the other boundary of the semimetallic region $M = 3 + b_z$. For other values of M inside the semimetallic region, clearly the two spin blocks are not decoupled at the Weyl nodes, since they sit at $k_z \neq 0$. However, this behaviour at the borders of the semimetal region suggests that, for every M inside the region, another couple of degenerate points have to be present.
These arise at $M = 3$ for positive and negative energy, giving rise to an "inverted cone" band structure also highlighted in [155]. It's important to notice that these points are not Weyl nodes, since they can be easily destroyed moving away from $M = 3$. This degeneracy has a close relation to band inversion: indeed, it determines the inversion of the orbital character of the gap, along with the parity eigenvalue in Γ, for the bands that do not show Weyl points. The parity eigenvalue of the other two bands similarly changes by virtue of the usual gap inversion associated with the WSM phase so that, once the system exits it, the bandgap sign is consistent with the topological character of the insulating phase.

5.3 Weyl semimetals and electron-electron interaction

In this section we finally move to the main result of this chapter, namely the effect of the electron-electron interactions on the topological properties of the model. Therefore, as we discussed in Chapter 2, we supplement the single-particle Hamiltonian (5.17) with an electron-electron interaction term which we take as local. In this work we do connect the results to a specific material, therefore we consider a model expression for the interaction Hamiltonian, namely a two-orbital Hubbard model which only features the density-density interaction terms, i.e. neglecting the spin-flip and pair-hopping terms from the Kanamori Hamiltonian

$$\begin{aligned}\hat{H}_{int} =& U \sum_{il} \hat{n}_{il\uparrow}\hat{n}_{il\downarrow} + \\ & U' \sum_{il \neq l'} \hat{n}_{il\uparrow}\hat{n}_{il'\downarrow} + \\ & (U' - J) \sum_{il<l'} (\hat{n}_{il\uparrow}\hat{n}_{il'\uparrow} + \hat{n}_{il\downarrow}\hat{n}_{il'\downarrow})\end{aligned} \tag{5.19}$$

where $\hat{n}_{\alpha\sigma} = c^\dagger_{\alpha\sigma} c_{\alpha\sigma}$.
Following the popular Kanamori parametrization we further impose $U' = U - 2J$, reducing the free parameters of the interaction to two constants U and J. The first term in (5.19) discourages double occupations of the same orbital with an energy cost U. The second and third terms give a reduced energy cost to configurations with electrons singly-occupying orbitals with opposite and parallel spins, respectively, therefore favouring local configuration with a high-value of the spin quantum number. If we consider the model with an integer number of fermions per site,

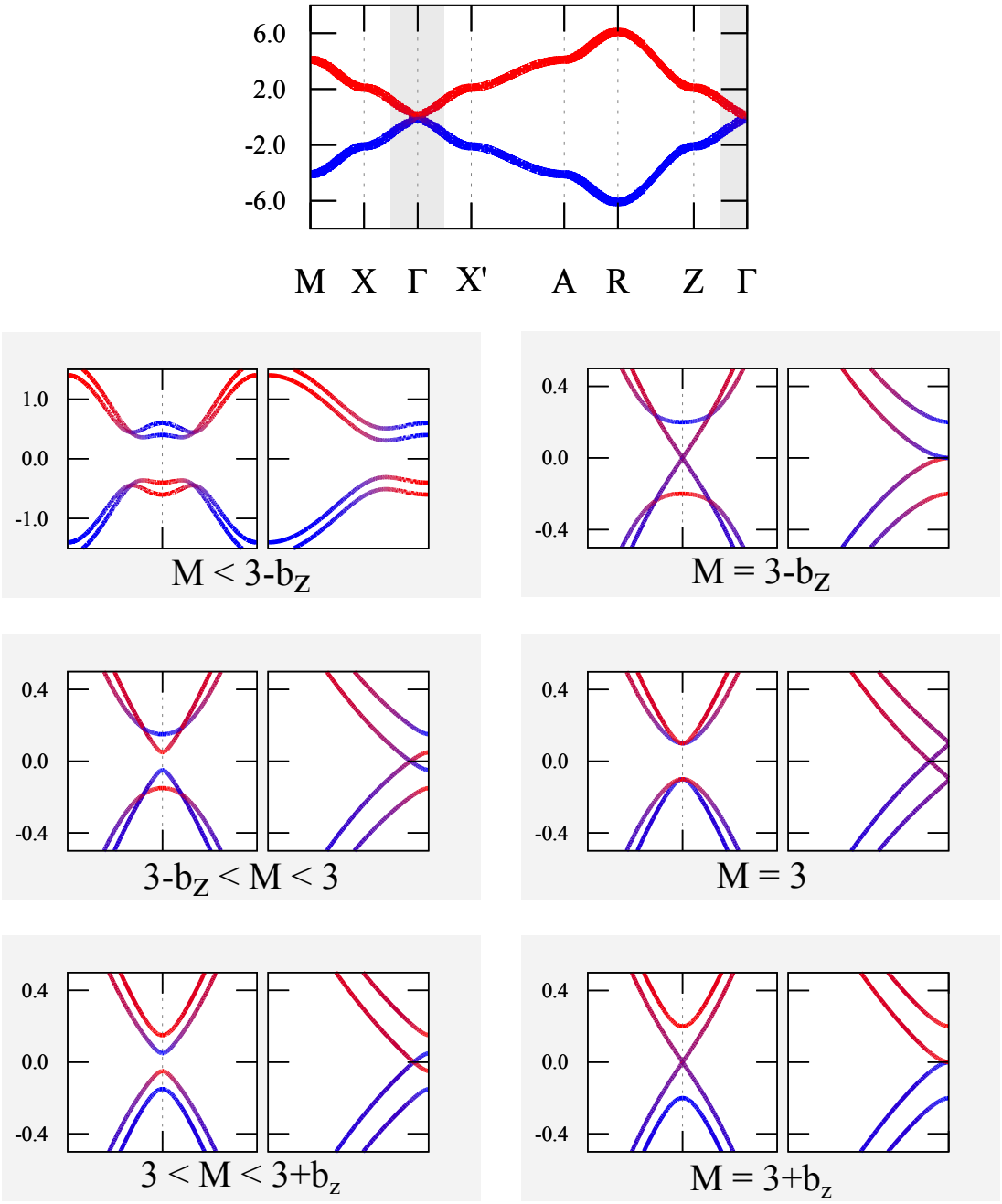

Figure 5.5: *Band structure along an high-symmetry path (cfr Fig. 5.3). The relevant parameters of the model are $\lambda = 0.5$, $b_z = 0.1$. The six couples of plot snippets correspond to the shaded regions in the top panel for different values of M. For $M < 3 - b_z$ the system is a topological insulator, for which the relevant invariant is still the one calculated for the three-dimensional BHZ by virtue of the conservation of the gap. At $M = 3 - b_z$ the gap closes at Γ, and the two Weyl points progressively detach and move symmetrically along the k_z direction, while along the other directions the system is gapped. For $M = 3$ the 4-band dispersion assumes the shape of an inverted cone: this is a consequence of the fact that at this value of M the bandgap around Γ is inverted, which means that the parity eigenvalue at the Γ point changes. The two Weyl points remain separate until $M = 3 + b_z$, where they touch again. For greater M (not shown), the system is a trivial band insulator.*

for example two electrons, as in the calculations that we show below, the interaction U drives a Mott transition towards a state with two electrons per site, while the J term favours high-spin configurations, so that the Mott insulator will be in a state with $S_z = \pm 1$.

5.3.1 Effective Topological Hamiltonian

The key parameters of the model are the interaction strength U and the energy difference between the orbitals M (as we already mentioned, all quantities are measured in terms of the kinetic term ϵ). The two parameters indeed are the control parameters for the correlation-induced physics, including the Mott transition, and for the topological transition respectively. We do not investigate in equal details the role of the precise value of the TRS-breaking field b_z or the spin-orbit coupling λ, which are however expected to have a mostly quantitative effect, as long as they are not unrealistically large.
On the other hand, the value of J, which favours high-spin configurations, has an important effect on the overall shape of the phase diagram in the U-M plane, leading to substantially different slopes of the transition lines. However, as it was already shown in the two-dimensional and three-dimensional BHZ models [154, 156], the presence or absence of J does not influence qualitatively the effect of electron interaction on the topological properties. In the following we will mainly focus on cases in which $J = 0$, considering the finite-J case when we will address the stability of our results. We will always consider the system with a density corresponding to two electrons per site, and study how the topological properties change in the whole U-M phase diagram using the formulas for interacting topological invariants derived in Chapter 2. We also monitor the effects of strong correlations, even if, as we shall see soon, in this model for $J = 0$ we do not have a Mott transition because the band insulator prevails for large values of U.
To study the different topological phases we rely on the topological Hamiltonian defined as

$$H_{top}(\mathbf{k}) = H(\mathbf{k}) + \Sigma(\omega = 0) \tag{5.20}$$

where in our case Σ is a 4×4 matrix living in the same space as $H(\mathbf{k})$. We can label the components of such matrix as $\Sigma_{\alpha\sigma,\beta\sigma'}$ in the spin-orbital indices, reflecting the way the space defined by $\Psi_{\mathbf{k}}$ is organized. An immediate simplification arises from the observation that, the system only ever being an insulator or a semimetal in the relevant region of parameters, $\mathrm{Im}\Sigma(\omega)$ vanishes for $\omega \to 0$. Thus only the real part of the Self-Energy enters in H_{top}, which remains hermitian. The Self-Energy thus enters simply as an additive normalization of the the single-particle matrix elements of the bare Hamiltonian.
A second simplification comes from the dependence on the spin and orbital indices of the Self-Energy. In all our calculations we find (see Fig. 5.7 below for some explicit results) that

- All the off-diagonal elements are zero: $\Sigma(\omega)_{\alpha\sigma,\beta\sigma'} = \delta_{\alpha\beta}\delta_{\sigma\sigma'}\Sigma_{\alpha\sigma,\alpha\sigma}(\omega)$
- All the diagonal elements have the same symmetry of the corresponding terms of the non-interacting Hamiltonian, namely

$$\Sigma_{a\sigma,a\sigma} = -\Sigma_{b\sigma,b\sigma}.$$

Therefore, all the information about the effect of the interaction on the topological properties is embodied by two numbers, the zero-frequency values of the spin-up and spin-down Self-Energy

in a given orbital. These can be used to define two effective parameters with the obvious meaning of correlation-corrected splitting and magnetic field

$$M_{\text{eff}} = M + \text{Tr}[\Gamma^5 \Sigma(0)]/4 \tag{5.21}$$

and

$$b_{\text{eff}} = b_z + \text{Tr}[\sigma_z \tau_z \Sigma(0)]/4, \tag{5.22}$$

where the Pauli matrices select the spin-symmetric and orbital antisymmetric components in the expression for M_{eff} and the spin-antisymmetric and orbital-symmetric components for b_{eff}. In other words, the topological Hamiltonian is exactly identical to the non-interacting one with interaction-renormalized parameters. M_{eff} will now control the effective energy separation between the interaction-modified orbitals, while b_{eff} corresponds to the effective lifting of the spin degeneracy in the presence of interaction

The topological invariants of the system are of immediate derivation: for the gapped phases, we will resort to the 4-dimensional ν of the unperturbed three-dimensional BHZ, which is simply (5.15) calculated with respect to the eigenvalues of the topological Hamiltonian. For the chirality of the Weyl points in the semimetallic phase, we will directly calculate the Berry flux of the occupied bands of H_{top} on a surface enclosing the gapless point in the following way [157]: once obtained the occupied eigenvalues $|u_n(\mathbf{k})\rangle$ we calculate the *overlap matrix* and the associated "discretized Berry phase"

$$S_{mn}(\mathbf{k}, \mathbf{k}') = \langle u_m(\mathbf{k}) | u_n(\mathbf{k}') \rangle \qquad \varphi(\mathbf{k}, \mathbf{k}') = \text{Im ln det } [S_{mn}](\mathbf{k}, \mathbf{k}') \tag{5.23}$$

the chirality will then be obtained, by Stokes' theorem, from

$$\oint \mathrm{d}\varphi \approx \text{Im ln} \prod_{s=0}^{N-1} \det [S_{mn}](\mathbf{k}, \mathbf{k}') \tag{5.24}$$

for a discretize N-step path running along the edges of a surface around the node. With these tools, we can properly construct the topological phase diagram of the system.

5.3.2 Topological characterization: phase diagram

We will consider the phase diagram of the system in the $U - M$ plane, with fixed $\epsilon = 1$, $\lambda = 0.5$ and $b_z = 0.1$. In Fig. 5.6 we present the topological phase diagram obtained in a static mean-field (left) and with the more accurate DMFT, which includes local quantum fluctuations beyond mean-field.

In general terms, a static mean-field is obtained by decoupling the two-particle operators in the interaction term H_{int} in terms of single-particle operators (where $\alpha - \delta$ denote generic labels for the fermions, which in our case are site, spin and orbital)

$$U_{\alpha\beta\gamma\delta} c^\dagger_\alpha c^\dagger_\beta c_\gamma c_\delta \to U_{\alpha\beta\gamma\delta} \Delta_{\gamma\delta} c^\dagger_\alpha c^\dagger_\beta \tag{5.25}$$

with the parameters $\Delta_{\gamma\delta} := \langle \Phi_{HF} | c^\dagger_\gamma c_\delta | \Phi_{HF} \rangle$ variationally determined by the condition

$$\frac{\delta}{\delta \Delta_{\mu\nu}} \left(E[\Delta] - \frac{1}{2} \sum_{\alpha\beta\gamma\delta} \Delta_{\alpha\beta} \Delta_{\gamma\delta} \big(U_{\alpha\gamma\delta\beta} - U_{\alpha\gamma\beta\delta} \big) \right) = 0 \tag{5.26}$$

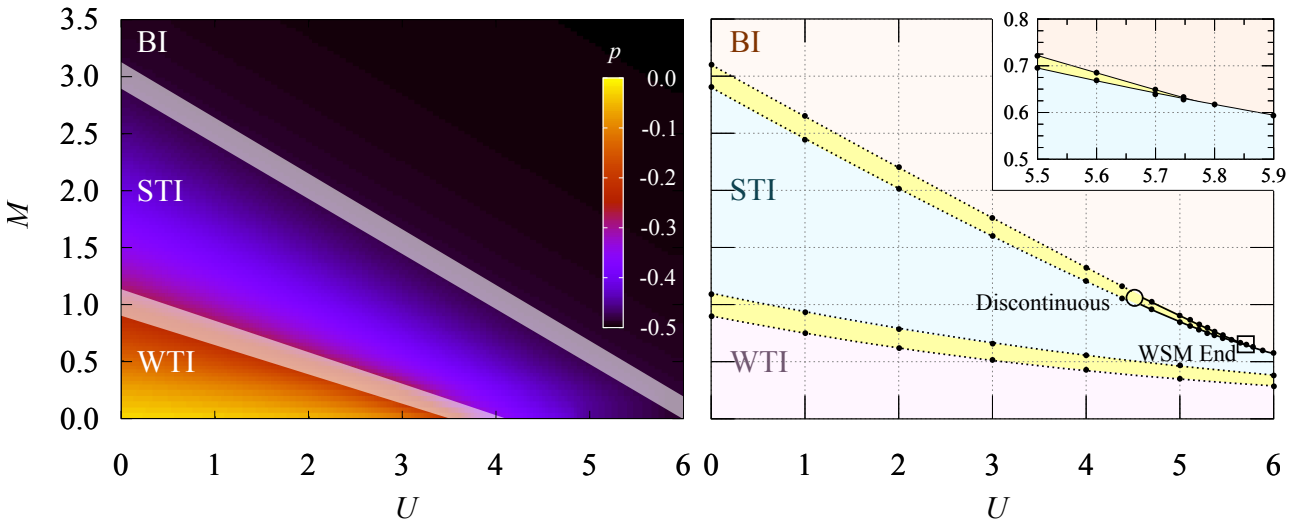

Figure 5.6: *Phase diagrams of the interacting system in (left) a mean-field framework and (right) according to DMFT. The three phases are distinguished by the value of the three-dimensional topological invariant: increasing M the system passes from a weak topological insulator with $\nu = (0;111)$ to a strong one with $\nu = (1;000)$ to a trivial band insulator with $\nu = (0;000)$. The left plot highlights the width of the semimetallic regions (found by directly searching for nonzero chirality points), the width of which barely changes with U. The heatmap shows the difference in orbital polarization, which varies smoothly with M and U, signalling a continuous phase transition. On the DMFT side, data have been collected along vertical lines for fixed U. The black dots represent the transition points between the regions for each set of data; the inset shows the closing of the semimetallic region at high values of U. The WSM phase transition is discontinuous over a critical value of $U \approx 4.5$. DMFT phase diagram originally from* [144].

where $E[\Delta]$ is the ground-state energy of the effective single-particle model obtained replacing the interaction with the mean-field terms according to (5.25).
In our case we consider only the density terms $\Delta_{i,a,\sigma i,a,\sigma} := \langle \Phi_{HF} | c^\dagger_{i,a,\sigma} c_{i,a,\sigma} | \Phi_{HF} \rangle = n_{i,a,\sigma}$. We also assume a uniform solution $n_{i,a,\sigma} \equiv n_{a\sigma}$, which leaves us with just four parameters. If we fix the density to half-filling, we are left with three parameters, the orbital polarization $p = 1/4(\sum_\sigma n_{a\sigma} - n_{b\sigma})$ and the magnetizations of the two orbitals $m_\alpha = 1/2(n_{\alpha\uparrow} - n_{\alpha\downarrow})$ and express the densities as

$$\begin{aligned} n_{a\uparrow} &= \frac{1}{2} + m_a + p \qquad & n_{b\uparrow} &= \frac{1}{2} + m_b - p \\ n_{a\downarrow} &= \frac{1}{2} - m_a + p \qquad & n_{b\downarrow} &= \frac{1}{2} - m_b - p \end{aligned} \tag{5.27}$$

Then the energy is minimized with respect to the three remaining parameters, obtaining the final solution in the mean-field approximation, which is by definition a Slater determinant, hence a many-body state composed by single particle states. It is straightforward to compute the topological invariants from the groundstate of the single-particle Hamiltonian.
In Fig. 5.6 we report the results, where we superimpose the transition lines separating the different insulators (BI, STI, WTI) and the WSM regions to a colour plot of the orbital polarization p, which measures the relative population of the two orbitals.

For $U = 0$ we naturally recover the non-interacting phase diagram, which reproduces the sequence of phases of the three-dimensional BHZ model, namely a WTI for small M followed by an STI and finally by the topologically trivial band insulator. Because of the b_z term the transition lines widen into semimetallic regions on width $2b_z$ centred around $M = 1$ and $M = 3$. The gap closes continuously as the system enters the semimetallic phase, and the positions of the Weyl points evolve continuously as before, annihilating at the phase boundaries.
When we introduce and increase U we clearly see that all the transition points decrease monotonically with U so that the topological insulators regions shrink, while the trivial solution invades most of the diagram. The regions of WSM retain their width of $2b_z$ at every value of U. This behavior can be easily understood because for $J = 0$ the Hubbard term wants to localize two electrons per site and, as far as the interaction is concerned, all the configurations with two electrons per site have the same energy. This means that it is always favourable to put two electrons in the lowest-lying level, which implies favouring the band insulator with a completely filled lower band. For finite and sizeable J the situation changes, because the local configurations with $S_z = \pm 1$ are favoured. This occupation contrasts the band insulator, which is unfavoured, and leads to a Mott transition to a high-spin Mott insulator when U is sufficiently large.
Irrespective of the value of J, since the Hartree-Fock approximation produces an effective single-particle system, the behavior of the Weyl points at the transition (not shown) remains exactly the same as in the non-interacting case, with a continuous annihilation at the transition points.
As mentioned above, the heatmap seen in the plot shows the value of the orbital polarization p in each point of the phase diagram. It is apparent that the behavior of this quantity correlates with the topological transitions. On the other hand $m_{a/b}$ are quite small and their behavior is not particularly important to shape up the phase diagram. As a matter of fact, the main effect of the interaction within the mean-field approximation is to change the polarization which increases in magnitude as the interaction grows, signalling that interactions favour the population imbalance between the orbitals and consequently leads to a wider region of band insulating behavior.
In the topological phase, the value of p is small: This implies that the occupied bands have mixed orbital characters, and therefore there is gap inversion. Moreover, the value of p is smaller in the weak topological insulator, where the gap inversion happens at three high-symmetry points, than in the strong topological insulator, where the gap inversion happens around Γ alone. In the trivial insulator, instead, p assumes the maximum value -0.5: one orbital is completely full, the other completely empty as it follows from the definition of a band insulator.

Let us now compare these observations with the DMFT results, which are summarized in the phase diagram in the right panel of Fig. 5.6. We first comment on the phase diagram and compare it with the mean-field version, postponing to the next sections a more in-depth analysis of the DMFT data which will highlight important differences with respect to mean-field. Once again, the topological regions are identified based on the values of the topological invariants defined above.
While the overall shape of the phase diagram appears similar, we have some important differences. Also in DMFT all the transition lines decrease with U even if all the evolutions are less sharp than in Hartree Fock. As a result, the WTI remains stable for a much larger window of U, which indeed does not appear to close in the range of interactions we considered, and the band insulator, while still strongly favoured by the interaction, extends to a smaller region with

respect to the static mean-field picture. Coming to the most important part of the diagram, we see that, while the WSM region between the WTI and the STI retains the same width for every value of U, the upper WSM region originating between the STI and the band insulator progressively shrinks as U grows and it appears to close at a critical interaction strength, as it can be better appreciated in the inset which magnifies this region. This behavior, which is clearly due to the dynamical correlations featured in DMFT but not in Hartree-Fock, will be investigated in details in the following sections.

5.3.3 Dynamical Nature of the DMFT results: Spectral functions and Self-Energies

Before discussing the nature of the topological phase transition, we enter in more details in the dynamical observables which are accessible with DMFT. We focus on two quantities: (i) the imaginary part of the Green's function computed on the real-frequency axis, which is proportional to the interacting density of states and (ii) the real-part of the Self-Energy in imaginary frequency. The former gives us direct information about the spectrum of the interacting system, so it enables us to support the information about the different topological phases, while the second, as discussed above, is instrumental to compute the effective parameters M_{eff} and b_{eff}. Some representative results for $U = 5.2$ and three values of M (0.65, 0.8, 0.9) which span the three different phases QSHI, WSM and BI, are reported in Fig. 5.7. The two orbitals are differentiated by colour, while the two spin components correspond to solid and dashed lines.
As discussed above, the real part of the Self-Energy affects the single-particle excitations and renormalizes M into M_{eff}. Comparing the right and left columns, we clearly see that $\mathrm{Re}\Sigma$ has positive sign for the unoccupied orbitals and negative sign for the occupied ones, this implies that the crystal-field splitting is enhanced by interaction, i.e. $M_{eff} > M$. The behavior of the spectral function reflects the information we obtained from the topological invariants. In the noninteracting system, the topology was associated with an inverted gap around Γ: in the first panel, we can see how the spectral weight associated to each orbital is mainly concentrated above or below the Fermi level, as a consequence of the symmetry dictated by M. However, there is also a distinct narrow peak of opposite orbital character across the Fermi energy, which is the signature of the band inversion qualifying the topological insulator.
For higher values of M (third panel), the spectral weight is instead completely above or below E_F for the two orbitals and we obtain a trivial band insulator. The middle panel shows how the Weyl semimetal phase reflects in the local density of states. The spectral weight is finite for every value of ω except 0, namely the system is gapless only in a discrete subset of k-points. We finally notice that, in the three examples, but also in any other point of the phase diagram, the self-energies never change sign as a function of frequency and they always show a similar behavior. The absolute value is minimum at zero frequency (which is the value which determines the topological Hamiltonian) and it increases gently as the frequency grows, where we recover a kind of static mean-field behavior. As we discuss in the following section, the degree of correlation of the system can be connected with the difference between the zero and large-frequency limits.

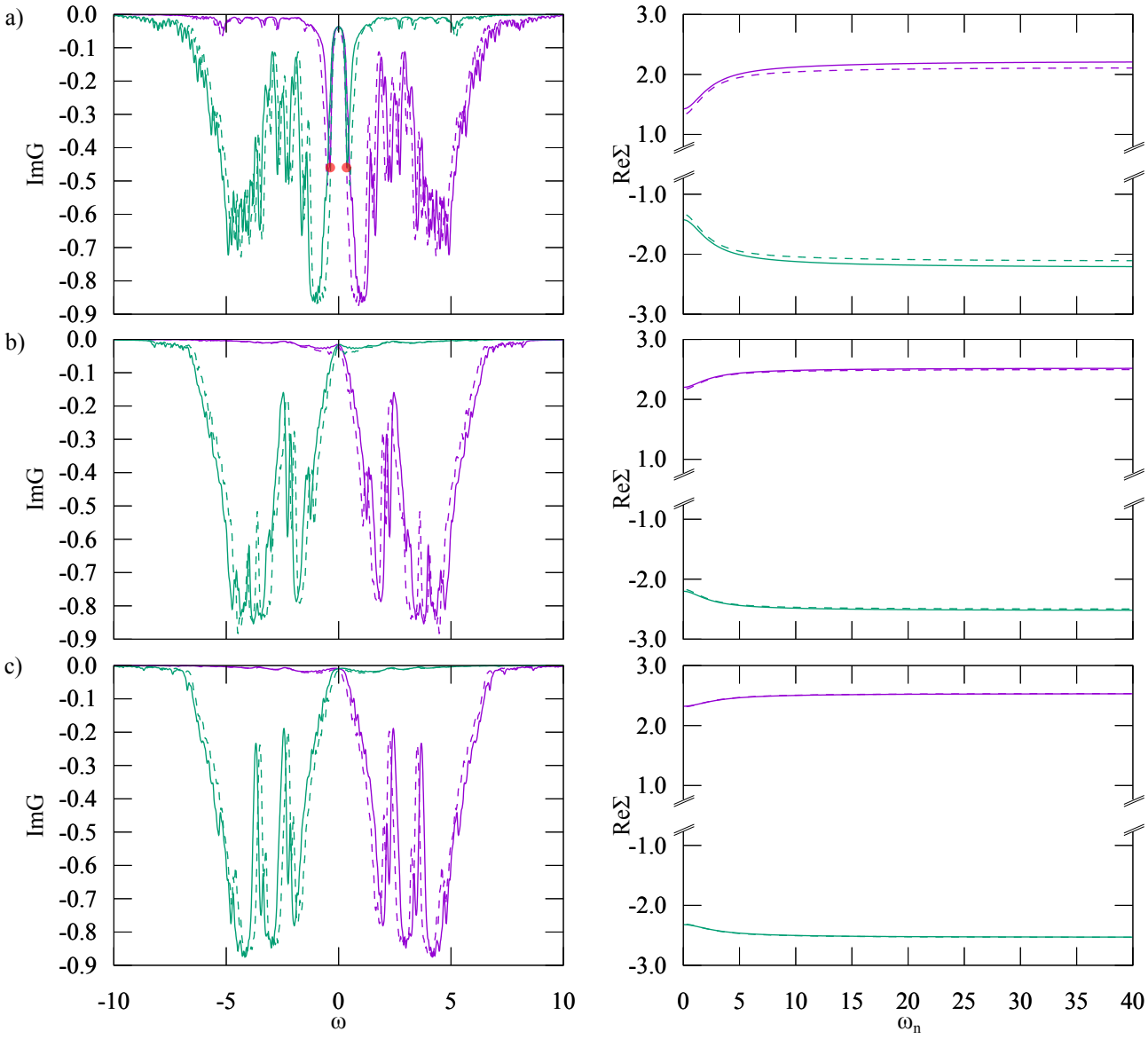

Figure 5.7: *Imaginary part of the local Green's function along the real frequency axis (left) and Real part of the Self-Energy along the Matsubara axis(right) for U=5.2 and different values of M (0.65, 0.8, 0.9 respectively). The colors represent the orbitals, the dotted and full lines show the lifting of the spin-degeneracy due to* b_z. a) *STI phase: the dynamical dependence of the Self-Energy is high, since the gap is small and inverted, as it can be seen from the spectral weight of each orbital across the Fermi energy (red dots). The absence of gap in 0 is purely a numerical effect due to broadening, and the imaginary part of the Self-Energy vanishes for* $\omega \to 0$ *as expected for an insulator.* b) *Inside the WSM phase: the gap vanishes only at* $\omega = 0$, *the frequency dependence of* Σ *is less pronounced.* c) *Band insulator: the large bandgap due to M makes dynamical effects less relevant, one band is completely full and one completely empty.*

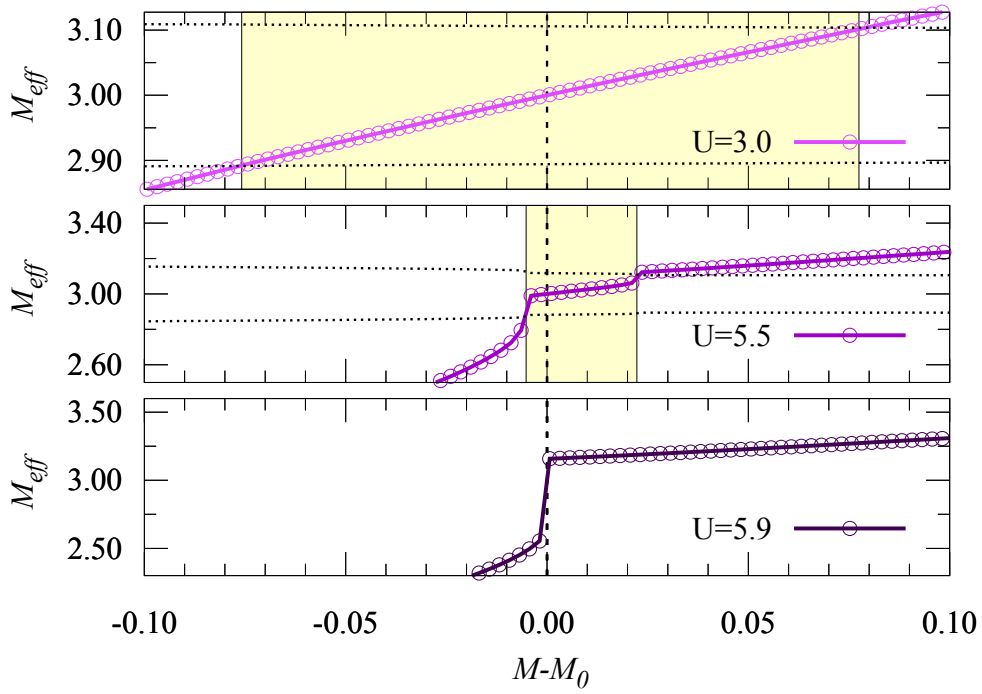

Figure 5.8: *Behaviour of M_{eff} (coloured lines) and b_{eff} (half of the width of the region enclosed in the dotted lines) for different values of U as a function of the bare M. The plots are centred at the value M_0 for which $M_{eff} = 3$. Picture originally from* [144].

5.3.4 Discontinuous Topological Phase Transition and Annihilation of Weyl points

We now turn to the most intriguing region identified in the DMFT phase diagram, namely the final branch of the upper semimetallic region for intermediate-to-high values of U ($\gtrsim 4.5$). In order to characterize the transition in this region, we discuss the behavior of the two effective parameters M_{eff} and b_{eff} which is reported in Fig. 5.8. First we observe that the effective parameters are properly defined, in the sense that the Weyl semimetallic region is always located around $M_{eff} = 3$ and its width is given by $2b_{eff}$, in total correspondence with the non-interacting results. Therefore in Fig. 5.8 we plot the evolution of M_{eff} as a function of $M_{eff} - M_0$, where M_0 is the point around which the WSM region is located (i.e., where $M_{eff} = 3$). We then plot with two dotted lines the "expected" extent of the Weyl semimetallic region on the effective parameter axis, (for values of U where it is present), namely $[3 - b_{eff}, 3 - b_{eff}]$. This width is compared with the yellow shaded region, representing the range of M for which nonzero chirality Weyl points were found by means of (5.24). Indeed, the shaded region and the dotted lines intercept the $M_{eff}(M)$ curve at the same points, supporting our identification of b_z as relating to the renormalized width of the WSM phase.
It is evident that the behaviour of the curves M_{eff} undergoes a qualitative change with the increase of interaction: for low values of U (top panel), the behaviour is an "adiabatic" continuation of the noninteracting one, though we observe a clear correlation-induced shrinking of the WSM region, which would span the whole range [-0.1;0.1] in the noninteracting limit.
For the intermediate value of $U = 5.5$, the evolution of the observables as a function of M becomes discontinuous. As long as the WSM region is present, the band-inversion value $M_{eff} = 3$

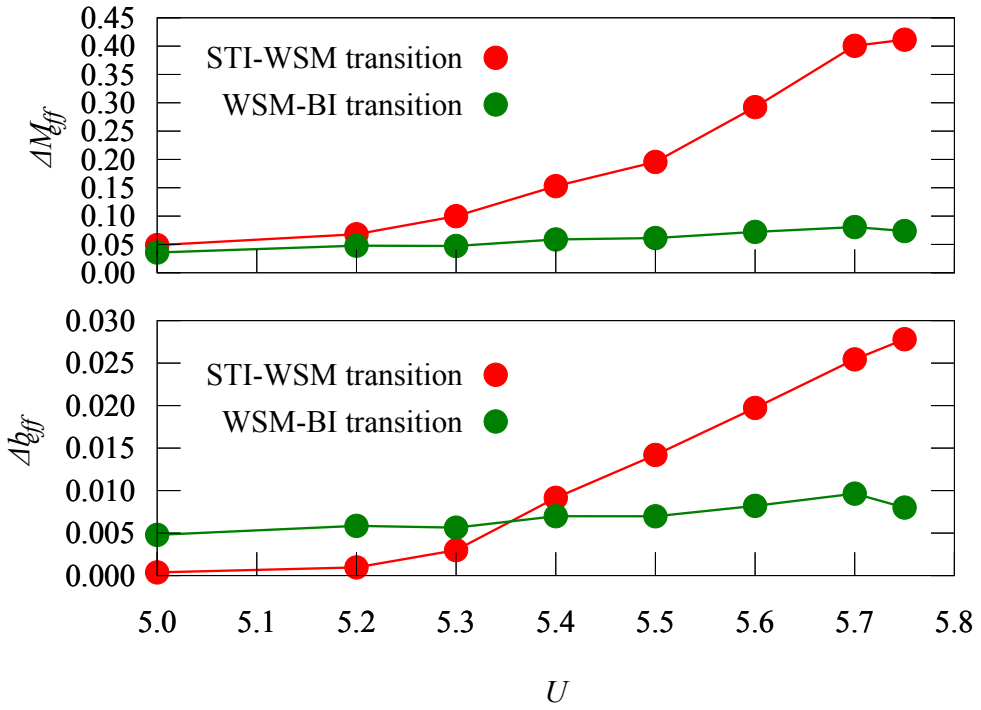

Figure 5.9: *Height of jump in the effective parameters M_{eff} (first panel) and b_{eff} (second panel) as a function of U. The first jump, from STI to WSM, is always bigger than the second with a notable exception: for lower values of U, the second jump in b_{eff} is bigger. This can be tentatively attributed to the fact that both the STI and WSM phases, with partially inverted gap, are more similarly affected by the lifting of the spin degeneracy than the BI. For higher values of U, however, the frequency dependence of Σ is so strong that it overrides this effect.*

falls inside its boundaries.
Therefore, we clearly find a surprising and new result, namely that the transitions connecting the Weyl semimetal to the neighbouring phases are both discontinuous in a sizeable window of parameters, in sharp contrast with the result we discussed for the non-interacting system. As we shall see in the following, a discontinuous disappearance of a Weyl semimetal implies that the two Weyl points on the k_z direction around Γ abruptly appear at distinct value of crystal momentum. They evolve continuously inside the semimetallic phase but never touch, and the gap opens discontinuously at the two ends of the WSM region.
Finally, after a second U threshold around $U = 5.8$ (see the third panel), the Weyl semimetal region closes, and the M_{eff} curve experiences a single jump which marks the topological transition from the STI to the BI, skipping the gap-closing value $M_{eff} = 3$. We have therefore a discontinuous topological phase transition, consistently with what was observed for the two-dimensional [156] and three-dimensional [154] BHZ model without TRS-breaking perturbations.
Before discussing the behavior of the Weyl points, we briefly comment on the amplitude of the jumps at the two boundaries of the WSM region and their dependence on U. The results are shown in Fig. 5.9, which shows both the jump of M_{eff} and that of b_{eff}. Interestingly the two jumps of M_{eff} are very similar for the smallest values of U where the transition is discontinuous, but then the jump at the transition between STI and WSM becomes significantly larger than the one at the WSM-BI transition, leading to a distinctively asymmetric behavior.

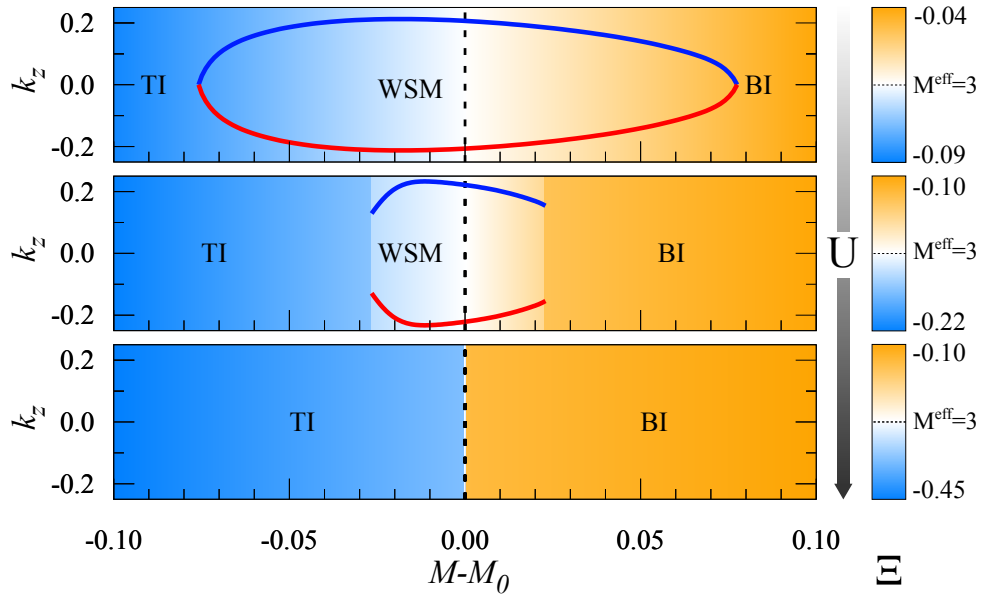

Figure 5.10: *Position of Weyl nodes along k_z (for $k_x = k_y = 0$) as a function of $M - M_0$ for increasing values of U and $b_z = 0.1$. The background colors in the main panels reflect the behavior of the correlation strength Ξ as defined in (5.28). Picture originally from [144].*

In Fig. 5.10 we finally come to the evolution of the position of the Weyl points as a function of M. We plot the value of the k_z coordinates of the gap-closing points for the topological Hamiltonian for the same three values of interaction as in figure Fig. 5.8. Here we find an explicit confirmation of the above speculation about the fate of the Weyl points in the presence of a discontinuous transition.
For small U we recover the standard result of non-interacting systems, with the Weyl points moving as a function of M and merging at the transition points where the Weyl cones leave the stage to the two gapped phases. For intermediate U we find instead that the Weyl point still move as M changes, but they do not coalesce at the transition point, instead disappearing when they are at a given distance in momentum space. Obviously no Weyl points are present for larger U, when the system undergoes a direct discontinuous transition between the STI and the BI.

5.3.5 Degree of Correlation and Discontinuous Transition

In Fig. 5.10 we also connect the nature of the transition to the WSM region with an estimator of the degree of correlation of the system, which is directly related to the ideas we discussed so far. We have repeatedly underlined that the effect of the correlations, as far as the topological phase transition is concerned, is embodied by the zero-frequency limit of the real part of the Self-Energy. We also know, and we verified explicitly, that a Hartree-Fock calculation, which neglects the dynamical character of the interaction effects, cannot describe a discontinuous topological phase transition. Thus we expect that our results stem directly from the dynamical nature of the Self-Energy or, in other words, from the dependence on frequency of this quantity. As we have seen already in the plots of Fig. 5.7, the typical behavior of the Self-Energy is quite smooth on the Matsubara axis. It starts from a zero-frequency value and then gently evolves

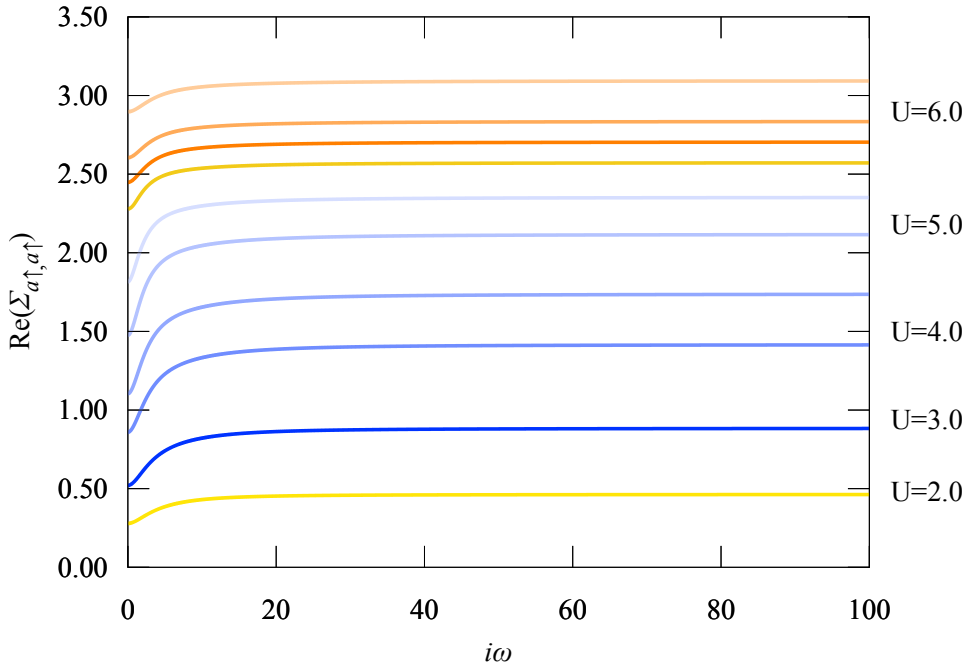

Figure 5.11: *Self-Energy behaviour on the Matsubara axis for $M = 0.75$ and different values of U. Only one component is plotted, the others being either related by symmetry or slightly perturbed due to the TRS-breaking term. Picture originally from* [144].

to a nearly constant high-frequency behavior. Therefore we can define an estimator for the correlation strength

$$\Xi = \frac{\mathrm{Tr}\left[\Gamma^5\Sigma(0) - \Gamma^5\Sigma(i\omega_n \to \infty)\right]}{\mathrm{Tr}\left[\Gamma^5\Sigma(0)\right]}, \tag{5.28}$$

which is simply the symmetrized difference between the zero-frequency and high-frequency real part of the Self-Energy. Since for $\omega \to \infty$ the Self-Energy is essentially flat, this limit can be regarded as a static Mean-Field "Hartree-Fock-like" limit.
For small values of U the DMFT Self-Energy is relatively small and frequency-independent, so the results are not different from a Hartree-Fock approximation, and we recover also a continuous phase transition. On the other hand, when U grows, we expect an increase of the dynamical effects measured by Ξ. Moreover, it is natural to expect that the STI will have a larger Ξ then the BI because the latter phase is an essentially non-interacting state, while the former can host important interaction effects despite being gapped. These different correlation effects on two sides of the transition conspire to make it discontinuous.

We superimpose a color plot of Ξ to the data showing the evolution of the positions of the Weyl points in Fig. 5.10. The plot shows that for the weakly correlated system the degree of correlation is weak and it smoothly evolves as a function of M while the Weyl point evolve continuously and merge. In the intermediate panel, where we observe the discontinuous disappearance of the Weyl points, we find that the STI becomes more correlated and that the transition occurs through two discontinuous jumps also of Ξ, which in turn evolves continuously within the WSM region. Finally, in the large-U regime, we find a sudden jump in the degree of correlation at a first-order topological phase transition.

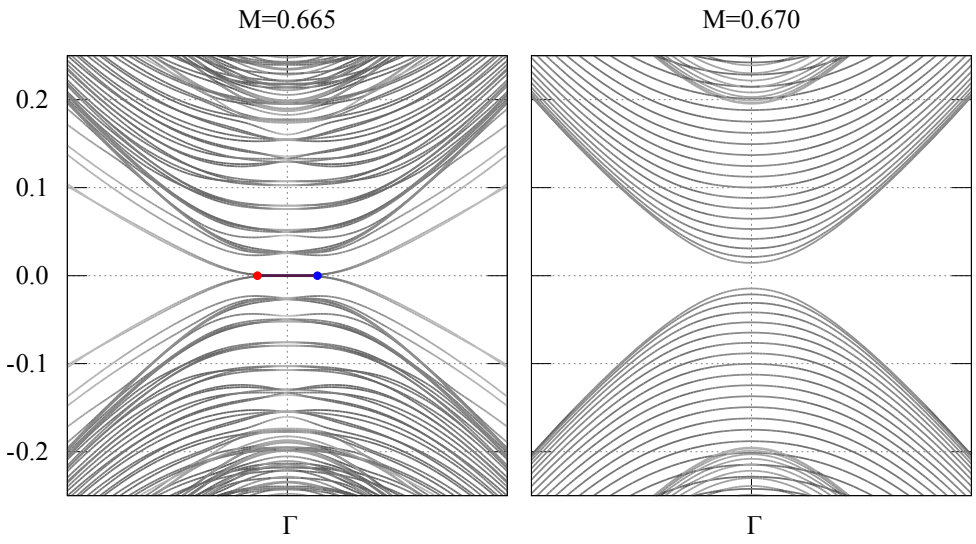

Figure 5.12: *Electronic structure of a slab geometry near the* Γ *point at* $U = 5.6$. *The two panels report the behavior for two different values of the mass term* M *across the WSM to BI transition. Left panel: the points (red and blue) indicate the Weyl nodes with opposite chirality. The band segment connecting them is the Fermi arc. Picture originally from* [144].

We end the analysis of the degree of correlation by showing some of the self-energies in Fig. 5.11. This shows the form of the real part of a diagonal element of the Self-Energy matrix (the others being related by symmetry or slightly perturbed as in Fig. 5.7) for a fixed M and increasing U. M is chosen so as to intercept, on an horizontal line in the phase diagram, almost every phase in it exhibited, except for the WTI which however does not show peculiar properties.
The diagram can be read in two ways: if we group the results by phase, we immediately notice how the STI curves (depicted in blue) have generally a more pronounced value of Ξ than the WSM (yellow) and the BI (orange). This intuitively explains why the semimetallic region in Fig. 5.8 shrinks more thoroughly approaching $M_{eff} = 3$ from the STI side. It also explains why the jumps from STI to WSM (red curves in Fig. 5.9) are higher than the ones from WSM to BI: the Self-Energy has a rather similar behaviour in the BI and the WSM, while the STI has a decisively more pronounced frequency dependence.
We can also read Fig. 5.11 focusing on the behaviour of $\Sigma(\omega)$ within the same region: the upper WSM is more correlated than the lower, which is a possible explanation for the absence of peculiar behaviour around the WTI-STI transition. Inside the STI, higher U means higher correlation, that is consistent with the insurgence of the discontinuous transition in Fig. 5.8. In the BI, instead, there is no strong increase of Ξ with U: the system has a fully occupied orbital and an empty one separated by a gap, and is therefore not reactive to correlation effects.

We finally discuss the effect of the discontinuous nature of the transition on the surface states. In the presence of Weyl semimetals, this is equivalent to a question about the effect of interactions on the Fermi arcs. In order to attack this problem, it it necessary to consider a system which actually has edges. This is unfortunately impossible to treat with standard DMFT, which assumes translation invariance. Therefore we resort to real-space DMFT, an

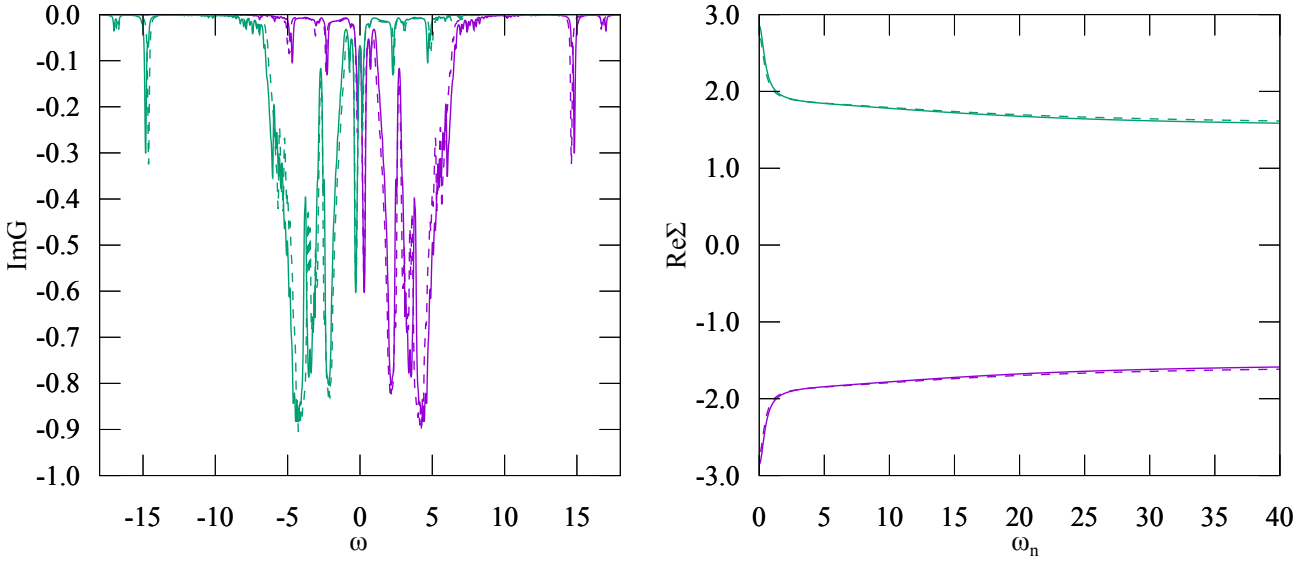

Figure 5.13: *Imaginary part of the local Green's function along the real frequency axis and real part of the Self-Energy along the Matsubara axis for* $U = 13.5$*,* $M = 5.22$ *and* $J = 0.25U$

extension of DMFT which allows to treat a finite number of inequivalent sites. In particular, we consider a layer version, where the three-dimensional system is decomposed into a number of two dimensional layers. Within each layer we enforce translational symmetry, while the different layers are inequivalent. From a technical point of view, an independent impurity model is introduced for every layers, and the layers are coupled by the self-consistency conditions. The resulting Self-Energy function Σ is site-independent within each layer while it is still local but layer dependent in the open direction, i.e. $\Sigma_{ij} = \Sigma_i \delta_{ij}$ where i is layer index.
In the noninteracting picture, approaching the topological transition is associated to the progressive shortening of the Fermi arcs until the two ends touch and the system gaps out to an insulating phase. In presence of interaction we expect the non-local annihilation of the Weyl points to provoke the sudden disappearance of a finite Fermi arc, since its very existence stems from the nonzero Berry flux of which Weyl nodes in the bulk. To show the effects of electronic interaction to the boundary states, we show in Fig. 5.12 the spectrum of the model for our layered system. Our results illustrate the sudden (dis)appearance of the Fermi arcs across the transition for a large value of the interaction U, reflecting the first-order character of the transition observed in the bulk system.

5.3.6 Robustness of the results with respect to model parameters

In this section we briefly discuss the effect of a finite value of the Hund's coupling J. We remind that we only consider the density-density interaction. We do not present a complete phase diagram for different values of J, but we provide some crucial information which has already been discussed in previous papers on the BHZ model.
In Fig. 5.13 we report again the imaginary part of the Green's function on the real frequency axis and the real part of the Self-Energy on the Matsubara axis for a relatively large ratio $J/U = 0.25$. If we compare with Fig. 5.7, an important difference strikes the eye, namely the Self-Energy changes sign with respect to $J = 0$. This is a completely general result that affects the overall shape of the phase diagram.

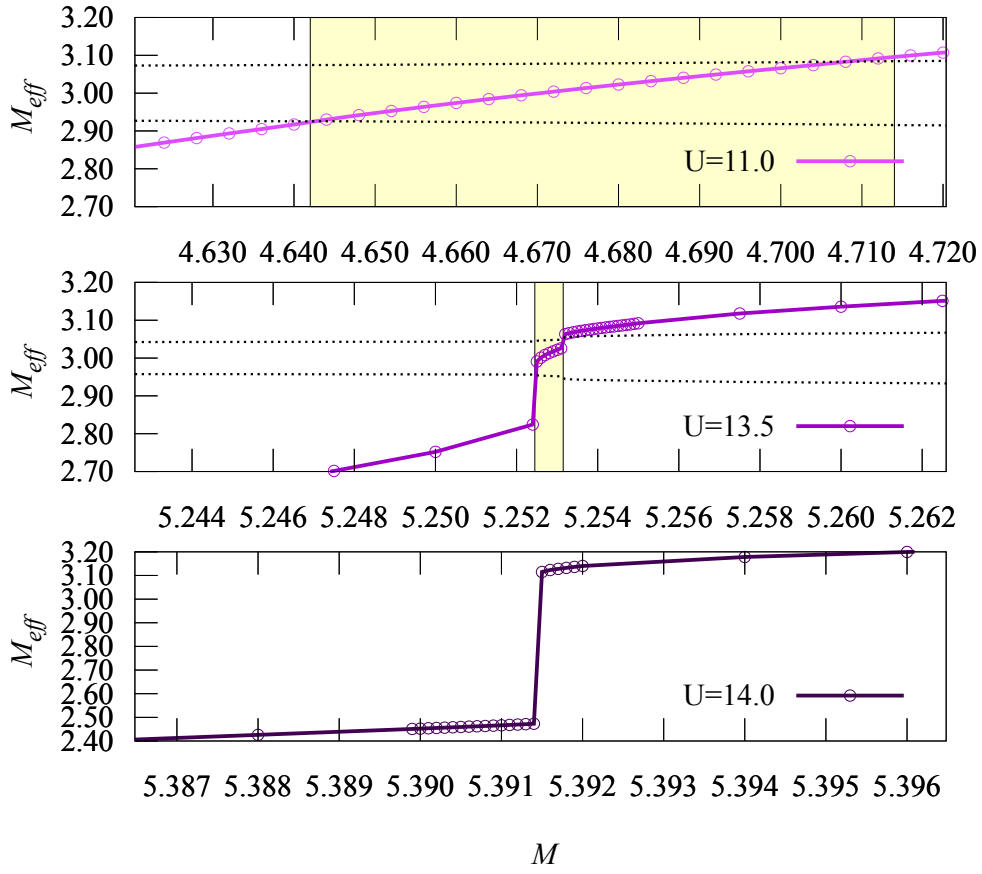

Figure 5.14: *Effective mass and splitting for $J = 0.25U$. Picture originally from* [144].

This means that, in this setup, the effect of Σ actually competes with M, leading to $M_{eff} < M$. This implies that the band insulator is disfavoured by increasing U and phases with small polarization like the STI are favoured. Therefore, the position in M of the transition points will increase with U in sharp contrast with $J = 0$.
However, as shown in Fig. 5.14, we still find the qualitative behavior that we discussed for $J = 0$, namely increasing U we move from the standard continuous transitions delimiting the WSM region to an intermediate interaction regime where the two boundaries of the WSM are characterized by a discontinuous transition and finally we observe a disappearance of the WSM and we are left with a first-order topological transition between STI and BI. The only main difference with respect to the $J = 0$ case is that the whole region is shifted to substantially larger values of U, but the main message remains unaffected. As we mentioned above, for finite J/U the phase diagram is different also because a Mott insulating solution is found for sufficiently large U [154, 156, 158]. This is not immediately relevant for the physics of the topological WSM phase transition, but shows a peculiar behaviour if studied under a cluster approach, and is therefore more directly investigated in Chapter 6.
In Fig. 5.15 we discuss another parametrization, where we only consider two parameters U and U' and take $J = 0$. The case $U = U'$ coincides with the model we studied in most of this chapter, for which, as discussed at length, the Self-Energy increases the effective M pushing the bands further apart.
The more we decrease U', the more we favor local configurations where the two orbitals are occupied with respect to those where one orbital is doubly occupied. This implies that the

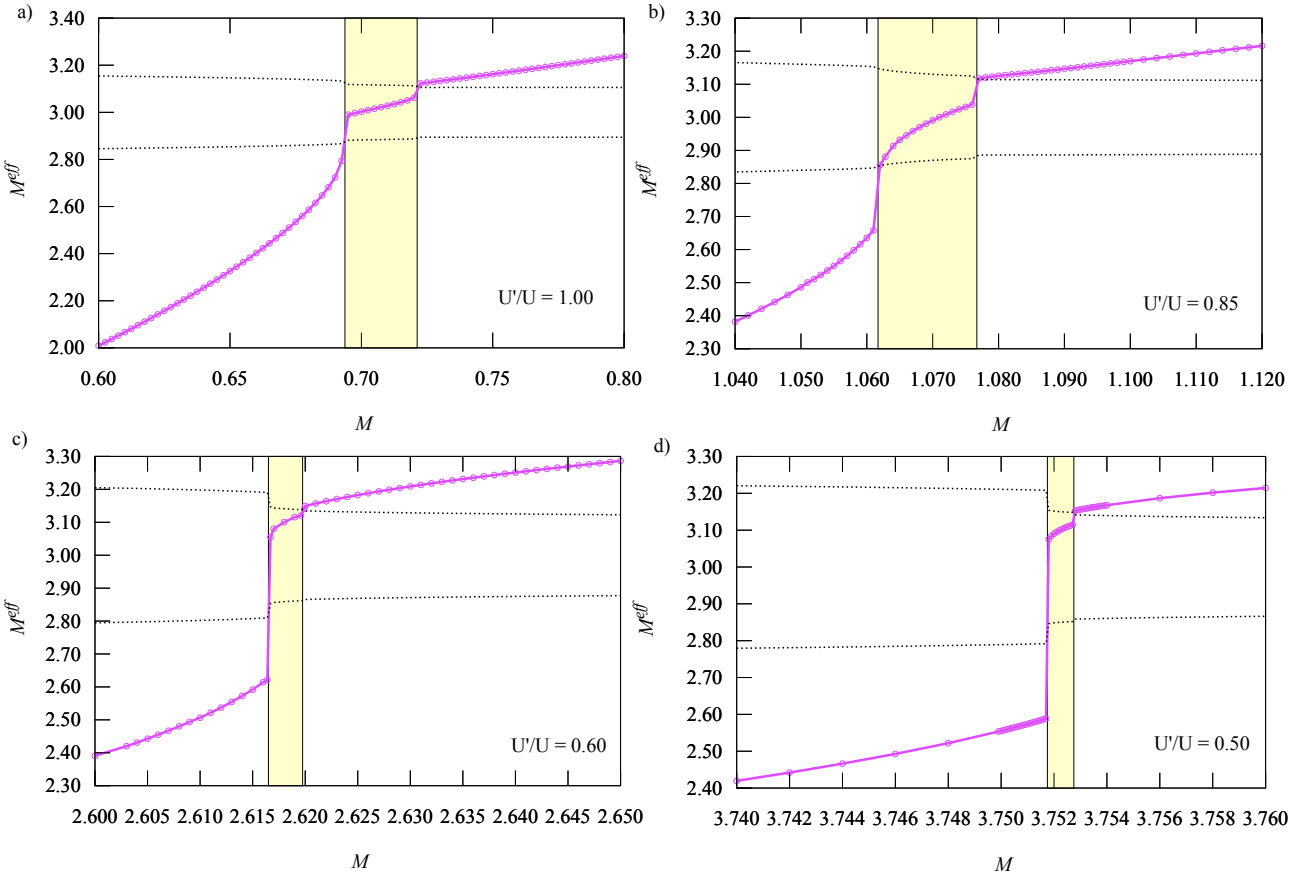

Figure 5.15: *Behaviour of M_{eff} and b_{eff} for $J = 0$ and different ratios U'/U. Picture originally from* [144].

topological insulator is favoured. In particular the WTI, with gap inversion at three k-points, will be preferred to the STI, which in turn will be stable with respect to the BI. Accordingly, as we decrease the U'/U ratio $M_{eff}/(M)$ is reduced, and the WSM region shrinks heavily from the STI side, because the gapped partially-polarized insulator becomes more and more energetically convenient with respect to the semimetal, that has more spectral weight around E_F, and to the orbitally doubly-occupied band insulator.

We finally briefly discuss the stability of the topological transition with respect to finite-temperature study. Even if from a purely theoretical perspective topological properties are defined only at zero temperature, in light of applications to materials, it is important to establish whether the fingerprints we observe can survive to experimentally accessible temperatures.
The exact diagonalization solver for DMFT can be easily extended to finite temperature. In particular, if we use a full diagonalization of the matrix, the full spectrum is available and it is is straightforward to compute exactly finite-temperature properties including the Green's function which is crucial for a DMFT calculation. Using a Lanczos-Arnoldi scheme, one can instead obtain a sufficient number of excited states to obtain an accurate low-temperature Green's function as discussed in [159]. In Fig. 5.16 we show ED data for the system for $U = 5.5$ and $J = 0$ configuration. The results show that the jump is washed out by a finite temperature of around $T = 1/20$ in hopping units. Assuming an hopping of around $200meV$, a number which

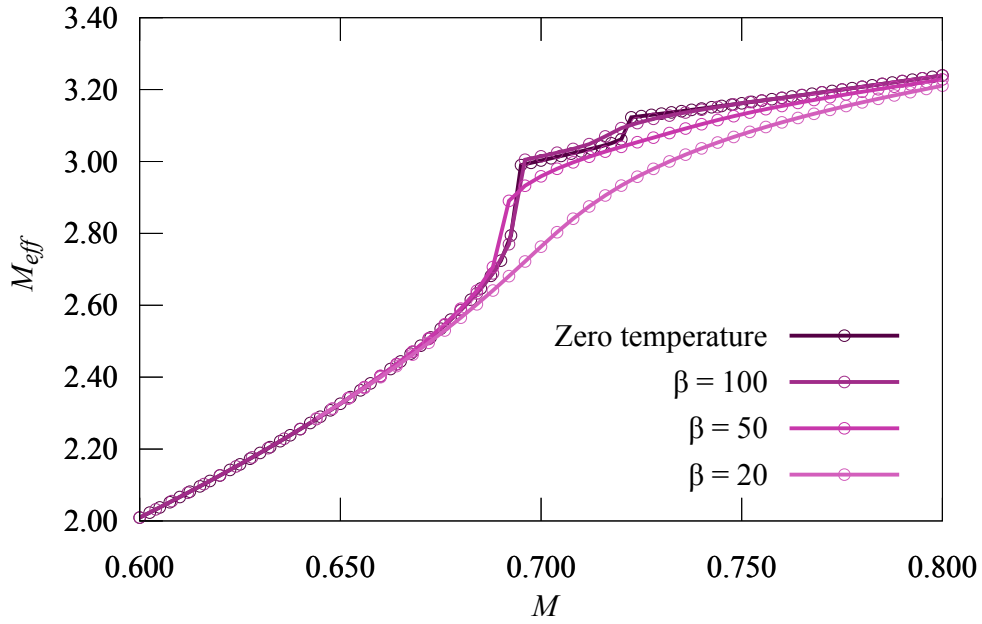

Figure 5.16: *Behaviour of M_{eff} and b_{eff} for $U = 5.5$, $J = 0$ and different temperatures. Picture adapted from* [144].

is reasonable for strongly correlated oxides, this would correspond to a temperature around $100K$. This leaves us with a sizeable -and potentially accessible in experiments- temperature window where this phenomenon may be revealed.

5.3.7 First-order topological transitions, second-order endpoints and critical phenomena

Up to now, we have referred to the topological phase transition above $U \approx 4.5$ as *discontinuous*. In this section we touch upon the "temptation" to treat it as a *first-order* phase transition in the Landau sense. This idea stems from the discontinuous behaviour of the first derivative of the Free energy across the phase transition. We will treat explicitly the behaviour of this quantity in the next chapter, where we will compare single-site and cluster results for a simpler two-dimensional BHZ model. Here, we just provide some suggestion that point towards a more conventional description of interaction-driven topological phase transitions.
In the above discussion we have introduced the concept of orbital polarization, which in the context of Hartree-Fock was related to the variational parameter p. We also remarked how this is a key observable whose evolution parallels the topological phase transition. Times a factor, we can relate this quantity to the operator $\hat{T}_i^z = \sum_\sigma \hat{n}_{ia\sigma} - \hat{n}_{ib\sigma}$, that we can evaluate locally on the converged DMFT ground state, obtaining the expected value T^z. We can then define the related *orbital compressibility* as

$$\kappa = \partial T^z / \partial M. \tag{5.29}$$

This is a well-defined thermodynamical response function. The behaviour of κ as a function of M for different U is reported in Fig. 5.17. Its value shows local maxima at the border of the semimetallic phase already for small U. Approaching the discontinuous phase transitions, this maxima get sharper and sharper and they tend to develop divergences which remind of a

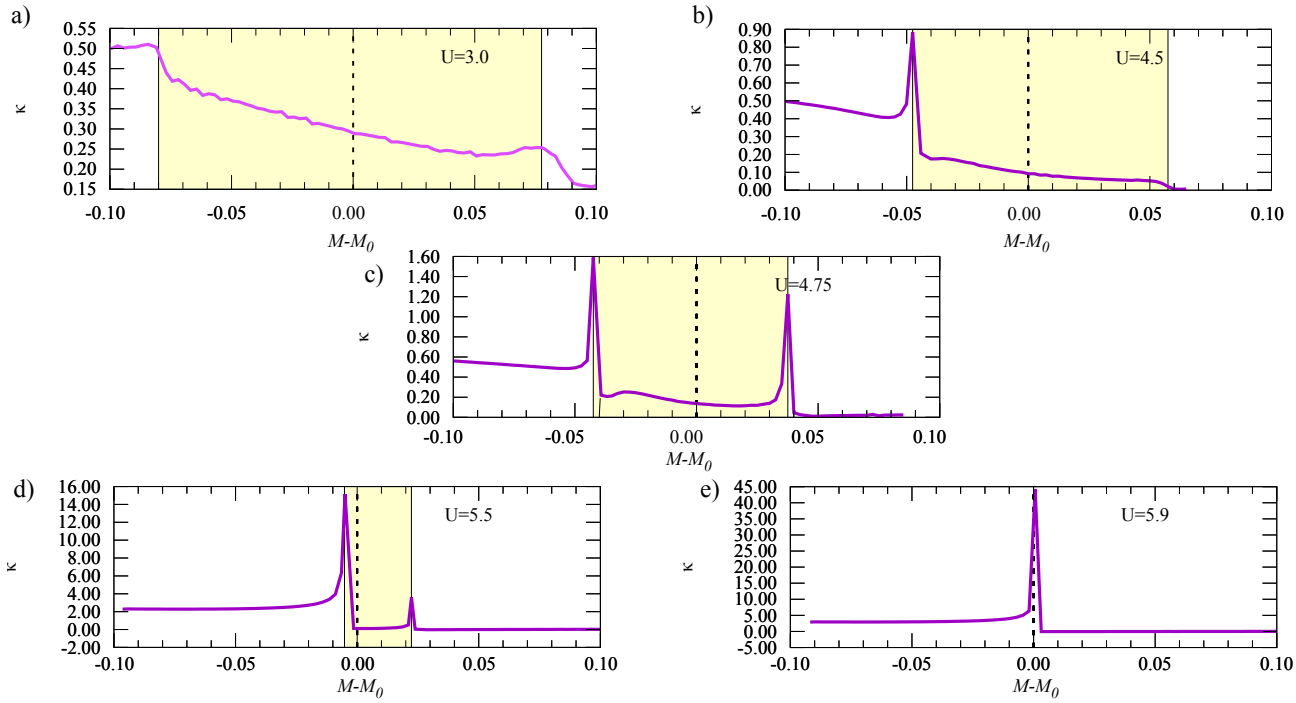

Figure 5.17: *Behaviour of the orbital compressibility k as a function of M for different values of U and $J = 0$, centred around M_0 for which $M_{eff} = 3$ in each case.*

standard thermodynamic instability, where the relevant susceptibility diverges.
The behavior of the orbital compressibility therefore acknowledges a difference between the phases in a thermodynamic sense, even if T_z can not be considered the order parameter as it does not vanish in any phase. These results suggest that, if an order parameter can be defined for our transition, it should be coupled with the orbital polarization. Along the lines of [156], the best choice in this direction would probably be to consider the difference of effective mass at the border of the phases, where jumps occur after $U \approx 4.5$. However, at the present level of understanding, we can not rigorously treat the discontinuous topological phase transitions within the theory of critical phenomena. This would require to define an order parameter and a free-energy which depends on it. This is a particularly difficult task as the discontinuous phenomenology takes place only when interactions are strong so any effective theory must be able to embody the dynamical effects of correlations in terms of a few scalar parameters. We shall abuse this terminology henceforth, with the assumption that "first order TQPT" means a topological phase transition across which the internal energy of the system and some conveniently defined quantities undergo a behaviour that is similar to that of the first-order phase transitions of Landau theory.
A last observation is in order: in its single-site formulation, DMFT is indeed a mean-field theory. Therefore a hypothetical effective theory of the discontinuous topological transition that we found in DMFT is expected to have mean-field character as far as the non-local correlations are concerned, even if it would effectively include the local dynamical correlations. Methods including non-local correlations beyond DMFT are necessary to include spatial fluctuations of a candidate order parameter.
A first necessary step to address some of this points is to verify whether the correlation-induced discontinuity survives to the inclusion of non-local correlations.

Chapter 6

Non-local correlation effects in the interacting BHZ model

The studies reported in [154], [156], [144] and in Chapter 5 have shown consistently that a topological phase transition in various versions of the BHZ model becomes discontinuous for sufficiently large repulsion, while it retains the standard continuous character when the interaction is small, and they lead to a nice consistent picture where the topological transition shares similarities with a thermodynamic transition. The key to explain these phenomena is identified in a different renormalization of the topological phase and the trivial phase, connected with the dynamical nature of the correlations as measured by the frequency dependence of the real part of the Self-Energy.

All these results have be obtained within Dynamical Mean-Field Theory, in which the Self-Energy is by construction momentum independent. Hence, all the non-trivial nature of the correlations is embodied in the frequency dependence, which becomes more and more pronounced as the correlations grow. The non-local correlations are instead treated in in a static mean-field way. The use of DMFT has been motivated by the fact that it can describe properly the competition between the local repulsion (and other local interactions like the Hund's coupling) and the mass term M which controls the topological transition. A natural question, which has not been addressed so far, is whether and to which extent this picture survives the inclusion of non-local correlations. This question is particularly pressing considering that the topological phases of the system are defined by the mapping from the k-space to the Hilbert space of wavefunctions (or equivalently, in Topological Field Theory language, the space of the Green's functions), and the topological invariants distinguishing those phase are derived from the properties of the system in specific regions of the Brillouin zone (chirality of the Weyl points in the Weyl semimetal) or in the entire BZ ($\mathbb{Z}_2$ topological indices).
In this picture, the *local* Self-Energy obtained from DMFT renormalizes only the local parameters of the model, such as the crystal-field splitting, while all the non-local terms are uniformly renormalized by the momentum-independent quasiparticle weight Z. In principle, a fully momentum-dependent Self-Energy $\Sigma(\mathbf{k}, \omega)$ might heavily modify the mapping from the k-space to the space of the Green's functions, for instance altering the condition for the closure of the bandgap, or even removing the topological protection of the gap itself and the definition of the topological phases along with it.
To address these concerns we can rely on the cluster methods outlined in Chapter 3, Cluster-Dynamical Mean-Field Theory and Variational Cluster Approximation. In all these methods

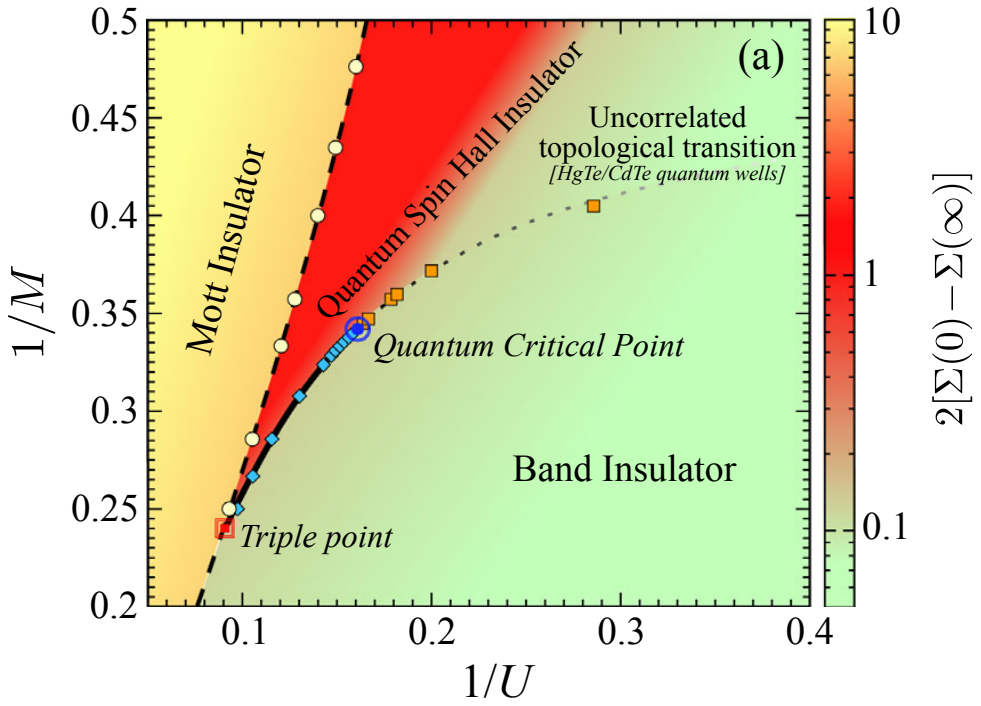

Figure 6.1: *Phase diagram of the 2d interacting BHZ model solved in the single-site DMFT approach (adapted from* [156]*)*

the Self-Energy in real space is not uniform, but it acquires non-local components within the cluster. Through a suitable periodization, the resulting Self-Energy can be recast in a k-dependent form that in principle allows us to evaluate the full phase diagram of the topological Hamiltonian and the associated renormalized dispersion.
In this chapter we will consider the 2d BHZ model first introduced in Chapter 1. We will examine it through the lens of both CDMFT and VCA, taking advantage of the different perspectives they provide and seeking confirmation of the single-site results. As we will see, the inclusion of non-local effects does not modify the picture substantially and, most importantly, does not spoil the nature of the topological transition determined by the local Self-Energy. The non-local features mainly lead to a modulation on top of a DMFT-like effect. Hence the dynamical behavior of the local part of the Self-Energy remains the main responsible for the onset of a discontinuous topological transition. We will also briefly comment on the Mott transition exhibited by the system under a specific interaction form and on the presence of magnetic ordering.

6.1 Model and methods

6.1.1 Single-site description

As in the previous chapter, our starting point is the formulation of the 2d BHZ model given with respect to the 4×4 Dirac matrices

$$\Gamma^0 = \mathbb{I} \otimes \mathbb{I}, \quad \Gamma^1 = \sigma_z \otimes \tau_x, \quad \Gamma^2 = -\mathbb{I} \otimes \tau_y, \quad \Gamma^3 = \sigma_x \otimes \tau_x, \quad \Gamma^4 = -\sigma_y \otimes \tau_x, \quad \Gamma^5 = \mathbb{I} \otimes \tau_z \quad (6.1)$$

In the space of spins $(\uparrow,\downarrow)$ and orbitals (a,b) spanned by $\Psi^{(\dagger)}_{\mathbf{k}} = (c^{(\dagger)}_{\mathbf{k}a\uparrow}\, c^{(\dagger)}_{\mathbf{k}b\uparrow}\, , c^{(\dagger)}_{\mathbf{k}a\downarrow}\, , c^{(\dagger)}_{\mathbf{k}b\downarrow})$, the Bloch Hamiltonian matrix has the well known form

$$H(\mathbf{k}) = \big[M - \epsilon(\cos(k_x) + \cos(k_y))\big]\Gamma^5 + \lambda \sin(k_x)\Gamma^1 + \lambda \sin(k_y)\Gamma^2 \tag{6.2}$$

We take $\epsilon = 2t$, where t is the nearest-neighbour hopping, as our energy unit, M is the crystal-field splitting responsible for the energy offset between the orbitals and λ is the spin-orbit coupling responsible for the protection of the topological bandgap. In this chapter we will consider $\lambda = 0.3$, in order to compare our results with the single-site ones obtained in [156]. The interaction will again be defined in the density-density Kanamori form

$$\hat{H}_{int} = U \sum_{il} \hat{n}_{il\uparrow}\hat{n}_{il\downarrow} + (U-2J) \sum_{il\neq l'} \hat{n}_{il\uparrow}\hat{n}_{il'\downarrow} + (U-3J) \sum_{il<l'} (\hat{n}_{il\uparrow}\hat{n}_{il'\uparrow} + \hat{n}_{il\downarrow}\hat{n}_{il'\downarrow}) \tag{6.3}$$

depending on the Hubbard U and the Hund's coupling J, which in the present calculation is fixed to $J = \frac{U}{4}$ as representative of a regime of relatively large local exchange. The topological phase diagram of the noninteracting BHZ model presents, as previously shown, a gapless Dirac point for $M = 2\epsilon$. For lower values of M, the system is a Quantum Spin Hall insulator (QSHI), for higher M a trivial Band Insulator (BI). The associated topological invariant is the $\mathbb{Z}_2$ scalar index given by the product of the parity eigenvalues of the occupied bands at the four High-Symmetry points of the 2d Brillouin zone: the inverted bandgap around Γ is, as in the original Quantum Well example, responsible for the nontrivial topology.
As in the previous chapter, the interacting phase diagram can be recovered from the study of the effective *topological Hamiltonian*

$$H_{top}(\mathbf{k}) = H(\mathbf{k}) + \mathrm{Re}\Sigma(\mathbf{k}, \omega = 0) \tag{6.4}$$

where Σ is a 4×4 matrix, the components of which we can again label as $\Sigma_{\alpha\sigma,\beta\sigma'}$ in the spin and orbital indices.
As we discussed previously, if the model is solved using DMFT, the Self-Energy is completely local in space and it depends only on the frequency. In the absence of spontaneous symmetry breaking and/or of local terms connecting different spin sectors, it is diagonal in the spin-orbit basis and satisfies the symmetries of the system. Since its imaginary part vanishes for $\omega \to 0$, consistently with the system being an insulator, the topological Hamiltonian only receives the contribution of the real part, which can be expressed as

$$\mathrm{Re}\Sigma = \Sigma_{a\uparrow,a\uparrow}\Gamma^5 \tag{6.5}$$

From this formulation and (6.2), it is clear that the only renormalized parameter of the system is the *effective mass*

$$M_{eff} = M + \Sigma_{a\uparrow,a\uparrow} \tag{6.6}$$

The single-site DMFT phase diagram for the 2d BHZ at $T = 0$ is shown in Fig. 6.1. In this case, the phases are plotted with respect to the reciprocal of the bare mass $\frac{1}{M}$ and of the interaction strength $\frac{1}{U}$. The topological phase transition between the QSH and BI phases is discontinuous up to a critical value of $\frac{1}{U}$, after which (i.e. for low interaction values) the system passes from a phase to the other in the usual way, through gap closing at the Γ point for $M_{eff} = 2$. The presence of a finite J allows, similarly to what we found in the previous chapter, the insurgence of a Mott insulating region, exhibiting an uniform occupation of the orbitals at each site. The

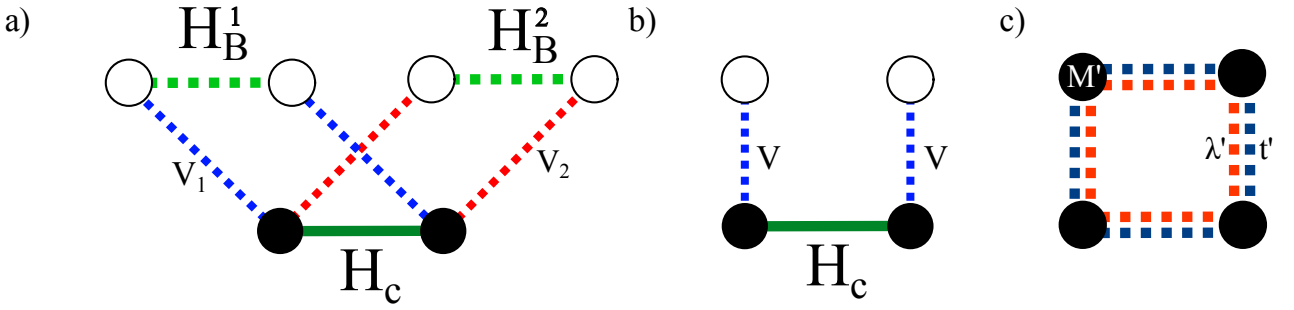

Figure 6.2: *Clusters used in different methods. Filled circles are interacting sites, empty circles are non-interacting ones. Dashed lines represent variable quantities, full lines represent fixed quantities (local cluster hamiltonian). a) CDMFT b) VCA c) Bathlesss VCA*

transition from the Mott region to the Quantum Spin Hall one is again discontinuous, and the width of the latter is progressively reduced till it disappears at a "triple point" for high enough U. As in the $J \neq 0$ case studied in the previous chapter, the slope of the $M_{eff} = 2$ transition line is positive as a function of U.

6.1.2 Cluster description

To study the same system from a cluster perspective, the Hamiltonian matrix needs to be rewritten in the *mixed representation* outlined in Chapter 3. Accordingly, we will use the bold notation for quantities expressed in this representation, and in general in the cluster basis. The interaction part, being on-site, is completely unaffected. On the contrary, the noninteracting part has to be recast in this representation. In particular, the Hamiltonian matrix will now be $4 \times N$-dimensional, where N is the number of cluster sites, and it will be defined in the reduced Brillouin Zone corresponding to the chosen cluster. Inside the cluster, the Hamiltonian will have a block structure: overall, it will consist of two decoupled spin blocks, as in the original formulation. We now introduce the structure of each spin block, which is based on the 2×2 T-matrices living in the orbital space (with $\sigma = \pm 1$ being the spin eigenvalue)

$$T_0 = \begin{bmatrix} M & 0 \\ 0 & -M \end{bmatrix} \quad T_x = \begin{bmatrix} -t & i\frac{\lambda}{2}\sigma \\ i\frac{\lambda}{2}\sigma & t \end{bmatrix} \quad T_y = \begin{bmatrix} -t & -\frac{\lambda}{2} \\ \frac{\lambda}{2} & t \end{bmatrix}. \tag{6.7}$$

T_0 is the on-site energy matrix, while T_x and T_y refer to the hopping along the positive x and y real space directions. The up and down spin blocks of H can be written as an $N \times N$ matrix (in the site space) whose elements are orbital 2×2 matrices.

$$\mathbf{H}_{\uparrow/\downarrow} = \begin{bmatrix} T_0 & T_{12} & \cdots & T_{1N} \\ T_{12}^* & T_0 & \cdots & T_{2N} \\ \vdots & \vdots & \ddots & \vdots \\ T_{1N}^* & T_{2N}^* & \cdots & T_0 \end{bmatrix} \tag{6.8}$$

where $T_{ab}^* := (\text{conjg } T_{ab})^T$. The nondiagonal T_{ij} matrices can be 0, T_x, T_y or their hermitian conjugate depending on the relative position of the sites i and j, and the consequent hopping matrix between them. To complete the expression in mixed representation, the bordering sites of different clusters are coupled by terms of the form

$$T_x^{(*)} e^{\mp i k_x R_x} + T_y^{(*)} e^{\mp i k_y R_y} \tag{6.9}$$

where $k_{x(y)}$ lives in the Reduced Brillouin Zone and $R_{x(y)}$ is the distance of the sites in the given direction.
We will consider three cluster definitions in the context of our study, as shown in Fig. 6.2:

a) CDMFT: The cluster consists of two correlated sites along the x direction (though we have checked for a restricted set of values that the properties for a cluster along y are analogous). The block-Hamiltonian for spin $\uparrow$ and $\downarrow$ of such a cluster in the mixed representation will have the form

$$\mathbf{H}(\mathbf{k}) = \begin{bmatrix} T_0 & T_x \\ T_x^* & T_0 \end{bmatrix} + \begin{bmatrix} T_y^* e^{ik_y} + T_y e^{-ik_y} & T_x^* e^{i2k_x} \\ T_x e^{-i2k_x} & T_y^* e^{ik_y} + T_y e^{-ik_y} \end{bmatrix} \tag{6.10}$$

Unfortunately, the 2×2 plaquette, respecting the symmetries of the original lattice, makes our calculations significantly heavier, hence the results of CDMFT calculation will inevitably deal with an unphysical asymmetry between the x and y directions. However, since the behaviour of the 2-sites clusters along x and y are analogous, we can safely assume we are not overlooking any relevant renormalization effect.

b) VCA: The results of CDMFT are compared with those obtained via VCA using cluster b. The Hamiltonian of the cluster is identical to that of the previous case; what varies is the expression for the noninteracting bath, that in this case consists of two 2-orbital sites with local energy fixed at the chemical potential and hybridization V. This is treated as the sole variational parameter of the model. The number of levels per spin is in this case only 8, which considerably speeds up the calculation. While the choice of a one-dimensional variational space may seem to be too crude an approximation, we have indeed checked that the shape of Ω with respect to the inclusion of other parameters, such as an energy offset between the bath orbitals or hopping between the cluster sites, shows stationary points precisely at (or very near to) the fixed values we have in the end chosen. The relevant effects of the phase transition are therefore well captured by the variation of the hybridization V alone. This simplification turns out to be very useful to visualize the physical content of our results. Relatedly, we have also checked the stability of the topological phases with respect to antiferromagnetism, as we will briefly report in the next section.

c) Bathless VCA: The inclusion of a noninteracting "auxiliary" bath is one of the tools VCA can exploit to enhance its descriptive power. It is however not required in principle for the implementation of the method, that can rely on the sole variation of the isolated cluster parameters. This scenario has been addressed with the help of cluster 6.2c, in which the variational parameters are the hopping amplitude t', the spin-orbit coupling λ' and the crystal-field splitting M'. The exclusion of the bath sites allows us to consider a square plaquette, respecting the symmetries of the original lattice while keeping the number of levels per spin the same as the previous case. The Hamiltonian in mixed representation will in this case have the form

$$\mathbf{H}(\mathbf{k}) = \begin{bmatrix} T_0 & T_x & 0 & T_y \\ T_x^* & T_0 & T_y & 0 \\ 0 & T_y^* & T_0 & T_x^* \\ T_y^* & 0 & T_x & T_0 \end{bmatrix} + \begin{bmatrix} 0 & T_x^* e^{i2k_x} & 0 & T_y^* e^{i2k_y} \\ T_x e^{-i2k_x} & 0 & T_y^* e^{i2k_y} & 0 \\ 0 & T_y e^{-i2k_y} & 0 & T_x e^{-i2k_x} \\ T_y e^{-i2k_y} & 0 & T_x^* e^{i2k_x} & 0 \end{bmatrix} \tag{6.11}$$

where the labelling of the sites runs counterclockwise from the bottom left one. In this instance, the computation time will be affected by the necessities of the multidimensional minimization routine, which will require multiple evaluations of the numerical gradient of Ω. Calculations have been made both with the `l-BFGS-b` and Nelder-Mead methods, giving similar results. While the definition of this cluster as the reference system is completely legitimate, its adequacy rests with the existence of stationary points for Ω, which is in principle not guaranteed as we will see in the following sections.

6.1.3 A note on antiferromagnetism

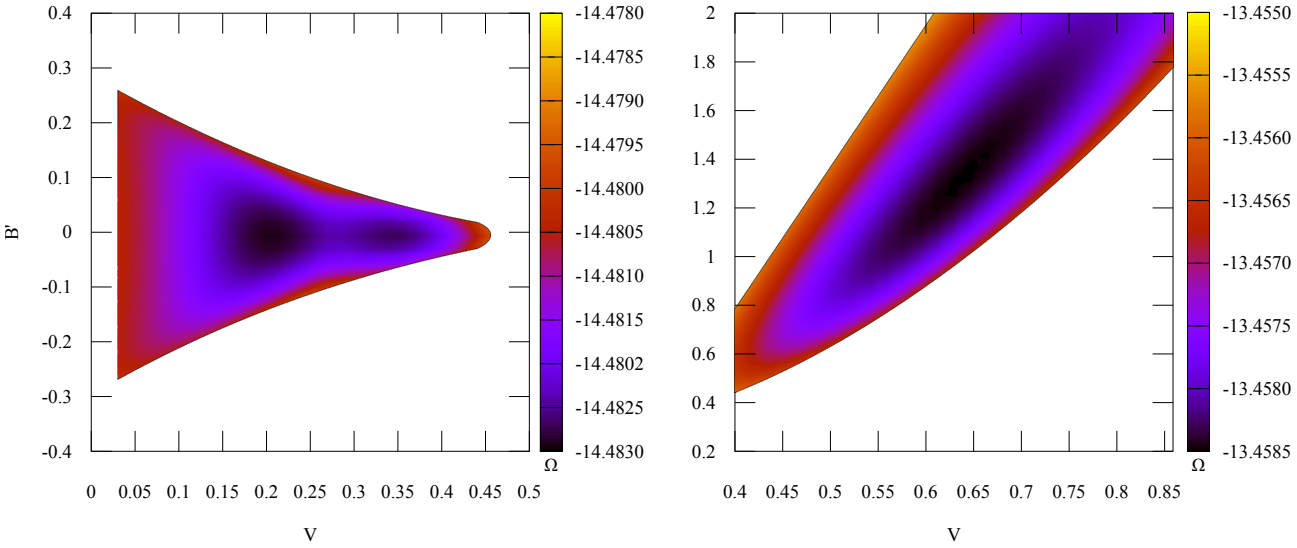

Figure 6.3: *Shape of Ω as a function of hybridization V and effective AFM field B' for U=8 and M in the band insulator and Mott region respectively. The paramagnetic solution is stable around the topological transition, while antiferromagnetic effects dominate in the Mott region.*

The presence of crystal-field splitting and spin-orbit coupling spoils the perfect nesting of the Fermi surface characteristic of the two-dimensional Hubbard model. This implies that, in contrast with the Hubbard model, we do not expect antiferromagnetism to manifest for arbitrarily low interaction.

This has been verified within DMFT both for the 2d and 3d BHZ cases [154, 156]. However, such a solution may very well be stable around the region of the phase diagram occupied by the Mott insulator, i.e. for large U, and, since the width of the non trivial region is dramatically shrunk in that area, it is better to check the stability of the solution with respect to antiferromagnetic ordering also in presence of nonlocal correlation effects before proceeding in our analysis.

In single-site DMFT, antiferromagnetic solutions are achieved by doubling the size of the cell to consider two independent sites in the spirit of real-space DMFT, and by breaking the symmetry of the bath relative to the two sites. This is however not immediately done with the replica construction we are employing, so it is easier to rely, to our end, on the VCA framework.

In absence of symmetry-breaking perturbations, the solution of a finite Hubbard cluster has to be $SU(2)$-invariant, from which derives the inability of Cluster Perturbation Theory in its original "divide et impera" formulation to describe spontaneous symmetry breaking [93]. VCA

is, in this case, a clear improvement: we can take advantage of the ability to include any noninteracting term (as long as the interacting part of $\hat{\Omega}$ is universal) and add a fictitious staggered magnetic field [160] of the form

$$\hat{b}_{AFM} = -B' \sum_{i\sigma} z_i (\hat{n}_{i\uparrow} - \hat{n}_{i\downarrow}) \tag{6.12}$$

to the cluster defined in Fig. 6.2b, where z_i is ± 1 for site 1 and 2 and the orbitals are identically affected. This staggered magnetic field will then be used, together with the previously defined V, as a variational parameter. In Fig. 6.3 we show, as an example, the heatmap of $\Omega(V, B')$ for a 2d BHZ system in a region close to the topological transition and inside the Mott insulator respectively for $U = 8$, which is high enough to warrant, in the single-site case and for suitable values of M, both the insurgence of an antiferromagnetic solution and a discontinuous topological phase transition. All the fixed parameters of the model are those defined in the previous section. As we can see from the right panel, antiferromagnetic ordering is indeed stable in the Mott region, as the stationary point is found for a nonzero value of B' (Ω has to be even with respect to the staggered field, so another equivalent minimum is found for opposite B'). However, near the topological phase transition the two local minima of Ω, the meaning of which will be elucidated in the following sections, are located at different values of V and zero staggered field. Hence, at least near the topological phase transition, the paramagnetic solution is indeed stable with respect to magnetically ordering, which is limited to the Mott insulating region.

6.2 Nonlocal effects and Topological characterization

All the information on the effects of correlations on the single-particle properties is encoded in the cluster Self-Energy. This is made up of various components which we can label as $\Sigma_{i\alpha\sigma,j\beta\sigma'}$, where σ, σ' refer to the spin, i, j to the site and α, β to the orbital degrees of freedom, which collectively form a square matrix $\mathbf{\Sigma}$ of size

$$N_{sites} \times N_{orb} \times N_{spin},$$

in our case equal to 8 in the mixed representation for clusters 6.2a and b. In principle, $\mathbf{\Sigma}$ has 64 entries for each frequency ω. However, the number of independent entries is strongly reduced by the symmetries of the interacting cluster.
First of all, we assume as an hypothesis that the two spin blocks are decoupled and identical, retaining the symmetry of the Hamiltonian, which allows us to take advantage of the spin-decoupled ED method described in Chapter 4. In the following we will consider the symmetry properties of the $\uparrow$-spin block, the other following a similar behaviour.

In order to study the topological phases of the system, we are interested in the behaviour of $\mathbf{\Sigma}$ at $\omega = 0$. Any component with vanishing real and imaginary parts for $\omega \to 0$ will not affect the topology of the interacting system. This is, for example, the case of the components $\Sigma_{ia\sigma,ib\sigma}$, relating the two orbitals on the same site, which has an identically zero imaginary part and a tiny finite real part that vanishes at $\omega = 0$: to the end of determining the topological phase of the system, its presence is completely irrelevant.
All the other components, for which at least one among the real and imaginary parts of $\mathbf{\Sigma}$ is finite in 0, have been collected in Fig. 6.4, where they are plotted along the Matsubara axis. The plots are relative to CDMFT data, though we verified that the VCA Self-Energies satisfy

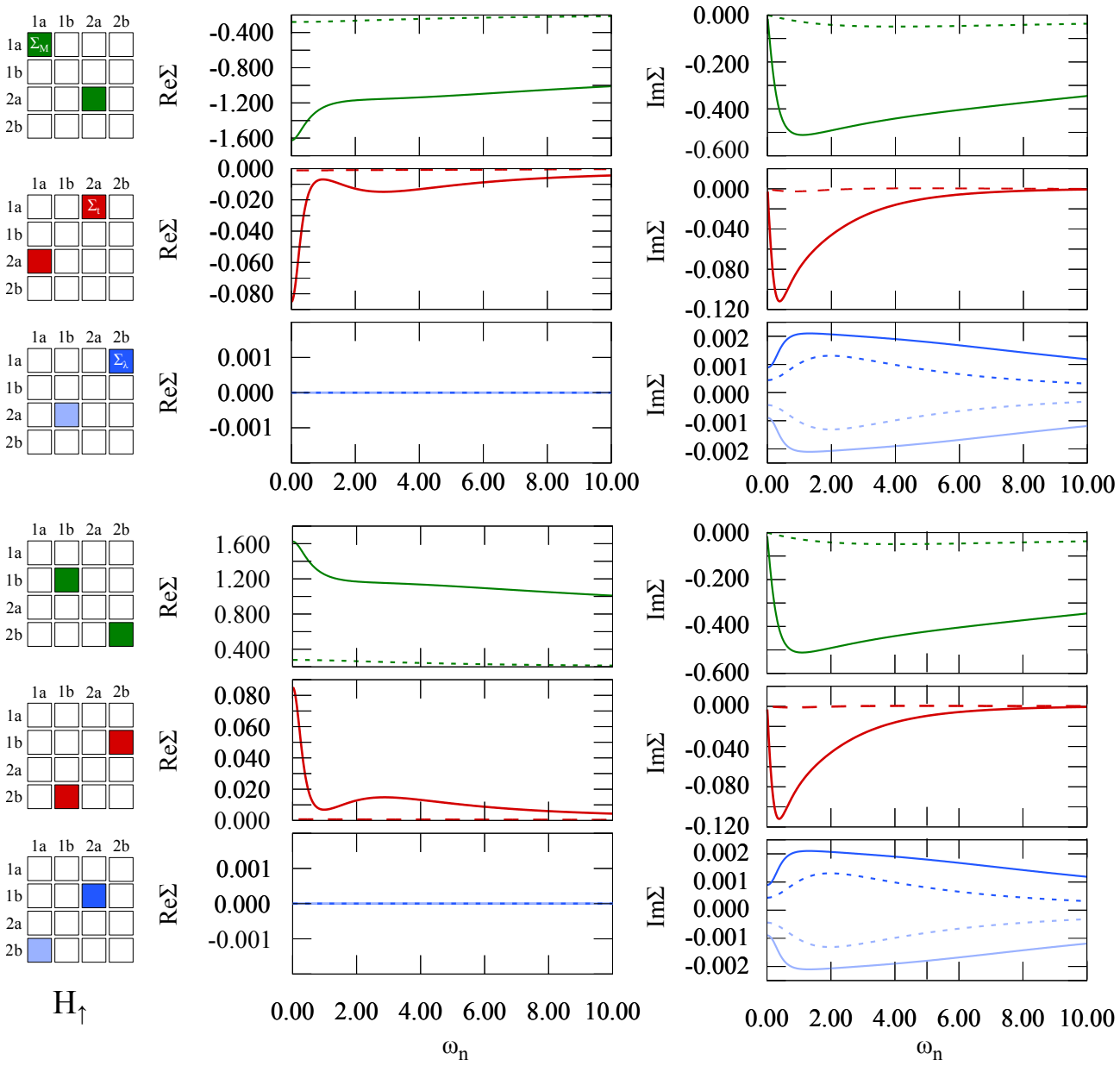

Figure 6.4: *CDMFT Self-Energy components for the 2-site cluster at low (U=2, dotted lines) and high (U=8, solid lines) interaction values, plotted along the Matsubara axis, for a value of M inside the topological insulating region. The first and last three plots respectively refer to aa and bb terms for the intra-orbital components and to ab and ba terms for the inter-orbital ones. In each case, the plotted components of the Self-Energy are identified by coloured squares in the block structures at the left, representing the* 4×4 $H_{\uparrow}$ *Hamiltonian, where sites are labelled by number and orbitals by letter. In the case of off-diagonal components in the site space, if the two entries in the* Σ *matrix not identical they are represented by different shades of the same color.*

the same symmetries. The diagrams on the left of the plot refer to the block structure of the spin-up Hamiltonian $H_\uparrow$ to which the plotted Self-Energy components correspond. We will omit the spin index henceforth. In each plot, the solid and dotted lines refer to the Self-Energy values obtained for an indicative low (U=2) and high (U=8) value of interaction respectively. The three different colors refer to $\mathbf{\Sigma}$ components relating different sites and orbitals, according to the following scheme:

In green we plotted the diagonal Self-Energies relating the same sites and orbitals. These have to satisfy the causality constraint which imposes a negative sign on their imaginary part, as is indeed the case. It is also to be noted that the imaginary parts vanish for $\omega = 0$, denoting the insulating character of the model. The components relative to the two orbitals show the same behaviour for the imaginary part, while the real part is opposite in sign, consistently with what we obtained for the single-site case. As we would expect, the renormalization given by the real part of the Self-Energy drastically increases with the interaction. The sign of the component is opposite to that of M for each orbital, which reflects the symmetry of the single-particle Hamiltonian [156]. Considering the symmetries, with a convenient sign the value of this class of Self-Energies in zero is determined by $\mathrm{Re}\Sigma_{1a,1a}(0)$, which we will refer to as Σ_M, where the meaning of the pedex will become clear in the following.

In red we find the components of the Self-Energy relating the same orbital on two different sites, which corresponds to processes analogous to the nearest-neighbour hopping. The corresponding imaginary parts are still identical for each orbital, and the real parts are opposite in sign. Again, the magnitude of the component increases with interaction. The value of this class of Self-Energies in 0 will be called, similarly to the previous case, $\mathrm{Re}\Sigma_{1a,2a}(0) := \Sigma_t$.

In blue the components of $\mathbf{\Sigma}$ relating different orbitals on different sites are depicted, which corresponds to processes analogous to the λ terms of the bare Hamiltonian.. The behaviour of this component is peculiar: the real part is identically 0, while the imaginary part is equal and opposite for the components $\Sigma_{1\alpha 2\alpha}$ and $\Sigma_{2\alpha,1\alpha}$ for both orbitals $\alpha = a, b$. Since these are off-diagonal, we are not bound by any requirement on the sign of $\mathrm{Im}\Sigma$. As the previously considered ones, these components have opposite value for different orbitals and exhibit a stronger frequency dependence for higher values of U. With a sign dictated by symmetries, the value of this class of components of Self-Energy in 0 is defined as $i\ \mathrm{Im}\Sigma_{1a,2b}(0) := i\ \Sigma_\lambda$.

To better visualize the way in which these terms enter in the topological Hamiltonian, and the reasons of the labels we attributed to the various entries of the Self-Energy, we recall the expression for the Σ-scheme periodization introduced in Chapter 3 for every spin-orbital component:

$$[\Sigma_{per}]_{\alpha\sigma,\beta\sigma'}(\mathbf{k},\omega) = \frac{1}{N_c}\sum_{ij} e^{-i\mathbf{k}(\mathbf{r}_i-\mathbf{r}_j)}\Sigma_{i\alpha\sigma,j\beta\sigma'}(\omega), \tag{6.13}$$

where the resulting periodized Self-Energy can be expressed in a 4×4 matrix in the spin-orbit space which now depends on momenta in the whole Brillouin zone. This periodization is the most reliable in a regime where the Self-Energy is well behaved and does not show singularities. From the definition of the Γ matrices, and using (6.13), we can recall the symmetry properties of each component of $\mathbf{\Sigma}$ shown in Fig. 6.4 (as well as those, not shown, for the opposite spin)

and verify that the 4×4 $\mathbf{k}$-dependent zero-frequency Self-Energy is given by

$$\Sigma_{per}(\mathbf{k}, \omega = 0) = \Sigma_M \Gamma^5 + \Sigma_t \cos(k_x)\Gamma^5 - \Sigma_\lambda \sin(k_x)\Gamma^1 \tag{6.14}$$

in the spin-orbital space. If we compare this expression with the noninteracting Hamiltonian (6.2) we immediately see that each of the Self-Energy terms corresponds to a term in the single-particle Hamiltonian. Coherently with their definition, then Σ_M will renormalize additively M, Σ_t will do the same for the $\epsilon = 2t$ term and Σ_λ for the spin-orbit coupling. Clearly, the asymmetry in the coupling of the last two terms, which do not renormalize hopping along y, derives from the chosen form of the cluster. The eigenvalues of the topological Hamiltonian, given by the sum of the noninteracting H and the periodized $\Sigma_{per}(\mathbf{k}, 0)$, are the spin-degenerate

$$E_{\pm,\sigma} = \pm\sqrt{\Big(\big(M + \Sigma_M\big) - \big(\epsilon - \Sigma_t\big)\cos(k_x) - \epsilon\cos(k_y)\Big)^2 + \big(\lambda - \Sigma_\lambda\big)^2 \sin^2(k_x) + \lambda^2 \sin^2(k_y)} \tag{6.15}$$

Our analysis then concludes that the effect of the interaction can be nicely summarized, at least at the level of the topological Hamiltonian, in terms of very transparent independent renormalizations of the different single-particle parameters.

In particular, the Σ_λ component, coupling to λ, affects the protection of the topological gap along the k_x direction. In principle, a strong enough renormalization, matching the value of the spin-orbit coupling, could cancel the $\sin^2(k_x)$ term with the consequent closing of the gap and destruction of the topological phase. However, in the case we consider, we are not even close to this situation. From the data of Fig. 6.4 and for similar data for other parameters, we see that the value of Σ_λ, by far the smallest of the three independent components, is even at high interaction values at least two orders of magnitude smaller than the value of λ, hence it appears to have a rather limited impact.

On the other hand, the renormalization of the hopping term is more significant, as the value of Σ_t is four to five times smaller than that of t. Since the λ terms in (6.15) are finite, the gap closing, associated to the phase transition, happens at Γ if the first term is zero. The Dirac cone will in this case be asymmetric in the two k directions as a consequence of the form of the cluster, and the requirement $M_{eff} < (>)2$ for the topological transition in the single-site picture will be replaced by the *topological condition*

$$\frac{M + \Sigma_M}{\epsilon - \frac{\Sigma_t}{2}} < (>)2. \tag{6.16}$$

In order to identify the topological phase of the system, and to compare the results with the single-site case, we will need to evaluate the behaviour of the previous expression as a function of M.

The precise low-energy behaviour of the Green's function in the context of the topological phase transition will be investigated in the following sections. However, we can get an intuitive idea of the effect on Σ_{per} on the low-energy physics by looking at the bands of the renormalized topological Hamiltonian defined by

$$Z_{\mathbf{k}}\big(H(\mathbf{k}) + \Sigma_{per}(\mathbf{k}, \omega = 0)\big)$$

where $Z_{\mathbf{k}}$ is the quasiparticle weight defined in Chapter 2, which has also a matrix structure in the spin-orbital space. This expression, which can be derived from the form of the Green's

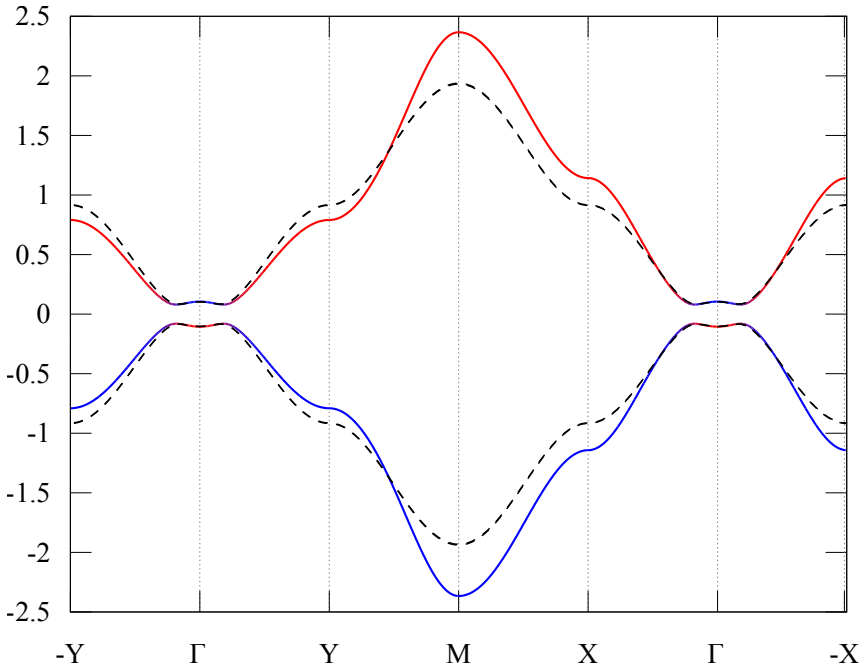

Figure 6.5: *Comparison between CDMFT (coloured) and DMFT (dashed) data for the renormalized Topological Hamiltonian $Z\cdot(H(\mathbf{k})+\Sigma(\mathbf{k}))$ at U=8 and M inside the QSHI region, which gives an approximate representation of the location of the poles of G near zero frequency. As it can be seen, the effect of Z accounts for a loss of symmetry in the two high-symmetry directions $-X\Gamma X$ and $-Y\Gamma Y$, while the purely local Self-Energy in the single-site approach makes for a uniform "compression" of the bands. The inverted gap region, however, is minimally affected, thus preserving the topological characterization of the system.*

function

$$G(\mathbf{k},\omega\to 0)=\left[\omega\mathbb{1}-H(\mathbf{k})-\Sigma_{per}(\mathbf{k},0)-\frac{\partial \mathrm{Re}\Sigma_{per}}{\partial\omega}\bigg|_0\omega\right]^{-1}=\left[\omega\mathbb{1}-Z_{\mathbf{k}}\big(H(\mathbf{k})-\Sigma_{per}(\mathbf{k},0)\big)\right]^{-1}Z_{\mathbf{k}}^{-1}$$

approximately coincides for low ω with the maxima of the spectral function $A(\mathbf{k},\omega)$, and identifies the energies of the quasiparticle excitations.

The relative band diagram is plotted in Fig. 6.5, along with the analogous result for the single-site case. From a topological point of view, we again see that the nontrivial phase is described, in band theory, by an inverted gap around the Γ point. It is more interesting to notice the way the bands are modified by interaction: since the Self-Energy is momentum-independent in the single-site picture, the quasiparticle weight is a constant. Consequently, the renormalized bands in DMFT are rigidly compressed. With a 2-site cluster, instead, the momentum dependence of Σ_{per} leads to a quasiparticle weight that varies inside the Brillouin zone, and accordingly the dispersion is non-uniformly distorted in the two k-directions, especially around the (π,π) M-point.

From these observations, it is possible to assert the existence of nonlocal effects of correlation, and their interplay with the noninteracting form of the Hamiltonian to alter the low-energy excitations' properties. It is now to be understood if and how these effects will alter the discontinuous character of the topological phase transition reported by single-site DMFT.

6.3 Discontinuous topological phase transition

To gain more insight into the destiny of the topological phase transition for high values of interaction, we will take advantage of the different but related perspectives that CDMFT and VCA offer on a cluster-based calculation. In the previous chapter, we have qualified the topological transition for large interactions as *discontinuous* by assessing the presence of jumps in the evolution of the Self-Energy with M, and later used the term *first order* in a thermodynamic sense by highlighting the presence of divergences in the orbital compressibility κ. In this chapter, we will first analyse the behaviour of the relevant components of the Self-Energy defined in the previous section near the topological phase transition, then we will characterize it in terms of the poles of the interacting Green's function and of the internal energy of the system. To identify the topological phase of the system we will use the topological condition defined in the previous character. While in deriving it we have made use of the Σ-scheme periodization procedure, its definition is actually general, depending only on the competition between the coefficients Σ_M and Σ_t. Even in the Reduced Brillouin Zone, when the value of the topological condition (6.16) is 2 the gap in the topological Hamiltonian is closed in Γ, and the orbital character of the gap is direct or inverted depending on the value of expression (6.16). There are other ways to assess the topological character of the system, such as the use of Wilson loops and Wannier centres of charge [161]. While we have checked the consistency of the results, we will stick to the use of expression (6.16), for the sake of an easier visualization and comparison with the single-site case.

6.3.1 Self-Energies

Each topological phase of the system is related to a specific form of the Self-Energy. In the single-site case, the pronounced frequency dependence of Σ in the QSHI phase, as opposed to the weaker one in the BI (and WSM), is responsible for the insurgence of a discontinuous phase transition: the strong correlation effects felt by the partially orbital-polarized topological insulator made impossible a continuous evolution of the Ground-State. This was instead achieved for lower values of interaction, where the Self-Energy, weakly dependent on frequency to the point of being almost constant, simply summed up with the crystal-field splitting M, shifting the transition point but keeping its continuous character.
In Fig. 6.6 we show the behaviour of the relevant components of $\mathbf{\Sigma}$ defined in the previous section (only one representative for each class has been plotted) for values of M immediately preceding and following the transition point. The plotted data refer only to the high interaction case $U = 8$ as, for lower values of U, the behaviour of the phase transition is continuous. The two columns of the plot refer to CDMFT and VCA data respectively; given the qualitative agreement of the behaviour of the $\mathbf{\Sigma}$ components, the two methods provide mutual validation. As in the single-site case, the correlation strength, which we estimate from the frequency dependence of the Self-Energy, is decidedly higher in the QSH region for both the Σ_M and Σ_t components. Interestingly enough, the situation is reversed for Σ_λ: here the absolute value of the Self-Energy in 0 is greater in the BI region. The fact that this is the case both for CDMFT and VCA in a sense validates the results given by the fit procedure of the former, which can lead to non-optimal solutions especially in the proximity of phase transitions. However, given the small magnitude of the Σ_λ component we can expect its variation to simply provide a slight modifications of the system parameters in the orbitally-polarized BI phase.

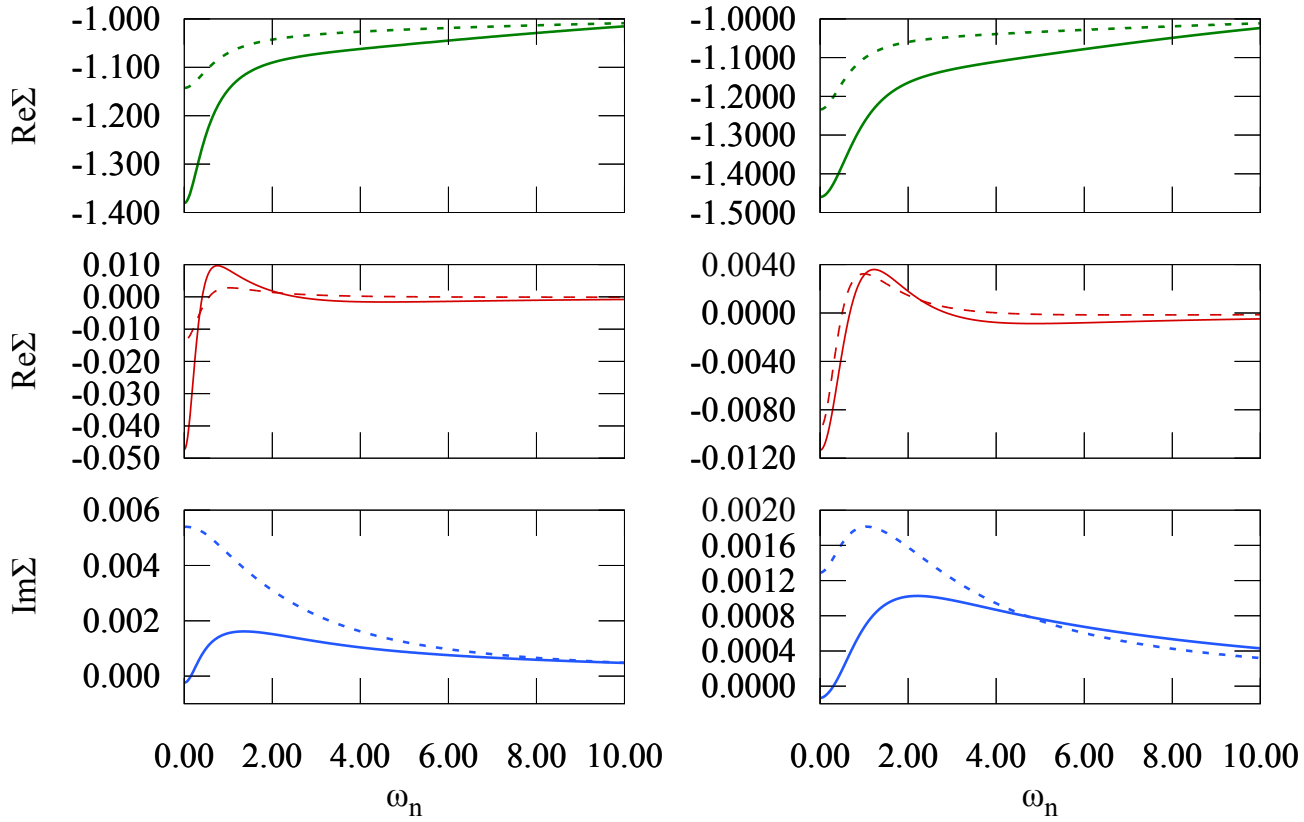

Figure 6.6: *Comparison between CDMFT (left) and VCA (right) data for the independent components of the cluster Self-Energy at the M values immediately before (solid line) and after (dashed line) the transition for U=8. The 3 panels show respectively the Σ_M, Σ_t and Σ_λ components. The VCA approximation captures a jump with comparable width only in the M channel, the other two being in comparison much smaller than their CDMFT counterparts.*

Already looking at Fig. 6.6 we can advance an hypothesis on the behaviour of the topological phase transition: the jump in the local component Σ_M is by far the most relevant being around ten times bigger than that of Σ_t, which is in turn greater than that of Σ_λ. The local effects of correlations appear therefore to dominate, and accordingly we expect that the behavior of the observables and the overall physical picture to be close to that discussed in Chapter 5 and in Refs. [154, 156].

6.3.2 Topological condition

We now use the zero-frequency values of the Self-Energy to compute the topological condition (6.16) as a function of the crystal-field splitting M for both CDMFT and VCA results. In addition, we can directly compare both with the single-site data, where the only significant difference is that $\Sigma_t = 0$ identically. A cumulative resume of the results is provided in Fig. 6.7. In general, the two cluster methods exhibit a good agreement with each other and with single-site results: CDMFT in particular is well in agreement with DMFT in the QSH region, while it is nearer to VCA in the band insulator. Most importantly, for sufficiently high interaction the discontinuous jump of the topological condition, with associated absence of gap-closing points in the topological Hamiltonian, is preserved and the location in M of the transition point is

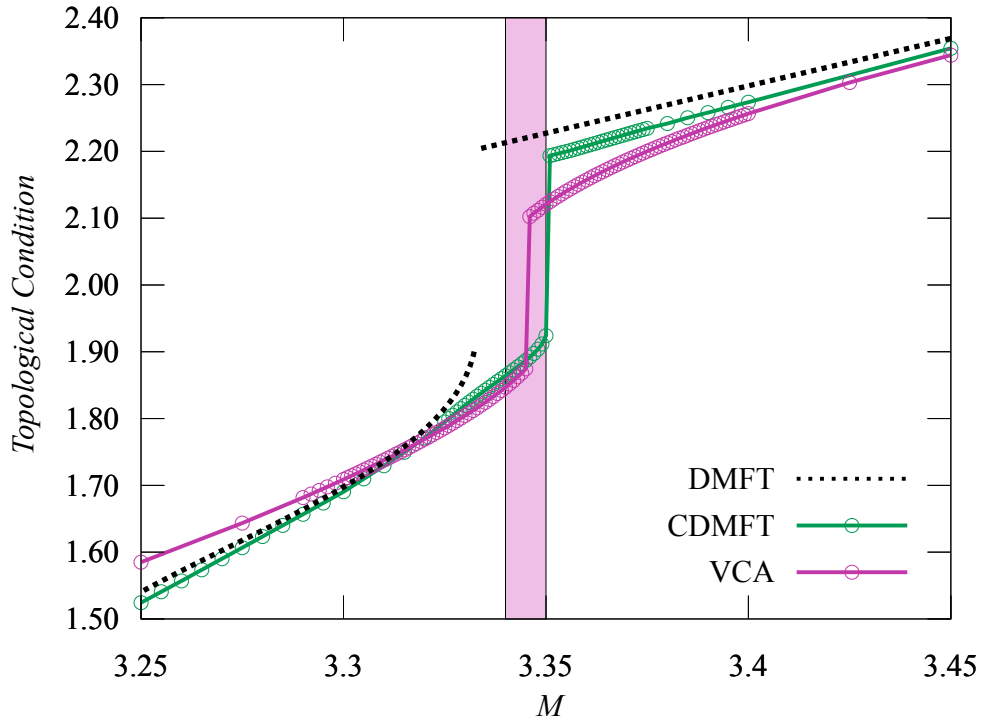

Figure 6.7: *(Color online)* a*Topological characterization of the system for U=8: the topological phase of the system, as obtained via the Topological Hamiltonian, depends on the ratio between M and ϵ The plots refer to the single-site DMFT results, the CDMFT one and the VCA one with reference cluster b.*

very close to the DMFT value.
The shaded region refers to one of the useful features of VCA, namely its ability to find multiple physically significant solutions for the system, and to determine their stability in terms of internal energy. In the shaded region, as we will see in the following sections, the VCA solver indeed finds two solutions as a function of the variational hybridization V.
CDMFT, by contrast, does not provide a similar information about the stability of solutions, and the information on coexistence can only be obtained by moving back and forth in the phase diagram and observing two solutions, coming respectively from large and small M, being compresent in an determinate region.
As it is apparent from Fig. 6.7, the right boundary of the region where VCA stops finding two available physical solutions coincides with that of the CDMFT coexistence region defined above: here, the QSH solution can no longer be carried over. This again shows that the two methods, applied on clusters Fig. 6.2a and Fig. 6.2b, are in good agreement in describing the topological phases of the system.
On this note, let us now consider the third cluster system proposed in Fig. 6.2c, which is the bathless square plaquette. With both minimization methods used (constrained BFGS and simplex), no solution following the behavior of Fig. 6.7 is found near the phase transition. Instead, the lowest stationary points exhibited by Ω are in regions where the variational $M^{'}$ is 2 to 3 times bigger than the real system one: the related Self-Energy is almost frequency independent, and the only relevant components are the diagonal ones. We can attribute this result to the lack of resolution in frequency domain of this approach. Indeed, the results of CDMFT and VCA in presence of bath suggest that, analogously to the one-site case, the discontinuous topological

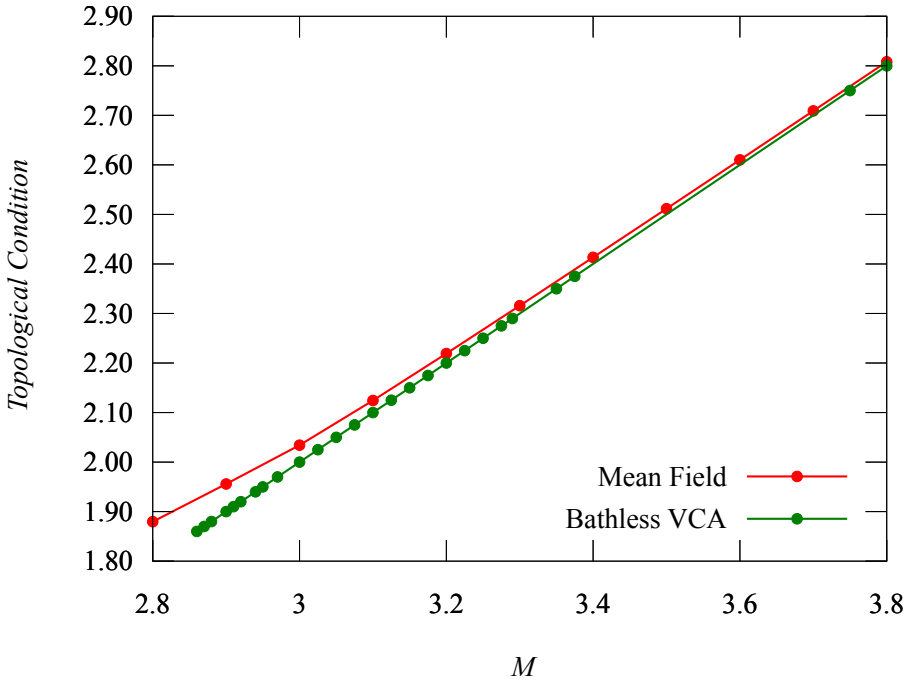

Figure 6.8: *Comparison between the topological condition for cluster Fig. 6.2c and a static Mean-Field result.*

phase transition is mainly a consequence of local quantum correlations, which, within VCA, are precisely addressed by the uncorrelated bath sites that this simple approach lacks. In principle, a better result could come by an increase of the cluster size, which would however start to grow too big to be solved with an ED routine.
Interestingly, this VCA solution with a "quasi-static" Self-Energy is rather in agreement with a static mean-field result obtained along the lines outlined in Chapter 5, using the average orbital magnetizations m_a, m_b and polarization p as variational parameters. This agreement can be seen from Fig. 6.8, where we have plotted the value of the topological condition for cluster Fig. 6.2c and the renormalized crystal-field splitting of the effective HF Hamiltonian.

6.3.3 Poles of the Green's function

As previously stated, the renormalized topological Hamiltonian shown in Fig. 6.5 describes the low-energy behaviour of the interacting system. There is a more quantitative way to show the behavior of the gap at the topological phase transition: the low energy excitations can be directly obtained from the poles of the interacting Green's function. For the single-band case, we recall that the shifted poles satisfy the equation

$$\omega - \epsilon_{\mathbf{k}} - \mathrm{Re}\Sigma(\mathbf{k}, \omega) = 0$$

the shift being due to the real part of the Self-Energy. In the general multi-band case, where Σ and G are matrices, this shift is provided in a diagonal basis by the real part of the eigenvalues of

$$H(\mathbf{k}) + \Sigma(\mathbf{k}, \omega)$$

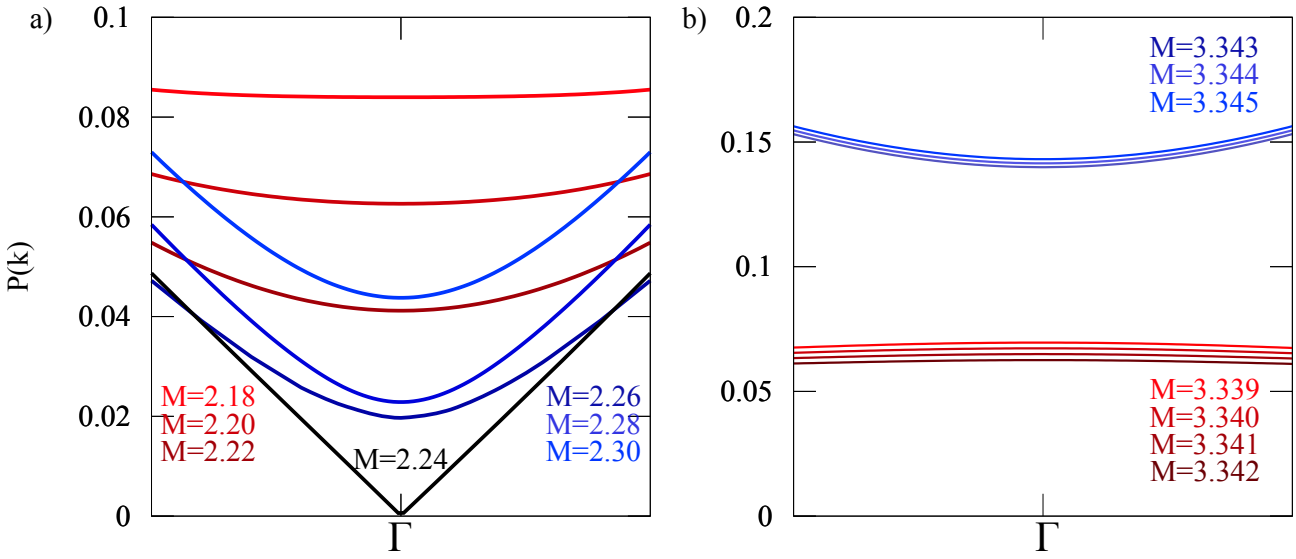

Figure 6.9: *Absence of gap closing in the evolution of the lowest positive pole of the Green's Function: this pictures shows for U=2.0 and U=8.0 the location of the lowest energy pole of G around the* Γ *point.*

with the imaginary part being again related to the lifetime of these excitations. Operationally, the calculation of the poles amounts to finding the zeros of the expression

$$D(\omega) = \mathrm{Re}\ \det\left[(\omega+\mu)\mathbb{I} - H(\mathbf{k}) - \Sigma_{per}(\mathbf{k},\omega)\right]. \tag{6.17}$$

The value of Σ_{per} in (6.17) is given by the periodized Self-Energy we have previously defined. Once the path in momentum space along which the poles have to be calculated is decided, the positive (or equivalently negative, since the DOS is symmetric with respect to $\epsilon_F = 0$) real frequency semiaxis is indicatively split in ranges according to the changes of sign of (6.17). Then, within each range a root-finding procedure is employed to obtain the location of the pole.

The results for the lowest positive-energy pole around the Γ point have been collected in Fig. 6.9. The k-path is a fraction of the high-symmetry line $Y - \Gamma - X$, chosen to highlight possible asymmetric renormalization effects. In the narrow region considered, however, these are barely visible. The two panels of Fig. 6.9 refer to data for small and large U, with the usual values of 2 and 8 respectively. As we can see, for low values of interaction the spectral gap in Γ is progressively reduced, until it disappears completely at the continuous topological phase transition. As expected from all the previous results, the picture is different for larger U: the Green's function of the system always presents an open spectral gap around the Fermi energy, and the location of the poles varies continuously within each phase on the two sides of the transition, but it jumps discontinuously at the transition point.

A similar behavior of the gap at an interacting topological transition has been proposed by Gurarie [162] who discussed this in terms of the behaviour of the *zeros* of the Green's function. He considered the general form of the determinant of a fully interacting Green's function

$$\det G = \frac{\prod_s(\omega - r_s)}{\prod_n(\omega - \epsilon_n)}$$

where ϵ_n are the poles of the Green's function and r_s are its zeros. A noninteracting Green's function has no zeros, and any topological phase transition is therefore associated to a gap clos-

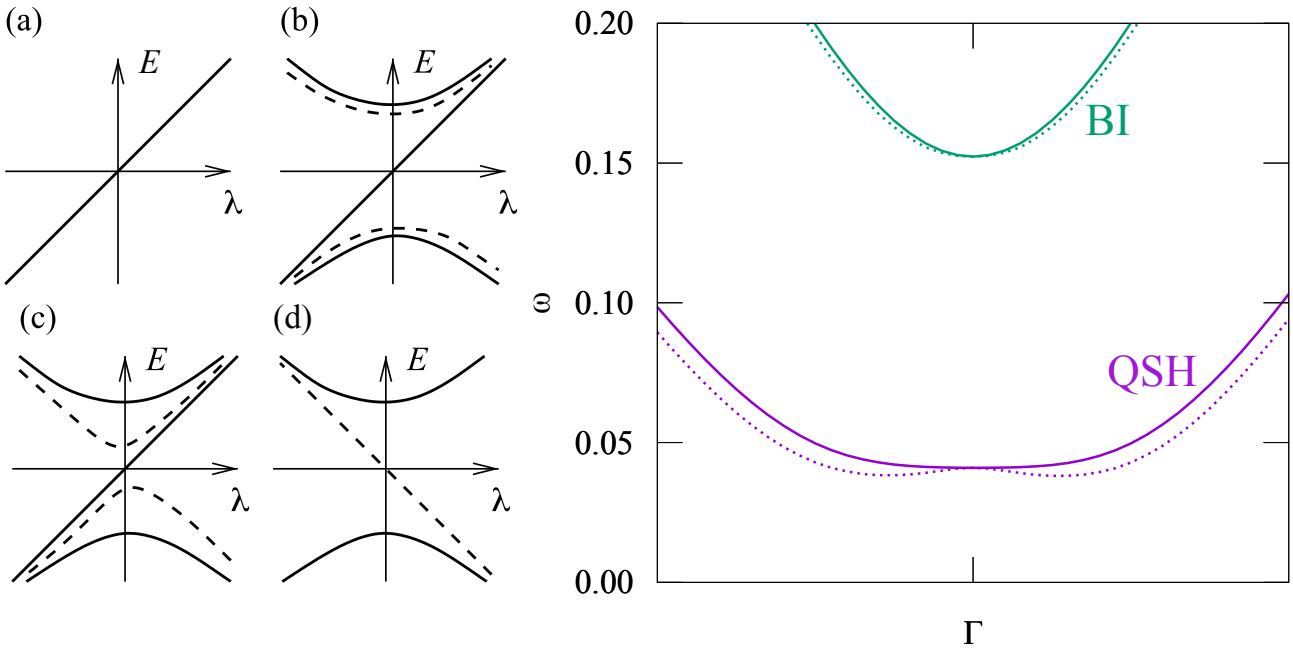

Figure 6.10: *On the left, an example in which the behaviour of zeros and poles of the Green's function can trigger a topological phase transition without the closing of the spectral gap (image taken from* [162]*. On the right, the calculated lowest pole and zero of the Green's function before and after the transition: neither crosses* $\omega = 0$*.*

ing. However, for an interacting system it has been demonstrated that a topological invariant can be defined in terms of the number of negative poles and zeros, through what is known as *mode counting* [163]:

$$N_1 = \sum_n \text{sgn } \epsilon_n - \sum_s \text{sgn } r_s$$

It is apparent that if a zero of the Green's function crosses the Fermi energy the topological invariant can change without any gap closing. An example of this behaviour is show on the left panel of Fig. 6.10. Panel (a) exhibits a topological system with a gap-closing level in a parameter space λ. As interactions are increased, zeros and poles of the relative Green's function appear together. If the zeros move closer to the positions of the original poles, they can "annihilate" with the latter, which amounts to a simplification of the corresponding factors in det$G$. Then, the system in panel (d) will have the same topological invariant as that in panel (a) (since the variations of the signs of zeros and poles compensate each other), but without any gap-closing state.

This mechanism, however, appears not to apply to our case, as it can be seen from the right panel of Fig. 6.10: here, the poles and zeros for the Green's function at M values at the border of the topological phases have been plotted. The data refer only to the high interaction case. The calculation of the zeros is analogous to that of the poles, with the only difference that the search procedure is performed on the inverse of (6.17). Both zeros and poles are in this case well separated from $\omega = 0$, hence no modification of the topological index can occur via the above described mechanism. It is important to notice that the zeros and poles, though very close to each other, do not coincide in Γ. If this were the case, neither of them would be seen as the corresponding factors would annihilate in det$G$.

6.3.4 Stability of the solutions: Energy perspective

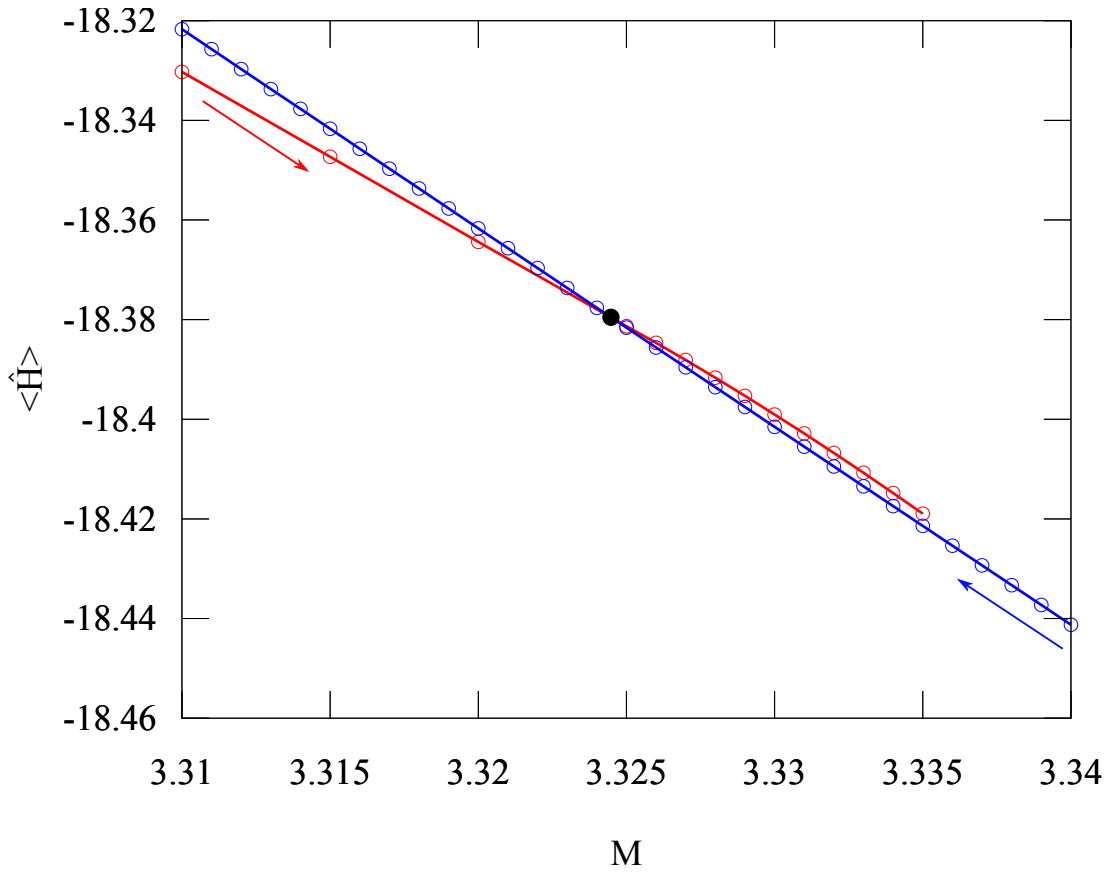

Figure 6.11: *Internal energy of the CDMFT solution for U=8: the arrows show the direction in M in which the data have been collected, the system is shown to carry the solution over the transition point (black dot) where it becomes energetically unfavourable.*

Though we have no solid argument to conclude that the topological phase transition is properly first order in the Landau sense, we can use this terminology without inaccuracy when talking about the behaviour of the internal energy of the system. This is defined as

$$\langle \hat{H} \rangle = K + V$$

where the first term is the kinetic energy and the second the potential. In our interacting model we will identify the two terms with the one-body and many-body parts of the fully interacting Hamiltonian respectively. Notice that in this way also the expectation values of the M and λ terms are included in the kinetic energy. The way of calculating the average of the two terms reflects their different nature [164]: the first term is effectively the average of a one-body observable with matrix representation given by $\mathbf{H}(\mathbf{k})$, the noninteracting Hamiltonian of the system in mixed cluster-superlattice representation. As such, it can be evaluated from the Green's function via the expression

$$K = \frac{1}{N} \sum_{\mathbf{k} \in RBZ} \int_0^\infty \frac{d\omega}{\pi} \mathrm{Re} \left\{ \mathrm{Tr} \left[\mathbf{H}(\mathbf{k}) \mathbf{G}(\mathbf{k}, i\omega) \right] - \frac{\mathrm{Tr}\, \mathbf{H}(\mathbf{k})}{i\omega - a} \right\} \tag{6.18}$$

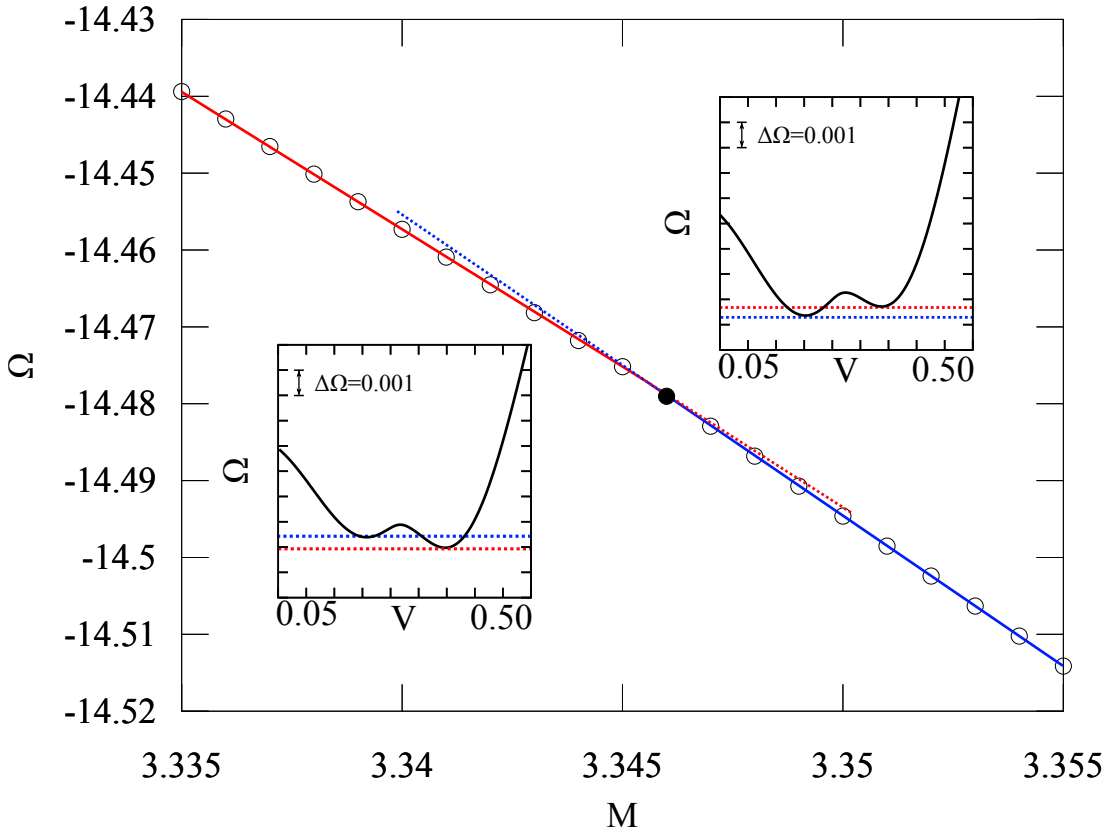

Figure 6.12: *Grand potential in the VCA framework for U=8: two solutions, QSHI and BI, are present in a region of coexistence around the transition point. The relative position of the minima flips at the transition.*

which we have encountered in Chapter 3. Here, the interacting k-dependent Green's function is obtained from

$$\mathbf{G}(\mathbf{k},\omega) = \frac{1}{(\omega+\mu)\mathbb{I} - \mathbf{H}(\mathbf{k}) - \mathbf{\Sigma}(\omega)},$$

where $\mathbf{\Sigma}$ is the Self-Energy of the cluster , without resorting to any periodization.
Unfortunately, we cannot rely on (6.18) for the calculation of the second average, since it is not a one-body observable. Rather, we have to compute directly the expectation value of the impurity (cluster) interaction term

$$V = \langle \Phi_{GS} | \hat{H}_{int} | \Phi_{GS} \rangle \tag{6.19}$$

where $\hat{H}_{int}$ is (6.3) and $|\Phi_{GS}\rangle$ is the Ground State eigenvector as obtained from the exact diagonalization procedure. Once the two averages have been independently calculated, the total form of the internal energy can be obtained and plotted, as it has been done in Fig. 6.11. As we briefly commented when talking about the topological condition, it is customary in a DMFT-based approach to start the convergence loop for a given point in parameter space from the converged form of the bath obtained for a point nearby. This speeds up convergence and in general assures us that, once a stable solution has been found, we can follow it in its full region of existence. Let us however look at Fig. 6.11: the two series of data, denoted by red and blue dots, have been obtained from converged solutions firmly in the QSH and BI phases

respectively, by progressively increasing/decreasing the value of M. As a result of the fit procedure, the system tends to follow the trajectory of each solution past the point where it becomes energetically unfavourable (black dot). After a certain interval in M, it is no longer possible to follow the original solution and the algorithm falls on the stable branch. In the sense of the energy behaviour, the topological phase transition is then bona fide first order: the internal energy of the system shows a kink at the black dot, where the phase transition happens. Accordingly its first derivative with respect to M will be discontinuous.

As opposed to CDMFT, where the energy is only computed a posteriori, within VCA the information about different solutions and their stability is a direct outcome of the calculation. We can then immediately follow the evolution of the internal energy with respect to M, as it is represented in Fig. 6.12 for the reference cluster of Fig. 6.2b. Again, the red and blue curve represent the QSH and BI solutions. As in the previous case, the two solutions follow the positions of two minima in the function $\Omega(V)$, which continuously evolve upon varying the crystal-field splitting M. For values of M inside the coexistence region depicted in Fig. 6.7, both solutions are present: in fact, it can be clearly seen from the two insets in Fig. 6.12 that Ω shows two local minima separated by a local maximum. This is in principle an acceptable solution in itself, but it is always metastable and therefore not interesting to our analysis. The insets show the positions of the minima for values of M immediately preceding and following the phase transition: it is easy to see that the relative energy difference changes sign going over the black dot. Coherently, the favoured minimum is the more strongly hybridized one inside the QSH region, and the less hybridized one in the BI. This reflects the stronger dependence on ω of the Self-Energy of the topological insulator. Following the stable solution, the energy curve again experiences a discontinuity in its first derivative at the transition point.
It is important to notice, at this point, how remarkably interaction affects the topological transition: for lower values of U, the Ω curve only shows one local minimum. This is consistent with the usual mechanics of topological phase transitions, where the ground state, which determines the topological mapping, is uniquely defined for each set of noninteracting parameters. Instead, adding interaction to the picture makes different topological phases *compete*, with their (meta)-stable characters changing inside a coexistence region.
We conclude our analysis of the properties of the internal energy of the system with an intriguing parallel. In the CDMFT framework, each solution is prolonged past the actual transition into the region where it is metastable: this process is interestingly similar to the *hysteresis* cycle a ferromagnet experiences when subject to an external magnetic field variation. Accordingly, the two-well shape of the Ω potential in the VCA framework well resembles the shape of the Free Energy of a magnetic system as a function of an external magnetic field h. Again, these parallels strengthen the case of an emergent thermodynamic description for our interacting topological transition and its change from continuous to discontinuous.

6.4 Mott transition

We can summarize the considerations on the phase diagram of a 2d BHZ model in presence of interaction via a sketch such as that of the left panel of Fig. 6.13. As previously stated, the presence of J in the formulation of the density-density Kanamori interaction implies a positive slope in U for the topological transition line.
We will now briefly consider the third phase of the system, the Mott insulator, which for

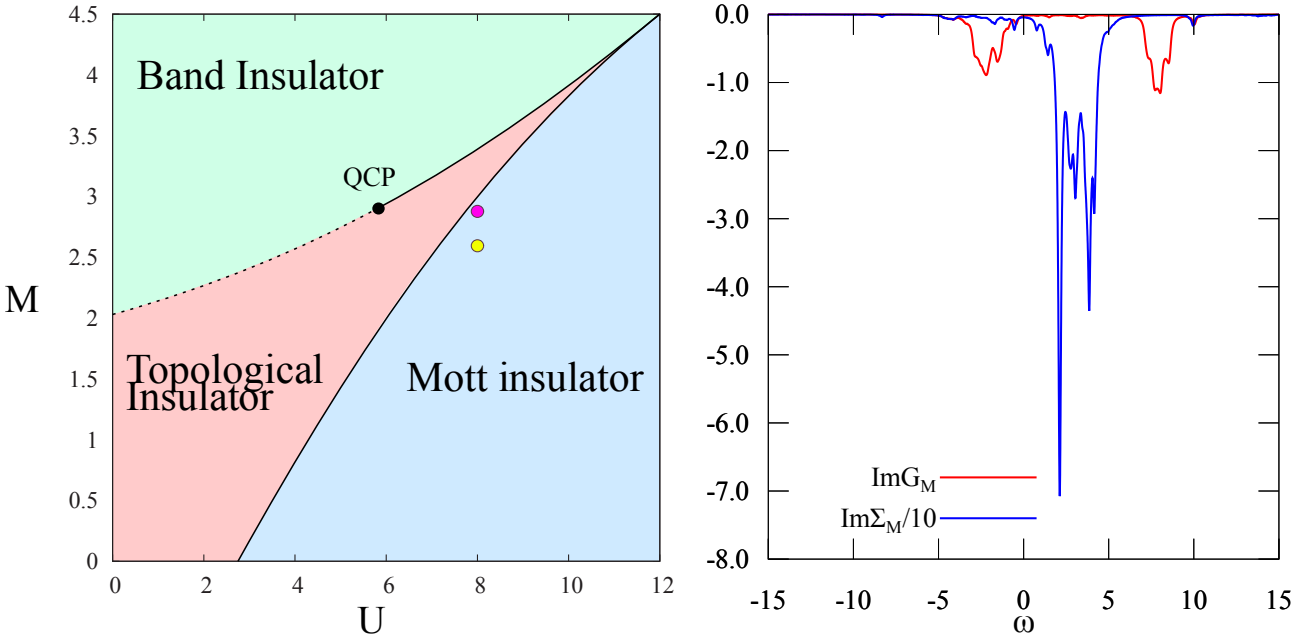

Figure 6.13: *On the left, a summary sketch of the phase diagram of the system (adapted from [165]). On the right, G_M and Σ_M along the real frequency axis. The data refer to the CDMFT approach, VCA being completely analogous.*

this model and filling can only exist for a sizeable value of the Hund's exchange coupling, determining an even occupation of the orbitals. This is in turn instrumental to stabilize, for large U, a high-spin Mott insulator over the band insulating state.

Indeed, as previously mentioned, in this region the 2d BHZ actually shows a stable antiferromagnetic solution. Nevertheless, as customary, we first focus on the paramagnetic solution, which highlights the pure correlation effects disentangling them from the ordering tendency which is often dominated by single-particle physics. Again, we compare results obtained via DMFT, CDMFT and VCA. We will refer to clusters Fig. 6.2a and b respectively. In this paramagnetic solution, the results for spin ↑ and ↓ spin will be identical.

In Fig. 6.13 we plotted the local components $\Sigma_{1a\uparrow,1a\uparrow} := \Sigma_M$ and $G_{1a\uparrow,1a\uparrow} := G_M$ on the real frequency axis. The imaginary part of Σ_M displays a divergence which for the single-band case is located at $\omega = 0$, and for the multi-band case is shifted [156, 158]: in our case, the two bands are symmetric with respect to 0, and so will be the behaviour of the respective Self-Energy components. As a result, by Kramers-Krönig relations, the real part of Σ_M will also be very large in the same region of ω, and therefore the Green's function will exhibit no poles in the area and a spectral gap will open. The poles of the Green's function will be centred around the two Hubbard bands typical of the Mott insulator.
As expected, this is the situation we encounter both in single-site and cluster methods for high U and low enough M (the data refer to the yellow dot in Fig. 6.13). However, both CDMFT and VCA show, in a narrow region near the phase transition to the topological insulator (around the purple dot), a peculiar behaviour which is reported, for the CDMFT case, in Fig. 6.14. The Self-Energy again shows a divergent behaviour, but its structure has become more complicated: in addition to a divergence inside the spectral gap, other peaks appear near the Fermi energy. At the same time, the spectral weight distribution of the Green's function becomes less clear:

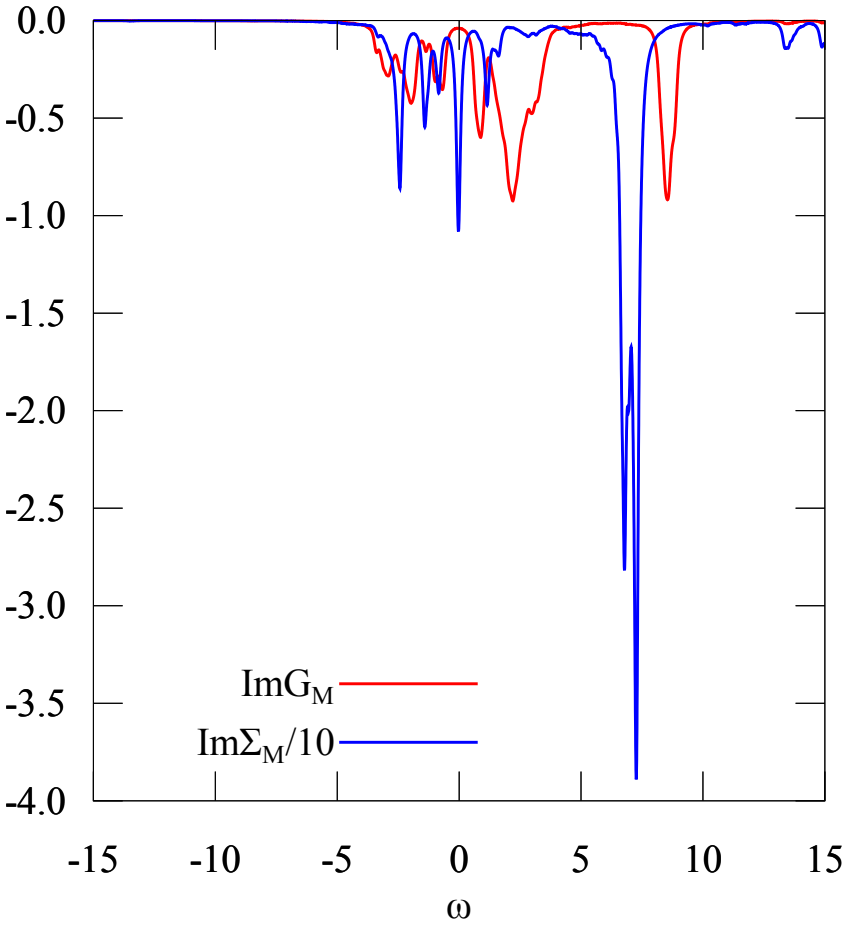

Figure 6.14: *G_M and Σ_M for points inside the Mott region of Fig. 6.13, but near the boundary with the topological insulator.*

while in the "standard" Mott region one of the two Hubbard bands was entirely below the Fermi energy and the other above, consistently with the expected $1-1$ orbital occupation at each site, here the lower band has spread out, with spectral weight close to the Fermi energy both above and below, and a tiny spectral gap for $\omega = 0$.
We can check the effect of this behaviour on the observables of the system by following, for example, the occupation of one orbital on the cluster as a function of M. In Fig. 6.15 the data obtained via single-site DMFT are compared with the CDMFT results (the VCA ones being qualitatively analogous to the latter). In the DMFT case, the discontinuous phase transition between the Mott insulator and the QSH is signalled by a jump in occupation from an even $1-1$ distribution to a fractional one, governed by the inverted bandgap region around Γ which then evolves continuously as M increases. In CDMFT, a "plateau" of occupation close to 0.5 is created between these two regions, while the single-site DMFT results are reproduced far from the transition. In the plateau region, the spectral weight of the Green's functions is accordingly distributed with respect to the Fermi level, as reported for one site (the other one being completely analogous) in the right panel of Fig. 6.15.
This behaviour is indeed what we expect for the occupation of an isolated finite cluster of two-orbital sites with the symmetries of our model: increasing M, one orbital becomes more and more favourable in energy; therefore, starting from the evenly-occupied Mott configuration, it

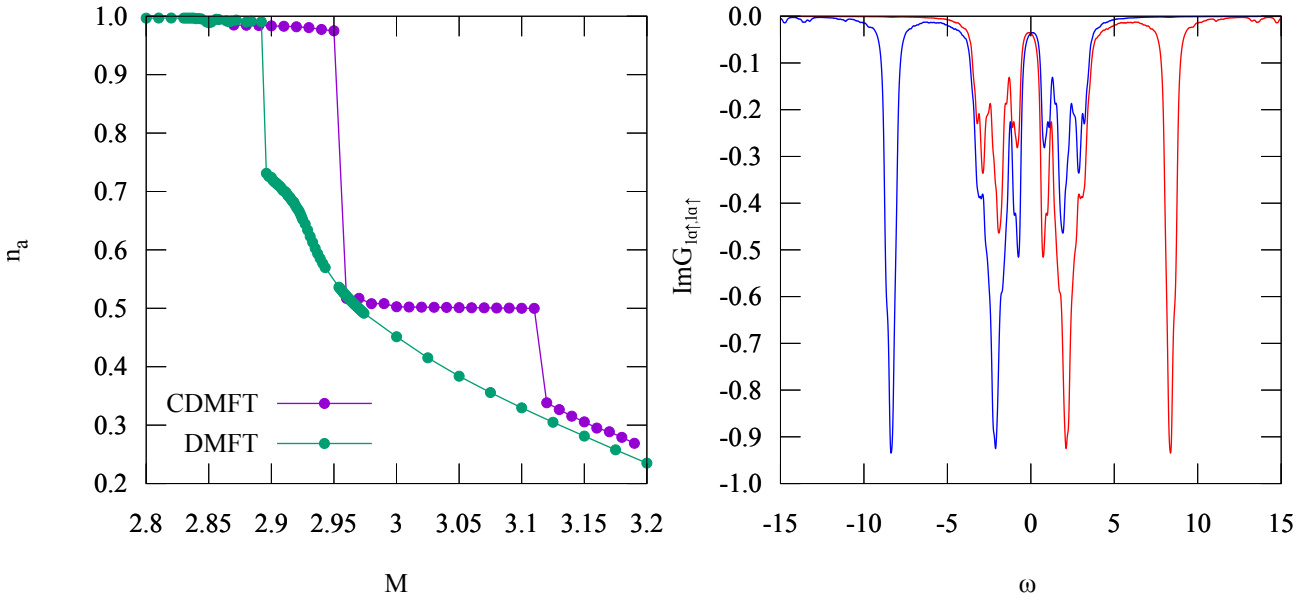

Figure 6.15: *a) Occupation of the lowest occupied orbital for various M, CDMFT vs DMFT data b)Local Green's function for site 1 of the cluster and both orbitals inside the "plateau" of 0.5-1.5 occupation (site 2 is completely analogous)*

is reasonable to assume that the system will progressively transfer charge from the unfavourable to the favourable orbital. In a finite cluster, this happens in discrete steps of one electron at a time, and therefore the average occupation of one orbital over the cluster will decrease in steps of $\frac{1}{N_c}$, where N_c is the cluster size, the other one increasing by the same amount. We can see this process at work in Fig. 6.16, where we considered two isolated clusters of size 3 and 4 respectively, and solved the system exactly. As we can see, the average occupation, depicted by a red line, follows the behaviour above outlined. The orange and green curves refer to the occupations of orbital a at each site in both cases. They are related by symmetry: in the 3-site cluster, the middle site will have a different behaviour from that of the two equivalent border sites (thicker lines), as it will be for the internal and border sites of the 4-site case.
It would appear that the CDMFT solution follows, in a narrow region between the standard Mott and QSH ones, the behaviour of an isolated cluster.

This result is however not trivial, since the hybridizations V are in fact finite throughout the whole region. We can check this assumption by considering the VCA results in the same area, which exhibit the same plateau-like behaviour. The shape of Ω as a function of the variational parameter V for the purple dot in the phase diagram of Fig. 6.13 is reported in the left panel of Fig. 6.17, and exhibits an interesting behaviour. As we previously saw for the first-order topological transition, two minima are present, separated by a metastable maximum. Observing the evolution of the curve increasing M we will see the minima relative energy change sign when the system stabilizes in the QSH phase. The right local minimum, denoted with a white dot, is therefore the topological insulator solution, while the left, signalled by a black dot, corresponds to the anomalous Mott-plateau behaviour. Between the two there will be a discontinuous phase transition, consistently with the behaviour of the occupation n_1 depicted in Fig. 6.15.

An observation regarding the $V = 0$ local minimum is in order: in the context of VCA, the status of the minima for which the optimal variational parameter is 0 is somewhat peculiar.

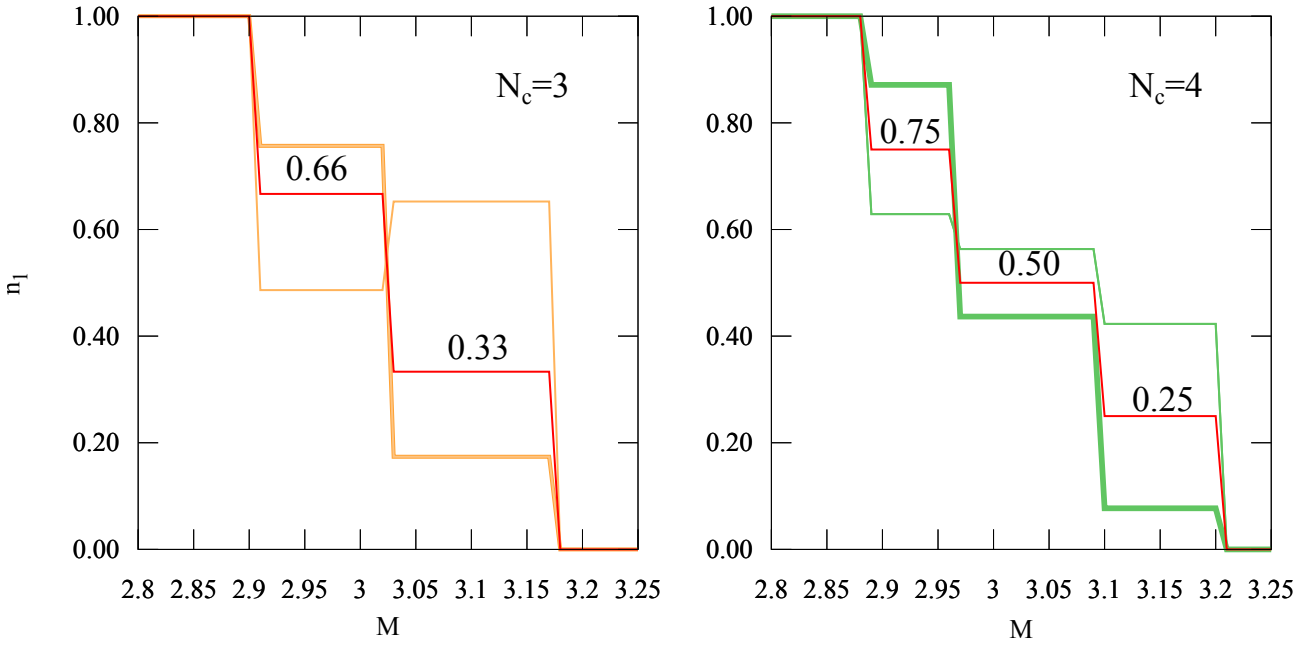

Figure 6.16: *Occupation for one orbital in the isolated cluster case: two clusters of 3 and 4 sites have been considered. In each graph, the red line corresponds to the average occupation among the sites.)*

It is referred to as a *trivial stationary point* [166] and is, in general, a less reliable solution than others, because it effectively decouples the reference systems and reduces the size of the variational space in which the Self-Energy can be determined. Therefore, in general, if other stationary points are present they should be preferred to the trivial one. However, this observation is true in the context of a systematic improvement of the description of the model, that is, if we study the same VCA problem via increasingly large and complicated reference clusters: in this case, a zero variational parameter would spoil the additional resolution gained increasing the size of the variational space.
The situation is slightly different in our case: we are, in fact, not considering a systematic improvement of the approximation via progressively more complicated clusters, but simply changing the external parameters of the full lattice model. While this does not allow us to conclude how much this solution is representative of the actual solution of the model, the fact that the system chooses this solution only for some values of the parameter suggests a physical reason for this result, also confirmed by the comparison with CDMFT.

In the right panel of Fig. 6.17 we consider CDMFT data for a series of systems at the same value of interaction (the usual $U = 8$) but different spin-orbit coupling λ. Since this is effectively a hopping term, increasing it should intuitively have the effect of shrinking the Mott region, and favouring the QSH solution, whose bandgap is protected by virtue of λ. In fact, for $\lambda = 0.5$ we can see that the anomalous flat plateau is shrunk by both sides, with the QSH being stable for higher values of M and a configuration with occupations continuously deviating from $1 - 1$ for lower crystal-field splitting. For $\lambda = 0.7$, the plateau is completely washed away.

The combination of the VCA and CDMFT results appears to suggest that, in the region close to the transition, the Mott insulating solution is very similar to that an isolated cluster, even in the CDMFT framework which features a finite value of hybridization V throughout the

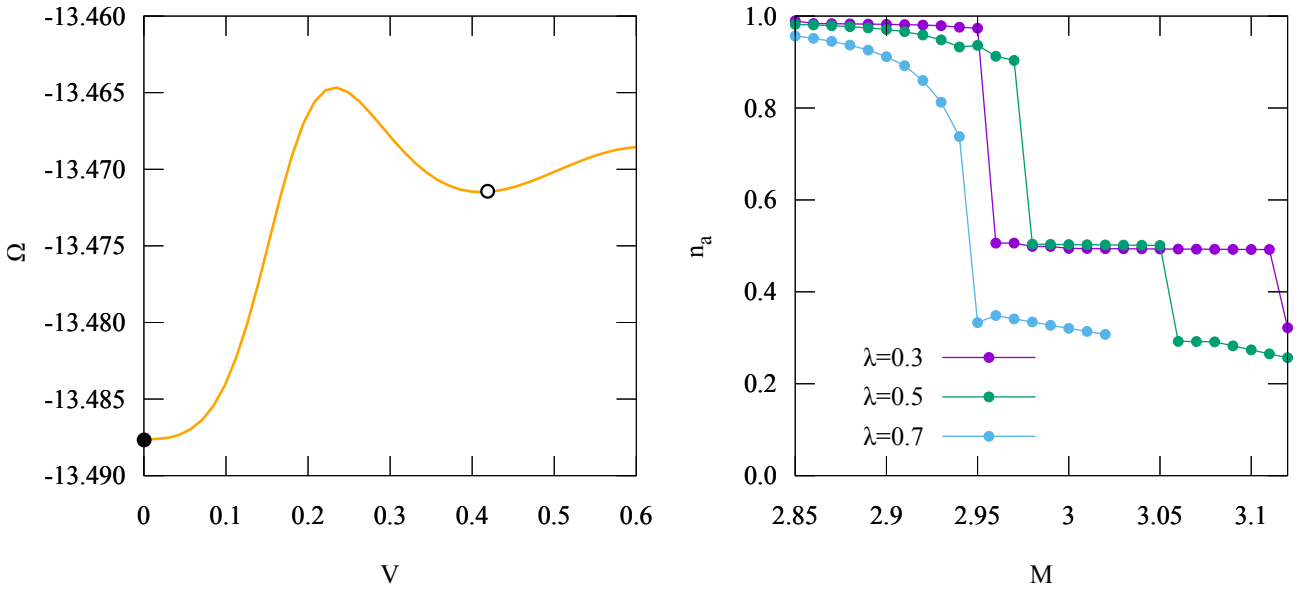

Figure 6.17: *a) Shape of the Ω potential inside the plateau, the decoupled and QSHI solutions are identified by a black and white dot respectively. b) Occupation for various values of λ.*

whole M range. We also notice that, in general, DMFT and CDMFT methods are perfectly able to tune the density to intermediate values which can not be obtained in the cluster. In this light, the fact that the actual solution "prefers" to retain the features of the isolated cluster is not a trivial drawback of the method; on the contrary, it seems to suggest the presence of a specific underlying behaviour. On the other hand, we can not conclude whether this possibility is realized without considering larger clusters, which may confirm or disprove the picture. Current implementations of the approach do not allow to perform these calculations which are left for future investigations.

Conclusions and Outlook

At the end of our analysis we can answer, at least for the systems we specifically considered, the question that we posed in the beginning. The topological phases of the BHZ model, as well as the Weyl semimetal region in a properly modified version of the same model, survive to the presence of strong correlations. Yet, the fingerprints of electron-electron interactions are visible and they strongly influence the topological phases and transitions.

A general result, observed in all the models we considered, is that the nature of the topological phase transition is qualitatively modified. In fact, the very concept of protection of the gap is challenged: in the presence of sizeable electron-electron interactions a topological quantum phase transition becomes discontinuous and can happen without gap closing.

The first results in this direction have been reported in previous literature that motivated the work reported in this thesis. The discontinuous character of the topological transition in the two- and three-dimensional BHZ model has been indeed shown using Dynamical Mean-Field Theory in Refs. [156] and [154] respectively.

One of the main new results we obtained has been to extend this analysis to the case of a three-dimensional BHZ model where a TRS-breaking term introduces regions of Weyl semimetal, centered around the transition points of the time-reversal symmetric model. Also in this case, we find that topological protection is affected by electron correlations. While in the context of noninteracting topological theory the Weyl points can disappear only if they coalesce and annihilate in the same point, in some region of parameters we find that couples of Weyl points with opposite chirality appear and disappear discontinuously without annihilating.

In all the above mentioned models the topological phase transitions has a different character in different regions of the parameter space. In particular, for low values of interaction they retain the continuous character of the non-interacting transitions, with the standard gap closing, whereas at higher values of the interaction they become discontinuous. Thus the point where the transition changes from continuous to discontinuous shares similarities with the critical point of a standard phase transition in the Landau sense, suggesting that, in our interacting framework, the topological transition acquires some similarity with thermodynamical phase transitions.

We associate this behavior to a connection between the topological transition and a strong response in the orbital channel which leads to a divergence of the orbital compressibility, which is a proper response function connected to a thermodynamic instability.

The discontinuous nature of the topological transitions in all the above models results from a different impact of electronic interactions on the two phases. While the topologically non-trivial phases experience a significant frequency-dependent renormalization as measured by the Self-Energy, the band insulator is basically unaffected. This different behaviour inhibits a continuous connection between the two phases as soon as the correlation effects in the topological

phase are significant. Finally, performing calculations in a geometry with open edges, we highlight that the abrupt formation and destruction of the Weyl semimetals is reflected in a similar destiny of the characteristic Fermi arcs observed at the surface.

The second part of the novel work of this thesis is a study of the effect of non-local correlations on the picture we just described. In fact, all the results we discussed have been obtained with DMFT, which treats non-local correlations at a mean-field level, while the local correlations retain their dynamical character. We have therefore implemented two different methods that explicitly address non-local correlations, the Variational Cluster Approximation (VCA) and Cluster Dynamical Mean-Field Theory (CDMFT) in the case of the two-dimensional BHZ model. We have indeed confirmed, through two complementary methods, that the local frequency-dependent properties of the Self-Energy are the driving force behind the discontinuous topological behaviour, while nonlocal renormalization effects and their dynamical character are significantly smaller than the local ones. They therefore play a minor role in affecting the topological phase transitions and they simply lead to mild dynamical corrections to the single-particle parameters, like the hopping and the spin-orbit coupling terms. This result strongly strengthens the generality of the results we discussed.
We finally show that the cluster methods also contribute to connect more firmly our results with the theory of thermodynamical phase transitions. Indeed within VCA, the grandcanonical potential is found to display two minima corresponding to the topological and trivial solutions which exchange their role as the overall minimum on the two sides of the transition. Also within CDMFT, the computation of the energy shows a clear first-order behavior of the internal energy as a function of the mass parameter M, confirming that this quantity, which is coupled with the density difference between the orbitals, acts like the relevant external field.

A further step in this direction will be the study of the three dimensional Weyl semimetal with the same cluster methods. In this system the role of k-space is prominent. The topological protection of the gapless Weyl points is precisely due to their separation in momentum space, and the Fermi arcs are only defined in some regions of the Brillouin zone. It is then natural that the ideal candidates to assess the effects of strong correlation on such a system are cluster methods, that give access to k-dependent Green's functions and Self-Energies. Beyond the static "compression" of the bands of the Topological Hamiltonian obtained within DMFT, such quantities could in principle affect differently various areas of the Brillouin Zone, with consequences on the position of the Weyl points and on the size and shape of the Fermi arcs.
From a computational point of view this poses some challenges: indeed, the k_z dependent term in the Hamiltonian of the three-dimensional BHZ model derived in Chapter 5 couples the spin blocks. It therefore becomes impossible to make use of the great computational advantage deriving from the decoupling of the spin blocks, with the dramatic consequences in terms of scaling evidenced in Chapter 4. A clever choice of cluster could, however, help to mitigate these problems.

The cluster picture has also lead to some puzzling features, such as the plateaux region near the Mott-QSHI transition. Here, it will be important to analyse the effects of antiferromagnetism that, while not relevant in the QSHI-BI phase transition, become prominent in the area occupied by the Mott insulator. Indeed, the inability of finding a correct description of the system in this area could be a consequence of the paramagnetic constraint we are assuming both

in CDMFT and VCA. While the practical inclusion of antiferromagnetism might be trickier in the case of CDMFT with our replica bath setup, VCA is, as stated in the text, perfectly suited to undertake this analysis, and indeed preliminary results for a small set of points confirm that the antiferromagnetic solution is correctly accounted for.

The use of cluster-based methods also allows to address, e.g., the Kane-Mele model, where the role of the two local orbitals in the BHZ model is now played by the inequivalent atoms in the unit cell, rendering this system better suited for a cluster than a single-site DMFT treatment. The persistence of these nontrivial discontinuous effects across different models and setups would be a key element in favour of the presence of an underlying general critical behaviour due to the interplay between topology and strong correlation.

Appendices

Appendix A

Derivation of known topological invariants and models

In this chapter, we will obtain the $\mathbb{Z}_2$ topological invariants for TRS and IS systems following the derivation originally developed by Fu and Kane, as pedagogically presented in [167]. This invariant will be useful in determining, from a bulk perspective, the topological character of the BHZ Hamiltonian as a function of its parameters.

A.1 $\mathbb{Z}_2$ invariant for TRS and IS systems

Let us start by finding a representation of the time-reveral operator for Fermions $T = -i\sigma_y\mathcal{K}$ in the Bloch wavefunction basis for a Kramers pair $|u_{\mathbf{k},1}\rangle$, $|u_{\mathbf{k},2}\rangle$. Defining

$$w_{\alpha\beta}(\mathbf{k}) = \langle u_{\alpha,-\mathbf{k}}|T|u_{\beta,\mathbf{k}}\rangle \tag{A.1}$$

and considering the consequent relation

$$|u_{\alpha,-\mathbf{k}}\rangle = \sum_{\beta} w^*_{\alpha\beta}(\mathbf{k})T|u_{\beta,\mathbf{k}}\rangle \tag{A.2}$$

we conclude that w is a unitary matrix and satisfies

$$w_{\beta,\alpha}(-\mathbf{k}) = -w_{\alpha\beta}(\mathbf{k}). \tag{A.3}$$

This greatly simplifies the expression of w at a TRIM:

$$w(\Lambda) = -\mathrm{i}w_{12}(\Lambda)\sigma_y \tag{A.4}$$

An important property relates the w matrix to the Berry connection, which in general is represented by the set of matrices $\mathbf{a} = (a_x, a_y, a_z)$, with elements

$$\mathbf{a}_{\alpha\beta}(\mathbf{k}) = -i\langle u_{\alpha,\mathbf{k}}|\nabla_{\mathbf{k}}|u_{\beta,\mathbf{k}}\rangle. \tag{A.5}$$

If we apply the T operator in its w-matrix representation to $\mathbf{a}$ and we take the trace, we find the following relation:

$$\mathrm{Tr}[\mathbf{a}(\mathbf{k})] = \mathrm{Tr}[\mathbf{a}(-\mathbf{k})] + i\mathrm{Tr}[w^\dagger(\mathbf{k})\nabla_{\mathbf{k}}w(\mathbf{k})] \tag{A.6}$$

We now apply this relation in the context of a 1D TRS-preserving system in order to derive an expression for the $\mathbb{Z}_2$ invariant. Let us assume that the system parameters vary in time with periodicity T. Time periodicity and TRS imply

$$H(t+T) = H(t) \qquad \text{and} \qquad H(-t) = TH(t)T^{-1} \tag{A.7}$$

from which it follows that the Kramers partners are degenerate for any k at $t = 0$ and $t = \frac{T}{2}$. In the expression for w at these TRS-symmetric times, this implies, from the degeneracy of Kramers partners, the following expression for w:

$$w = \begin{pmatrix} 0 & e^{-i\xi(k)} \\ -e^{-i\xi(-k)} & 0 \end{pmatrix} \tag{A.8}$$

where $\xi(k)$ is a generic phase factor. The Berry connection then satisfies the relation

$$a_{11}(-k) = a_{22}(k) - \frac{\partial}{\partial k}\xi(k). \tag{A.9}$$

We now refer to the charge polarization P_ρ that can be expressed, from the modern theory of ferroelectricity as developed by Resta and Vanderbilt[27], in terms of the trace of the Berry connection as

$$P_\rho = \int_{-\pi}^{\pi} \frac{dk}{2\pi} \mathrm{Tr}[a(k)] = \int_{-\pi}^{\pi} \frac{dk}{2\pi} a_{11}(k) + \int_{-\pi}^{\pi} \frac{dk}{2\pi} a_{22}(k) = P_1 + P_2 \tag{A.10}$$

where we split the contribution due to each Kramers partner. We can then define the *Time-Reversal polarization* as

$$P_\theta = P_1 - P_2 = 2P_1 - P_\rho. \tag{A.11}$$

Let us now calculate this quantity at the TR symetric times. We start from the definition of P_1, splitting the integral in positive and negative k and using (A.9) and $\chi(k) = i \log w_{12}(k)$:

$$\begin{aligned} P_1 &= \frac{1}{2\pi}\left(\int_0^{\pi} dk a_{11}(k) + \int_{-\pi}^{0} dk a_{11}(k) \right) \\ &= \int_0^{\pi} \frac{dk}{2\pi} \mathrm{tr}[a(k)] - \frac{1}{2\pi}[\xi(\pi) - \xi(0)] \\ &= \int_0^{\pi} \frac{dk}{2\pi} \mathrm{tr}[a(k)] - \frac{i}{2\pi} \log \frac{w_{12}(\pi)}{w_{12}(0)} \end{aligned} \tag{A.12}$$

which leads to

$$P_\theta = 2P_1 - P_\rho = \int_0^{\pi} \frac{dk}{2\pi} [A(k) - A(-k)] - \frac{i}{\pi} \log \frac{w_{12}(\pi)}{w_{12}(0)}. \tag{A.13}$$

Now (A.5) comes into play: through it and some algebraic manipulation we can rewrite the time-reversal polarization as

$$\begin{aligned} P_\theta &= i \int_0^{\pi} \frac{dk}{2\pi} \frac{\partial}{\partial k} \log(\det[\mathrm{w(k)}]) - \frac{i}{\pi} \log \frac{w_{12}(\pi)}{w_{12}(0)} \\ &= \frac{i}{\pi} \frac{1}{2} \log \frac{\det[w(\pi)]}{\det[w(0)]} - \frac{i}{\pi} \log \frac{w_{12}(\pi)}{w_{12}(0)} \\ &= \frac{1}{i\pi} \log \left(\frac{\sqrt{w_{12}^2(0)}}{w_{12}(0)} \frac{w_{12}(\pi)}{\sqrt{w_{12}^2(\pi)}} \right). \end{aligned} \tag{A.14}$$

where in the last equivalence we used the relation $\det[w] = w_{12}^2$.
The argument of the log is ± 1; therefore, restricting the codomain of the log function to $[0, 2\pi]$ we will get or the time-reversal polarization the two possible values of 0 and 1. We can now consider the difference in P_θ calculated at $t = 0$ and $t = \frac{T}{2}$. This effectively creates a partition of the Hilbert space based on the mapping between the periodic (k, t) space to the space of wavefunctions. The difference in P_θ is the $\mathbb{Z}_2$ invariant for a 1d TRS system.
We can extend this derivation to a multi-band case rather easily: in the case of $2N$ bands forming N Kramers partners, the w matrix will assume the generalized form

$$w(k) = \begin{bmatrix} 0 & e^{-i\xi_1(k)} & 0 & 0 & \cdots \\ -e^{-i\xi_1(k)} & 0 & 0 & 0 & \cdots \\ 0 & 0 & 0 & e^{-i\xi_2(k)} & \\ 0 & 0 & -e^{-i\xi_2(k)} & 0 & \cdots \\ \vdots & \vdots & \vdots & \vdots & \ddots \end{bmatrix} \tag{A.15}$$

which is antisymmetric at the TR times, where it holds

$$w_{12}(\Lambda_i) w_{34}(\Lambda_i) w_{2N-1,2N}(\Lambda_i) = e^{-i\sum_n = 1^N \xi_n(\Lambda_i)} = \mathrm{Pf}[w(\Lambda_i)] \tag{A.16}$$

where we used the definition of thethe *Pfaffian* of the skew-symmetric w matrix. A derivation analogous to that presented in the 2-band case can be repeated for the multi-band scenario, giving the expression for the topological invariant as

$$(-1)^\nu = \prod_{i=1}^{4} \frac{\mathrm{Pf}[w(\Lambda_i)]}{\sqrt{\det[w(\Lambda_i)]}} \tag{A.17}$$

where Λ_i are the four Time-Reversal invariant point in the toroidal (k, t) space. An intuitive extension to the 2d case can be achieved by identifying the time coordinate with the second direction in k-space.

A.2 $\mathbb{Z}_2$ invariant with inversion symmetry

The inversion operator is a unitary operator which satisfies, in momentum spaces,

$$\Pi|\mathbf{k}, \sigma\rangle = |-\mathbf{k}, \sigma\rangle \tag{A.18}$$

and has eigenvalues ± 1. An Hamiltonian H is symmetric under Π if

$$H(-\mathbf{k}) = H(\mathbf{k}) \tag{A.19}$$

Let us now consider the trace of the Berry connection $\mathbf{A}(\mathbf{k}) = \mathrm{tr}[\mathbf{a}(\mathbf{k})]$ and define its associated curvature

$$\mathbf{F}(\mathbf{k}) = \nabla_{\mathbf{k}} \times \mathbf{A}(\mathbf{k}) \tag{A.20}$$

Considering both TRS and IS, the curvature has to satisfy

$$\begin{aligned} TRS \rightarrow \mathbf{F}(-\mathbf{k}) &= -\mathbf{F}(\mathbf{k}) \\ IS \rightarrow \mathbf{F}(-\mathbf{k}) &= +\mathbf{F}(\mathbf{k}) \end{aligned} \tag{A.21}$$

and is therefore identically 0 for every $\mathbf{k}$. Then, it exists a gauge in which the trace of $\mathbf{a}$ also vanishes. We find that gauge by considering the matrix

$$\nu_{\alpha\beta}(\mathbf{k}) = \langle u_{\alpha\mathbf{k}}|\Pi T|u_{\beta\mathbf{k}}\rangle \tag{A.22}$$

which is a unitary antisymmetric matrix that satisfies

$$\mathbf{A}(\mathbf{k}) = \frac{i}{2}\mathrm{tr}[\nu^\dagger\nabla_{\mathbf{k}}\nu] = \frac{i\nabla_{\mathbf{k}}}{2}\log(\det[\nu(\mathbf{k})]) = i\nabla_{\mathbf{k}}\log\mathrm{Pf}[\nu(\mathbf{k})] \tag{A.23}$$

so, in order to nullify the trace we have to choose the phase in $|u\rangle$ that satisfies $\mathrm{Pf}[\nu(\mathbf{k})] = 1$. We can then calculate the w-matrix of a IS system: remembering that $\Pi^2 = 1$, we can write for a TRIM Λ_i

$$\begin{aligned} w_{\alpha\beta}(\Lambda_i) &= \langle u_\alpha(-\Lambda_i)|\Pi\Pi T|u_\beta(\Lambda_i)\rangle \\ &= \xi_\alpha(\Lambda_i)\langle u_\alpha(\Lambda_i)|\Pi T|u_\beta(\Lambda_i)\rangle \\ &= \xi_\alpha(\Lambda_i)\nu_{\alpha\beta}(\Lambda_i) \end{aligned} \tag{A.24}$$

where $\xi_\alpha = \pm 1$ is the eigenvalue of Π for band α at Λ_i. Since w and ν are antisymmetric, $\xi_\alpha = \xi_\beta$ when $w_{ab} \neq 0$, that is when the bands are in a Kramers pair, hence $\xi_\alpha = \xi_\beta = \xi_{2n}$ if the two bands constitute the n-th Kramers pair in a total of 2N bands. Finally, from the form of the w matrix in the case of N Kramers pairs (A.15), we have

$$\mathrm{Pf}[w(\Lambda_i)] = \mathrm{Pf}[\nu(\Lambda_i)]\prod_{n=1}^{N}\xi_{2n}(\Lambda_i) \tag{A.25}$$

which, with our condition on $\mathrm{Pf}[\nu(\mathbf{k})] = 1$, gives that the contributions to the product (A.17) are

$$\frac{\mathrm{Pf}[w(\Lambda_i)]}{\sqrt{\det[w(\Lambda_i)]}} = \prod_{n=1}^{N}\xi_{2n}(\Lambda_i) \tag{A.26}$$

therefore the $\mathbb{Z}_2$ index ν is given by

$$(-1)^\nu = \prod_{i=1}^{4}\prod_{n=1}^{N}\xi_{2n}(\Lambda_i) \tag{A.27}$$

A beautiful extension of the $\mathbb{Z}_2$ invariant to 3d systems has been proposed by Moore and Balents based on general homotopy arguments. However, an intuitive way of derive its formulation is the following, due to Fu, Kane and Mele[29]: considering for simplicity a cubic lattice, there are 8 TRIMs in 3d. Each face of this cube has the symmetry of a 2 BZ, therefore having an associated $\mathbb{Z}_2$ topological invariant. However, only 3 of these 6 invariants are independent, since the product of the invariant for opposite faces involves the parity eigenvalue at all 8 TRIMs and is therefore fixed. So, the 3d system can topologically be described by a 4-vector of invariants $(\nu_0;\nu_1,\nu_2,\nu_3)$. The second to fourth indices are the topological invariants of the 2d BZ equivalent to the $k_{x,y,z} = \pi$ faces of the cubic BZ, respectively. ν_0 is, instead, the uniquely 3d topological invariant derived from a product over the 8 TRIMS. Equivalently, it is nonzero if the 2d topological invariant for opposite $k_i = 0$ and $k_i = \pi$ faces are different. These four invariants define the two topologically non-trivial phasese of the 3d system: if $\nu_0 = 0$, the system is said to be a weak topological insulator; it is a strong one if $\nu_0 = 1$, the definition being based on the persistence of the surface states in presence of disorder.

A.3 $\mathbb{Z}_2$ classification of the BHZ Hamiltonian

In order to obtain a suitable tight-binding formulation for a general BHZ Hamiltonian, we start from a 2-dimensional square lattice with two orbitals per site. This is a reasonable assumption with respect to the Quantum Well construction, since HgTe crystallizes in the cubic zinc-blende structure, hence the in-plane Hamiltonian will be that of a square lattice, and the two orbitals and spin degrees of freedom will correspond to the relevant subbands. We write the tight-binding Hamiltonian in second quantization as [30]

$$\hat{H}_{BHZ} = \sum_i \sum_{\alpha=a,b} \sum_{s=\uparrow\downarrow} \epsilon_\alpha c^\dagger_{i,\alpha,\sigma} c_{i,\alpha,\sigma} - \sum_i \sum_{a,b} \sum_{\mu=\pm x,\pm y} \sum_{s=\uparrow\downarrow} t^{\alpha\beta}_{\mu s} c^\dagger_{i+\mu,\alpha,\sigma} c_{i,\beta,\sigma} \tag{A.28}$$

fo site i, orbitals a, b and spin $\uparrow, \downarrow$. The hopping term has the following representation:

$$t_{\mu,\sigma} = \begin{pmatrix} t_{aa} & t_{ab} e^{i s_z \theta_\mu} \\ t_{ab} e^{-i s_z \theta_\mu} & -t_{bb} \end{pmatrix} \tag{A.29}$$

where $s_z = \pm 1$ depending on spin and θ_μ can conventionally be chosen as the angle between the negative y-axis and the bond direction. Once rewritten in k-space and acting on the spinor space $\Psi(\mathbf{k}) = (\mathrm{c}_{\mathbf{k}a\uparrow}\, \mathrm{c}_{\mathbf{k}b\uparrow}\, , \mathrm{c}_{\mathbf{k}a\downarrow}\, , \mathrm{c}_{\mathbf{k}b\downarrow})$, the $\mathbf{k}$-dependent Hamiltonian matrix has the following formulation:

$$H(\mathbf{k}) = \sum_{a=0}^{5} d_a(\mathbf{k}) \Gamma^a \tag{A.30}$$

where the Dirac Γ matrices in the spin-orbital basis, including the identity, are made from the Pauli matrices σ_i and τ_i in the following way:

$$\Gamma^0 = \mathbb{I} \otimes \mathbb{I} = \begin{pmatrix} \mathbb{I} & 0 \\ 0 & \mathbb{I} \end{pmatrix} \tag{A.31}$$

$$\Gamma^1 = \sigma_z \otimes \tau_x = \begin{pmatrix} \tau_x & 0 \\ 0 & -\tau_x \end{pmatrix} \tag{A.32}$$

$$\Gamma^2 = -\mathbb{I} \otimes \tau_y = \begin{pmatrix} -\tau_y & 0 \\ 0 & -\tau_y \end{pmatrix} \tag{A.33}$$

$$\Gamma^3 = \sigma_x \otimes \tau_x = \begin{pmatrix} 0 & \tau_x \\ \tau_x & 0 \end{pmatrix} \tag{A.34}$$

$$\Gamma^4 = -\sigma_y \otimes \tau_x = \begin{pmatrix} 0 & -i\tau_x \\ i\tau_x & 0 \end{pmatrix} \tag{A.35}$$

$$\Gamma^5 = \mathbb{I} \otimes \tau_z = \begin{pmatrix} \tau_z & 0 \\ 0 & \tau_z \end{pmatrix} \tag{A.36}$$

and the coefficients are the following;

$$d_0 = \frac{\epsilon_a + \epsilon_b}{2} - (t_{aa} - t_{bb})(\cos(k_x) + \cos(k_y)) \tag{A.37}$$

$$d_1 = 2t_{ab} \sin(k_x) \tag{A.38}$$

$$d_2 = 2t_{ab} \sin(k_y) \tag{A.39}$$

$$d_3 = 0 \tag{A.40}$$

$$d_4 = 0 \tag{A.41}$$

$$d_5 = \frac{\epsilon_a - \epsilon_b}{2} - (t_{aa} + t_{bb})(\cos(k_x) + \cos(k_y)), \tag{A.42}$$

which satisfy the symmetry requirements of the BHZ model near the Γ point.
In the spin-orbital basis, Γ^5 also coincides with the representation of the inversion operator. Therefore, since Γ^0 and Γ^5 are symmetric under both T and Π, and the Hamiltonian at the TRIMs has the form

$$H(\Lambda_i) = d_0(\Lambda_i)\Gamma^0 + d_5(\Lambda_i)\Gamma^5, \tag{A.43}$$

the model is both TRS and IS invariant, hence the use of (A.27) is justified. Kramers degeneracy will also imply the equivalence of a and b eigenvalues for opposite spin at the TRIMs, so that the two energy eigenstates will be, considering that the eigenvalues of $\Pi = \Gamma^5$ are ± 1,

$$\begin{aligned} \langle +|H(\Lambda_i)|+\rangle &= d_0(\Lambda_i) + d_5(\Lambda_i) = E_+ \\ \langle -|H(\Lambda_i)|-\rangle &= d_0(\Lambda_i) - d_5(\Lambda_i) = E_- \end{aligned} \tag{A.44}$$

where we have labelled the eigenstates in terms of their parity. Depending on the relative position of the two orbitals (which in the original QW realization depends on the relative position of the subbands given by the thickness of the well) the parity eigenvalue of the occupied eigenstate will be ± 1. This will determine a topological invariant based on the product of the following quantities, for each of the TRIMs $\Lambda_i = [0/\pi, 0/\pi]$:

$$\begin{aligned} \delta(\Lambda_i) &= -\mathrm{sgn}[d_5(\Lambda_i)] \\ &= -\mathrm{sgn}\left[\frac{\epsilon_a - \epsilon_b}{2} - (t_{aa} + t_{bb})\left((-1)^{\Lambda_i(x)/\pi} + (-1)^{\Lambda_i(y)/\pi}\right)\right] \end{aligned} \tag{A.45}$$

The topological condition then reduces to the following: if $\epsilon_a - \epsilon_b > 4(t_{aa} + t_{bb})$, $\delta < 0$ for every TRIM, so the system is in a trivial phase. If instead $\epsilon_a - \epsilon_b > 4(t_{aa} + t_{bb})$, $\delta([0,0])$ changes sign, and the system becomes a TI. If we consider a simplified version of the model, in which $\epsilon_a = -\epsilon_b = M$ and $t_{aa} = t_{bb} = \epsilon/2$, the condition simplifies to

$$\begin{aligned} M > 2\epsilon &\rightarrow \nu = 0 \\ M < 2\epsilon &\rightarrow \nu = 1 \end{aligned} \tag{A.46}$$

which is the condition used throughout this work.

A.4 Simplified expression for the interacting TKNN invariant

As an example of the relation between the interacting topological invariants and their simpler formulation in terms of "R-zeros", we show the simple case of the first Chern number, the other demonstrations being more involved but conceptually similar.
The starting point of Wang and Zhang's demonstration of the equivalence between (N_2) and

(C_1), as presented in [65], is the Lehmann representation of the Green's function on the Matsubara axis at T=0

$$G_{\alpha\beta}(i\omega,k)=\sum_m\left[\frac{\langle 0|c_{k\alpha}|m\rangle\langle m|c^\dagger_{k\beta}|0\rangle}{i\omega-(E_m-E_0)}+\frac{\langle m|c_{k\alpha}|0\rangle\langle 0|c^\dagger_{k\beta}|m\rangle}{i\omega+(E_m-E_0)}\right] \tag{A.47}$$

where $|0\rangle$ is the GS and $|m\rangle$ are the eigenvectors of the full Hamiltonian. The next step is to decompose G in its real and imaginary parts $G=G_1+iG_2$, which are both hermitian. Then

$$\begin{aligned}(G_2)_{\alpha\beta}&=-\sum_m\frac{\omega}{\omega^2+(E_m-E_0)^2}\left[\langle 0|c_{k\alpha}|m\rangle\langle m|c^\dagger_{k\beta}|0\rangle+\langle m|c_{k\alpha}|0\rangle\langle 0|c^\dagger_{k\beta}|m\rangle\right]\\&=-\sum_m d_m\left[u^*_{m\alpha}(k)u_{m\beta}(k)+v^*_{m\alpha}(k)v_{m\beta}(k)\right]\end{aligned} \tag{A.48}$$

where clearly $\mathrm{sign}(d_m)=\mathrm{sign}(\omega)$ and therefore, for a vector $|\alpha\rangle$,

$$\mathrm{sign}(\langle\alpha|G_2|\alpha\rangle)=-\mathrm{sign}(\omega). \tag{A.49}$$

If $|\alpha\rangle$ is an eigenvector of G with eigenvalue μ_α^{-1} this, along with tha fact that G_1 and G_2 are hermitian, implies

$$\mathrm{sign}[\mathrm{Im}(\mu_\alpha(i\omega,k))]=\mathrm{sign}(\omega) \tag{A.50}$$

After this preparation, the crucial step of the demonstration is to introduce a smooth trajectory

$$G(i\omega,k,\lambda)=(1-\lambda)G(i\omega.k)+\lambda[i\omega+G^{-1}(0,k)]^{-1} \tag{A.51}$$

which is indeed smooth in the sense that it doesn't contain singularities. This can be shown by noting that the eigenvalues at every λ are nonzero. They are nonzero for $i\omega=0$ by hypothesis, and for $i\omega\neq 0$ because

$$\mathrm{Im}[\mu_\alpha^{-1}(i\omega,k,\lambda)]=\langle\alpha|\alpha\rangle^{-1}\left[(1-\lambda)\langle\alpha|G_2(i\omega,k)|\alpha\rangle-\lambda\omega\sum_s|\alpha_s|^2(\omega^2+\epsilon_s^2)^{-1}\right] \tag{A.52}$$

where we used the expansion

$$|\alpha(i\omega,k,\lambda)\rangle=\sum_s\alpha_s(i\omega,k,\lambda)|s(k)\rangle \tag{A.53}$$

for $|s(k)\rangle$ orthonormal eigenvectors of $-G^{-1}(0,k)$ and ϵ_s the associated eigenvalues. Therefore, since the deformation is smooth, R-zeros and L-zeros are kept separate and the topological invariant N_2 is preserved. As a consequence of its nature as a topological invariant, then, $N_2(\lambda=0)=N_2(\lambda=1)$.
We now need to prove that $N_2(\lambda=1)=C_1$: to do so, we express the Green's function in the basis of the eigenvectors of $G^{-1}(0,k)$ defined in chapter 2,

$$G(i\omega,k,1)=\frac{1}{i\omega-H(k)}=\sum_\alpha\frac{|k\alpha\rangle\langle k\alpha|}{i\omega-\mu_\alpha(0,k)} \tag{A.54}$$

where we identified $H(k) = -G^{-1}(0,k)$ for brevity and then write, from the definition of N_2,

$$\begin{aligned} N_2 &= \frac{1}{24\pi^2}\int dk_0 d^2k \mathrm{Tr}[\epsilon^{\mu\nu\rho} G\partial_\mu G^{-1} G\partial_\nu G^{-1} G\partial_\rho G^{-1}] \\ &= \int \frac{i\ d\omega\ d^2k}{8\pi^2}\mathrm{Tr}\Big[G\partial_{i\omega}G^{-1}\Big(G\partial_{k_x}G^{-1}G\partial_{k_y}G^{-1} - G\partial_{k_y}G^{-1}G\partial_{k_x}G^{-1}\Big)\Big] \\ &= i\int \frac{d^2k}{4\pi}\int\frac{d\omega}{2\pi}\epsilon^{ij}\sum_{\alpha\beta\gamma\delta}\langle\alpha k|\frac{|\beta k\rangle\langle\beta k|}{i\omega-\mu_\beta(0,k)}\frac{|\gamma k\rangle\langle\gamma k|}{i\omega-\mu_\gamma(0,k)}\partial_{k_i}H(k)\frac{|\delta k\rangle\langle\delta k|}{i\omega-\mu_\delta(0,k)}\partial_{k_j}H(k)|\alpha k\rangle \end{aligned} \tag{A.55}$$

We then sum over complete sets to obtain

$$N_2 = i\int\frac{d^2k}{4\pi}\int\frac{d\omega}{2\pi}\varepsilon^{ij}\sum_{\alpha\beta}\frac{\langle ak|\partial_{k_x}H(k)|\beta k\rangle\langle\beta k|\partial_{k_y}H(k)|\alpha k\rangle}{(i\omega-\mu_\alpha(0,k))^2(i\omega-\mu_\beta(0,k))} \tag{A.56}$$

and solve the integral over frequencies, which has opposite residues at $-i\mu_\alpha(0,k)$ and $-i\mu_\beta(0,k)$, meaning that only terms in which $|\alpha k\rangle$ is a R-zero and $|\beta k\rangle$ is a L-zero or vice-versa give a finite contribute to N_2. We can then rewrite the previous expression as

$$N_2 = i\int\frac{d^2k}{4\pi}\Bigg(2\varepsilon^{ij}\sum_{\substack{\alpha\in R-space\\ \beta\in L-spacw}}\frac{\langle\alpha k|\partial_{k_i}H(k)|\beta k\rangle\langle\beta k|\partial_{k_j}H(k)|\alpha k\rangle}{(\mu_\alpha(0,k)-\mu_\beta(0,k))^2}\Bigg) \tag{A.57}$$

which is strikingly similar to the Kubo formula that enters the derivation of the first Chern number. Indeed, it is now a simple matter of manipulation: substituting, due to orthogonality of L and R spaces

$$\sum_{\beta\in L-space}|\beta k\rangle\langle\beta k| \to \mathbb{I} - \sum_{\alpha\in R-space}|\alpha k\rangle\langle\alpha k|$$

and considering that

$$\begin{aligned} \langle\alpha k|\partial_{k_i}H(k)|\beta k\rangle &= \langle\alpha k|\partial_{k_i}\Big(H(k)|\beta k\rangle\Big) - \langle\alpha k|H|\partial_{k_i}\beta k\rangle \\ &= \big(\mu_\beta(0,k)-\mu_\alpha(0,k)\big)\langle\beta k|\partial_{k_i}\alpha k\rangle \\ &= -\big(\mu_\beta(0,k)-\mu_\alpha(0,k)\big)\langle\partial_{k_i}\beta k|\alpha k\rangle \end{aligned} \tag{A.58}$$

we get

$$N_2 = \frac{1}{2\pi}\int d^2k(-i)\sum_{\alpha\in R-space}\langle\partial_{k_x}\alpha k|\partial_{k_y}\alpha k\rangle - \langle\partial_{k_y}\alpha k|\partial_{k_x}\alpha k\rangle = \frac{1}{2\pi}\int d^2\mathcal{F}_{xy} = C_1. \tag{A.59}$$

Appendix B

Methods: some explicit calculations

B.1 The cavity method derivation of DMFT

We will derive the DMFT self-consistency equations through the cavity construction[84] for a 1 band Hubbard model, the general Hamiltonian of which is written as

$$\hat{H} = -\sum_{ij,\sigma} t_{ij}(c^\dagger_{i\sigma}c_{j\sigma} + \text{h.c.}) - \mu\sum_{i\sigma}\hat{n}_{i\sigma} + U\sum_i \hat{n}_{i\uparrow}\hat{n}_{i\downarrow} \tag{B.1}$$

to which it corresponds a partition function that can be written in the path-integral formalism in term of the Grassmann variables $c, c^\dagger$ as

$$Z = \int \mathcal{D}[c^\dagger, c]e^{-S} \tag{B.2}$$

The action in imaginary time is given by

$$\begin{aligned} S &= \int_0^\beta d\tau \mathcal{L}[\tau, c^\dagger, c] \\ &= \int_0^\beta \left(\sum_{i\sigma} c^\dagger_{i\sigma}(\tau)(\partial_\tau - \mu)c_{i\sigma}(\tau) - \sum_{ij,\sigma} t_{ij}\left(c^\dagger_{i\sigma}(\tau)c_{j\sigma}(\tau) + \text{h.c.}\right) + U\sum_i \hat{n}_{i\uparrow}(\tau)\hat{n}_{i\downarrow}(\tau)\right) \end{aligned} \tag{B.3}$$

and can be rewritten as to single out the contribution of a specific site as the sum of the three terms

$$S_0 = \int_0^\beta d\tau \left(\sum_\sigma c^\dagger_{0\sigma}(\tau)(\partial_\tau - \mu)c_{0\sigma}(\tau) + U\hat{n}_{0\uparrow}(\tau)\hat{n}_{0\downarrow}(\tau)\right) \tag{B.4}$$

$$S^{(o)} = \int_0^\beta d\tau \left(\sum_{i\neq 0,\sigma} c^\dagger_{i\sigma}(\tau)(\partial_\tau - \mu)c_{i\sigma}(\tau) - \sum_{ij\neq 0,\sigma} t_{ij}\left(c^\dagger_{i\sigma}(\tau)c_{j\sigma}(\tau) + \text{h.c.}\right) + U\sum_{i\neq 0} \hat{n}_{i\uparrow}(\tau)\hat{n}_{i\downarrow}(\tau)\right) \tag{B.5}$$

$$\Delta S = -\int_0^\beta d\tau \sum_{i\sigma}(c^\dagger_{i\sigma}(\tau)\eta_{i\sigma}(\tau) + \text{h.c.}) \tag{B.6}$$

where the last first term is the on-site contribution, the second the contribution of the lattice in presence of the "cavity", that is with site 0 removed, and the third is the hybridization part between the two components, in which the "source terms" $\eta_i = t_{i0}c_{0\sigma}$ and its conjugate have

been defined.
It is now a matter of integrating out from the partition function all the fermionic degrees of freedom not related to site 0, to obtain an effective action

$$\frac{1}{Z_{eff}} e^{-S_{eff}[c^\dagger_{0\sigma}, c_{0\sigma}]} = \frac{1}{Z} \int \prod_{i\neq 0,\sigma} \mathcal{D}c^\dagger_{i\sigma} \mathcal{D}c_{i\sigma} e^{-S} \tag{B.7}$$

which, under the split expression of S, gives

$$S_{eff} = S_0 + \text{const.} + \ln \left\langle e^{-\int_0^\beta d\tau \Delta S} \right\rangle_{S^{(0)}} \tag{B.8}$$

The last term is the generating functional of the Green's function of the cavity, hence the linked cluster theorem can be applied to rewrite it as a series in the n-point Greens functions

$$\sum_{n=1}^{\infty} \sum_{i_1 \ldots j_n} \int_0^\beta d\tau_{i_1} \ldots d\tau_{j_n} \eta^\dagger_{i_i}(\tau_{i_1}) \ldots \eta^\dagger_{i_n} G^{(o)}_{i_1 \ldots j_n} \eta_{j_1} \ldots \eta_{j_n} \tag{B.9}$$

where the cavity Green's functions $G^{(o)}$ represent the propagation of electrons leaving and returning to the cavity site.
Now the dimensionality argument of Metzner and Vollhardt on the scaling of the hopping amplitude comes into play. In the limit of ∞-dimenions, any n-point Green's function above $n = 2$ gives a vanishing contribution: this has to do with the the t_{ij} term embedded in η scales as $(\frac{1}{\sqrt{d}})^{|i-j|}$, and can be verified by looking at the lowest order terms: the two-point Green's function scales as $d^{-|i-j|/2}$,so considering the two contribution by η and $\eta^\dagger$ and the d-dimensional summation outside the integral the total contribution is of order 1.
The 4-points Green's function instead falls off like $(1/\sqrt{d})^{|i-j|}(1/\sqrt{d})^{|i-k|}(1/\sqrt{d})^{|i-l|}$. When $i \neq j \neq k \neq l$, there are four sums contributing a factor d^4 and four t factors contributing d^{-2}. Since $|i-j|$, $|i-l|$ and $|i-k|$ are at least 2, the total contribution scales as $1/d$.
If, instead, $i = j \neq k \neq l$ there are three sums contributing d^3, four factors t contributing d^{-2} and the Green's function contribution which is also d^{-2}, so the result again scales as $1/d$. A similar argument holds for any higher order.
The expression for the effective action is therefore greatly simplified and assumes a quadratic form

$$S_{eff} = \int_0^\beta d\tau d\tau' \sum_{ij} t_{i0} t_{0j} c^\dagger_{0\sigma}(\tau) c_{0\sigma}(\tau') G^{(o)}(\tau, \tau') + S_0 \tag{B.10}$$

whch lets us introduce the Weiss field encountered in the text with the form, in frequency space,

$$\mathcal{G}_0^{-1}(i\omega_n) = i\omega_n + \mu - \sum_{ij} t_{i0} t_{0j} G^{(o)}_{ij}(i\omega_n) \tag{B.11}$$

end rewrite the effective action in the form

$$S_{eff} = -\int_0^\beta d\tau d\tau' c^\dagger_{0\sigma}(\tau) \mathcal{G}_0^{-1} c_{0\sigma}(\tau') + \int_0^\beta d\tau U \hat{n}_{0\uparrow}(\tau) \hat{n}_{0\downarrow}(\tau) \tag{B.12}$$

The final step is to obtain a self-consistency relation: to that end, we establish the relation between the Green's function of the lattice in presence of the cavity and that of the full lattice. These are related by

$$G^{(o)}_{ij} = G_{ij} - \frac{G_{i0} G_{0j}}{G_{00}} \tag{B.13}$$

which can be interpreted as the removal of all the path that visit site 0 only once. The Weiss Green's function then can be rewritten as

$$\mathcal{G}_0^{-1} = i\omega_n + \mu - \sum_{ij} t_{i0}t_{0j}\left[G_{ij}(i\omega_n) - G_{i0}(i\omega_n)G_{00}^{-1}(i\omega_n)G_{0j}(i\omega_n)\right] \tag{B.14}$$

Now we pass in Fourier space through

$$G_{ij}(i\omega_n) = \sum_{\mathbf{k}} e^{i\mathbf{k}\cdot\mathbf{R_{ij}}} G(\mathbf{k}, i\omega_n) \qquad \epsilon(\mathbf{k}) = \sum_{ij} t_{ij} e^{i\mathbf{k}\cdot\mathbf{R_{ij}}} \tag{B.15}$$

and consider the local Green's function of the original lattice obtained as the sum over the k-vectors. We then transform the sum into an integral over the energy weighted by the non-interacting density of states

$$D(\epsilon) = \sum_{\mathbf{k}} \delta(\epsilon - \epsilon_{\mathbf{k}}) \tag{B.16}$$

to rewrite the expression of the Weiss field in terms of $\zeta = i\omega_n + \mu - \Sigma(i\omega_n)$:

$$\mathcal{G}_0^{-1}(i\omega_n) = i\omega_n + \mu - \int_{-\infty}^{+\infty} d\epsilon \frac{D(\epsilon)\epsilon^2}{\zeta - \epsilon} + \left(\int_{-\infty}^{\infty} d\epsilon \frac{D(\epsilon)\epsilon}{\zeta - \epsilon}\right)^2 \Big/ \int_{-\infty}^{\infty} d\epsilon \frac{D(\epsilon)}{\zeta - \epsilon} \tag{B.17}$$

Using the general algebraic relations

$$\int_{-\infty}^{\infty} d\epsilon \frac{D(\epsilon)\epsilon^2}{\zeta - \epsilon} = \zeta \int_{-\infty}^{\infty} d\epsilon \frac{D(\epsilon)\epsilon}{\zeta - \epsilon} \tag{B.18}$$

$$\int_{-\infty}^{\infty} d\epsilon \frac{D(\epsilon)\epsilon}{\zeta - \epsilon} = -1 + \zeta \int_{-\infty}^{\infty} d\epsilon \frac{D(\epsilon)}{\zeta - \epsilon} \tag{B.19}$$

we finally obtain by direct calculation

$$\mathcal{G}_0^{-1}(i\omega_n) = i\omega_n + \mu - \zeta + [\tilde{D}(i\omega_n + \mu - \Sigma)]^{-1} = \Sigma + [\tilde{D}(i\omega_n + \mu - \Sigma)]^{-1} \tag{B.20}$$

which from the definition of the inverse of the Hilbert transform is equivalent to the self-concistency condition and, once convergence of the iterative solving method has been reached, to the Dyson equation for the impurity problem.

B.2 Properties of the Luttinger-Ward functional

We will follow the demonstrations as presented in [166] The usual diagrammatic derivation of the Luttinger-Ward functional implies all the properties enunciated in chapter 3. As in the main text, will distinguish the functional $\hat{\Phi}_U$ from its value at a certain point $\Phi_{\mathbf{H},U}$ (where $\mathbf{H}$ is the noninteracting hopping matrix and U the interaction), the same convention applying to $\mathbf{\Sigma}$ and $\mathbf{G}$. The bold quantities will again refer to matricial entities in the mixed representation. The functional is universal by construction, as it depends on the fully interacting $\mathbf{G}$ belonging to the "space of Green's functions", and any diagram only depends on U and $\mathbf{G}$. Since there is no zero-order diagram in the functional's expansion, it reduces to 0 in the noninteracting limit. The functional derivative of $\hat{\Phi}$ corresponds to the removal of a propagator from each of

the diagrams, which gives the usual formulation of the Self-Energy in skeleton expansion. This proves the relation

$$\frac{1}{T}\frac{\delta\hat{\Phi}_U[\mathbf{G}]}{\delta\mathbf{G}} = \hat{\mathbf{\Sigma}}_U[\mathbf{G}] \tag{B.21}$$

We now address the property

$$\Omega_{\mathbf{H},U} = \Phi_{\mathbf{H},U} + \mathrm{Tr}\ln\mathbf{G}_{\mathbf{H},U} - \mathrm{Tr}(\mathbf{\Sigma}_{\mathbf{H},U}\mathbf{G}_{\mathbf{H},U}) \tag{B.22}$$

by taking the derivative with respect to the chemical potential μ. Deriving the first term on RHS we have

$$\frac{\partial}{\partial\mu}\Phi_{\mathbf{H},U} = \frac{\partial}{\partial\mu}\hat{\Phi}_U[\mathbf{G}_{\mathbf{H},U}] = \sum_{\alpha\beta}\sum_n \frac{\delta\hat{\Phi}_U[\mathbf{G}_{\mathbf{H},U}]}{\delta[\mathbf{G}_{\mathbf{H},U}]_{\alpha\beta}(i\omega_n)}\frac{\partial[\mathbf{G}_{\mathbf{H},U}]_{\alpha,\beta}(i\omega_n)}{\partial\mu} \tag{B.23}$$

that, making use of the functional derivative, gives

$$\frac{\partial}{\partial\mu}\Phi_{\mathbf{H},U} = \mathrm{Tr}\left(\mathbf{\Sigma}_{\mathbf{H},U}\frac{\partial\mathbf{G}_{\mathbf{H},U}}{\partial\mu}\right) \tag{B.24}$$

The second term gives

$$\frac{\partial}{\partial\mu}\mathrm{Tr}\big[\ln[\mathbf{G}_{\mathbf{H},U}]\big] = \mathrm{Tr}\left(\mathbf{G}^{-1}_{\mathbf{H},U}\frac{\partial\mathbf{G}_{\mathbf{H},U}}{\partial\mu}\right) \tag{B.25}$$

and the third

$$\frac{\partial}{\partial\mu}\mathrm{Tr}(\mathbf{\Sigma}_{\mathbf{H},U}\mathbf{G}_{\mathbf{H},U}) = \mathrm{Tr}\left(\frac{\partial\mathbf{\Sigma}_{\mathbf{H},U}}{\partial\mu}\mathbf{G}_{\mathbf{H},U}\right) + \left(\mathbf{\Sigma}_{\mathbf{H},U}\frac{\partial\mathbf{G}_{\mathbf{H},U}}{\partial\mu}\right) \tag{B.26}$$

Now, remembering that $\mathbf{G}$ and $\mathbf{\Sigma}$ here are the physical quantities of a system, hence Dyson's equation holds, we have, by combining some terms of the previous two equations

$$\begin{aligned}
&\mathrm{Tr}\left(\mathbf{G}^{-1}_{\mathbf{H},U}\frac{\partial\mathbf{G}_{\mathbf{H},U}}{\partial\mu}\right) - \mathrm{Tr}\left(\frac{\partial\mathbf{\Sigma}_{\mathbf{H},U}}{\partial\mu}\mathbf{G}_{\mathbf{H},U}\right) = \\
&\mathrm{Tr}\left[\left(\mathbf{G}^{-1}_{\mathbf{H},U}\frac{\partial\mathbf{G}_{\mathbf{H},U}}{\partial\mu}\mathbf{G}^{-1}_{\mathbf{H},U} - \frac{\partial\mathbf{\Sigma}_{\mathbf{H},U}}{\partial\mu}\right)\mathbf{G}_{\mathbf{H},U}\right] = \\
&\mathrm{Tr}\left[\frac{\partial(-\mathbf{G}^{-1}_{\mathbf{H},U} - \mathbf{\Sigma}_{\mathbf{H},U})}{\partial\mu}\mathbf{G}_{\mathbf{H},U}\right] = \\
&\mathrm{Tr}\left[-\left(\frac{\partial}{\partial\mu}\mathbf{G}^{-1}_{0\mathbf{H}}\right)\mathbf{G}_{\mathbf{H},U}\right] = \\
&-\mathrm{Tr}\mathbf{G}_{\mathbf{H},U}
\end{aligned} \tag{B.27}$$

from which, remembering $\mathrm{Tr}\mathbf{G}_{\mathbf{H},U} = \langle N\rangle_{\mathbf{H},U} = -\frac{\partial\Omega_{\mathbf{H},U}}{\partial\mu}$ we get the result

$$\frac{\partial}{\partial\mu}\big(\Phi_{\mathbf{H},U} + \mathrm{Tr}\ln\mathbf{G}_{\mathbf{H},U} - \mathrm{Tr}\mathbf{\Sigma}_{\mathbf{H},U}\mathbf{G}_{\mathbf{H},U}\big) = \frac{\partial\Omega_{\mathbf{H},U}}{\partial\mu} \tag{B.28}$$

References

[1] L. Landau, "On the theory of phase transitions," Zh. Eksp. Teor. Fiz. **7**, 19–32 (1937).

[2] V. Ginzburg and L. Landau, "On the Theory of superconductivity," Zh. Eksp. Teor. Fiz. **20**, 1064–1082 (1950).

[3] P. W. Anderson, "Plasmons, gauge invariance, and mass," Phys. Rev. **130**, 439–442 (1963).

[4] Y. Nambu, "Nobel lecture: Spontaneous symmetry breaking in particle physics: A case of cross fertilization," Rev. Mod. Phys. **81**, 1015–1018 (2009).

[5] P. Anderson, "Resonating valence bonds: A new kind of insulator?" Materials Research Bulletin **8**, 153 – 160 (1973).

[6] P. W. Anderson, "The resonating valence bond state in la2cuo4 and superconductivity," Science **235**, 1196–1198 (1987).

[7] L. Savary and L. Balents, "Quantum spin liquids: a review," Reports on Progress in Physics **80**, 016502 (2016).

[8] A. Kitaev, "Fault-tolerant quantum computation by anyons," Annals of Physics **303**, 2 – 30 (2003).

[9] X.-G. Wen, "Topological orders and edge excitations in fractional quantum hall states," Advances in Physics **44**, 405–473 (1995).

[10] M. B. Hastings and X.-G. Wen, "Quasiadiabatic continuation of quantum states: The stability of topological ground-state degeneracy and emergent gauge invariance," Phys. Rev. B **72**, 045141 (2005).

[11] X. Chen, Z.-C. Gu, and X.-G. Wen, "Local unitary transformation, long-range quantum entanglement, wave function renormalization, and topological order," Phys. Rev. B **82**, 155138 (2010).

[12] T. Fukui and Y. Hatsugai, "Entanglement chern number for an extensive partition of a topological ground state," Journal of the Physical Society of Japan **83**, 113705 (2014).

[13] H. Araki, T. Fukui, and Y. Hatsugai, "Entanglement chern number for three-dimensional topological insulators: Characterization by weyl points of entanglement hamiltonians," Phys. Rev. B **96**, 165139 (2017).

[14] K. v. Klitzing, G. Dorda, and M. Pepper, "New method for high-accuracy determination of the fine-structure constant based on quantized hall resistance," Phys. Rev. Lett. **45**, 494–497 (1980).

[15] B. I. Halperin, "Quantized hall conductance, current-carrying edge states, and the existence of extended states in a two-dimensional disordered potential," Phys. Rev. B **25**, 2185–2190 (1982).

[16] R. B. Laughlin, "Quantized hall conductivity in two dimensions," Phys. Rev. B **23**, 5632–5633 (1981).

[17] D. J. Thouless, M. Kohmoto, M. P. Nightingale, and M. den Nijs, "Quantized hall conductance in a two-dimensional periodic potential," Phys. Rev. Lett. **49**, 405–408 (1982).

[18] F. D. M. Haldane, "Model for a quantum hall effect without landau levels: Condensed-matter realization of the "parity anomaly"," Phys. Rev. Lett. **61**, 2015–2018 (1988).

[19] B. Bernevig and T. Hughes, *Topological Insulators and Topological Superconductors* (Princeton University Press, 2013).

[20] K. S. Novoselov, A. K. Geim, S. V. Morozov, D. Jiang, Y. Zhang, S. V. Dubonos, I. V. Grigorieva, and A. A. Firsov, "Electric field effect in atomically thin carbon films," Science **306**, 666–669 (2004), https://science.sciencemag.org/content/306/5696/666.full.pdf .

[21] C.-Z. Chang, J. Zhang, X. Feng, J. Shen, Z. Zhang, M. Guo, K. Li, Y. Ou, P. Wei, L.-L. Wang, Z.-Q. Ji, Y. Feng, S. Ji, X. Chen, J. Jia, X. Dai, Z. Fang, S.-C. Zhang, K. He, Y. Wang, L. Lu, X.-C. Ma, and Q.-K. Xue, "Experimental observation of the quantum anomalous hall effect in a magnetic topological insulator," Science **340**, 167–170 (2013).

[22] C. L. Kane and E. J. Mele, "Z_2 topological order and the quantum spin hall effect," Phys. Rev. Lett. **95**, 146802 (2005).

[23] Y. K. Kato, R. C. Myers, A. C. Gossard, and D. D. Awschalom, "Observation of the spin hall effect in semiconductors," Science **306**, 1910–1913 (2004).

[24] S. Murakami, N. Nagaosa, and S.-C. Zhang, "Spin-hall insulator," Phys. Rev. Lett. **93**, 156804 (2004).

[25] C. L. Kane and E. J. Mele, "Quantum spin hall effect in graphene," Phys. Rev. Lett. **95**, 226801 (2005).

[26] L. Fu and C. L. Kane, "Time reversal polarization and a Z_2 adiabatic spin pump," Phys. Rev. B **74**, 195312 (2006).

[27] R. Resta and D. Vanderbilt, "Theory of polarization: A modern approach," in *Physics of Ferroelectrics: A Modern Perspective* (Springer Berlin Heidelberg, Berlin, Heidelberg, 2007) pp. 31–68.

[28] J. E. Moore and L. Balents, "Topological invariants of time-reversal-invariant band structures," Phys. Rev. B **75**, 121306 (2007).

[29] L. Fu, C. L. Kane, and E. J. Mele, "Topological insulators in three dimensions," Phys. Rev. Lett. **98**, 106803 (2007).

[30] L. Fu and C. L. Kane, "Topological insulators with inversion symmetry," Phys. Rev. B **76**, 045302 (2007).

[31] B. A. Bernevig, T. L. Hughes, and S.-C. Zhang, "Quantum spin hall effect and topological phase transition in hgte quantum wells," Science **314**, 1757–1761 (2006).

[32] Y. Yao, F. Ye, X.-L. Qi, S.-C. Zhang, and Z. Fang, "Spin-orbit gap of graphene: First-principles calculations," Phys. Rev. B **75**, 041401 (2007).

[33] D. G. Rothe, R. W. Reinthaler, C.-X. Liu, L. W. Molenkamp, S.-C. Zhang, and E. M. Hankiewicz, "Fingerprint of different spin–orbit terms for spin transport in HgTe quantum wells," New Journal of Physics **12**, 065012 (2010).

[34] M. König, S. Wiedmann, C. Brüne, A. Roth, H. Buhmann, L. W. Molenkamp, X.-L. Qi, and S.-C. Zhang, "Quantum spin hall insulator state in hgte quantum wells," Science **318**, 766–770 (2007).

[35] N. Ashcroft and N. Mermin, *Solid State Physics* (Saunders College, Philadelphia, 1976).

[36] F. Bloch, "Über die quantenmechanik der elektronen in kristallgittern," Zeitschrift für Physik **52**, 555–600 (1929).

[37] G. H. Wannier, "The structure of electronic excitation levels in insulating crystals," Phys. Rev. **52**, 191–197 (1937).

[38] A. A. Abrikosov and I. M. Khalatnikov, "The theory of a fermi liquid (the properties of liquid 3he at low temperatures)," Reports on Progress in Physics **22**, 329–367 (1959).

[39] J. M. Luttinger and J. C. Ward, "Ground-state energy of a many-fermion system. ii," Phys. Rev. **118**, 1417–1427 (1960).

[40] R. Martin, L. Reining, and D. Ceperley, *Interacting Electrons: Theory and Computational Approaches* (Cambridge University Press, 2016).

[41] T. Koopmans, "Über die zuordnung von wellenfunktionen und eigenwerten zu den einzelnen elektronen eines atoms," Physica **1**, 104 – 113 (1934).

[42] A. Zee, *Quantum Field Theory in a Nutshell: Second Edition*, In a Nutshell (Princeton University Press, 2010) Chap. II.5, pp. 123–131.

[43] A. Damascelli, Z. Hussain, and Z.-X. Shen, "Angle-resolved photoemission studies of the cuprate superconductors," Rev. Mod. Phys. **75**, 473–541 (2003).

[44] E. Pavarini, E. Koch, D. Vollhardt, A. Lichtenstein, and eds, *The LDA+DMFT approach to strongly correlated materials, chapter 6* (2011).

[45] J. Slater, *Quantum Theory of Atomic Structure*, International series in pure and applied physics No. v. 2 (McGraw-Hill, 1960).

[46] J. Kanamori, "Electron Correlation and Ferromagnetism of Transition Metals," Progress of Theoretical Physics **30**, 275–289 (1963).

[47] A. Georges, L. d. Medici, and J. Mravlje, "Strong correlations from hund's coupling," Annual Review of Condensed Matter Physics **4**, 137–178 (2013).

[48] F. Hund, "Zur deutung verwickelter spektren, insbesondere der elemente scandium bis nickel," Zeitschrift für Physik **33**, 345–371 (1925).

[49] C. Castellani, C. R. Natoli, and J. Ranninger, "Magnetic structure of v_2o_3 in the insulating phase," Phys. Rev. B **18**, 4945–4966 (1978).

[50] O. Gunnarsson, O. K. Andersen, O. Jepsen, and J. Zaanen, "Density-functional calculation of the parameters in the anderson model: Application to mn in cdte," Phys. Rev. B **39**, 1708–1722 (1989).

[51] F. Aryasetiawan, M. Imada, A. Georges, G. Kotliar, S. Biermann, and A. I. Lichtenstein, "Frequency-dependent local interactions and low-energy effective models from electronic structure calculations," Phys. Rev. B **70**, 195104 (2004).

[52] J. Hubbard, "Electron Correlations in Narrow Energy Bands," Proc. R. Soc. A Math. Phys. Eng. Sci. **276**, 238–257 (1963).

[53] J. Hubbard, "Electron correlations in narrow energy bands. ii. the degenerate band case," Proc. Roy. Soc. (London), Ser. A **277** (1964), 10.1098/rspa.1964.0019.

[54] J. Hubbard and B. H. Flowers, "Electron correlations in narrow energy bands iii. an improved solution," Proceedings of the Royal Society of London. Series A. Mathematical and Physical Sciences **281**, 401–419 (1964).

[55] J. Hubbard and B. H. Flowers, "Electron correlations in narrow energy bands - iv. the atomic representation," Proceedings of the Royal Society of London. Series A. Mathematical and Physical Sciences **285**, 542–560 (1965).

[56] N. F. Mott, "The basis of the electron theory of metals, with special reference to the transition metals," Proceedings of the Physical Society. Section A **62**, 416–422 (1949).

[57] J. H. de Boer and E. J. W. Verwey, "Semi-conductors with partially and with completely filled3d-lattice bands," Proceedings of the Physical Society **49**, 59–71 (1937).

[58] D. B. McWhan, A. Menth, J. P. Remeika, W. F. Brinkman, and T. M. Rice, "Metal-insulator transitions in pure and doped v_2o_3," Phys. Rev. B **7**, 1920–1931 (1973).

[59] E. H. Lieb and F. Y. Wu, "Absence of mott transition in an exact solution of the short-range, one-band model in one dimension," Phys. Rev. Lett. **20**, 1445–1448 (1968).

[60] X.-L. Qi, T. L. Hughes, and S.-C. Zhang, "Topological field theory of time-reversal invariant insulators," Phys. Rev. B **78**, 195424 (2008).

[61] S. Raghu, X.-L. Qi, C. Honerkamp, and S.-C. Zhang, "Topological mott insulators," Phys. Rev. Lett. **100**, 156401 (2008).

[62] Z. Wang, X.-L. Qi, and S.-C. Zhang, "Topological order parameters for interacting topological insulators," Phys. Rev. Lett. **105**, 256803 (2010).

[63] S. C. ZHANG, "The chern–simons–landau–ginzburg theory of the fractional quantum hall effect," International Journal of Modern Physics B **06**, 25–58 (1992).

[64] K. Ishikawa and T. Matsuyama, "Magnetic field induced multi-component qed3 and quantum hall effect," Zeitschrift für Physik C Particles and Fields **33**, 41–45 (1986).

[65] Z. Wang and S.-C. Zhang, "Simplified topological invariants for interacting insulators," Phys. Rev. X **2**, 031008 (2012).

[66] Z. Wang, X.-L. Qi, and S.-C. Zhang, "Topological invariants for interacting topological insulators with inversion symmetry," Phys. Rev. B **85**, 165126 (2012).

[67] Z. Wang, X.-L. Qi, and S.-C. Zhang, "Equivalent topological invariants of topological insulators," New Journal of Physics **12**, 065007 (2010).

[68] M. C. Gutzwiller, "Effect of correlation on the ferromagnetism of transition metals," Phys. Rev. Lett. **10**, 159–162 (1963).

[69] M. C. Gutzwiller, "Effect of correlation on the ferromagnetism of transition metals," Phys. Rev. **134**, A923–A941 (1964).

[70] M. C. Gutzwiller, "Correlation of electrons in a narrow s band," Phys. Rev. **137**, A1726–A1735 (1965).

[71] W. F. Brinkman and T. M. Rice, "Application of gutzwiller's variational method to the metal-insulator transition," Phys. Rev. B **2**, 4302–4304 (1970).

[72] K. Huang, *Statistical Mechanics* (Wiley, 1987).

[73] W. Metzner and D. Vollhardt, "Correlated lattice fermions in $d = \infty$ dimensions," Phys. Rev. Lett. **62**, 324–327 (1989).

[74] E. Müller-Hartmann, "Correlated fermions on a lattice in high dimensions," Zeitschrift für Physik B Condensed Matter **74**, 507–512 (1989).

[75] A. Georges and G. Kotliar, "Hubbard model in infinite dimensions," Phys. Rev. B **45**, 6479–6483 (1992).

[76] W. Metzner, "Linked-cluster expansion around the atomic limit of the hubbard model," Phys. Rev. B **43**, 8549–8563 (1991).

[77] G. Hülsenbeck and F. Stephan, "Hubbard-like models in high spatial dimensions," Zeitschrift für Physik B Condensed Matter **94**, 281–289 (1994).

[78] V. Janiš, "A new construction of thermodynamic mean-field theories of itinerant fermions: application to the falicov-kimball model," Zeitschrift für Physik B Condensed Matter **83**, 227–235 (1991).

[79] V. JANIŠ and D. VOLLHARDT, "Comprehensive mean field theory for the hubbard model," International Journal of Modern Physics B **06**, 731–747 (1992).

[80] E. Economou, *Green's Functions in Quantum Physics*, Springer Series in Solid-State Sciences (Springer Berlin Heidelberg, 1983).

[81] P. W. Anderson, "Localized magnetic states in metals," Phys. Rev. **124**, 41–53 (1961).

[82] X. Y. Zhang, M. J. Rozenberg, and G. Kotliar, "Mott transition in the d=∞ hubbard model at zero temperature," Phys. Rev. Lett. **70**, 1666–1669 (1993).

[83] H. Park, K. Haule, and G. Kotliar, "Cluster dynamical mean field theory of the mott transition," Phys. Rev. Lett. **101**, 186403 (2008).

[84] A. Georges, G. Kotliar, W. Krauth, and M. J. Rozenberg, "Dynamical mean-field theory of strongly correlated fermion systems and the limit of infinite dimensions," Rev. Mod. Phys. **68**, 13–125 (1996).

[85] M. Balzer, B. Kyung, D. Sénéchal, A.-M. S. Tremblay, and M. Potthoff, "First-order mott transition at zero temperature in two dimensions: Variational plaquette study," EPL (Europhysics Letters) **85**, 17002 (2009).

[86] M. Capone, M. Civelli, S. S. Kancharla, C. Castellani, and G. Kotliar, "Cluster-dynamical mean-field theory of the density-driven mott transition in the one-dimensional hubbard model," Phys. Rev. B **69**, 195105 (2004).

[87] M. Hashimoto, I. M. Vishik, R.-H. He, T. P. Devereaux, and Z.-X. Shen, "Energy gaps in high-transition-temperature cuprate superconductors," Nature Physics **10**, 483–495 (2014).

[88] M. H. Hettler, A. N. Tahvildar-Zadeh, M. Jarrell, T. Pruschke, and H. R. Krishnamurthy, "Nonlocal dynamical correlations of strongly interacting electron systems," Phys. Rev. B **58**, R7475–R7479 (1998).

[89] G. Kotliar, S. Y. Savrasov, G. Pálsson, and G. Biroli, "Cellular dynamical mean field approach to strongly correlated systems," Phys. Rev. Lett. **87**, 186401 (2001).

[90] G. Biroli and G. Kotliar, "Cluster methods for strongly correlated electron systems," Phys. Rev. B **65**, 155112 (2002).

[91] E. Koch, G. Sangiovanni, and O. Gunnarsson, "Sum rules and bath parametrization for quantum cluster theories," Phys. Rev. B **78**, 115102 (2008).

[92] M. Civelli, *Investigation of strongly correlated electron systems with cellular dynamical mean field theory*, Ph.D. thesis, Rutgers The State University of New Jersey - New Brunswick (2006).

[93] M. Potthoff, "Self-energy-functional approach to systems of correlated electrons," The European Physical Journal B - Condensed Matter and Complex Systems **32**, 429–436 (2003).

[94] C. Gros and R. Valentí, "Cluster expansion for the self-energy: A simple many-body method for interpreting the photoemission spectra of correlated fermi systems," Phys. Rev. B **48**, 418–425 (1993).

[95] D. Sénéchal, D. Perez, and M. Pioro-Ladrière, "Spectral weight of the hubbard model through cluster perturbation theory," Phys. Rev. Lett. **84**, 522–525 (2000).

[96] E. Pavarini, E. Koch, D. Vollhardt, and A. Lichtenstein, *DMFT at 25: Infinite Dimensions: Lecture Notes of the Autumn School on Correlated Electrons 2014*, Schriften des Forschungszentrums Jülich Reihe Modeling and Simulation (Forschungszentrum Jülich, 2014).

[97] M. Nuss, E. Arrigoni, M. Aichhorn, and W. von der Linden, "Variational cluster approach to the single impurity anderson model," (2011), arXiv:1110.4533 [cond-mat.str-el] .

[98] D. Sénéchal, "An introduction to quantum cluster methods," (2008), arXiv:0806.2690 [cond-mat.str-el] .

[99] D. Sénéchal, "Cluster perturbation theory," in *Strongly Correlated Systems: Theoretical Methods*, edited by A. Avella and F. Mancini (Springer Berlin Heidelberg, Berlin, Heidelberg, 2012) pp. 237–270.

[100] E. Gull, A. J. Millis, A. I. Lichtenstein, A. N. Rubtsov, M. Troyer, and P. Werner, "Continuous-time monte carlo methods for quantum impurity models," Rev. Mod. Phys. **83**, 349–404 (2011).

[101] K. G. Wilson, "The renormalization group: Critical phenomena and the kondo problem," Rev. Mod. Phys. **47**, 773–840 (1975).

[102] R. Bulla, T. A. Costi, and T. Pruschke, "Numerical renormalization group method for quantum impurity systems," Rev. Mod. Phys. **80**, 395–450 (2008).

[103] S. R. White, "Density matrix formulation for quantum renormalization groups," Phys. Rev. Lett. **69**, 2863–2866 (1992).

[104] U. Schollwöck, "The density-matrix renormalization group," Rev. Mod. Phys. **77**, 259–315 (2005).

[105] D. J. García, K. Hallberg, and M. J. Rozenberg, "Dynamical mean field theory with the density matrix renormalization group," Phys. Rev. Lett. **93**, 246403 (2004).

[106] I. Peschel, X. Want, M. Kaulke, and K. Hallberg, *Density matrix renormalization : a new numerical method in physics : lectures of a seminar and workshop held at the Max-Planck-Institut für Physik komplexer Systeme, Dresden, Germany, August 24th to September 18th, 1998*, Vol. 528 (1999).

[107] D. Bauernfeind, M. Zingl, R. Triebl, M. Aichhorn, and H. G. Evertz, "Fork tensor-product states: Efficient multiorbital real-time dmft solver," Phys. Rev. X **7**, 031013 (2017).

[108] M. Ganahl, M. Aichhorn, H. G. Evertz, P. Thunström, K. Held, and F. Verstraete, "Efficient dmft impurity solver using real-time dynamics with matrix product states," Phys. Rev. B **92**, 155132 (2015).

[109] A. Dolfen, *Massively parallel exact diagonalization of strongly correlated systems* (206).

[110] C. Lanczos, "An iteration method for the solution of the eigenvalue problem of linear differential and integral operators," J. Res. Natl. Bur. Stand. B **45**, 255–282 (1950).

[111] W. E. ARNOLDI, "The principle of minimized iterations in the solution of the matrix eigenvalue problem," Quarterly of Applied Mathematics **9**, 17–29 (1951).

[112] A.Krylov, "De la résolution numérique de l'équation servant à déterminer dans des questions de mécanique appliquée les fréquences de petites oscillations des systèmes matériels," Bulletin de l'Académie des Sciences de l'URSS , 491–539 (1931).

[113] E. Polizzi, "Density-matrix-based algorithm for solving eigenvalue problems," Phys. Rev. B **79**, 115112 (2009).

[114] H. Lin, J. Gubernatis, H. Gould, and J. Tobochnik, "Exact diagonalization methods for quantum systems," Computers in Physics **7**, 400–407 (1993).

[115] C. C. Paige, *The computation of eigenvalues and eigenvectors of very large sparse matrices.*, Ph.D. thesis, University of London (1971).

[116] R. Lehoucq, D. Sorensen, and C. Yang, *ARPACK Users' Guide: Solution of Large-scale Eigenvalue Problems with Implicitly Restarted Arnoldi Methods*, Software, Environments, Tools (Society for Industrial and Applied Mathematics, 1998).

[117] M. P. Forum, *MPI: A Message-Passing Interface Standard*, Tech. Rep. (USA, 1994).

[118] K. J. "Maschhoff and D. C. Sorensen, "P_arpack: An efficient portable large scale eigenvalue package for distributed memory parallel architectures," in *Applied Parallel Computing Industrial Computation and Optimization*, edited by J. "Waśniewski, J. Dongarra, K. Madsen, and D. Olesen (Springer Berlin Heidelberg, Berlin, Heidelberg, 1996) pp. 478–486.

[119] E. Pavarini, E. Koch, A. Lichtenstein, and D. E. Vollhardt, *The LDA+DMFT approach to strongly correlated materials, chapter 8*, Schriften des Forschungszentrums Jülich : Modeling and Simulation, Vol. 1 (2011).

[120] M. Caffarel and W. Krauth, "Exact diagonalization approach to correlated fermions in infinite dimensions: Mott transition and superconductivity," Phys. Rev. Lett. **72**, 1545–1548 (1994).

[121] M. Civelli, *Investigation of Strongly Correlated Electron Systems with Cellular Dynamical Mean Field Theory*, Ph.D. thesis (2007).

[122] M. Aichhorn, E. Arrigoni, M. Potthoff, and W. Hanke, "Variational cluster approach to the hubbard model: Phase-separation tendency and finite-size effects," Phys. Rev. B **74**, 235117 (2006).

[123] D. Sénéchal, "The variational cluster approximation for hubbard models: Practical implementation," in *2008 22nd International Symposium on High Performance Computing Systems and Applications* (2008) pp. 9–15.

[124] R. Piessens, *Quadpack: A Subroutine Package for Automatic Integration*, Computational Mathematics Series (Springer-Verlag, 1983).

[125] K. Seki, T. Shirakawa, and S. Yunoki, "Variational cluster approach to thermodynamic properties of interacting fermions at finite temperatures: A case study of the two-dimensional single-band hubbard model at half filling," Phys. Rev. B **98**, 205114 (2018).

[126] R. H. Byrd, P. Lu, J. Nocedal, and C. Zhu, "A limited memory algorithm for bound constrained optimization," SIAM Journal on Scientific Computing **16**, 1190–1208 (1995).

[127] S. Murakami, "Phase transition between the quantum spin hall and insulator phases in 3d: emergence of a topological gapless phase," New Journal of Physics **9**, 356–356 (2007).

[128] L. Lu, Z. Wang, D. Ye, L. Ran, L. Fu, J. D. Joannopoulos, and M. Soljačić, "Experimental observation of weyl points," Science **349**, 622–624 (2015).

[129] L. X. Yang, Z. K. Liu, Y. Sun, H. Peng, H. F. Yang, T. Zhang, B. Zhou, Y. Zhang, Y. F. Guo, M. Rahn, D. Prabhakaran, Z. Hussain, S.-K. Mo, C. Felser, B. Yan, and Y. L. Chen, "Weyl semimetal phase in the non-centrosymmetric compound TaAs," Nature Physics **11**, 728 EP – (2015).

[130] S.-Y. Xu, I. Belopolski, N. Alidoust, M. Neupane, G. Bian, C. Zhang, R. Sankar, G. Chang, Z. Yuan, C.-C. Lee, S.-M. Huang, H. Zheng, J. Ma, D. S. Sanchez, B. Wang, A. Bansil, F. Chou, P. P. Shibayev, H. Lin, S. Jia, and M. Z. Hasan, "Discovery of a weyl fermion semimetal and topological fermi arcs," Science **349**, 613 (2015).

[131] S. Nakatsuji, N. Kiyohara, and T. Higo, "Large anomalous hall effect in a non-collinear antiferromagnet at room temperature," Nature **527**, 212 EP – (2015).

[132] K. Deng, G. Wan, P. Deng, K. Zhang, S. Ding, E. Wang, M. Yan, H. Huang, H. Zhang, Z. Xu, J. Denlinger, A. Fedorov, H. Yang, W. Duan, H. Yao, Y. Wu, S. Fan, H. Zhang, X. Chen, and S. Zhou, "Experimental observation of topological Fermi arcs in type-II Weyl semimetal $MoTe_2$," Nat. Phys. **12**, 1105–1110 (2016).

[133] B. Q. Lv, N. Xu, H. M. Weng, J. Z. Ma, P. Richard, X. C. Huang, L. X. Zhao, G. F. Chen, C. E. Matt, F. Bisti, V. N. Strocov, J. Mesot, Z. Fang, X. Dai, T. Qian, M. Shi, and H. Ding, "Observation of Weyl nodes in TaAs," Nat. Phys. **11**, 724–727 (2015).

[134] M. Ikhlas, T. Tomita, T. Koretsune, M.-T. Suzuki, D. Nishio-Hamane, R. Arita, Y. Otani, and S. Nakatsuji, "Large anomalous nernst effect at room temperature in a chiral antiferromagnet," Nature Physics **13**, 1085 EP – (2017).

[135] J. Jiang, Z. K. Liu, Y. Sun, H. F. Yang, C. R. Rajamathi, Y. P. Qi, L. X. Yang, C. Chen, H. Peng, C. C. Hwang, S. Z. Sun, S. K. Mo, I. Vobornik, J. Fujii, S. S. Parkin, C. Felser, B. H. Yan, and Y. L. Chen, "Signature of type-II Weyl semimetal phase in $MoTe_2$," Nat. Commun. **8**, 1–6 (2017).

[136] K. Kuroda, T. Tomita, M. T. Suzuki, C. Bareille, A. A. Nugroho, P. Goswami, M. Ochi, M. Ikhlas, M. Nakayama, S. Akebi, R. Noguchi, R. Ishii, N. Inami, K. Ono, H. Kumigashira, A. Varykhalov, T. Muro, T. Koretsune, R. Arita, S. Shin, T. Kondo, and S. Nakatsuji, "Evidence for magnetic weyl fermions in a correlated metal," Nature Materials **16**, 1090 EP – (2017).

[137] B. Q. Lv, H. M. Weng, B. B. Fu, X. P. Wang, H. Miao, J. Ma, P. Richard, X. C. Huang, L. X. Zhao, G. F. Chen, Z. Fang, X. Dai, T. Qian, and H. Ding, "Experimental discovery of weyl semimetal TaAs," Phys. Rev. X **5**, 1–8 (2015).

[138] C.-H. Min, H. Bentmann, J. N. Neu, P. Eck, S. Moser, T. Figgemeier, M. Ünzelmann, K. Kissner, P. Lutz, R. J. Koch, C. Jozwiak, A. Bostwick, E. Rotenberg, R. Thomale, G. Sangiovanni, T. Siegrist, D. Di Sante, and F. Reinert, "Orbital fingerprint of topological fermi arcs in the weyl semimetal TaP," Phys. Rev. Lett. **122**, 116402 (2019).

[139] S.-M. Huang, S.-Y. Xu, I. Belopolski, C.-C. Lee, G. Chang, B. Wang, N. Alidoust, G. Bian, M. Neupane, C. Zhang, S. Jia, A. Bansil, H. Lin, and M. Z. Hasan, "A Weyl Fermion semimetal with surface Fermi arcs in the transition metal monopnictide TaAs class," Nature Communications **6**, 7373 EP – (2015).

[140] T. Ohtsuki, Z. Tian, A. Endo, M. Halim, S. Katsumoto, Y. Kohama, K. Kindo, M. Lippmaa, and S. Nakatsuji, "Strain-induced spontaneous hall effect in an epitaxial thin film of a luttinger semimetal," Proceedings of the National Academy of Sciences **116**, 8803 (2019).

[141] L. Lu, L. Fu, J. D. Joannopoulos, and M. Soljacic, "Weyl points and line nodes in gyroid photonic crystals," Nature Photonics **7**, 294 EP – (2013), article.

[142] T. Dubček, C. J. Kennedy, L. Lu, W. Ketterle, M. Soljačić, and H. Buljan, "Weyl points in three-dimensional optical lattices: Synthetic magnetic monopoles in momentum space," Phys. Rev. Lett. **114**, 225301 (2015).

[143] P. Kotetes, M. T. Mercaldo, and M. Cuoco, "Synthetic weyl points and chiral anomaly in majorana devices with nonstandard andreev-bound-state spectra," Phys. Rev. Lett. **123**, 126802 (2019).

[144] L. Crippa, A. Amaricci, N. Wagner, G. Sangiovanni, J. C. Budich, and M. Capone, "Nonlocal annihilation of weyl fermions in correlated systems," Phys. Rev. Research **2**, 012023 (2020).

[145] A. Turner and A. Vishwanath, *Topological Insulators: Chapter 11. Beyond Band Insulators: Topology of Semimetals and Interacting Phases*, Contemporary Concepts of Condensed Matter Science (Elsevier Science, 2013).

[146] H. Nielsen and M. Ninomiya, "Absence of neutrinos on a lattice: (ii). intuitive topological proof," Nuclear Physics B **193**, 173 – 194 (1981).

[147] X. Wan, A. M. Turner, A. Vishwanath, and S. Y. Savrasov, "Topological semimetal and fermi-arc surface states in the electronic structure of pyrochlore iridates," Phys. Rev. B **83**, 205101 (2011).

[148] V. Dwivedi and S. T. Ramamurthy, "Connecting the dots: Time-reversal symmetric weyl semimetals with tunable fermi arcs," Phys. Rev. B **94**, 245143 (2016).

[149] H. B. Nielsen and M. Ninomiya, "ADLER-BELL-JACKIW ANOMALY AND WEYL FERMIONS IN CRYSTAL," Phys. Lett. B **130**, 389–396 (1983).

[150] P. Hosur and X. Qi, "Recent developments in transport phenomena in weyl semimetals," Comptes Rendus Physique **14**, 857 – 870 (2013), topological insulators / Isolants topologiques.

[151] H.-J. Kim, K.-S. Kim, J.-F. Wang, M. Sasaki, N. Satoh, A. Ohnishi, M. Kitaura, M. Yang, and L. Li, "Dirac versus weyl fermions in topological insulators: Adler-bell-jackiw anomaly in transport phenomena," Phys. Rev. Lett. **111**, 246603 (2013).

[152] A. G. Grushin, "Consequences of a condensed matter realization of lorentz-violating qed in weyl semi-metals," Phys. Rev. D **86**, 045001 (2012).

[153] S. A. Parameswaran, T. Grover, D. A. Abanin, D. A. Pesin, and A. Vishwanath, "Probing the chiral anomaly with nonlocal transport in three-dimensional topological semimetals," Phys. Rev. X **4**, 031035 (2014).

[154] A. Amaricci, J. C. Budich, M. Capone, B. Trauzettel, and G. Sangiovanni, "Strong correlation effects on topological quantum phase transitions in three dimensions," Phys. Rev. B **93**, 235112 (2016).

[155] C. J. Tabert and J. P. Carbotte, "Optical conductivity of weyl semimetals and signatures of the gapped semimetal phase transition," Phys. Rev. B **93**, 085442 (2016).

[156] A. Amaricci, J. C. Budich, M. Capone, B. Trauzettel, and G. Sangiovanni, "First-Order Character and Observable Signatures of Topological Quantum Phase Transitions," Phys. Rev. Lett. **114**, 185701 (2015).

[157] R. Resta, "Macroscopic polarization in crystalline dielectrics: the geometric phase approach," Rev. Mod. Phys. **66**, 899–915 (1994).

[158] P. Werner and A. J. Millis, "High-Spin to Low-Spin and Orbital Polarization Transitions in Multiorbital Mott Systems," Phys. Rev. Lett. **99**, 126405 (2007).

[159] M. Capone, L. de' Medici, and A. Georges, "Solving the dynamical mean-field theory at very low temperatures using the lanczos exact diagonalization," Phys. Rev. B **76**, 245116 (2007).

[160] C. Dahnken, M. Aichhorn, W. Hanke, E. Arrigoni, and M. Potthoff, "Variational cluster approach to spontaneous symmetry breaking: The itinerant antiferromagnet in two dimensions," Phys. Rev. B **70**, 245110 (2004).

[161] A. A. Soluyanov and D. Vanderbilt, "Computing topological invariants without inversion symmetry," Phys. Rev. B **83**, 235401 (2011).

[162] V. Gurarie, "Single-particle green's functions and interacting topological insulators," Phys. Rev. B **83**, 085426 (2011).

[163] G. E. Volovik, "Quantum phase transitions from topology in momentum space," in *Quantum Analogues: From Phase Transitions to Black Holes and Cosmology*, edited by W. G. Unruh and R. Schützhold (Springer Berlin Heidelberg, Berlin, Heidelberg, 2007) pp. 31–73.

[164] D. Sénéchal, "Bath optimization in the cellular dynamical mean-field theory," Phys. Rev. B **81**, 235125 (2010).

[165] J. C. Budich, B. Trauzettel, and G. Sangiovanni, "Fluctuation-driven topological hund insulators," Phys. Rev. B **87**, 235104 (2013).

[166] M. Potthoff, "Static and dynamic variational principles for strongly correlated electron systems," AIP Conference Proceedings **1419**, 199–258 (2011).

[167] Y. Ando, "Topological insulator materials," Journal of the Physical Society of Japan **82**, 102001 (2013).